Stability Analysis and Control of DC-DC Converters using Nonlinear Methodologies

Haimeng Wu

B.Sc., M.Sc.

A thesis submitted for the degree of

Doctor of Philosophy

May, 2016

School of Electrical and Electronic Engineering

Newcastle University

United Kingdom

Abstract

Switched mode DC-DC converters exhibit a variety of complex behaviours in power electronics systems, such as sudden changes in operating region, bifurcation and chaotic operation. These unexpected random-like behaviours lead the converter to function outside of the normal periodic operation, increasing the potential to generate electromagnetic interference degrading conversion efficiency and in the worst-case scenario a loss of control leading to catastrophic failure.

The rapidly growing market for switched mode power DC-DC converters demands more functionality at lower cost. In order to achieve this, DC-DC converters must operate reliably at all load conditions including boundary conditions. Over the last decade researchers have focused on these boundary conditions as well as nonlinear phenomena in power switching converters, leading to different theoretical and analytical approaches. However, the most interesting results are based on abstract mathematical forms, which cannot be directly applied to the design of practical systems for industrial applications.

In this thesis, an analytic methodology for DC-DC converters is used to fully determine the inherent nonlinear dynamics. System stability can be indicated by the derived Monodromy matrix which includes comprehensive information concerning converter parameters and the control loop. This methodology can be applied in further stability analysis, such as of the influence of parasitic parameters or the effect of constant power load, and can furthermore be extended to interleaved operating converters to study the interaction effect of switching operations. From this analysis, advanced control algorithms are also developed to guarantee the satisfactory performance of the converter, avoiding nonlinear behaviours such as fast- and slow-scale bifurcations. The numerical and analytical results validate the theoretical analysis, and experimental results with an interleaved boost converter verify the effectiveness of the proposed approach.

Keywords- Nonlinear Analysis, Stability, Bifurcation, DC-DC Boost Converters, Monodromy Matrix

Acknowledgement

Contents

Table of Figures

Symbols

A	State matrix
B	System matrix
C	Capacitor
D	Diode
d	Duty cycle
eig	Eigenvalues
f	Switching frequency
g	Mapping Functions
f	Vector field
$f_{\Sigma-}$	Vector field before switching
$f_{\Sigma+}$	Vector field after switching
h=0	Switching condition or hyper-surface or switching manifold
I	Identity matrix
i_L	Inductor current
I_{ref}	Reference current
K_i	Gain of integral
K_P	Gain of proportional
K_D	Derivative coefficient
K_{vc}	Gain of voltage sensor
K_{iL}	Gain of current sensor
L	Inductance
M	Monodromy Matrix
m_c	Slope of compensation ramp
a_c	Amplitude of slope compensation ramp m_c
a_m	Amplitude of compensation signal m_a
n	Normal form

n	Number of variables
P	Output power
R	Resistance
R_s	Conduction resistance of switches
R	State space
S	Switching device
S	Saltation Matrix
T	One clock switching period
u	External input
V_{con}	Control voltage
V_i	Input voltage
v_{ip}	output of the integrator
V_c	Output voltage
x	State vector (State variables)
φ	Flow
μ	Vector parameters
Φ	Fundamental solution matrix
Σ	Hyper-surface or switching manifold

Abbreviations

AC	Alternating Current
CCM	Continuous Conduction Mode
CCS	Code Composer Studio
CMC	Current Mode Control
CPL	Constant Power Load
DAC	Digital to Analogue Converter
DC	Direct Current
DCM	Discontinuous Conduction Mode

DDS	Direct Digital Synthesizer
DPWM	Digital Pulse-Width-Modulator
DSCs	Digital Signal Controllers
DSP	Digital Signal Processor
EMC	Electromagnetic Compatible
EMI	Electromagnetic Interference
ESR	Equivalent Series Resistance
FPGA	Field Programmable Gate Array
EV	Electric Vehicle
GPIO	General Purpose Input and Output
HEV	Hybrid Electric Vehicle
ISR	Interrupt Service Routine
LTI	Linear Time Invariant
PWM	Pulse Width Modulation
PCM	Peak Current Mode
PI	Proportional and Integral
PID	proportional-integral-derivative
PV	Photovoltaic
SPI	Serial Peripheral Interface
SRAM	Static Random-access Memory
STM	State Transition Matrix
SWC	Sinewave Compensation
TDFC	Time Delayed Feedback Control
UPOs	Unstable Periodic Orbits
VSC	Variable Slope Compensation
FFT	Fast Fourier Transform
QCSC	Quadratic Curve Slope Compensation

1 Introduction

1.1 Background

Power electronics is an application-oriented discipline that copes with the conversion and control of electrical power, which is applied in many areas such as commercial, residential, telecommunications, transportation, aerospace and utility applications. After more than four decades of technological evolution, power electronics is now one of the most significant branches in the field of electrical engineering. Key drivers of this evolution were improvements in power semiconductor technologies, control methods, packaging techniques and circuit topologies. In power electronics systems, a power converter is designed in order to match the input requirements with the output requirements. Thus power converters are able to transform AC input values into DC output values in a controlled manner or vice versa. They can also be designed to change AC to AC and DC to DC as illustrated in Figure 1.1.
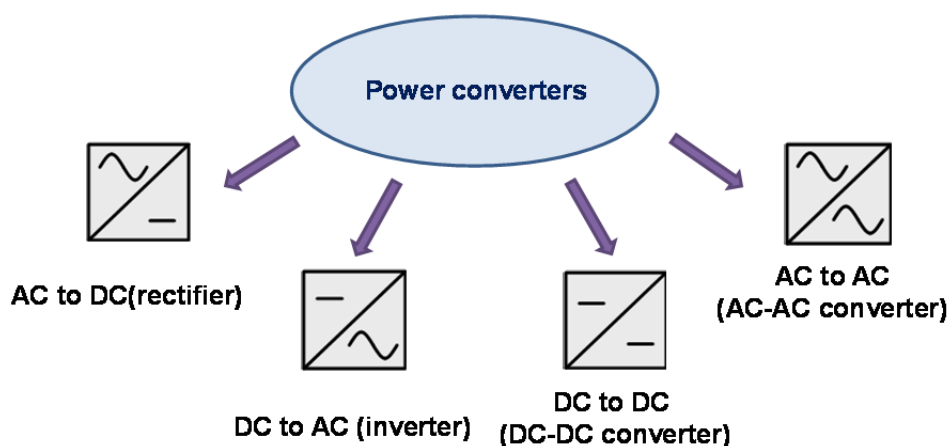
Figure 1.1 Types of power converters

However, although DC-DC converters are widely used in many applications, most of them have been designed without the consideration of switching actions. DC-DC converters are inherently nonlinear and piecewise smooth systems which show a variety of nonlinear phenomena such as bifurcation that can lead to sub-harmonics and chaos when circuit parameters are varied. Thus can lead to challenges for power electronics engineers to deal with these complex behaviours in the course of product design. Without thorough knowledge of existing circuits, experience-based trial-and-error procedures are often applied in practical applications to guarantee that the circuits work in the expected operating region [1]. As a result, circuit designs and the

components and parameters used are adjusted accordingly to fulfil given criteria based on lessons learned from the past rather applying an appropriate systematic design methedology.

1.2   Nonlinear phenomena in power switching converters
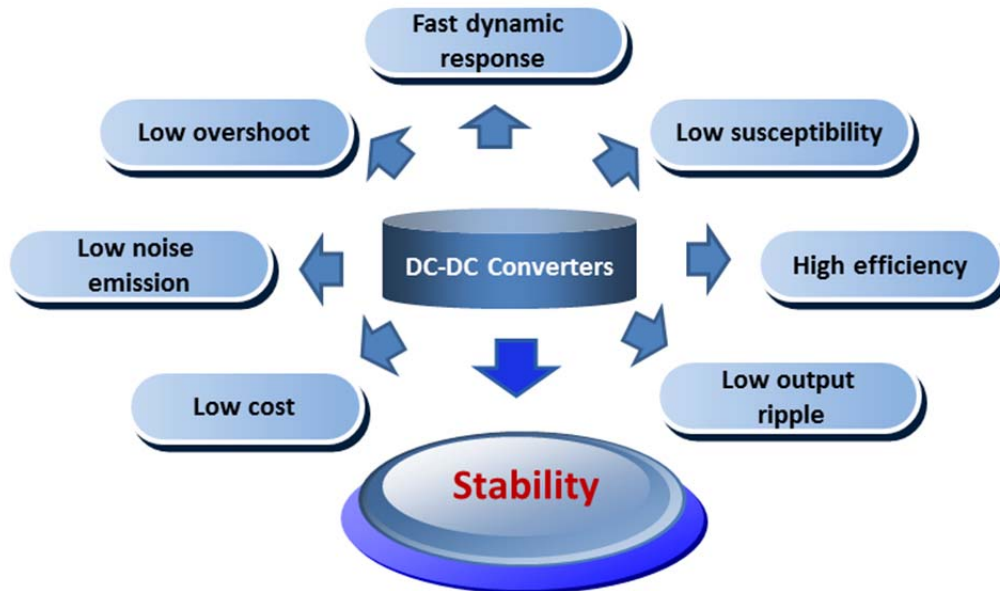
Figure 1.2 General requirements of high-performance power DC-DC converters

The general requirements of high-performance DC-DC converters are shown in Figure 1.2. Expected features are described as low cost, low output voltage ripple and low overshoot, low susceptibility, fast dynamic response, high conversion efficiency and stability. Among these features, system stability is essential in power converter design, and determines whether the converters can run reliably. Due to the inherent switching action of the circuit, there is a periodic oscillation around a predefined value in the steady-state operating point of any DC-DC converter. However, when a converter operates in an unexpected mode such as bifurcation or chaotic mode, the amplitudes of voltage and current will vary dramatically, accompanying an increase in losses which consequently results in efficiency deficits. In addition, it is highly likely that electromagnetic interference (EMI) will arise, causing the converter to malfunction and in the worst case can cause the complete loss of the converter. Hence, gaining full knowledge of the stability of DC-DC converters will guarantee satisfactory performance.

A typical DC-DC converter is comprised of power switches, passive components,

diodes and control circuits. Normally, in order to regulate the output of the converter and achieve the required conversion, the switches and other components are utilized to chop and restructure the electric power, and these are controlled by control circuits. In the process of the operational analysis of the converter, even though each subinterval of operation can be characterized by a linear circuit, the switching action itself makes the converter model a highly nonlinear system which is much harder to solve analytically than with linear circuits. Conventionally, most power electronics practitioners employ the linearized averaging technique for the analysis of power converters using the framework of linear systems theory, and thus discontinuities introduced by the switching action of the circuit are ignored. In fact, the switching action is strongly related to the system's fast scale stability. Because of a lack of knowledge on the nonlinearities caused by switching, some converter components which are chosen to guarantee the stable operation of the system are significantly oversized, giving a larger, more expensive and less efficient product.

Nonlinearities of power electronics circuits have attracted considerable research attention. Fundamental research work on the nonlinear phenomena of power electronics commenced approximately from the late 1980's. After Brockett and Wood [2] first described the phenomena of bifurcation and chaos in a controlled DC-DC buck converter in 1984, Hamill et al [3] extended their work in a more detailed study of this nonlinear phenomena using an iterative mapping approach [4], where the chaotic operation of the buck converter was demonstrated by simulation and validated in experiments. Krein and Bass [5] reported on the nonlinear behaviour of unboundedness, chattering and chaos in a simple power electronics circuit. Since then, much interest has been directed to the investigation of complex phenomena observed in power electronics [6, 7]. In 1994, Tse [8] described the nonlinear dynamics of simple feedback boost converters operating in discontinuous mode, exhibiting a typical period-doubling route to chaos under specific operating conditions. Fossas and Olivar [9] studied the dynamics of the buck converter analytically in detail, identifying the topology of its chaotic attractor and investigating the evolution of trajectories when close to the attractors. Banerjee [10] reported the coexisting attractors in voltage mode controlled buck converters, and Di Bernardo [11, 12] explained the transitions of sudden jumps from periodic solutions to chaos due to border collisions rather than standard bifurcations such as "period-doubling"

and "saddle-node".

Many researchers have extended this research field from simple basic DC-DC converters, such as buck [13-15], boost [16-18], buck-boost [19-21], and Cuk converters [22-24] to forward [25, 26] and parallel connected converters [27-29]; from AC-DC power factor converters [30-32] and resonant converters [33, 34] to DC-AC inverters [35-37] and interleaved converters [38-40]. These studies report a variety of complex behaviours such as bifurcation, chaos, attractors, and border collisions. Some mechanisms causing these nonlinear phenomena have been examined, and the evaluation of dynamic behaviour has been studied when some circuit parameters are varied.

1.3   Previous work on nonlinear analysis in power switching converters

To study and analyse the inherent stability of these power converters, prominent stability analysis techniques for DC-DC converters are illustrated in Figure 1.3. The state-space averaging technique [27, 28, 41, 42] is widely used by converter designers to estimate the stability and dynamic behaviour of power converters. In this method, the actual nonlinear system is linearized around a steady-state operating point to yield a linear model. This gives a simple and accurate model at slow timescale, but fails to predict nonlinear behaviour at a fast timescale. Nonlinear behaviours can be generally classified into two categories at slow and fast timescales. Slow timescale means that the dynamic behaviour investigated is much slower than the switching frequency, whereas fast timescale means that the dynamic behaviour investigated is around the switching frequency. For example, fast timescale instability refers to nonlinear phenomena such as period-doubling bifurcation and slow timescale instability includes nonlinear behaviour such as Hopf bifurcation. The conventional averaging methodology was extended in frequency-dependent averaged models [43] by taking into account the effect of fast-scale dynamics. A multi-frequency averaging approach [44-46] was then proposed to improve the conventional state-space averaging models, modelling the dynamic behaviour of pulse width modulation (PWM) controlled DC–DC converters by applying and expanding the frequency-selective averaging method [47]. An analysis method based on the Krylov-Bogoliubov-Mitropolsky (KBM) algorithm [48] was developed to recover the ripple components of state variables from the averaged model.

However, even such improved models cannot describe chaotic dynamics completely and effectively. To address fast-scale nonlinearities, discrete nonlinear modelling is the most widely used approach. Nonlinear map-based modelling [4, 11, 12, 35, 49-51] developed from sampled-data modelling [52-54] in the early stages applies an iterative map for the analysis of system stability which is obtained by sampling the state variables of the converter synchronously with PWM clock signals. This method is commonly referred to as the Poincaré map method and the maps generated can be classified into stroboscopic, S-switching and the A-switching maps according to the different samplings moment. Stability is indicated by the eigenvalues of the fixed point of the Jacobian of the map, even though in some cases the map itself cannot be derived in close-form because of the transcendental form of the system's equations. Hence the map has to be obtained numerically.
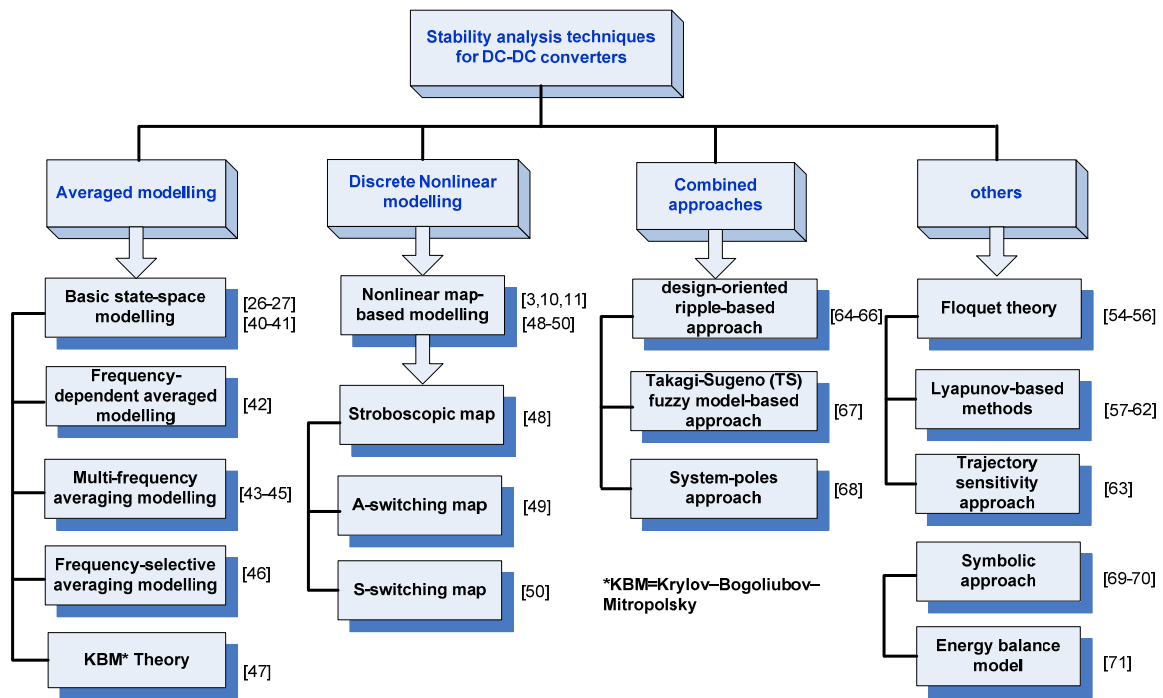
Figure 1.3 Stability analysis techniques for power switching converters

Other alternative approaches such as Floquet theory [18, 55-57], Lyapunov-based methods [58-63] and the trajectory sensitivity approach [64] have been applied effectively for the nonlinear analysis of power converters. Specifically, the evolution of perturbation is studied directly in Floquet theory to predict system stability, by deriving the absolute value of the eigenvalues of the complete-cycle solution matrices. In Lyapunov-based methods, piecewise-linear Lyapunov functions are searched for and constructed to describe system stability. For the trajectory sensitivity approach, systems are linearized around a nominal trajectory rather than around an equilibrium

point and stability can be determined by observing the change in a trajectory due to small initial or parameter variations. There also have some combined approaches developed from state-space averaging and discrete modelling. Examples of these methods are the design-oriented ripple-based approach [65-67]; Takagi–Sugeno (TS) fuzzy model-based approach [68] and system-poles approach [69]. Apart from the aforementioned approaches, other individual methods, such as the symbolic approach [70, 71] and energy balance model [72], have been proposed to analyse the nonlinearities of switching power converters. A recent review paper on stability analysis methods for switching mode power converters has summarised some approaches presented [73].

1.4   Previous nonlinear control methods in power switching converters

Based on the above methodologies, various control techniques are proposed to tackle nonlinear behaviours, and these can be classified into two categories: feedback-based and non-feedback based techniques. In the former group, in order to achieve stable control, a small time-dependent perturbation is tailored to make the system operation change from unstable periodic orbits (UPOs) to targeted periodic orbits. The first well-known chaos control method was proposed by Ott et al [74], named the Ott-Grebogi-Yorke (OGY) approach. One advantage of this method is that a priori analytical knowledge of the system dynamics is not required, which makes it easier to implement. Then, Pyragas [58, 75] presented an extended delay feedback control technique to stabilise the UPOs in dynamic systems over a large domain of parameters. Some further extended studies of those approaches have also been published [76, 77]. Batlle et al [78] introduced the time-delay stabilization approach for the buck converter for the first time. After that, an alternative chaos controlling approach, called the linear Time Delayed Feedback Control (TDFC) method, was proposed to stabilize the UPOs in the field of nonlinear dynamics [79-82]. In this method, the information of the current state and prior one-period state is used to generate signals for the stabilizing control algorithm. This technique has been further studied [83-85], and washout filter-aided feedback control [86-88] was proposed to address the Hopf bifurcation of dynamic systems. The benefits, limitations and extensions of this method have been summarised in [89]. Other filter-based non-invasive methods for the control of chaos in power converters have also been proposed [15, 90, 91]. Apart from the aforementioned control methods, a self-stable

chaos-control method [92], predictive control [93], frequency-domain approach [94], two-parameter chaotic control [14], and a chaotic particle swarm optimization (PSO) algorithm [95] have been proposed to eliminate bifurcations and chaotic behaviour in various switching DC-DC converters.
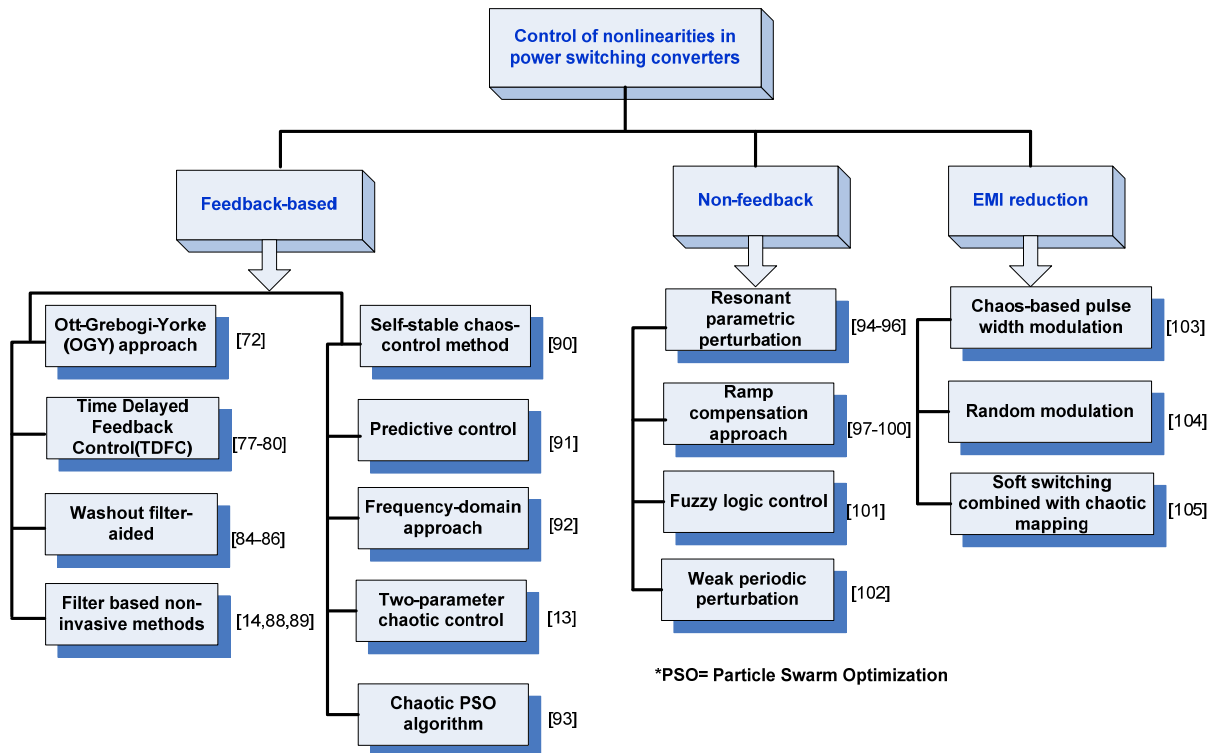
Figure 1.4 Control of nonlinearities in power switching converters

In the non-feedback category, the control target is not set at the particular desired operating state, whereas the chaotic system can be converted to any periodic orbit. Resonant parametric perturbation [96-98] is one of the most popular methods. In this approach, some parameters at appropriate frequencies and amplitude are normally perturbed to induce the system to stay in stable periodic regions, converting the system dynamic to a periodic orbit. Other examples of this type of method include the ramp compensation approach [99-102],fuzzy logic control [103] and weak periodic perturbation [104]. Compared to feedback-based methods, no online monitoring and processing are required in a non-feedback approach, which makes it easy to implement and suitable for specific practical applications.

Chaotic operation is usually undesirable in switching DC-DC converters because it may cause EMI and additional power losses due to the higher current and voltage ripples. However, some researchers believe that chaotic behaviours are not always harmful; they may have benefits for power converters in some cases, including even

to reduce EMI. The methods of chaos-based pulse width modulation [105], random modulation [106], and soft switching combined with chaotic mapping [107] have been proposed for the EMI reduction, and are displayed in Figure 1.4. It is shown that, at some chaotic modes, the converter fulfils Electromagnetic Compatible (EMC) standards without adding any filters [108, 109]. This concept of the "anti-control of chaos" has attracted increasing attention in recent years due to its potentially wide application.

1.5   Objectives

The phenomena of bifurcation and chaos are ubiquitous in circuits and systems of power electronics. In such systems, when some selected parameters (input, output rate and load condition, etc) change, the system tends to produce nonlinear behaviours, such as period-doubling bifurcation, Hopf bifurcation, coexisting attractors and boundary collision. The study of power electronic systems in terms of the bifurcation behaviour recognition is already relatively mature so far. Many studies have reported various bifurcation behaviours and revealed the inherent theoretical parameters and causes and effects of bifurcation. In recent years, researchers have begun to explore potential applications of the complex behaviour existing in power electronic systems in the field of industrial power electronics. One research interest is to apply the current research outcomes to cope with the bifurcation behaviour of practical power electronic systems. However, the most interesting results for bifurcation behaviour is basically based on abstract mathematical forms, which cannot be directly and effectively applied to the design of practical systems for industrial application. Thus relatively intuitional and design-oriented approaches are needed in the future study and research work.

The work in this thesis focuses on the stability analysis and control of fast timescale nonlinear behaviour in DC-DC switching converters, aiming to increase the knowledge of nonlinear modelling and to fill gaps in theoretical research and practical application. The nonlinear analysis method based on Monodromy matrix is utilized in this research, which enables a deeper understanding of boundary operation conditions to be gained. It helps in the development of new control methods that can be applied to address instability issues. Furthermore, this design-oriented method provides an alternative useful design concept from the perspective of fast-scale

stability, which shows its potentials in practical applications.

1.6   Contribution to knowledge

The main original contributions of this research work are as follows:

- The Monodromy matrix-based nonlinear analysis method is applied for the first time to investigate the influence of parasitic parameters on the fast-scale stability and to study DC-DC converters with constant power load with different operation modes and control algorithms.

- A nonlinear analysis method is developed to study the higher order topology with more complex control algorithms such as in interleaved boost converters, which fully reveals the interaction effect of switching operations on system stability.

- A new mixed signal technique is proposed to achieve digital peak current control, which is successfully implemented in the test platform. The experimental results demonstrate the effectiveness of the proposed approach for the nonlinear analysis of power switching converters.

- Two effective control methods: a real time cycle to cycle variable slope compensation control and an improved quadratic curve slope compensation control are developed based on the knowledge of the derived Monodromy matrix to control the nonlinearity of DC-DC converters.

- A control method is proposed for the first time to stabilise the nonlinear behaviour of boost DC-DC converters with reduced inductance.

Most of the above outcomes have been published in the following papers:

[1]   **Haimeng Wu**, Volker Pickert, Damian Giaouris, "Nonlinear analysis and control for an interleaved boost converter based on the Monodromy matrix" *Energy Conversion Congress and Exposition (ECCE) 2014*, IEEE, Pittsburgh, USA,2014

[2]   **Haimeng Wu**, Volker Pickert "Stability analysis and control of nonlinear phenomena in bidirectional boost converter based on the Monodromy matrix" *Applied Power Electronics Conference and Exposition (APEC) 2014*, IEEE, Page(s): 2822-2827, 2014.

[3]   **Haimeng Wu,** Volker Pickert, Simon Lambert, Xiang Lu "Nonlinear analysis of boost converters with constant power loads at different modes of operation" *The 8th IET International Conference on Power Electronics, Machines and Drives 2016*, Glasgow, UK,2016 (Accepted)

1.7   Overview of the thesis

This thesis analyses the stability of DC-DC converters and control of nonlinear behaviour using the Monodromy matrix. The research starts from single phase boost converters with consideration given to parasitic parameters. Then work is extended to boost converters with constant power load. Based on the research findings from prior work, further research is carried out with interleaved boost converter. The theoretical study is presented in detail and is validated numerically and experimentally.

The thesis is structured as follows:

Chapter 2 presents general knowledge concerning the nonlinear dynamics of systems and methods for the analysis of power switching converters, including identification approaches and modelling strategies. In addition, the fundamental principles of the Monodromy matrix-based method are illustrated and the characterization of nonlinear systems behaviour in terms of various measurable properties is discussed.

In chapter 3, the proposed method is employed in a study of the influence of external and parasitic parameters on system stability in a bidirectional boost converter applying peak current control. Furthermore, based on knowledge of the Monodromy matrix of the system, a new control algorithm is proposed to address nonlinear phenomena and to expand the range of stable operation.

Chapter 4 demonstrates that this method of nonlinear analysis is effective in the stability analysis of power switching converters with constant power load and different operational modes and control algorithms. Theoretical and simulation-based analyse of a single phase boost converter with constant power load are presented in this chapter.

In chapter 5, an analysis is conducted of interleaved boost converters, which have a higher order topology and more complex interleaving operation compared with single-phase converters. The Monodromy matrix is employed to fully determine the understanding of the inherent nonlinear dynamics of these converters, and especially for the interaction effect of switching operations. The derivation of the Monodromy matrix at different operational conditions and a study of the control loop are presented and illustrated accordingly.

Chapter 6 proposes a new mixed signal technique for digital peak current control, which contains a DSP controller with an external high performance waveform generator. The design of hardware and corresponding software of the test system is described in detail, and experimental results demonstrate that this system works effectively for the nonlinear analysis of power switching converters.

In chapter 7, the influence of slope amplitude at conventional fixed slope compensation and sinewave compensation is studied theoretically and experimentally. A real-time cycle to cycle variable slope compensation (VSC) control method and improved quadratic curve slope compensation (QCSC) control are proposed to control the nonlinearity of DC-DC converters and to guarantee that converter operation remains stable, avoiding fast- and slow-scale bifurcations. Furthermore, a case study of reduced inductance in interleaved boost converters shows the potential of the used nonlinear analysis method in practical applications.

Finally, the conclusions of the study and recommendations for future research to extend the current findings are discussed in the chapter 8.

2 Overview of nonlinear dynamical analysis for power switching converters

This chapter presents general background knowledge concerning power electronics systems, including description methods in dynamical systems and modelling strategies. Stability analysis approaches based on equilibrium points and periodic solution are discussed and in particular the conventional Poincaré map approach and Monodromy matrix based method from Filippov's theory are demonstrated in detail. Moreover, the nonlinear system behaviour and the characterization of systems in terms of some measurable properties are discussed at the end of this chapter.

2.1   Description of power electronics system

Most power electronics systems are hybrid dynamic systems that exhibit both continuous and discrete characteristics to some extent. For example, during the switching event of a power switch, the power electronics system experiences a discrete change whereas before and after the switching event the circuit operates in continuous modes. In continuous-time systems, differential equations are commonly used to express the evolution of the system, and the system variables are real numbers that vary continuously in time. In contrast, in discrete-time systems, iterated maps or difference equations are usually employed to describe the system behaviour. The evolution of systems is represented at a set of discrete times and the effects of continuous evolution are expressed as discrete jumps from one system state to another. Power electronics systems can also be identified as piecewise-smooth dynamical systems (or non-smooth dynamical systems) according to the appropriate mathematical definition and representation, since they are discontinuous systems described by differential equations with discontinuities at the right-hand side.

In mathematics, a linear system is defined as a general deterministic system that can be described by an identity linear map (also called a linear transformation or linear function). It satisfies the properties of homogeneity and additivity that are called the superposition principle [110]. Power electronics systems, however, belong to the group of nonlinear systems and therefore do not satisfy this superposition principle. Specifically, there is no directly proportional relationship between the output of a

nonlinear system and its input.

A dynamical system can be classified as an autonomous or non-autonomous system according to whether or not it is independent of time. If the system equations are time-independent, the system is referred to as an autonomous system; otherwise, it is non-autonomous.

2.2   Power switching converters
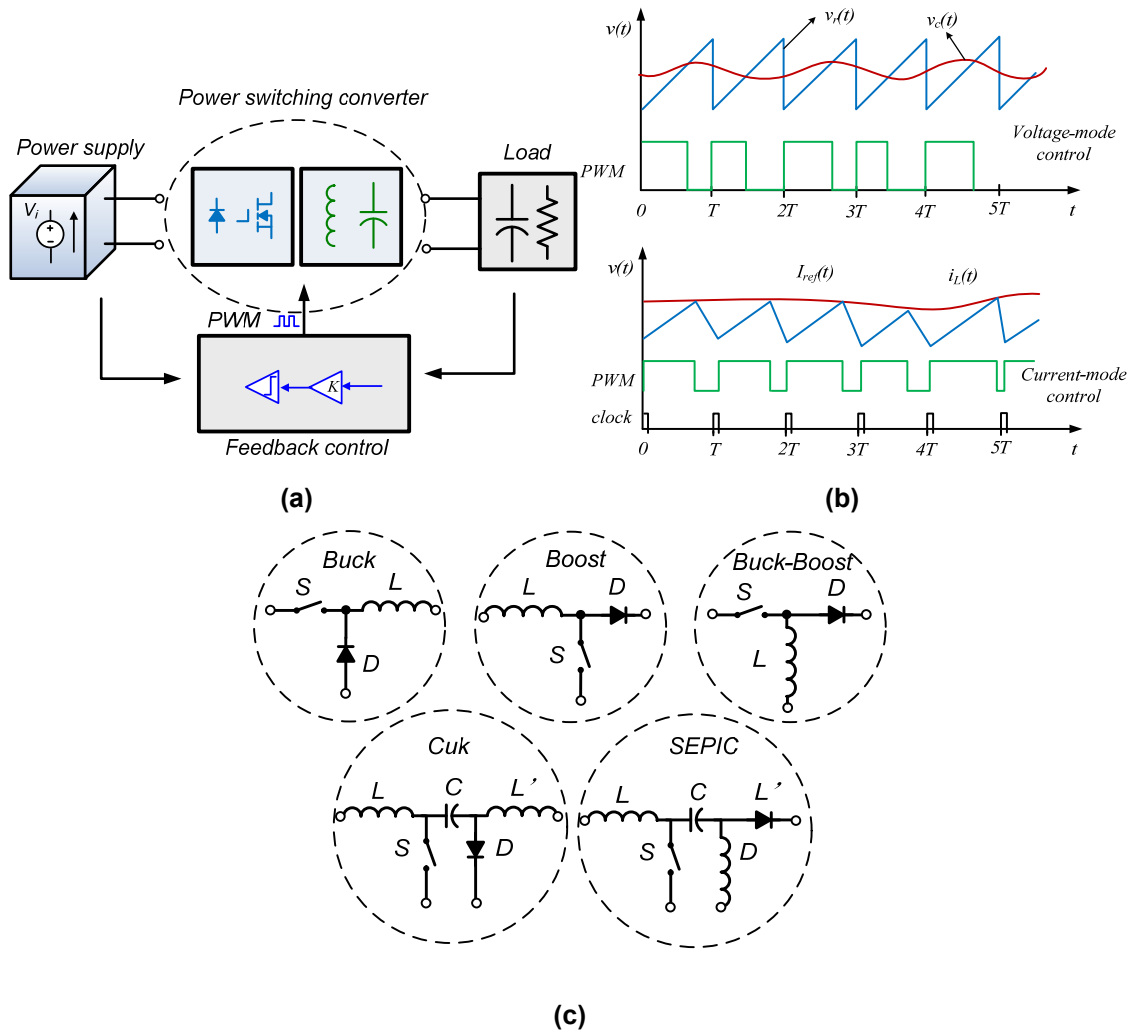
Figure 2.1 Power electronics systems
(a) Diagram of a power converter system (b) voltage-mode and current-mode control
(c) Typical elementary non-isolated DC-DC power switching converters

Power switching converters normally consist of power switches, diodes and passive components such as capacitors, inductors and transformers, and convert the electrical power from the power supplies to various loads. Power circuits operate by toggling among a set of circuit topologies at subintervals, due to the actions of active power switches. Feedback controls such as voltage-mode or current-mode control (as shown in Figure 2.1(b)) are usually employed in system to regulate the duty cycle

of switches, so as to achieve the required power output. A typical diagram of the structure of a power converter system is shown in Figure 2.1 (a); and the topologies of the elementary non-isolated DC-DC power switching converters, the buck, boost, buck-boost, Cuk and SEPIC converters, are illustrated in Figure 2.1 (c).

In power switching converters, the voltage across capacitors, currents through inductors and other time-dependent parameters are generally used as state variables to represent the system. External periodic clock signals are commonly required for pulse width modulation (PWM) in power electronics systems, which lead the state variables to be functions of the switching frequency; hence, most power electronics systems are non-autonomous dynamical systems.

2.3   Modelling approaches for power switching converters

In many practical engineering applications, physical systems are often modelled and simplified as linear systems, approximated by linear equations. Therefore, classical automatic control theory can be employed for system analysis.
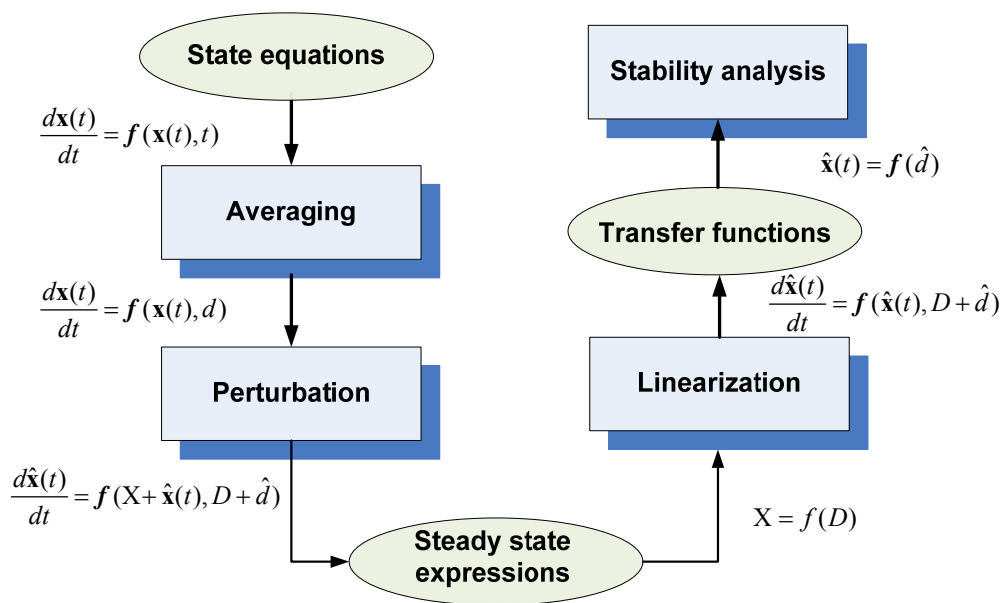
Figure 2.2 Procedural diagram of the state-space averaging approach

The general procedural diagram of the state-space averaging approach is illustrated in Figure 2.2. The state equations of the system are employed to obtain the steady-state expressions through the process of averaging and perturbation. The system is linearized at this steady-state operating point to generate the transfer functions which

represent the small-signal behaviour of the system. Hence the stability of the system can be analysed using the Bode magnitude and phase plot in the frequency domain. As we know, most systems are inherently nonlinear in nature, and the nonlinear equations of a system are always difficult to solve. Although the process of linearization makes the study of these systems more efficient and easier, the investigation of some of the nonlinear phenomena which are hidden by linearization is not possible. In power electronics circuits, switching components (such as power switches and diodes), nonlinear inductors or transformers, and nonlinear components in control circuits can be sources of nonlinearity [111]. Active switches are operated in turn-on and turn-off states in response to feedback signals depending on the state variables. The diodes are operated as passive switches with highly nonlinear v-i characteristics. The nonlinear properties of transformers and choke inductors bring potential unwanted nonlinearity into practical applications. In addition, the comparators, amplifiers and digital controllers involved in control circuits are also nonlinear components which produce further issues of nonlinearity.

The following differential equation is commonly used to describe a continuous-time dynamical system.

$$\dot{\mathbf{x}}(t) = \frac{d\mathbf{x}(t)}{dt} = f(\mathbf{x}(t), \mu, t) \tag{2.1}$$

where $\mathbf{x}(t) = (x_1, x_2, x_3 \ldots x_n)^T \in \mathbb{R}^n$ are the system variables (state vectors), and all state variables constitute state space $\mathbb{R}^n$; $f = (f_1, f_2, f_3 \ldots f_n)^T$ refers to the connecting function; and μ is a vector of the parameters. For the initial condition $\mathbf{x}(t_0) = \mathbf{x}_0$, the vector field **f** can produce an n-dimension flow of the dynamical system $\mathbf{x}(t) = \varphi(x_0, t)$, which is the solution of the system. The differential equation for the general solution of system can be expressed as follows:

$$\mathbf{x}(t) = \Phi(x_0, t)\mathbf{x}(t_0) \tag{2.2}$$

where $\Phi(x_0, t)$ is the fundamental solution matrix, describing the evolution of system variables related to the initial conditions. For a discrete-time dynamical system, the following expression can be employed to describe the relationship of the system state with regard to the discrete time:

$$\mathbf{x}(n+1) = g(\mathbf{x}(n), n) \tag{2.3}$$

where $x(\text{n}) = (x_{1n}, x_{2n}, x_{3n} \ldots x_{nn})^T \in \mathbb{R}^n$ represents the state variables at time of t_n (n=1,2, $\cdots$) and function $g = (g_1, g_2, g_3 \ldots g_n)^T$ maps the relationship between the current state x(n) and the next state x(n+1).

2.4 Stability of the equilibrium points solution

In Lyapunov's stability theory [110], the stability of a dynamical system can be studied near to a point of equilibrium, which is a constant solution to the system's differential equations in mathematics. The dynamical behaviour of a given system can be studied by computing the trajectory of variables from initial conditions, according to equation 2.1 or 2.3. If the system is linear, the equation 2.1 could be expressed in the following form:

$$\dot{\mathbf{x}} = \mathbf{A}\mathbf{x} + \mathbf{B}\mathbf{u} \tag{2.4}$$

where **A** and **B** are time-dependent matrices which relate to the system parameters, and **u** represents the external input of the system. When the magnitude of $\dot{\mathbf{x}}$ equals 0, the points of the system are named as equilibrium points or fixed points. From equation 2.4, we can see that the term **Bu** can shift the position of the equilibrium points. The state matrix **A** determines the stability of these equilibrium points; in other words, the stability of the system can be indicated by the eigenvalues and eigenvector of matrix **A**. The eigenvalues can be obtained by solving the following equation:

$$|\mathbf{A} - \lambda\mathbf{I}| = \mathbf{0} \tag{2.5}$$

In nonlinear systems there can be more than one equilibrium point, since the behaviour of the vector field may be displayed differently for the different part of the state space. In order to study the stability of a nonlinear system, the concept of small perturbation injection is applied. Specifically, the fixed point is defined as stable when the trajectory converges back after adding a small perturbation to the original system. The local properties of the system are investigated by its linearization around the fixed points.

It can be assumed that a general nonlinear dynamical system is described by the following expression:

$$\dot{\mathbf{x}}(t) = f(\mathbf{x}(t)) \tag{2.6}$$

For the given initial condition $\mathbf{x}(t_0) = \mathbf{x}_0$ and an equilibrium state

$\mathbf{x}(t)^* = \begin{bmatrix} x_1^*, x_2^*, x_3^* \dots x_n^* \end{bmatrix}^T$, the system can be linearized at the equilibrium point x*

using the following equation:

$$\begin{bmatrix} \Delta \dot{x}_1 \\ \Delta \dot{x}_2 \\ \dots \\ \Delta \dot{x}_n \end{bmatrix} = \begin{bmatrix} \partial f_1/\partial x_1 & f_1/\partial x_2 & \cdots & f_1/\partial x_n \\ \partial f_2/\partial x_1 & \partial f_2/\partial x_2 & \cdots & \partial f_2/\partial x_n \\ \dots & \dots & \dots & \dots \\ \partial f_n/\partial x_1 & \partial f_n/\partial x_2 & \cdots & \partial f_n/\partial x_n \end{bmatrix}_{\mathbf{x}=\mathbf{x}^*} \times \begin{bmatrix} \Delta x_1 \\ \Delta x_2 \\ \dots \\ \Delta x_n \end{bmatrix} \tag{2.7}$$

where $\Delta x_1 = x_1 - x_1^*, \Delta x_2 = x_2 - x_2^*, \cdots \Delta x_n = x_n - x_n^*$

This can also be written in the form of

$$\Delta \dot{\mathbf{x}}(t) = \mathbf{A}(\mathbf{x}(t)^*) \times \Delta \mathbf{x}(t) \tag{2.8}$$

Here $\Delta \mathbf{x}(t) = \mathbf{x}(t) - \mathbf{x}(t)^*$ is the small perturbation near the equilibrium points, and

the matrix $\mathbf{A}(\mathbf{x}(t)^*, t)$ is called the Jacobian matrix, containing calculation of the

numerical values of the partial derivatives at the fixed points. The stability of the

system can be studied using the eigenvalues of this Jacobian matrix. This

representation of the dynamical system is widely used in the field of engineering,

since the nominal operating point of most systems is generally located at an

equilibrium point. A simple workable model can then be obtained by employing this

linear approximation when the perturbation is small enough. For these linear

systems, closed-form solutions can be found, but in nonlinear systems the properties

of the whole vector cannot be studied by simply breaking it up into linear regions and

then adding them up to gain the whole. Thus, the closed-form solutions are not

available, and numerical approaches must be employed.

2.5   Stability of the periodic solution

To study the stability of dynamical system in the periodic orbit, the Poincaré map

approach [19], Floquet theory [20] and Trajectory sensitivity [21] method are possible

solutions, which are similar to some extent in investigating the evolution of system

perturbation.

2.5.1 Poincaré map approach

The Poincaré map approach is a discrete mapping method invented by Henri Poincaré, describing the system in the form of discrete sampling rather than in a continuous-time manner. Specifically, it studies the periodic orbit of the system by placing a surface called the Poincaré section, which converts the continuous-time orbit into discrete observations as shown in Figure 2.3 [1, 111] .
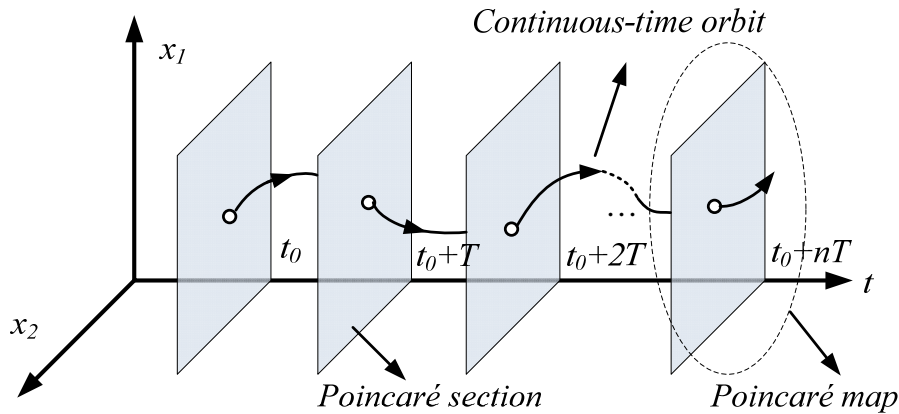
Figure 2.3 Poincaré map of a time-dependent non-autonomous system with T period

Assuming that a time-dependent non-autonomous system has an external forcing function of period T, and the vector field is smooth (differentiable everywhere) in its domain; the solution of the system can be represented as follows given the initial condition x_0:

$$\mathbf{x}(t_0 + T) = \mathbf{x}_0 + \int_{t_0}^{t_0+T} f(\varphi(\tau, \mathbf{x}_0), \tau)d\tau$$

(2.9)

A certain lower-dimensional subspace of the system state space, named the Poincaré section, can be placed to obtain stroboscope maps at intervals of T as illustrated in Fig. 2.3. The Poincaré map is the intersection of a periodic orbit in the state space with this Poincaré section. Hence the representation of this periodic continuous-time system can be transformed into a description of a discrete-time system of one dimension smaller. The evolution of the system in state space can then be described as a map form represented by equation 2.3. The fixed point $\mathbf{x}_0$ of the Poincaré map is a periodic steady-state solution in continuous-time system [4], and the Jacobian matrix at its fixed point can be used to investigate the stability of this map, which describes the original continuous-time system. The detailed derivation can be found in Appendix 1.

2.5.2 Trajectory sensitivity
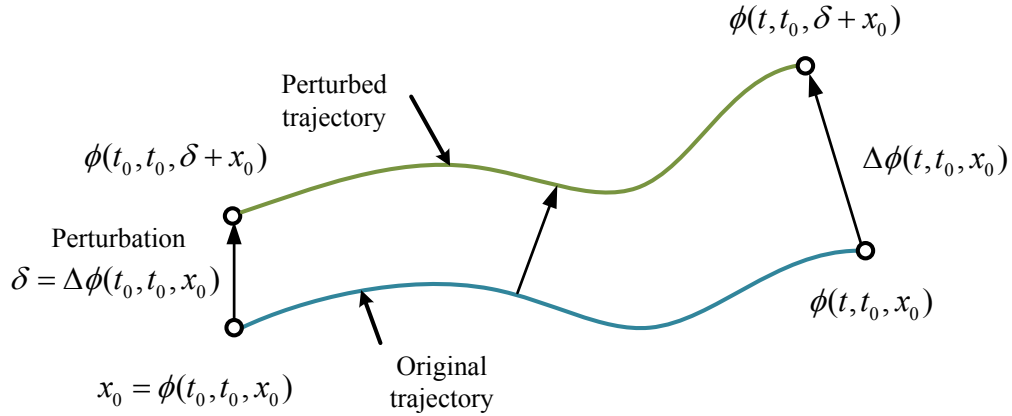
Figure 2.4 Diagram of Trajectory sensitivity approach

The principle of the trajectory sensitivity approach is as follows:

Assume there is a system that has a generic initial value:

$$\frac{dx(t)}{dt} = f(x(t),t)\,|_{x(t)=\phi(t,t_0,x_0)}, \qquad x(t_0) = x_0$$

(2.10)

Then according to the theory of trajectory sensitivity, the stability of the system can be analysed using the solution $\phi(t,t_0,x_0)$ by adding a small perturbation δ and observing its evolution as illustrated in Figure 2.4. The solution from equation 2.10 reveals the relationship between this perturbation $\Delta\phi(t,t_0,x_0)$ and the original one which can be proved as follows:

$$\Delta\phi(t,t_0,x_0) = \frac{\partial\phi(t,t_0,x_0)}{\partial x_0}\Delta\phi(t_0,t_0,x_0) = \Phi(t,t_0)\Delta\phi(t_0,t_0,x_0)$$

(2.11)

where $\Phi(t,t_0)$ represents the state transition matrix (STM) of equation 2.11. The system is stable when the perturbation tends to zero when t→∞. For a periodic orbit with a period of T, the following equation can be proved

$$\Delta\phi(kT + t_0,t_0,x_0) = \Phi^k(T + t_0,t_0)\Delta\phi(t_0,t_0,x_0)$$

(2.12)

where $\Phi(T + t_0,t_0)$ is termed the Mondromy matrix, which is the state transition matrix over the entire period T. This equation can be written in the following form:

$$\Delta\phi(kT + t_0,t_0,x_0) = E\Lambda^k E^{-1}\Delta\phi(t_0,t_0,x_0)$$

(2.13)

where E is the eigenmatrix of the fundamental solution of the periodic system for one complete cycle. The stability of the system can be identified by the magnitudes of the eigenvalues of this fundamental solution. More detailed derivation of trajectory

sensitivity approach can be found in Appendix 2.

2.5.3 Floquet theory
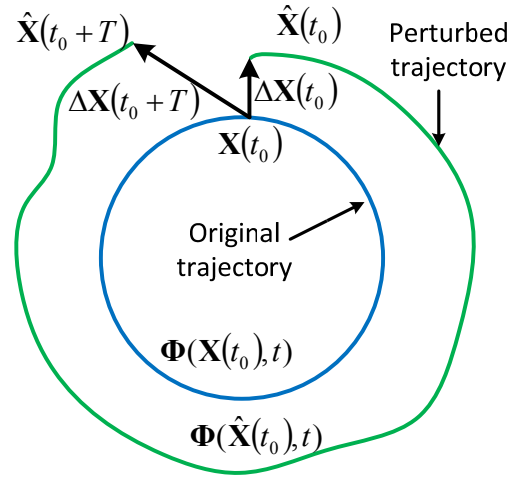
Figure 2.5 Periodic solution and its perturbed solution

In Floquet theory, a similar conclusion can be obtained to that of the trajectory sensitivity approach. As shown in Figure 2.5, it is assumed that a given system has an initial condition $\mathbf{x}(t_0)$ at time t_0, and it is perturbed to $\hat{\mathbf{x}}(t_0)$, such that the initial perturbation is $\Delta\mathbf{x}(t_0)=\mathbf{x}(t_0)-\hat{\mathbf{x}}(t_0)$. After the evolution of the original trajectory and the perturbed trajectory during time t, the perturbation at the end of the period can be related to the initial perturbation by

$$\Delta\mathbf{x}(t_0+T)=\mathbf{\Phi}\Delta\mathbf{x}(t_0) \tag{2.14}$$

where Φ is called the state transition matrix (STM), which is a function of the initial state and time. For any power converter, the ON and OFF state of the switches makes the system to evolve through different linear time-invariant (LTI) subsystems, Therefore, for each subsystem, the STM can be obtained by the expression when the initial conditions are given.

$$\mathbf{\Phi}=e^{\mathbf{A}(t-t_0)} \tag{2.15}$$

where A is the state matrix that appears in the state equation $\dot{\mathbf{x}}=\mathbf{Ax}+\mathbf{Bu}$.

2.5.4 Filippov's method

In smooth systems, the fundamental matrix can be used to map the perturbation from the initial condition to the end of the period. Nevertheless, the vector field of a power electronics system is piecewise smooth and the vector field is discontinuous at the

switching instant, which means that the aforementioned methodologies cannot be utilized directly for stability analysis. As a result, some information representing the switching event needs to be introduced to fully describe the dynamic behaviour of the system.
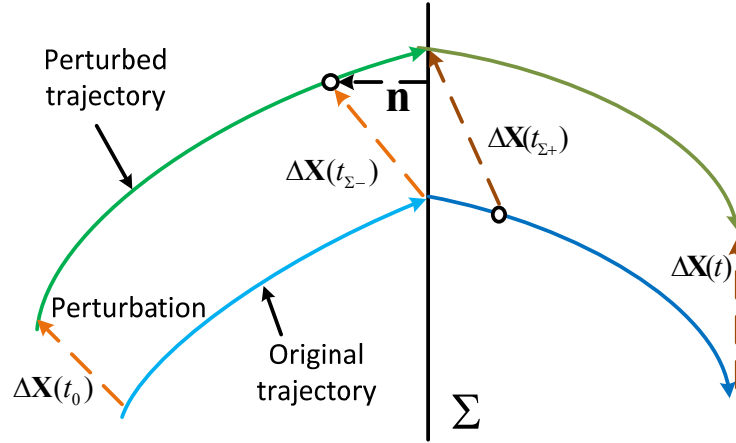
Figure 2.6 Concept of the Filippov method with Saltation matrix

With the assumption that there is no jump in the state vector at switching instants, the Filippov method can be applied in the study of this discontinuous vector field, calculating the evolution of vectors during the interval of $[t_{\Sigma^-}, t_{\Sigma^+}]$. The concept of this approach is illustrated in Figure 2.6, and it describes the behaviour of a perturbation crossing the switching surface Σ. Assuming that there is an initial perturbation $\Delta x(t_0)$ at time of t_0, it then evolves to $\Delta x(t_{\Sigma^-})$, starting to cross the switching manifold at time of t_{Σ^-}. After time $(t_{\Sigma^+}, t_{\Sigma^-})$, it comes out of the switching surface and becomes $\Delta x(t_{\Sigma^+})$. The saltation matrix S is used to map the perturbation before and after the switching manifold as follows[112].

$$\Delta \mathbf{x}(t_{\Sigma^+}) = \mathbf{S}\,\Delta \mathbf{x}(t_{\Sigma^-}) \qquad (2.16)$$

$$\mathbf{S} = \mathbf{I} + \frac{(f_{\Sigma^+} - f_{\Sigma^-})\mathbf{n}^T}{\mathbf{n}^T f_{\Sigma^-} + \dfrac{\partial h}{\partial t}} \qquad (2.17)$$

where I is the identity matrix of the same order of state variables; h contains information of the switching condition; **n** represents the normal vector to the switching surface; and f_{Σ^-} and f_{Σ^+} are the differential equations before and after the switching instant. The detailed derivation for the saltation matrix S can be found in Appendix 3. Hence the fundamental solution of a periodic system for one complete cycle, which is named the Monodromy matrix, can be represented as follows:

$$\mathbf{M} = \Phi(t_0, t_0 + T) = \Phi(t_{\Sigma+}, t_0 + T) \cdot \mathrm{S} \cdot \Phi(t_0, t_{\Sigma-}) \qquad (2.18)$$

where $\Phi(t_0, t_{\Sigma-})$ and $\Phi(t_{\Sigma+}, t_0+T)$ are the state transition matrices in the time intervals of $[t_0, t_{\Sigma-}]$ and $[t_{\Sigma-}, t_0+T]$ respectively.

2.6   Nonlinear behaviours of dynamical systems

Power electronics systems are classified as deterministic systems where the evolution of system variables is fully determined by the differential equations which represent them. In other words, the future state of the system is completely determined by the given initial conditions. Some systems could have many equilibrium solutions or they may not have any steady-state solutions, depending on the initial state. For a case where the equilibrium solutions are confined to a particular region of state space, this is also called an attractor; and it can take the form of a fixed point, limit cycle or periodic orbit, or chaotic attractor and quasi-periodic orbit [1]. If a system becomes unstable and is attracted to another equilibrium solution with the variation of the system's parameters, the behaviour can be regarded as bifurcation. Thus, in general, bifurcation is a phenomenon describing systems which produce a sudden qualitative or topological change when a small change is made to system parameter. This behaviour can be observed in both continuous and discrete dynamical systems. In power electronics systems, the converters are commonly designed for steady-state operation with specific output ripples. However, the operating mode can be changed substantially when parameters such as input voltage or load vary.

Chaos in a dynamical system refers to a particular aperiodic and random-like behaviour which is highly sensitive to initial conditions [113]. It is commonly known as a butterfly effect where small differences in initial conditions yield widely diverging outcomes, resulting in large differences in a later state. When the system is in a chaotic state, its trajectory is unpredictable in the long term. Although the properties of being random and impossible to predict, there are some feasible approaches to investigate the chaos. The study of routes to chaos, which attempts to describe the evaluation of chaotic behaviour through a series of bifurcations, is one of the most effective ways to do this [114].

In power electronics systems, the converters are generally designed in the region of

periodic operation. Any nonlinear behaviour such as bifurcations or chaos may increase the potential for EMI issues and the power conversion efficiency of the system may degrade. Hence the prediction of the bifurcation point given variation in the system's parameters should be a practical and effective way to analyse the system's stability. A more detailed stability analysis of DC-DC switching converters is presented in the following chapters.

2.7 Characterization of dynamical systems
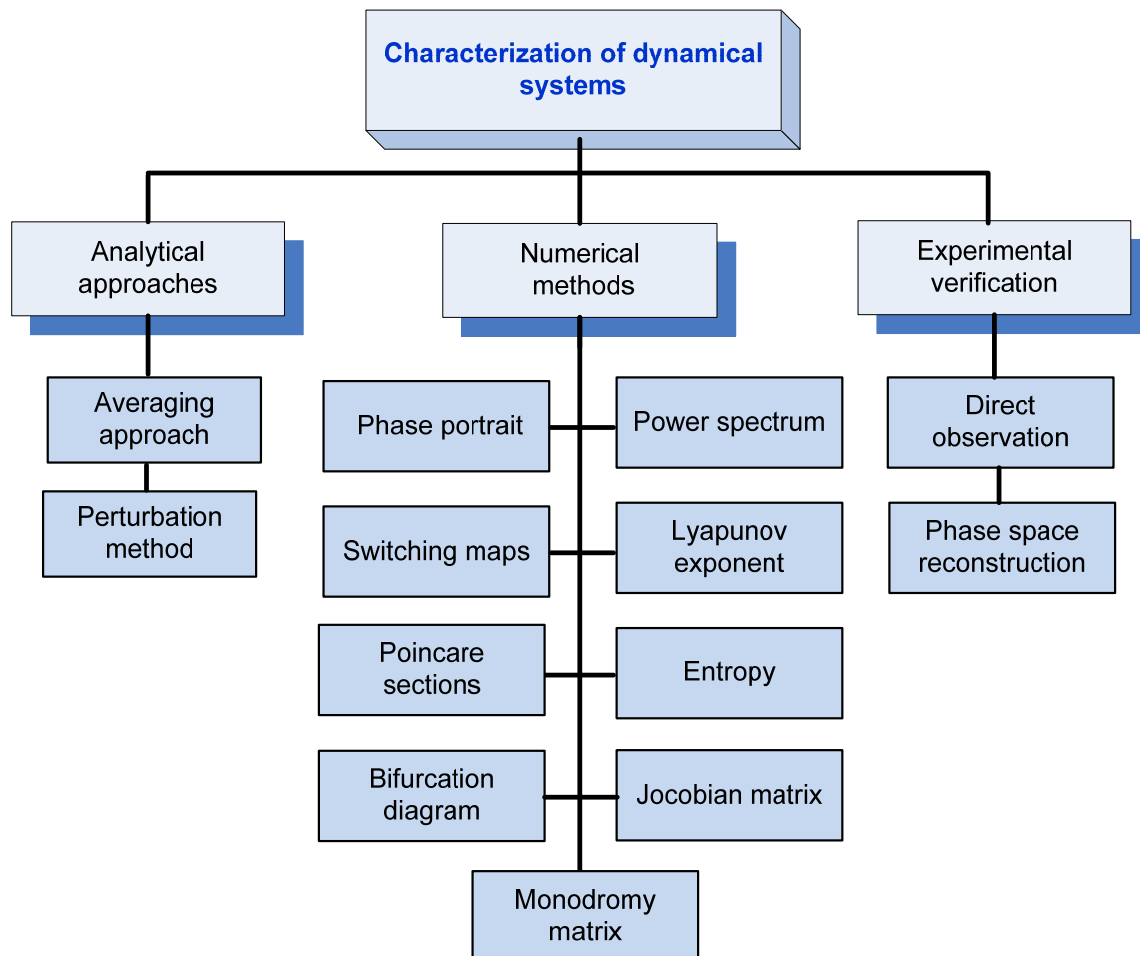
Figure 2.7 Typical characterization of dynamical system

The differential equations produced for power electronics converters in the form of continuous or discrete time can be solved either numerically or analytically. Computer-aided software or specialized simulation tools are employed in the numerical nonlinear analysis method, which describes the operation of power converters in terms of state equations or a component-based circuit model respectively. These methods are powerful and effective in demonstrating and investigating the nonlinear behaviour of power converters, while the settings of the

simulation environment may dramatically affect the results. Hence, experimentation and theoretical analysis are needed to verify the simulation results. In contrast, analytical methods employ analytical expressions to represent the characteristics of the power converters which exhibit definite relationships among system parameters. However, the complexity of practical circuits often requires approximate treatments to some extent in the process of modelling, which can reduce accuracy. Therefore, both methods are normally combined in the analysis of power converters in terms of practical implementation. The typical characterization of dynamical systems in terms of analytical, numerical and experimental approaches is summarized in Figure 2.7. The following discussion considers the measurable properties in the group of numerical methods.

2.7.1 Capture of complex behaviour
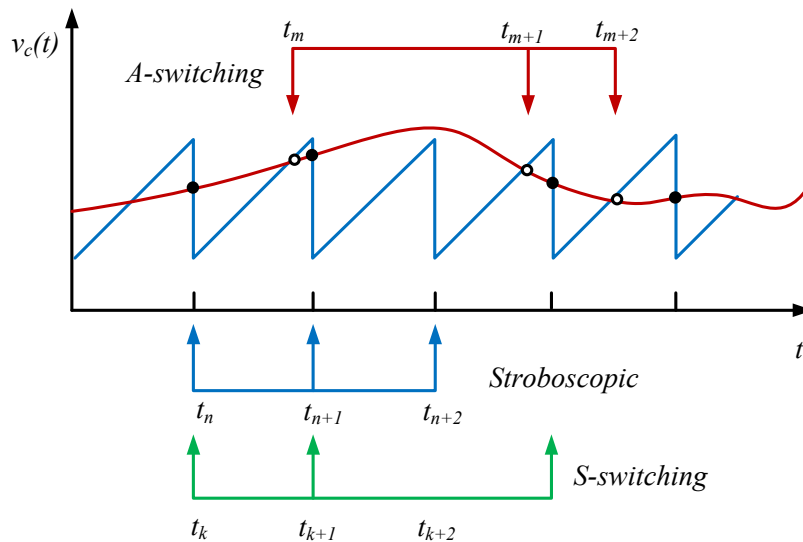
Figure 2.8 Different sampling mode for sampled-data maps under voltage-mode control

Switching maps are commonly used in stability analysis to characterize a dynamical system, including A-switching, S-switching and stroboscopic maps, according to the different sampling events as shown in Figure 2.8 [50]. The specific patterns of maps can be generated from sampling the state at time instants, exhibiting the system's behaviour under different sampling modes. Among these methods, the stroboscopic sampling approach is most widely used in the periodically driven systems (such as fixed-frequency switching converters) to reveal the periodicity of the system. If the sampled data remains at a constant value, this indicates that the waveform is periodic and its period is equal to the sampling period; whereas if the sampled data cycles through N values, this demonstrates that the waveform is periodic and its

period equals to N-time sampling period, However, if the sampled data exhibit no clear pattern, the system may be in a quasi-periodic or chaotic state.

The phase portrait is a geometric representation of the equilibrium solution for a dynamical system; and it especially refers to the projection of a trajectory from a higher order dimension to a 2-dimension phase plan. Switching maps, phase portraits and Poincaré sections are three widely used formats to record and demonstrate the properties of system with fixed parameters.

For a system with varying parameters, the bifurcation diagram is a graphical representation method generally used to study the nonlinear phenomena. In this approach, a chosen parameter is varied and plotted along one of the axes and the monitoring state variables are sampled and plotted as discrete points on the other axis. If there is only one point corresponding to that parameter, the system is operating in period-1; if there are two points, it is in the state of period-2; if there are a large amount of points which can be observed in response to the variation of that parameter, the system is in a chaotic state. A typical bifurcation diagram is illustrated in Figure 2.9.
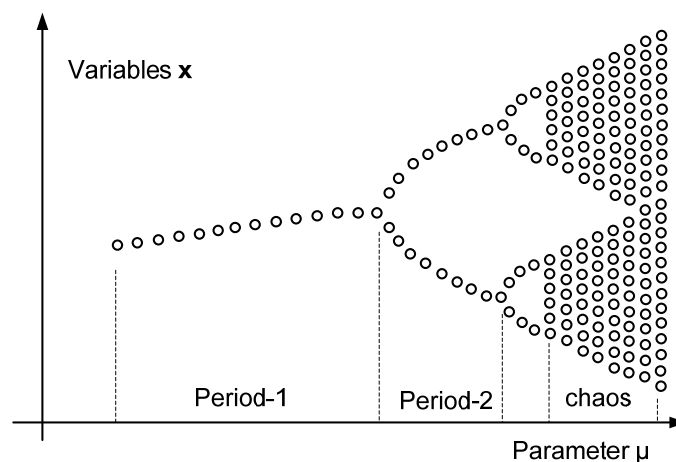
Figure 2.9 Typical bifurcation diagram

2.7.2 Jacobian matrix

For a continuous-time dynamical system given equation 2.1, the real parts of the eigenvalues indicate the stability of the fixed points. With the variation of parameter μ, the Jacobian matrix and its eigenvalues will change accordingly; the fixed point will be stable if the real parts of all the eigenvalues are negative. Different types of bifurcations will occur depending on where the eigenvalues cross the unit circle. Figure 2.10 gives the three typical types evolution of the locus of eigenvalues in

continuous time systems and the corresponding names of bifurcation are shown below.
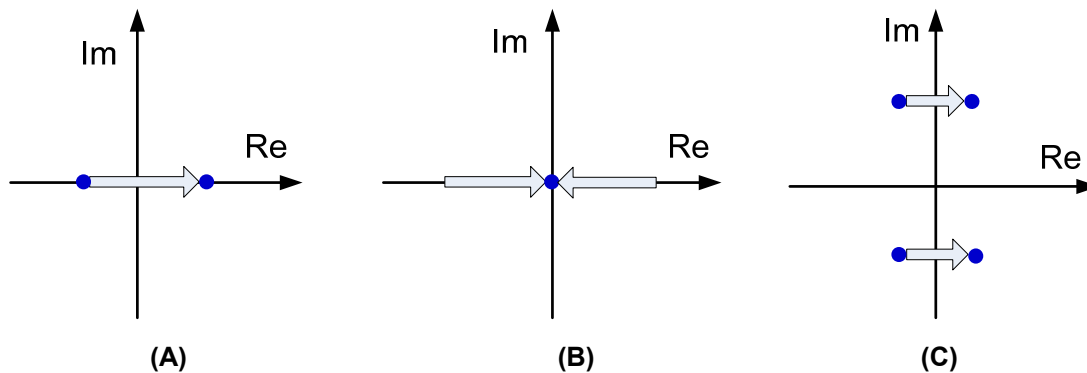
Figure 2.10 Evolution of the locus of eigenvalues in continuous-time dynamical systems
(A) Pitchfork, (B) Saddle-node, (C) Hopf bifurcation

A) Pitchfork bifurcation: the eigenvalues cross the imaginary axis on the real axis

B) Saddle-node bifurcation: the eigenvalues touch the imaginary axis from the positive and negative direction on the real axis.

C) Hopf bifurcation: the eigenvalues cross the imaginary line from the left-hand plane to the right-hand plane off the real line.

When it comes to a discrete-time system given equation 2.3, the eigenvalues of the Jacobian matrix can be applied to predict the stability of the fixed points as well. If all the eigenvalues have magnitudes less than unity, the fixed points will be stable. Bifurcation phenomena can be classified into three typical types according to the behaviour of eigenvalues when some parameters vary, as illustrated in Figure 2.11. According to the mode of crossing the unit circle, there are three typical bifurcations as follows:

A) Period-doubling bifurcation: one of the eigenvalues is equal to -1, and it is placed at the unit circle on the negative real line.

B) Saddle-node bifurcation: one of the eigenvalues equals 1, and it reaches the unit circle on the positive real line.

C) Neimark bifurcation: the modulus of a complex conjugate pair of eigenvalues equals 1, and they touch the unit circle away from the real and imaginary lines.

(A)   **(B)**   **(C)**
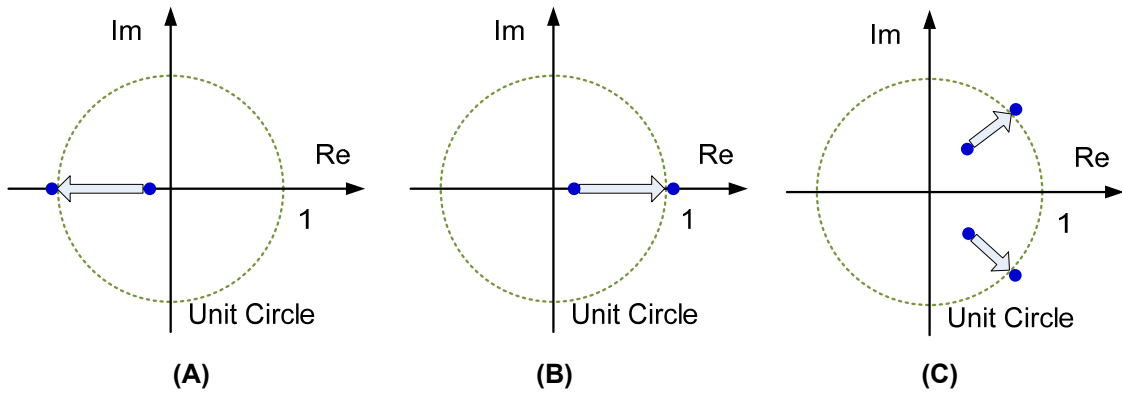
Figure 2.11 Evolution of the locus of eigenvalues in discrete-time dynamical systems

(A) Period-doubling, (B) Saddle-node, (C) Neimark

2.7.3 Lyapunov exponent

The Lyapunov exponent is one of the indicators available for evaluating the stability of a dynamical system [1, 102, 115]. It is a quantity that characterizes the rate of separation for very close trajectories. Specifically, suppose that two trajectories have an initial separation of ε_0, and it expands or contracts exponentially with respect to time given by the expression below:

$$\varepsilon(t) = \varepsilon_0 e^{\lambda t}$$

(2.19)
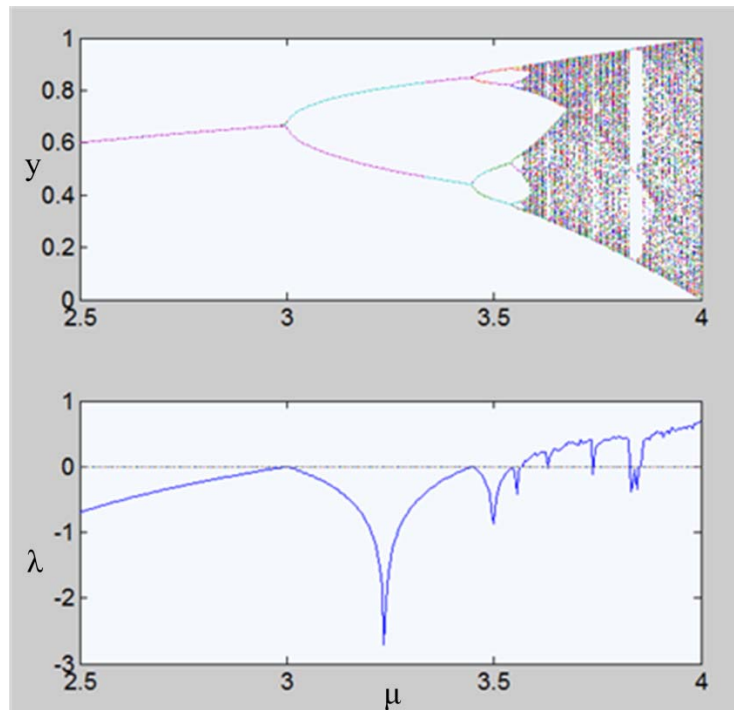
Figure 2.12 Bifurcation diagram and corresponding calculated average Lyapunov exponent

The behaviour of a dynamical system can be predicted from the calculated values of λ. If $\lambda > 0$, the separation is expanding and two trajectories diverge exponentially in

time; otherwise, if λ<0, the separation is contracting and it will tend towards 0 in the long run. The Nth order system has N Lyapunov exponents. The system will be unstable or chaotic if it has at least one positive Lyapunov exponent. The definition and calculation of maximal and average Lyapunov exponents are discussed elsewhere [1, 111]. However, the iterative equations of the system need to be derived in order to calculate the Lyapunov exponent; and the derivation process is relatively complex and the appropriate approximation treatment of a nonlinear system must be implemented. Figure 2.12 shows an example of a bifurcation diagram and the corresponding calculated average Lyapunov exponent for the system given below:

$$x_{n+1} = \mu x_n (1 - x_n) \qquad (2.20)$$

2.7.4 Other measurable properties

The power spectrum can be used as a feasible method to demonstrate the operating state of a system in terms of the frequency domain [26, 116]. The feature of a continuous wide band frequency spectrum is a significant characteristic for a chaotic system, but it's only a necessary condition for indicating the attributes of the system since random noise has the same feature. For a periodic operating system, the power spectrum will exhibit some peak signals related to the switching frequency, which contains the information about the system state. Entropy can be introduced to quantify the complex state of DC-DC switching converters [71, 117]. The switching instant and topological structural symbolic sequence is transformed into a decimal symbolic sequence and the calculated values of entropy represent the complexity of system state. This is an alternative way to the Lyapunov exponent without deriving the close-form iterative equation of the system.

2.7.5 Monodromy matrix

A Monodromy matrix is the fundamental solution for a periodic system for one complete cycle, which is theoretical foundation for the method of stability analysis adopted in this thesis. The derivation of the Mondromy matrix for a piecewise smooth system has been shown in section 2.5.4. The comprehensive information about the system is included in this matrix, and the influence of system parameters on system stability can be studied effectively and thoroughly. Further analysis of boost DC-DC converters based on this Monodromy matrix is presented in the following chapters.

3 Stability analysis of single phase DC-DC boost converters with resistive load

This chapter discusses the stability analysis and control of single phase DC-DC boost converters with resistive load. The theoretical analysis starts from a simple boost converter with peak current control, which exhibits the typical nonlinear phenomena in operation. The detailed derivation of **the** transition and saltation matrix is presented to obtain the Monodromy matrix that contains comprehensive information used to determine the system's stability. In addition, this Monodromy matrix-based method is applied in the analysis of a bidirectional DC-DC converter for the first time to demonstrate the influence of external and parasitic parameters. Finally, a new control algorithm can be developed to improve the system's performance by controlling the nonlinear behaviour and extending the region of stable operation.

3.1   Simple boost converter

The monodromy matrix based method combines the concept of Floquet theory and Fillipov's method that are illustrated in detail at Chapter 2. A general procedure of nonlinear analysis of a simple boost converter using this method is presented as an example in this section. The circuit of a simple boost converter is shown in Figure 3.1(a). Active power switches are operating in the ON and OFF states to achieve the expected power conversion as illustrated in Figure 3.1 (b). The system is toggled between two subintervals in a complete cycle. For each subinterval, state variables evolve continuously in a smooth trajectory, and thus the system is regarded as linear time-invariant (LTI) and can be described by a linear state equation in the form of equation 2.4. Figure 3.1 indicates the phase portrait orbit of output voltage and inductor current, where the solution of each subsystem can be represented by the STM $\Phi_{on}(0.dT)$ and $\Phi_{off}(dT.T)$. If the inductor current i_L and capacitor voltage v_c are chosen as state variables, the state equations can be expressed as follows, when the switch is ON:

29

$$\begin{cases} \dfrac{dv_c}{dt} = -\dfrac{v_c}{RC} \\ \dfrac{di_L}{dt} = \dfrac{V_i}{L} \end{cases} \tag{3.1}$$

(a)

(b)   **(c)**
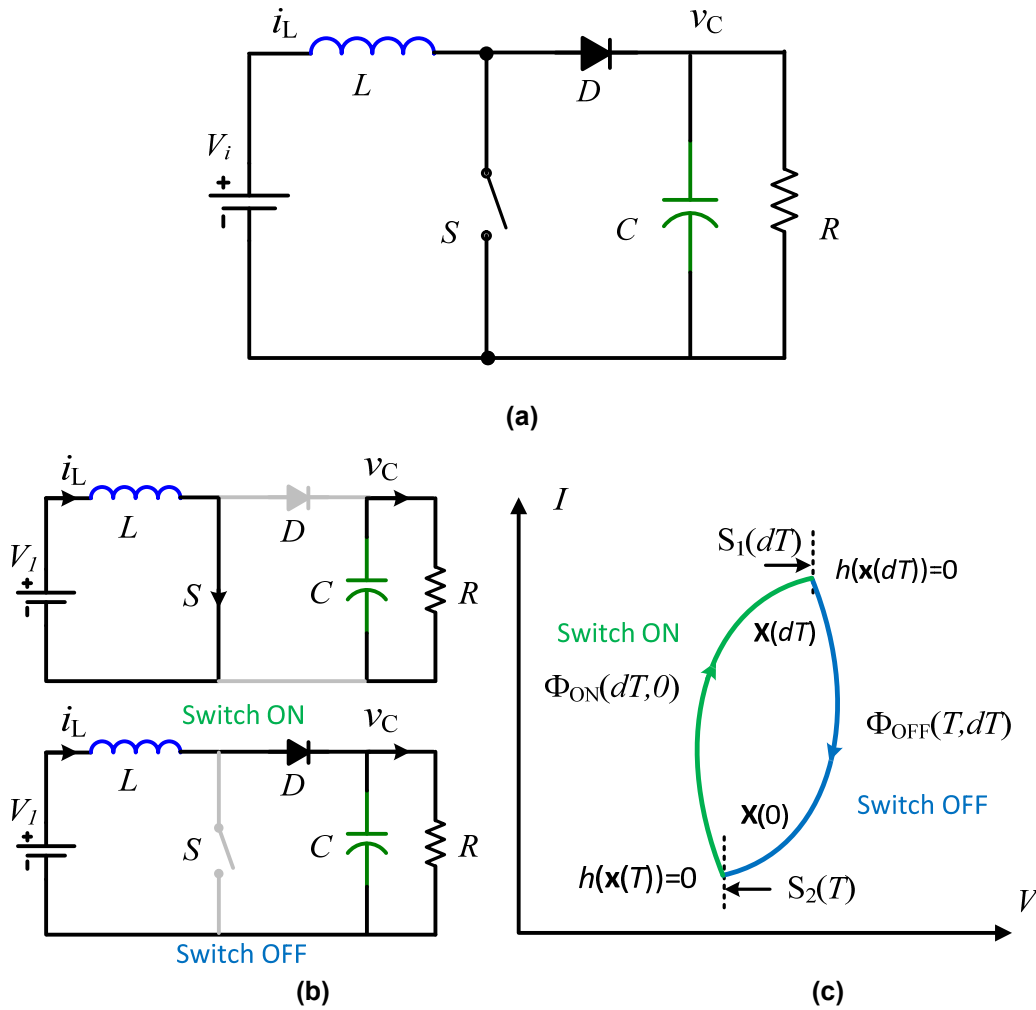
Figure 3.1 (a) Topology of the boost converter;
(b) two operation states of boost converter;
(c) phase portrait orbit of output voltage and inductor current

Similarly, when the switch is off, the state equations can be obtained as:

$$\begin{cases} \dfrac{dv_c}{dt} = \dfrac{i_L R - v_c}{RC} \\ \dfrac{di_L}{dt} = \dfrac{V_i - v_c}{L} \end{cases} \tag{3.2}$$

If the state vector **x** is used to express the above equations 3.1 and 3.2, the state equations can be rewritten in the form of the following equations:

30

$$\dot{\mathbf{x}}(t) = \begin{cases} f_{on}(\mathbf{x},t) = \mathbf{A}_{on}\mathbf{x} + \mathbf{B}_{off}\mathbf{u} \\ f_{off}(\mathbf{x},t) = \mathbf{A}_{off}\mathbf{x} + \mathbf{B}_{off}\mathbf{u} \end{cases}$$

(3.3)

where $\mathbf{x} = (x_1, x_2)$ and x_1 is the capacitor voltage v_c, and x_2 is the inductor current i_L. Thus, the state matrices for the ON and OFF periods are:

$$\mathbf{A}_{on} = \begin{bmatrix} -\dfrac{1}{RC} & 0 \\ 0 & 0 \end{bmatrix}$$

(3.4)

$$\mathbf{A}_{off} = \begin{bmatrix} -\dfrac{1}{RC} & \dfrac{1}{C} \\ -\dfrac{1}{L} & 0 \end{bmatrix}$$

(3.5)

$$\mathbf{B}_{on} = \mathbf{B}_{off} = \begin{bmatrix} 0 & 0 \\ 0 & \dfrac{1}{L} \end{bmatrix}$$

(3.6)

$$\mathbf{u} = \begin{bmatrix} 0 \\ V_i \end{bmatrix}$$

(3.7)

The right-hand sides of the state equations are obtained as:

$$f_{on} = \begin{bmatrix} -\dfrac{x_1}{RC} \\ \dfrac{V_i}{L} \end{bmatrix}$$

(3.8)

$$f_{off} = \begin{bmatrix} \dfrac{x_2 R - x_1}{RC} \\ \dfrac{V_i - x_1}{L} \end{bmatrix}$$

(3.9)

During the first subinterval, the solution of the system is:

$$\begin{aligned} \mathbf{x}(dT) &= e^{\mathbf{A}_{on} dT}\mathbf{x}(0) + \int_0^{dT} e^{\mathbf{A}_{on}(dT-\tau)}\mathbf{B}_{on}\mathbf{u}\,d\tau \\ &= \mathbf{\Phi}_{on}(0,dT)\mathbf{x}(0) + \mathbf{\Psi}_{on}(0,dT) \end{aligned}$$

(3.10)

For the second subinterval, the state vector can be obtained by:

$$\begin{aligned} \mathbf{x}(T) &= e^{\mathbf{A}_{off}(1-d)T}\mathbf{x}(dT) + \int_{(1-d)T}^{T} e^{\mathbf{A}_{off}(T-\tau)}\mathbf{B}_{off}\mathbf{u}\,d\tau \\ &= \mathbf{\Phi}_{off}(dT,T)\mathbf{x}(dT) + \mathbf{\Psi}_{on}(dT,T) \end{aligned}$$

(3.11)

The transition matrix is given by the matrix exponential, hence:

$$\begin{cases} \boldsymbol{\Phi}_{on}(0,dT) = e^{\mathbf{A}t} = e^{\mathbf{A}_{on}\,dT} \\ \boldsymbol{\Phi}_{off}(dT,T) = e^{\mathbf{A}_{off}\,(1-d)T} \end{cases} \qquad (3.12)$$

Substituting x(dT) with equation 3.10 yields:

$$\mathbf{x}(T) = \boldsymbol{\Phi}(0,T)\mathbf{x}(0) + \boldsymbol{\Psi}(0,T) \qquad (3.13)$$

where

$$\begin{cases} \boldsymbol{\Phi}(0,T) = \boldsymbol{\Phi}_{off}(dT,T) \times \boldsymbol{\Phi}_{on}(0,dT) \\ \boldsymbol{\Psi}(0,T) = \boldsymbol{\Phi}_{off}(dT,T) \times \boldsymbol{\Psi}_{on}(0,dT) + \boldsymbol{\Psi}_{on}(dT,T) \end{cases} \qquad (3.14)$$

For a periodic solution, **x**(0) equals **x**(T), and thus **x**(0) can be given by the following expression:

$$\mathbf{x}(0) = [\mathbf{I} - \boldsymbol{\Phi}(0,T)]^{-1} \times \boldsymbol{\Psi}(0,T) \qquad (3.15)$$

Here **I** is the identity matrix which has the same order as the system matrix **A**. It is noted that a nonsingular condition of the inverted matrix $[\mathbf{I} - \boldsymbol{\Phi}(0,T)]^{-1}$ must be satisfied to obtain a valid solution. The duty cycle can be calculated numerically from the switching conditions according to the control algorithm.

3.2   Peak current control with slope compensation

As shown in Figure 3.1(c), the orbit of the phase portrait is not smooth at the switching instant, and in order to obtain full information about the periodic orbit, the external conditions causing the switching action need to be taken into account. For example, a boost converter under peak current control with slope compensation is illustrated in Figure 3.2(a).
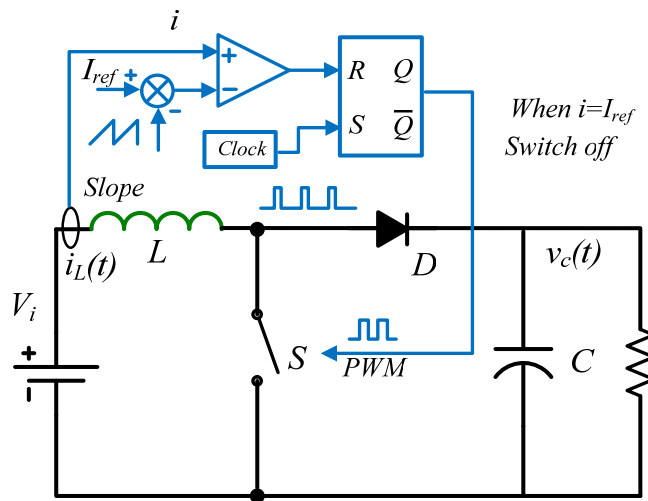
(a)
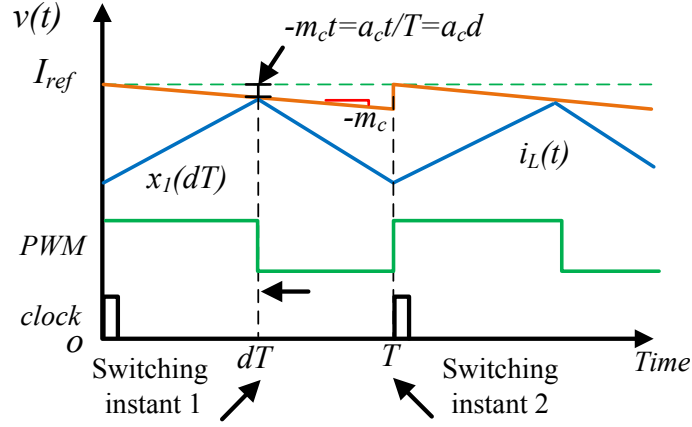
(b)
Figure 3.2 Boost converter under peak-current control with slope compensation:
(a) topology and control diagram (b) operation principle of slope compensation

The operational principle of the slope compensation has two switching events in one clock period as shown in Figure 3.2 (b). One happens at the beginning of each cycle, another occurs at the time when the inductor current i_L is equal to the reference current. If the slope of the compensation ramp is m_c in a clock period and the amplitude of this slope at the end of each clock is represented as a_c, the current reference evolves at: $I_{ref} + m_c t, t \subset [0,T]$. The switching condition can be defined as $h(x,t) = 0$ and can be expressed as:

$$h_1(x,t) = I_{ref} + m_c t - i_L(t) = 0 \tag{3.16}$$

Substituting equation 3.10 into 3.16, the equation can be rewritten in the following form:

$$h_1(x,t) = I_{ref} - a_c d - (e^{\mathbf{A}_{on} dT} i_L(0) + \int_0^{dT} e^{\mathbf{A}_{on}(dT-\tau)} \mathbf{B}_{on} \mathbf{u} \, d\tau) = 0 \tag{3.17}$$

By employing equation 3.17, this nonlinear equation can be solved to obtain the value of the duty cycle d, and then the state vector in the steady state and state transition matrices can be calculated accordingly, which corresponds to the location of the periodic orbit of the continuous system. As mentioned in the last chapter, the information of the switching instant is not contained in the state transition matrices. From Fillipov's method, the saltation matrix should be derived to describe the behaviour of the switching event. The normal vector is expressed as:

$$\mathbf{n} = \begin{bmatrix} \partial h_1 / \partial x_1 \\ \partial h_2 / \partial x_2 \end{bmatrix} = \begin{bmatrix} 0 \\ 1 \end{bmatrix} \tag{3.18}$$

The partial differential equation of the switching function is:

$$\frac{\partial h}{\partial t} = \frac{\partial h_1}{\partial t} = m_c \qquad (3.19)$$

By substituting the expression 3.19 and by adding vector fields before and after the switching and the normal vector into the expression of the saltation matrix, the following is obtained:

$$\mathbf{S}_1(dT) = \mathbf{I} + \frac{(f_+ - f_-)\mathbf{n}^T}{\mathbf{n}^T f_- + \dfrac{\partial h}{\partial t}} = \mathbf{I} + \frac{(f_{off} - f_{on})\mathbf{n}^T}{\mathbf{n}^T f_{on} + \dfrac{\partial h}{\partial t}}$$

$$= \begin{bmatrix} 1 & (\dfrac{x_2 R - x_1}{RC} + \dfrac{x_1}{RC})(\dfrac{V_i}{L} + \dfrac{a_c}{T})^{-1} \\ 0 & 1 + (\dfrac{V_i - x_1}{L} - \dfrac{V_i}{L})(\dfrac{V_i}{L} + \dfrac{a_c}{T})^{-1} \end{bmatrix} = \begin{bmatrix} 1 & \dfrac{x_2}{C}(\dfrac{V_i}{L} + \dfrac{a_c}{T})^{-1} \\ 0 & 1 - \dfrac{x_1}{L}(\dfrac{V_i}{L} + \dfrac{a_c}{T})^{-1} \end{bmatrix} \qquad (3.20)$$

The second saltation matrix S2 is related to the switching event from the off-to-on state at the initial instant of every clock cycle, which means that the rising edge of the ramp causes the term $\dfrac{\partial h_2(x,t)}{\partial t}$ in equation 2.17 to be infinity. Hence $S_2(T)$ turns out to be an identity matrix.

$$\mathbf{S}_2(T) = \mathbf{I} \qquad (3.21)$$

For a whole period T, the Monodromy matrix is expressed as:

$$\mathbf{\Phi}_{cycle} = \mathbf{S}_2(T) \times \mathbf{\Phi}_{off}(dT, T) \times \mathbf{S}_1(dT) \times \mathbf{\Phi}_{on}(dT, 0) \qquad (3.22)$$

The Monodromy matrix relates the evolution of the perturbation from the beginning to the end of the clock period:

$$\Delta \mathbf{X}(T) = \mathbf{\Phi}_{cycle}(T, 0) \times \Delta \mathbf{X}(0) \qquad (3.23)$$

Perturbations will die down and the system will be stable when all the eigenvalues of the Monodromy matrix are located in the unit circle.

Simulation results of the boost converter with peak current control are illustrated in Figure 3.3 to show the nonlinear phenomena in power converter circuits. The parameters of the circuit are set as follows: V_i=5V, L=1.5mH, C=10μF, R=40Ω, f=10kHz and m_c=0. The controller has no slope compensation in this case and the current reference level is changed gradually from 0.1A to 0.8A in steps. During the steady state, the values of output voltage and corresponding current reference are recorded in every switching period. With these settings a bifurcation diagram of output voltage and current reference is produced and shown as Figure 3.3(a). The

related waveforms of output voltage and phase portrait are shown in Figure 3.3(b).

(a)

(b)
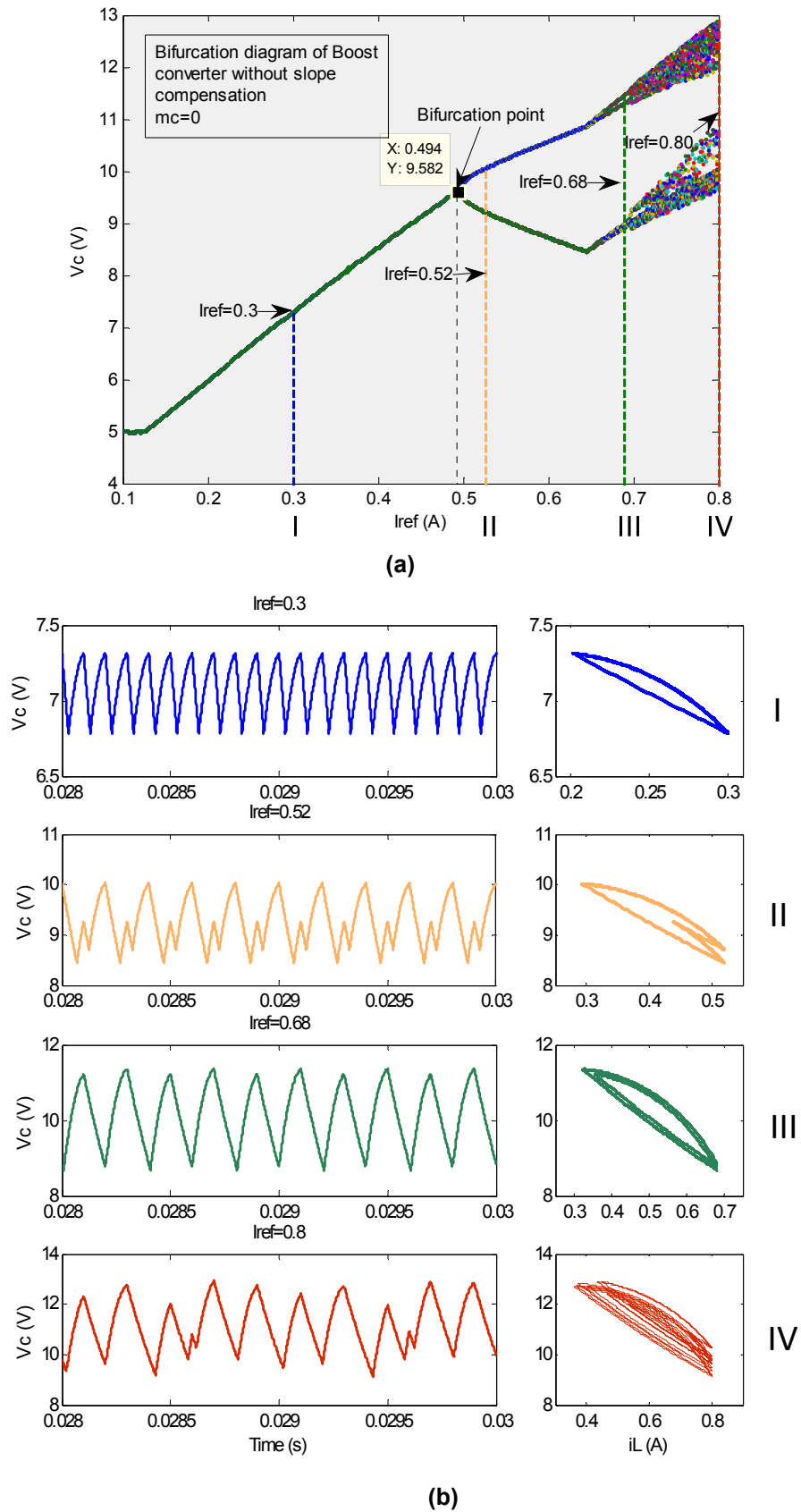
Figure 3.3 Nonlinear phenomena in boost converter under peak-current control:
(a) bifurcation diagram of output voltage under different current references;
(b) waveforms of output voltage and phase portrait.

From Figure 3.3, it is clear that the system changes from a stable state to period–doubling bifurcation state, and finally moves into a chaotic state. When the amplitude of compensation ramp at the end of each period is set to 0.05, a new bifurcation diagram evolves, as illustrated in Figure 3.4(a). Compared with Figure 3.3(a), it is evident that the range of stability has increased from 0.494A to 0.679A, providing a demonstration that the added slope compensation extends the stable range.
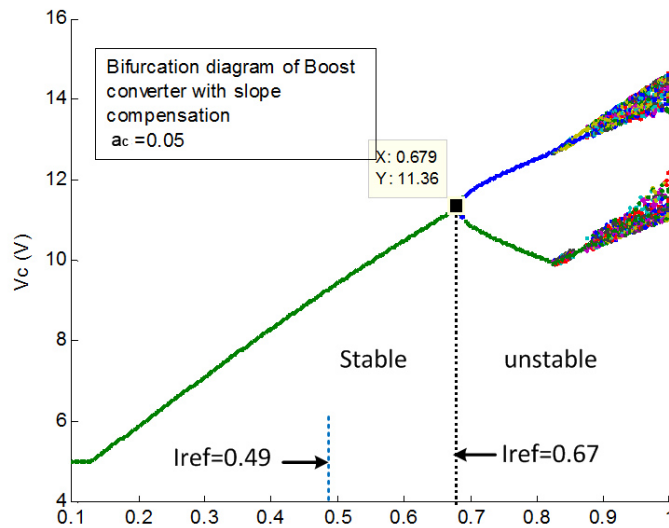
(a)
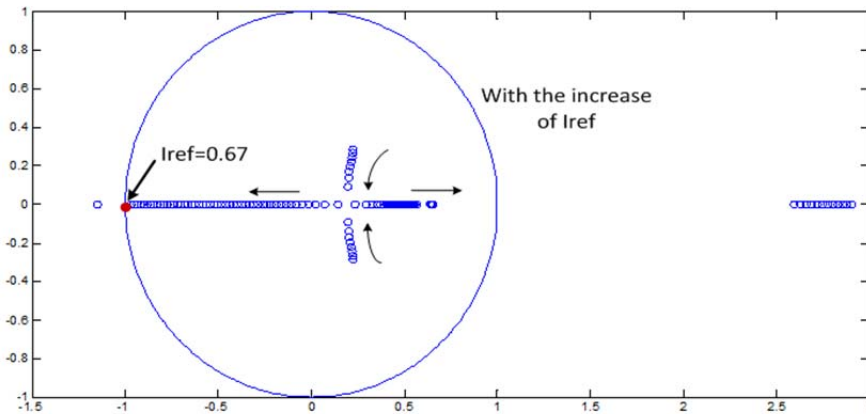
(b)

Figure 3.4 Simulation results with slope compensation (a_c=0.05):
(a) bifurcation diagram of boost converter under peak-current with slope compensation;
(b) locus of eigenvalue of Monodromy matrix under different current reference

In addition, the calculated eigenvalues of the Monodromy matrix show that when I_{ref} equals 0.67A, one of the eigenvalues is nearly equal to -1. This demonstrates that the original stable system becomes unstable and a double-periodic orbit is starting to emerge. Therefore, there is a good agreement between the locus of eigenvalues

based on the analytical calculation and the bifurcation diagram from a component model-based simulation. Inspecting the movement of eigenvalues when the chosen parameters vary enables us to obtain stability information, such as the occurrence of bifurcations and the boundaries of operating regions.

3.3   Peak current control with voltage feedback
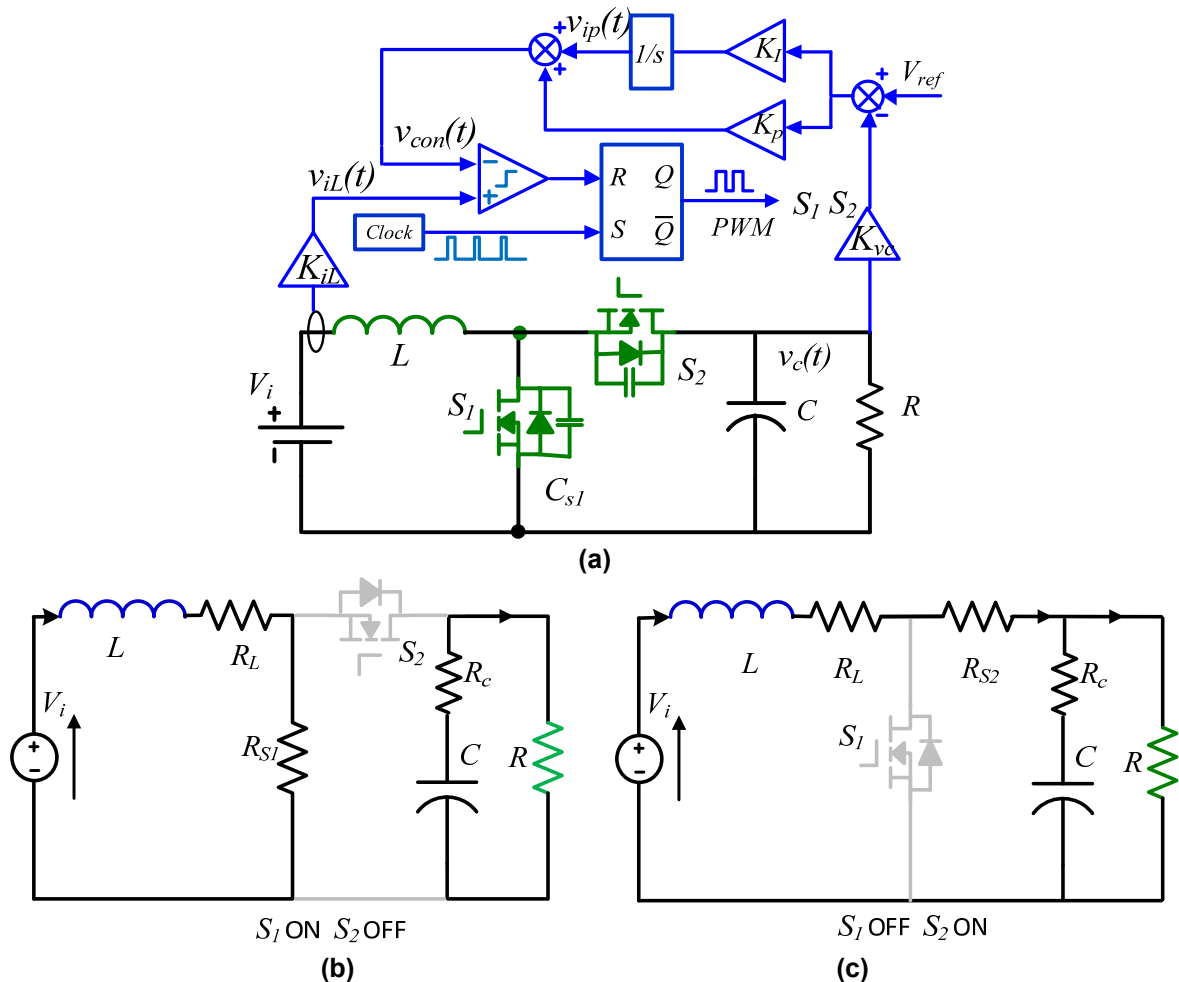
Figure 3.5 (a) Diagram of converter under conventional peak current control with voltage feedback (b) state of S_1 is on, S_2 is off (c) state of S_1 is off, S_2 is on

In the previous analysis, the switching elements in the circuit are considered to be ideal; switches are regarded as short circuits when they are on and open circuits when they are off. So far, the effect of parasitic elements such as the resistances of the inductor and capacitor are commonly ignored to simplify the procedure of the analysis. However, in a realistic model, these neglected factors may have a significant influence on the stability of DC-DC converters, and few studies can be found which focus on the investigation of the relationships between parasitic parameters and system stability in power switching converters [16, 118]. The adopted

analytic approach based on Monodromy matrix can be used not only to investigate the fundamental parameters, but also allows the study of parasitic elements which influence the stability of the circuit. The following section shows the first time that Monodromy matrix is applied in analysis of the bidirectional boost converter considering some parasitic parameters.

The diagram of a bidirectional boost converter under cascaded control, which consists of inner peak current loop and outer voltage feedback loop is shown in Figure 3.5(a). The parasitic parameters of the components are taken into account as illustrated in Figure 3.5(b). The parameters K_i and K_p represent the gains of the (Proportional and Integral) PI controller; K_{vc} and K_{il} are the gains of signals from a practical sampled output voltage v_c and inductor current i_L to the controller respectively; R_{s1} and R_{s2} are the conduction resistance of the switches, and R_L and R_c are equivalent series resistances the of inductor and capacitor respectively. The inductor current i_L, capacitor voltage v_c and the output of the integrator in the feedback loop v_{ip} are chosen as state variables. S_1 and S_2 operate in a complementary way using PWM control, wherein S_1 is on and S_2 is OFF or vice versa. When the switch S_1 is ON, the state equations can be expressed as:

$$\begin{cases} \dfrac{dv_c}{dt} = -\dfrac{v_c}{(R+R_c)C} \\[2ex] \dfrac{di_L}{dt} = \dfrac{V_i}{L} - \dfrac{(R_L + R_{S1})i_L}{L} \\[2ex] \dfrac{dv_{ipi}}{dt} = K_I(K_{vc}\dfrac{R}{R_c+R}v_c - V_{ref}) \end{cases} \qquad (3.24)$$

When the switch is off, the state equations are obtained as:

$$\begin{cases} \dfrac{dv_c}{dt} = \dfrac{i_L R - v_c}{(R+R_C)C} \\[2ex] \dfrac{di_L}{dt} = \dfrac{V_i - \dfrac{R}{R_C+R}v_c}{L} - \dfrac{(R_L + R_{S2} + \dfrac{RR_C}{R_C+R})i_L}{L} \\[2ex] \dfrac{dv_{ipi}}{dt} = K_I(K_{vc}((\dfrac{RR_C}{R_C+R})i_L + \dfrac{R}{R_c+R}v_c) - V_{ref}) \end{cases}$$
$$(3.25)$$

By replacing v_c, i_L, v_{ip} with the state vector x_1, x_2, x_3 the, the linear vector fields before and after switching are:

$$f_{on} = \begin{bmatrix} -\dfrac{x_1}{(R+R_c)\,C} \\[3mm] \dfrac{V_i}{L} - \dfrac{(R_L + R_{S1})x_2}{L} \\[3mm] K_I(K_{vc}\dfrac{R}{R+R_c}x_1 - V_{ref}) \end{bmatrix} \tag{3.26}$$

$$f_{off} = \begin{bmatrix} \dfrac{x_2 R - x_1}{(R+R_C)C} \\[3mm] \dfrac{V_i}{L} - \dfrac{R}{(R+R_C)L}x_1 - (\dfrac{R_L + R_{S2}}{L} + \dfrac{RR_C}{(R+R_C)L})x_2 \\[3mm] K_I(K_{vc}((\dfrac{RR_C}{R+R_C})x_2 + \dfrac{R}{R+R_C}x_1) - V_{ref}) \end{bmatrix} \tag{3.27}$$

Thus, the state matrices for these two subintervals are shown in the following:

$$A_1 = \begin{bmatrix} -\dfrac{1}{(R+R_c)\,C} & 0 & 0 \\[3mm] 0 & -\dfrac{(R_L + R_{S1})}{L} & 0 \\[3mm] K_i K_{vc}\dfrac{R}{R+R_c} & 0 & 0 \end{bmatrix} \tag{3.28}$$

$$A_2 = \begin{bmatrix} -\dfrac{1}{(R+R_C)C} & \dfrac{R}{(R+R_C)C} & 0 \\[3mm] -\dfrac{R}{(R+R_C)L} & -\dfrac{R_L + R_{S2}}{L} - \dfrac{RR_C}{(R+R_C)L} & 0 \\[3mm] K_i K_{vc}\dfrac{R}{(R+R_C)} & K_i K_{vc}\dfrac{R\cdot R_C}{(R+R_C)} & 0 \end{bmatrix} \tag{3.29}$$

$$B_1 = B_2 = \begin{bmatrix} 0 & 0 & 0 \\[2mm] 0 & \dfrac{1}{L} & 0 \\[2mm] 0 & 0 & -K_I \end{bmatrix} \tag{3.30}$$

$$u = \begin{bmatrix} 0 \\ V_i \\ V_{ref} \end{bmatrix} \tag{3.31}$$

On-to-off switching events occur when the output of the PI controller equals the value of inductor current i_L. Therefore, the switching condition can be defined as

$h(x,t) = 0$, where:

$$h_1(x,t) = K_p(V_{ref} - K_{vc}\frac{R}{R+R_c}v_c) + v_{ip} - K_{iL}i_L \qquad (3.32)$$

Hence, the normal vector to the switching manifold and the rate of change are

$$\mathbf{n} = \begin{bmatrix} \partial h_1/\partial x_1 \\ \partial h_2/\partial x_2 \\ \partial h_3/\partial x_3 \end{bmatrix} = \begin{bmatrix} \dfrac{-K_p K_{vc} R}{R+R_c} \\ -K_{iL} \\ 1 \end{bmatrix} \qquad (3.33)$$

and

$$\frac{\partial h}{\partial t} = 0 \qquad (3.34)$$

By applying equation 2.17, the saltation matrix can be calculated as follows

$$\mathbf{S}_{1t} = \begin{bmatrix} 1 - \dfrac{\rho^2 K_p K_{vc} x_2}{\sigma C} & -\dfrac{\rho K_{iL} x_2}{\sigma C} & \dfrac{\rho x_2}{\sigma C} \\ \dfrac{\rho^2 K_p K_{vc}(x_1 + R_C x_2)}{\sigma L} & 1 + \dfrac{\rho K_{iL}(x_1 + R_C x_2)}{\sigma L} & -\dfrac{\rho(x_1 + R_C x_2)}{\sigma L} \\ \dfrac{\rho^2 R_C K_i K_p K_{vc}^2 x_2}{\sigma} & \dfrac{-\rho R_C K_i K_{iL} K_{vc} x_2}{\sigma} & 1 + \dfrac{\rho K_i K_{vc} R_C x_2}{\sigma} \end{bmatrix} \qquad (3.35)$$

Here,

$$\sigma = \frac{\rho K_P K_{vc} x_1}{(R+R_c)C} - \frac{K_{iL} V_i}{L} + \frac{(R_L + R_{S1}) K_{iL} x_2}{L} + K_I(K_{vc}\rho x_1 - V_{ref}) \qquad (3.36)$$

$$\rho = \frac{R}{R+R_C} \qquad (3.37)$$

S_{1t} is the saltation matrix related to the ON-to-OFF switching event of S_1; and matrix S_{2t} is related to the off-to-on switching event at the initial instant of every clock cycle, which leads the rising edge of the ramp causes the term of $\partial h/\partial t$ in equation 2.17 to be infinite. Therefore S_{2t} turns out to be the identity matrix.

$$\mathbf{S}_{2t} = \mathbf{I} \qquad (3.38)$$

Furthermore, the state transition matrices are given by the exponential matrix:

$$\boldsymbol{\Phi}_1 = e^{\mathbf{A}_1 dT} \qquad (3.39)$$

$$\boldsymbol{\Phi}_2 = e^{\mathbf{A}_2 (1-d)T} \qquad (3.40)$$

The Monodromy matrix **M** can be calculated by the following expression:

$$\mathbf{M} = \boldsymbol{\Phi}_{cycle} = \boldsymbol{\Phi}_1 \times \mathbf{S}_{1t} \times \boldsymbol{\Phi}_2 \times \mathbf{S}_{2t} \qquad (3.41)$$

This matrix contains all of the comprehensive information about system input and load conditions, the parameters of the converter and the coefficients of the control loop, therefore the influence of any system parameters on system stability can be analysed using this matrix.

3.4   Simulation verification
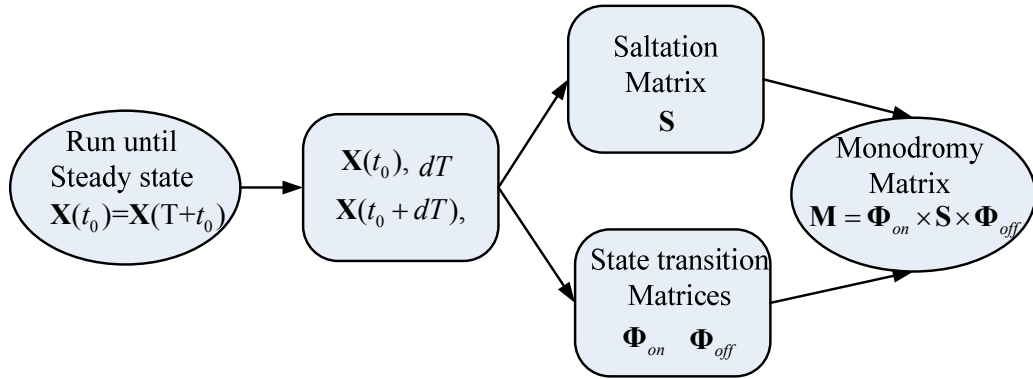
Figure 3.6 Procedure for calculating the Monodromy matrix.

The procedure for calculating the Monodromy matrix is shown in Figure 3.6. The two vector fields before and after the switching instant contain the information needed to calculate the state transition matrices. When the system is running until the steady state, the values of state vectors $\mathbf{X}(t_0)$, $\mathbf{X}(t_0+dT)$ and the duty cycle d can be obtained, and then these values are fed into the expressions of the saltation matrix and state transition matrices respectively for the calculation of the Monodromy matrix.

In order to verify the effectiveness of the proposed approach and the designed controller, the circuit based on a Simulink model is built and tested as shown in Figure 3.7, which is the equivalent circuit to represent the state-space equations of the DC-DC converters. Numerical and analytical calculations in Matlab are implemented to crosscheck the simulation results. The specifications of parameters are shown as follows: V_i=250~400V, V_{out}=600V, L=50~200μH, C=250μF, R=6Ω, f=20kHz, K_i=200, K_p=1, K_{vc}=1/120, K_{iL}=1/120, V_{ref}=5V, R_l=0.05Ω, R_c=0.01Ω, P_{out}=60kW.
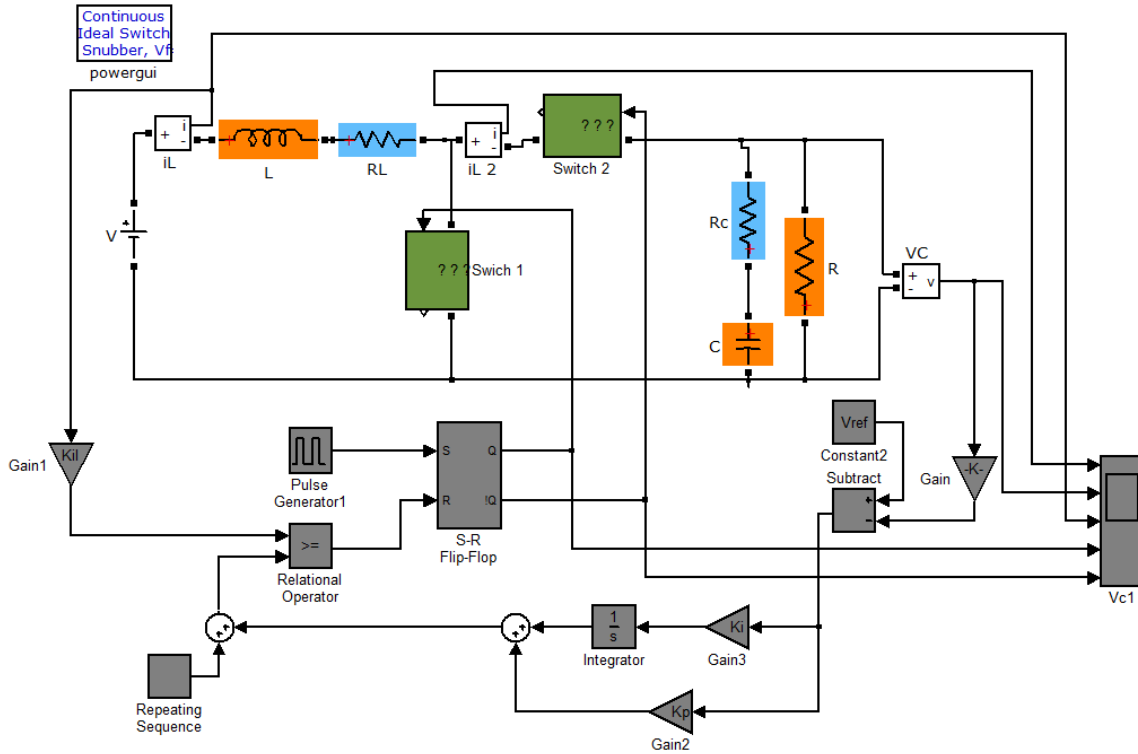
Figure 3.7 Simulink model of the bidirectional boost converter in Matlab

As mentioned above, the presented Monodromy matrix that contains system parameters can be used to study and predict the stability of the system. The bifurcation diagram of the input voltage and voltages at different inductance levels is illustrated in Figure 3.8(a). It shows that, with the increase of inductance value, the bifurcation phenomenon occurs from the point where V_{in} equals 300V when the value of inductance is 50μH to the point of which V_{in} equals 268V when the value of inductance is 150μH. There is no bifurcation phenomenon when the value of inductance is equal to 200μH within the input voltage range of 250V to 310V, which indicates a stable system.

In other words, the stable range of the system is improved by increasing the inductance value. In Figure 3.8(b), it is noted that eigenvalues 2 and 3 changed slightly at the variation of input voltage. Because they are relevant with the voltage of output capacitor and the output of integer respectively, which demonstrates that they are inconsequential in determining the fast-scale stability of the system and only the associated eigenvalue 1 is strongly related to the system's stability.
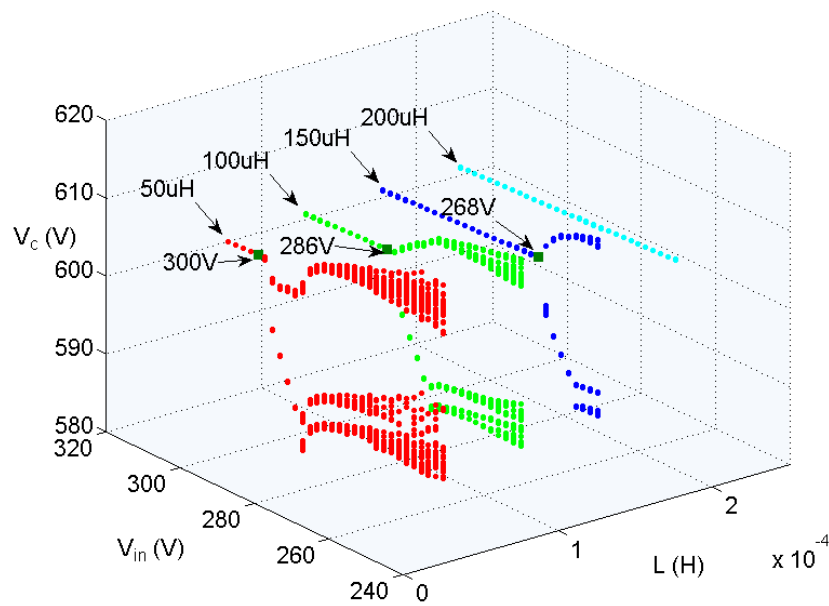
(a)
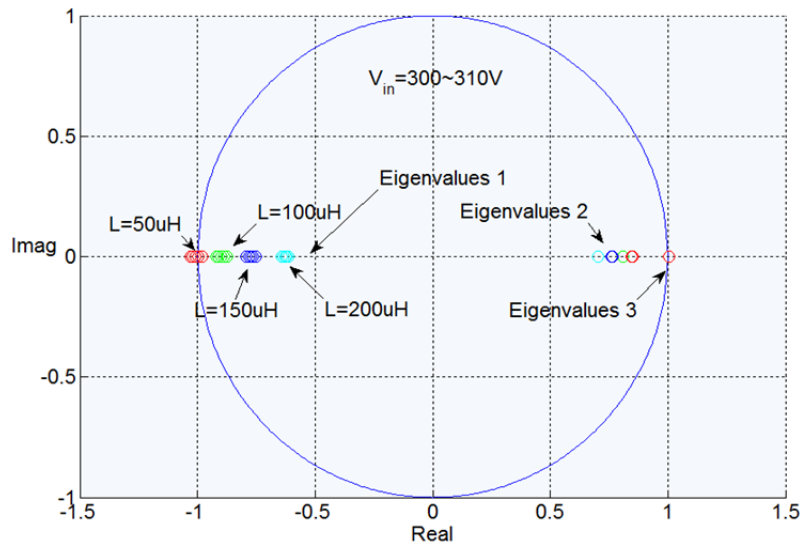
(b)

Figure 3.8 (a) Bifurcation diagram of input voltage and output voltage at different inductance; (b) corresponding locus of eigenvalues when V$_{in}$=300~310V

Figure 3.9 shows the bifurcation diagram of input and output voltage at different parasitic parameters such as the equivalent series resistance (ESR) of the inductor and of the output capacitor. With the condition of setting the values of inductor ESR from 0Ω to 0.3Ω with steps of 0.1Ω, the bifurcation point of the input voltage is varied from 282V to 287V. Similarly, by setting the ESR of the output capacitor from 0Ω to 0.15Ω in steps of 0.05Ω, the system exhibits bifurcation point varying from 272V to 279V. It is evident that the parasitic parameters affect the fast-scale stability of DC-DC converter to some extent, depending on the specific values of parasitics.

43
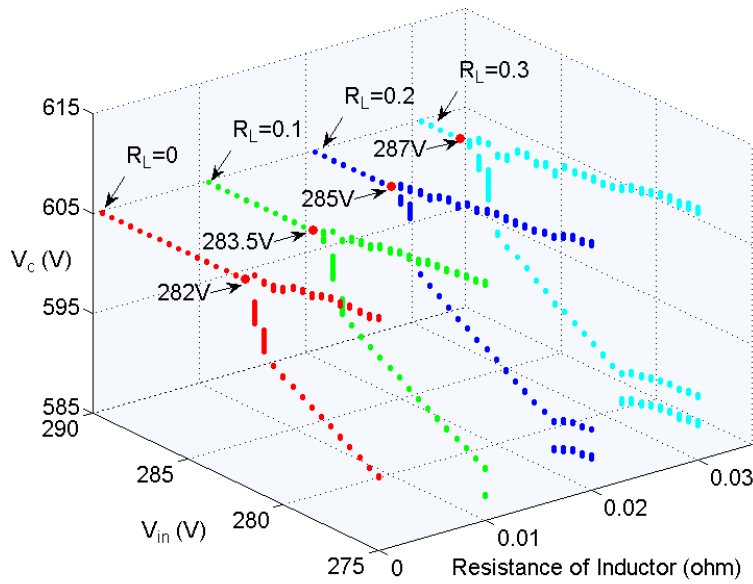
(a)
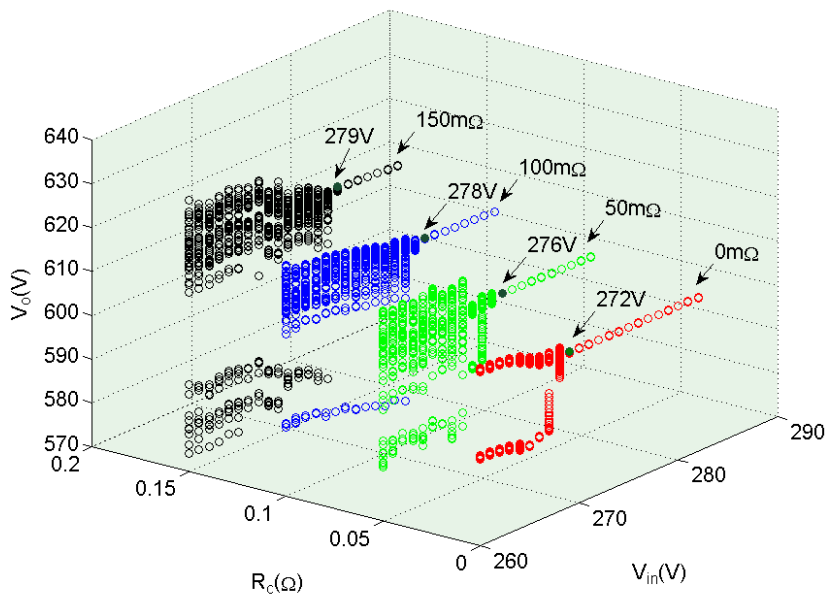
(b)

Figure 3.9 Bifurcation diagram of input and output voltage at different parasitics:
(a) different equivalent series resistance (ESR) of inductor
(b) different ESR of output capacitor

3.5   Controller design

The theoretical analysis of boost converters with voltage feedback control has been presented above. It is well known that the system will lose stability when some circuit parameters are varying, and thus the information about the stable operation range is expected from the circuit designer. Another concern in the design of DC-DC converters is the investigation of the control of converters so that they operate in a

stable period-1 over a wide range of input parameters as that is what is expected. The controller should also be relatively simple and easy to implement in practical applications.

The adopted Monodromy approach using the location of eigenvalues cannot only predict the unstable point, but also indicates the stabile margin for a given system. In addition, based on the derived matrix, new stabilisation control schemes can be developed to improve the performance of an objective system. In the following section, the concept and implementation of a proposed controller design is presented

As the stability of the system is governed by the eigenvalues of saltation matrix over a complete period, the principle of this control method is to force them to remain within the unit circle for a wider range of input parameters. By studying the expression 2.17 of the saltation matrix, it can be noticed that this matrix can be influenced by smooth vector fields before and after the switching (f- and f+) or the switching manifold ($\partial h/\partial x$ and $\partial h/\partial t$). Since the vector fields relate to the physical parameters of the converter, this implies that we cannot change them for a given system. But it is possible to alter the switching manifold(s) either by adding an external time-varying signal to alter the term $\partial h/\partial t$ or by adding a signal that is a function of a state variable (output voltage or inductor current) to alter the term $\partial h/\partial x$.

3.5.1 Variable periodical slope compensation method

(a)
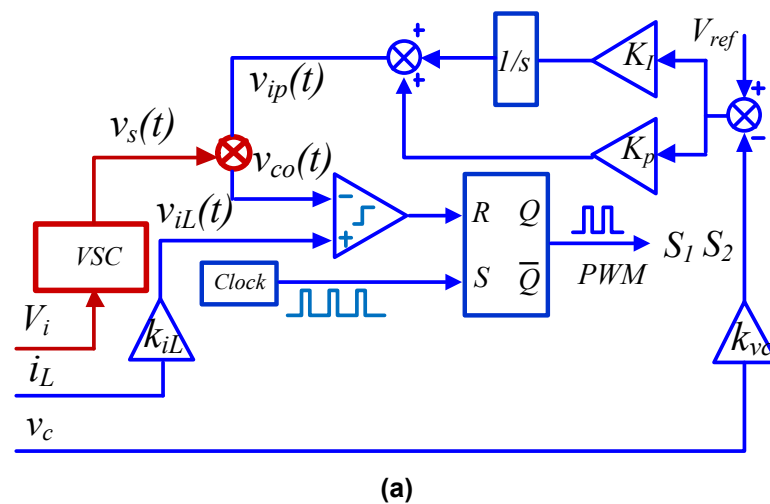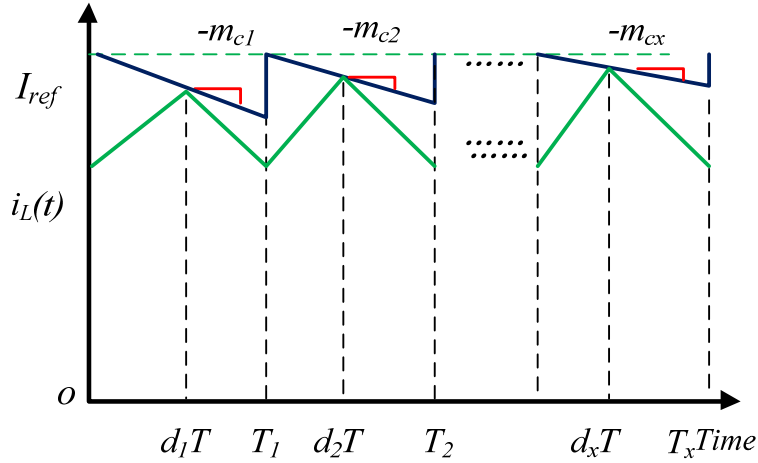
(b)
Figure 3.10 (a) Diagram of the supervising controller
(b) proposed variable periodical slope compensation method

By altering various coefficients in the Monodromy matrix, the stability of the system will be influenced correspondingly. Based on this concept, the variable periodical slope compensation method is proposed as illustrated in Figure 3.10. By adding a variable slope signal to the switching manifold h, the time derivative of the switching manifold ($\partial h/\partial t$) term is changed and then the switching manifold becomes:

$$h_1(x,t) = K_p(x_1 - V_{ref}) + x_3 - \frac{a_{cx}t}{T} - x_2 \tag{3.42}$$

where a_{cx} represents the corresponding amplitude of the variable ramp. There is no effect on its normal vector, but compared to conventional PI control the $\partial h/\partial t$ changes from 0 to:

$$\frac{\partial h}{\partial t} = -\frac{a_{cx}}{T} \tag{3.43}$$

Specifically, it changes the original σ into $\sigma + a_{cx}/T$. By modifying the parameter a_{cx} in the Monodromy matrix according to the different input conditions, the eigenvalues can be located at any chosen location within the unit circle which indicates a stable period-1 operation. The proposed method can keep the magnitude of the eigenvalues exactly the same for different input voltages. For the controller design, the relationship between the input voltage and the required value of a_{cx} must be obtained.

Therefore, the following nonlinear transcendental equation should be solved numerically: $|eig(\mathbf{M}(0,T))| = R$. Here R is the radius of the circle on which the eigenvalues of the Monodromy matrix lie. Figure 3.11 illustrates the input voltage and the a_c required in order to place the eigenvalues on a circle whose radius is 0.85.

Based on these values, a second order polynomial expression can be created:

$$m_{cx}T = -a_{cx} = 2.782 \times 10^{-5} \times V_{in}^2 + 2.333 \times 10^{-1} \times V_{in} - 79.33 \qquad (3.44)$$

This is drawn as the solid blue line in Figure 3.11.
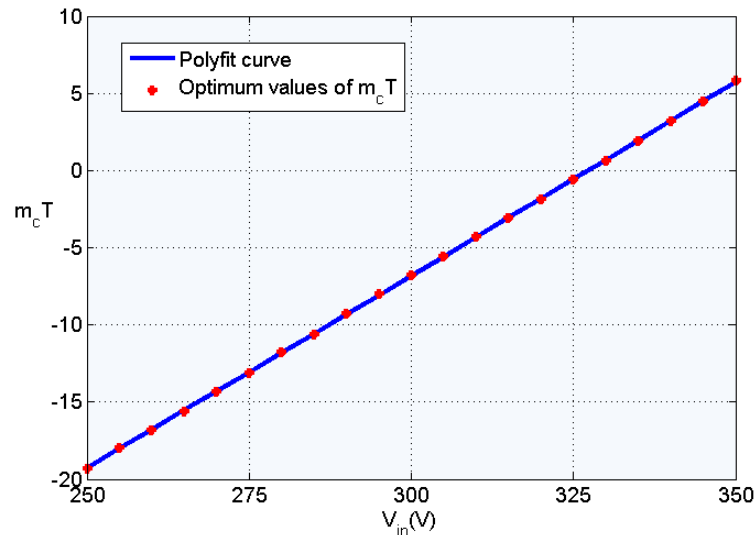
Figure 3.11 Polyfit curve and calculated values of m$_{cx}$ vs. input voltage

3.5.2 Simulation results

A supervising controller is designed based on the derived Monodromy matrix according to the approach presented in Chapter 2. The bifurcation point of the original system without supervising control can be indicated by the locus of eigenvalues of the Monodromy matrix in Figure 3.12. When the input voltage is equal to 318V, the system jumps into the period of bifurcation in Figure 3.12(a); meanwhile, one of the corresponding eigenvalues reaches the border of the unit circle in Figure 3.12(b), which means that the system becomes unstable at this moment.

(a)

47
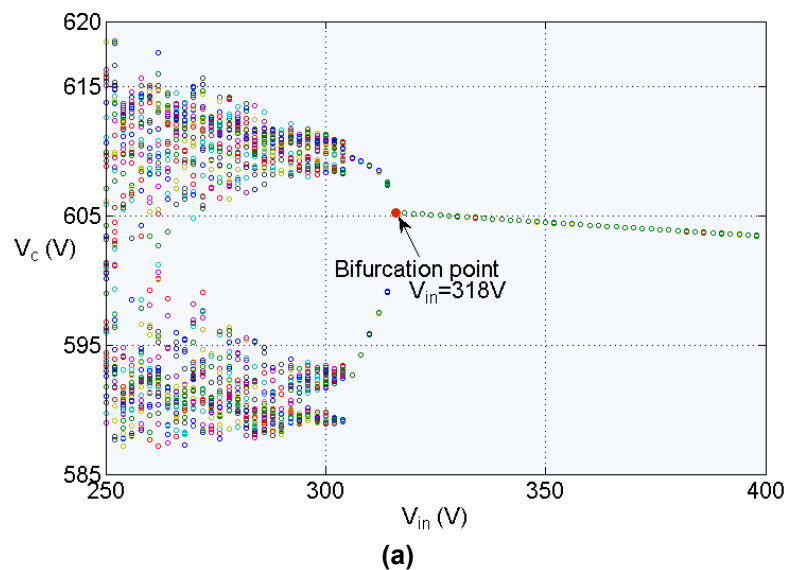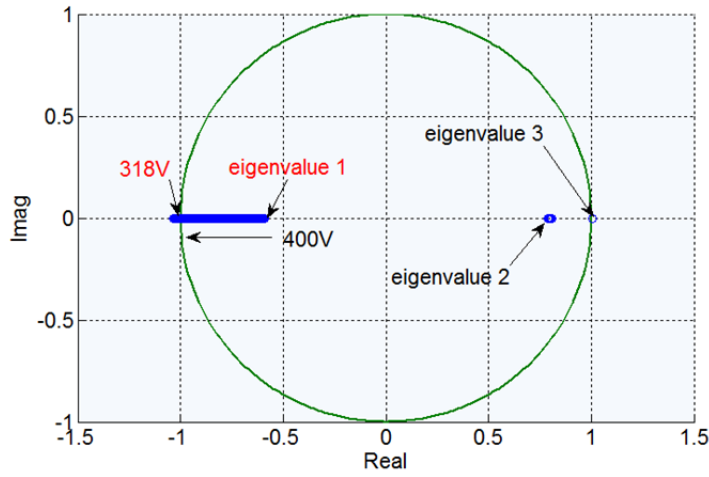
(b)

Figure 3.12 (a) Bifurcation diagram of output voltage vs. input voltage without supervising control;

(b) corresponding locus of eigenvalues of the Monodromy matrix at different input voltages.
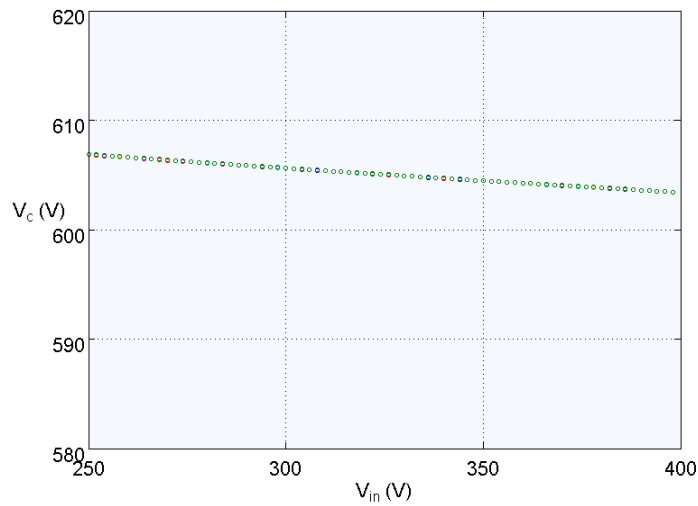
(a)
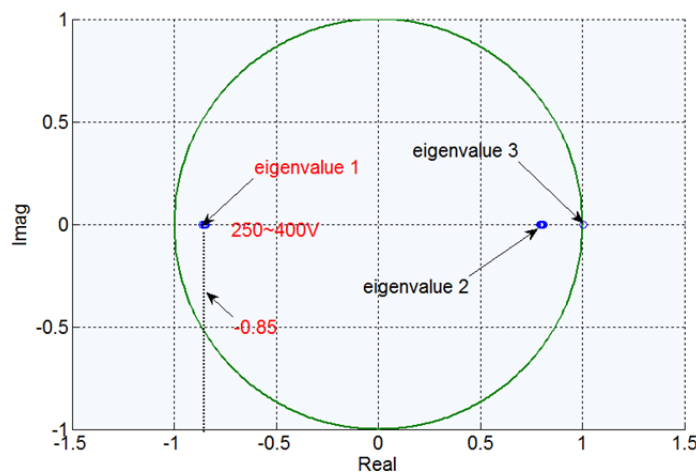
(b)

Figure 3.13 (a) Bifurcation diagram of output voltage vs. input voltage with supervising control;

(b) corresponding locus of eigenvalues of Monodromy matrix at different input voltages.

48

In contrast, Figure 3.13(a) shows the diagram of output voltage vs. input voltage in the system with supervising control, which demonstrates that the system can remain stable within the whole range of input voltages from 250V to 400V. The corresponding locus of eigenvalues of the Monodromy matrix in Figure 3.13(b) indicates that the related eigenvalues are located at the expected places with a certain stability margin as set.

Figure 3.14 shows the influence of inductance L on system stability. By applying the supervising controller the system can remain stable when the inductance L is larger than 140µH as illustrated in Figure 3.14(b); however, without the supervising control, the system exhibits an unstable state with the variation of inductance L from 20µH to 500µH as shown in Figure 3.14(a). From the simulation results above, it is evident that the supervising controller extends the stable range of the original system, and it can also be used to set the stable margin.
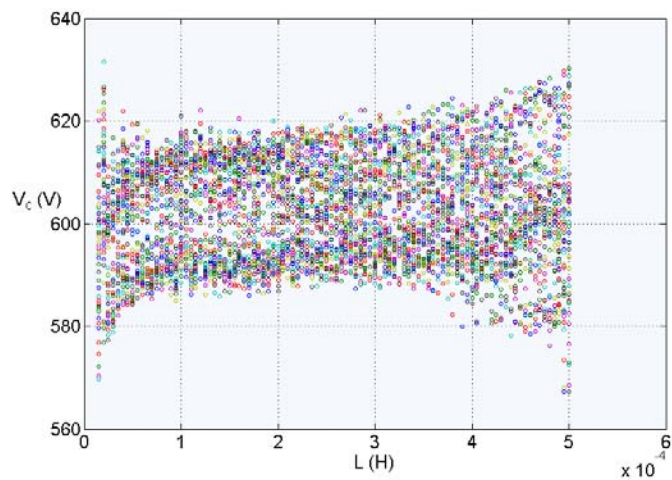
(a)
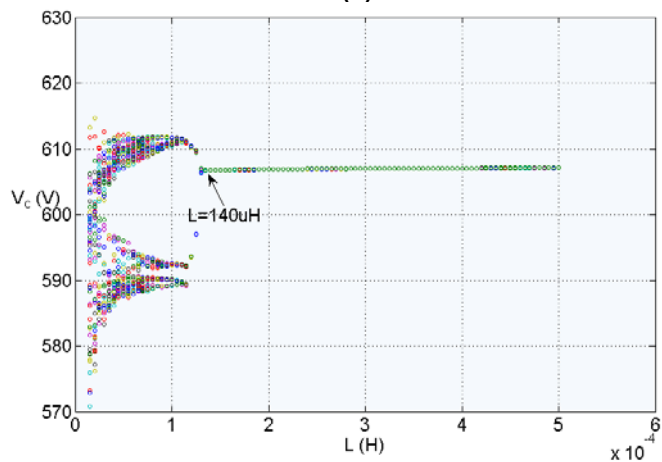
(b)

Figure 3.14 (a) Output voltage vs. inductance L without supervising control;
(b) output voltage vs. inductance L with supervising control (Vin=250V)

49

3.6 Summary

The stability of boost converters under peak current control with slope compensation is analysed by using the Monodromy matrix. Simulation results show the nonlinear phenomena in the boost converter and demonstrate the effectiveness of the Monodromy matrix for bifurcation prediction. This study presents the influence of parasitic parameters to system stability theoretically and numerically. In addition, the analysis of the boost converter under peak-current control with voltage control is presented to verify that the proposed approach can be applied in various conventional control methods. Furthermore, based on the expression of the saltation matrices, advanced control methods can be proposed to extend the stable range under the given parameters.

4 Nonlinear analysis and control of boost converters with constant power loads

This chapter presents the nonlinear analysis of a boost converter with constant power load (CPL). The characteristics of CPL and the boundary conditions of operation between the continuous conduction mode (CCM) and discontinuous conduction mode (DCM) are discussed and analysed. For the first time, the Monodromy matrix has been applied to the converters with CPL at these two conduction modes and the corresponding findings are compared with each other. Analytical and numerical results are presented for both peak current and averaged current cascaded controllers.

4.1 Background

The study on the nonlinear phenomena of single phase DC-DC boost converters with resistive load has been presented in the last chapter. The analysis on this typical type of load is significant in most cases but not the only application. With the development of power electronics technology power distribution systems based on power electronics converters are becoming more and more increasingly common in applications such as smart grids, automotive systems, aircraft and ships. In these muti-converter systems, the downstream DC-DC converters, DC-AC inverters and motor drives tightly regulate their outputs, exhibiting the characteristics of negative impedance. A large amount of research work has been conducted to analyse and overcome the potential instability caused by the CPL [119-131]. System transfer functions of the simple buck and boost converter with CPL in different conduction modes (CCM and DCM) and control modes (voltage and current mode control) have been derived to investigate the system stability in [119, 126, 129]. The controllability of the non-isolated DC-DC Converters with CPL has also been analysed in [130]. In order to analyse, control, and stabilize automotive converters with CPL, a large-signal analysis of a buck converter loaded by a CPL and the corresponding design of a feedback strategy has been carried out in [121, 124, 132]. Based on a large-signal model of the boost converter, the local behaviour around the operation point and its basin of attraction can be defined in [120] . A phase plane analysis and the attraction region have been presented to demonstrate system stability and a reduced order

large signal model for a step-down cascaded system with CPL set up based on Lyapunov stability theory [128, 131, 133].

These stability analysis methods published in the literature can be categorized in two types: small signal methods based on state-space averaging models, and large signal approaches based on nonlinear models. In the small signal category, system stability is studied around the system's operating point using a linearized model. Classical linear analysis tools can then be effectively employed which are widely used and familiar to most application engineers. Nevertheless, some effects caused by the nonlinear components are ignored in these approaches, which limit their domain of validity. For large signal analysis techniques, the objectives and a simplified hypothesis of CPL usually determine the level of the complexity of the models. Large-signal phase plane analysis and Lyapunov-based stability analysis methods are often employed to estimate the domain of attraction of the system operating point. Compared to the small signal linear methods, these approaches are less intuitive but more flexible in terms of validity.

In spite of the availability of the stability analysis methods mentioned above, most publications present results concerning the stability of DC-DC converters with a conventional resistive load [17, 22, 56]. In this chapter, the adopted nonlinear analysis based on the Monodromy matrix is employed for the first time to demonstrate the feasibility of fast-scale stability analysis for a boost converter with CPL.

4.2   Characteristics of CPLs

In general, there are three typical types of loads in the system. One type is constant voltage loads, which operate at a constant voltage at the terminal. The second kind can be constant current loads, which is delivered certain current from the feeder converter. The other group is the CPL, which requires constant power from the feeder converter, and the system permits a certain range of voltage fluctuations at the terminal. For example, the battery is a constant power load when it is switched to constant current charging mode. Figure 4.1 shows a diagram of a renewable power distribution generation system, which employs the sources of PV and a wind turbine. In this system, when the DC-AC inverter drives a motor to tightly regulate the constant speed, the subsystem of the inverter and motor can be regarded as a

constant power load (Figure 4.2). Another example is the subsystem of the DC-DC converter controlling the output voltage as shown in Figure 4.2.
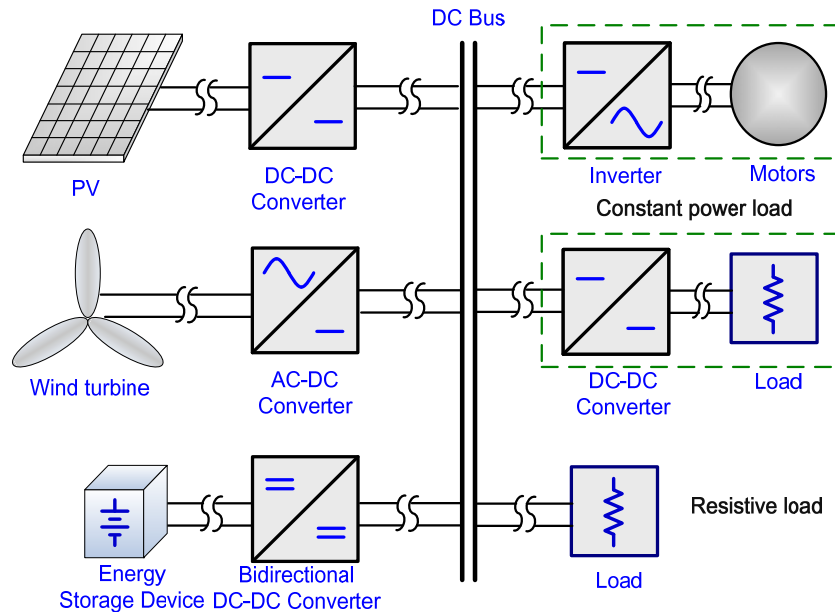
Figure 4.1 Diagram of renewable power distribution generation system

The characteristics of a constant power load and a conventional resistive load are demonstrated in Figure 4.3. In a CPL, power is constant and can be represented by the product of voltage and the current of the load. Therefore, if the voltage across a CPL is increasing, the corresponding current through it is decreasing and vice versa. In the steady state, the CPL operates at the equilibrium operating point around the output voltage of the feeder converter. This can produce a destabilizing effect on this feeder converter to which the CPL is connected [119].
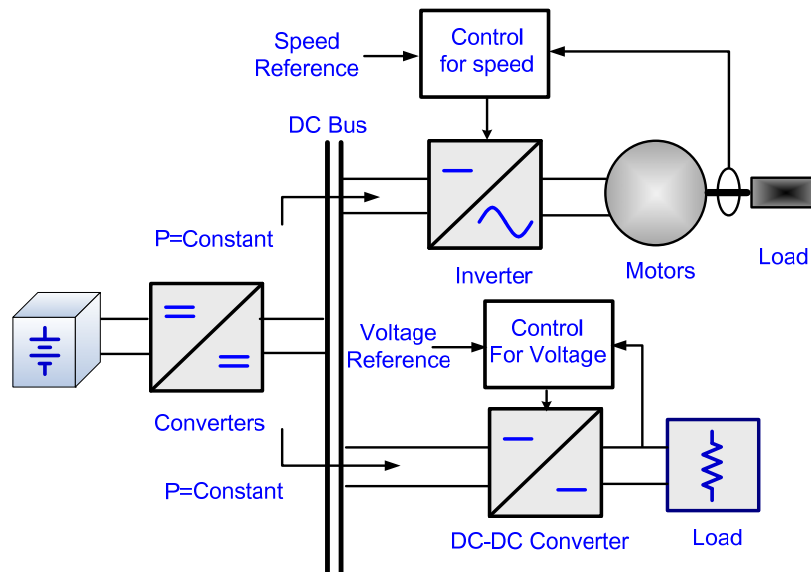
Figure 4.2 Typical DC-AC inverter and DC-DC voltage regulator present a constant power load characteristic to the system

Specifically, in spite of the feature of instantaneous positive impedance (V/I > 0), the

incremental impedance of CPL is always negative (dV/dI < 0), which is different when compared to the positive impedance of the typical resistive load. This characteristic of negative impedance might affect the stability of distributed power generation systems. Therefore, this demonstrates the limitations of classical linear control methods and effective stabilizing control approaches are proposed to ensure large-signal stability.
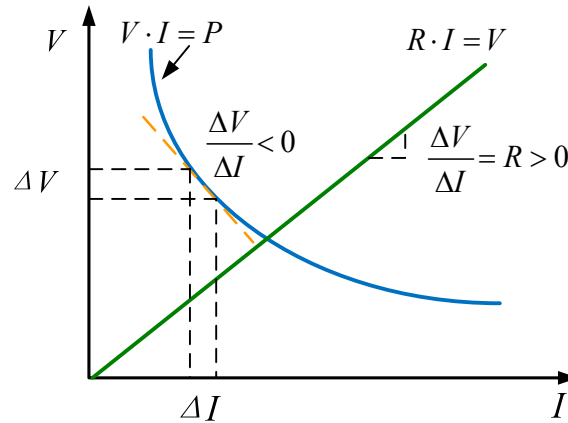
Figure 4.3 Characteristics of constant power load and conventional resistive load

4.3   Operation of boost converter with constant power load

When the voltage ripple of the output capacitor is neglected, the inductor voltage and capacitor current are given by:

$0 < t < D_1 T_s$	$D_1 T < t < (D_1 + D_2)T_s$	$(D_1 + D_2)T_s < t < T_s$
① $\begin{cases} v_L(t) = V_i \\ i_c(t) = -\dfrac{P}{V_c} \end{cases}$ (4.1)	② $\begin{cases} v_L(t) = V_i - V_c \\ i_c(t) = i_L(t) - \dfrac{P}{V_c} \end{cases}$ (4.2)	③ $\begin{cases} v_L(t) = 0 \\ i_c(t) = -\dfrac{P}{V_c} \end{cases}$ (4.3)

There are two subintervals in the CCM operation, as illustrated in Figure 4.4 (b) and three subintervals in the DCM operation as shown in Figure 4.4.(b). With the assumption of the energy conversion ratio μ, the average input can be represented by $P/\mu V_i$. The peak value I_p is equal to the slope multiplied by the length of the first subinterval $D_1 Ts$, and if half of the peak current is less than the average input current, the system is operating in the CCM mode,

$$i_p = \frac{V_i D T_s}{L} \leq \frac{2P}{\mu V_i} \tag{4.4}$$

By applying the principle of inductor volt-second balance, the following is obtained

$$DTV_i + (1-D)T(V_i - V_c) = 0 \tag{4.5}$$

Thus,

$$D = (1 - \frac{V_i}{V_c}) \tag{4.6}$$

(a)

(b)   **(c)**
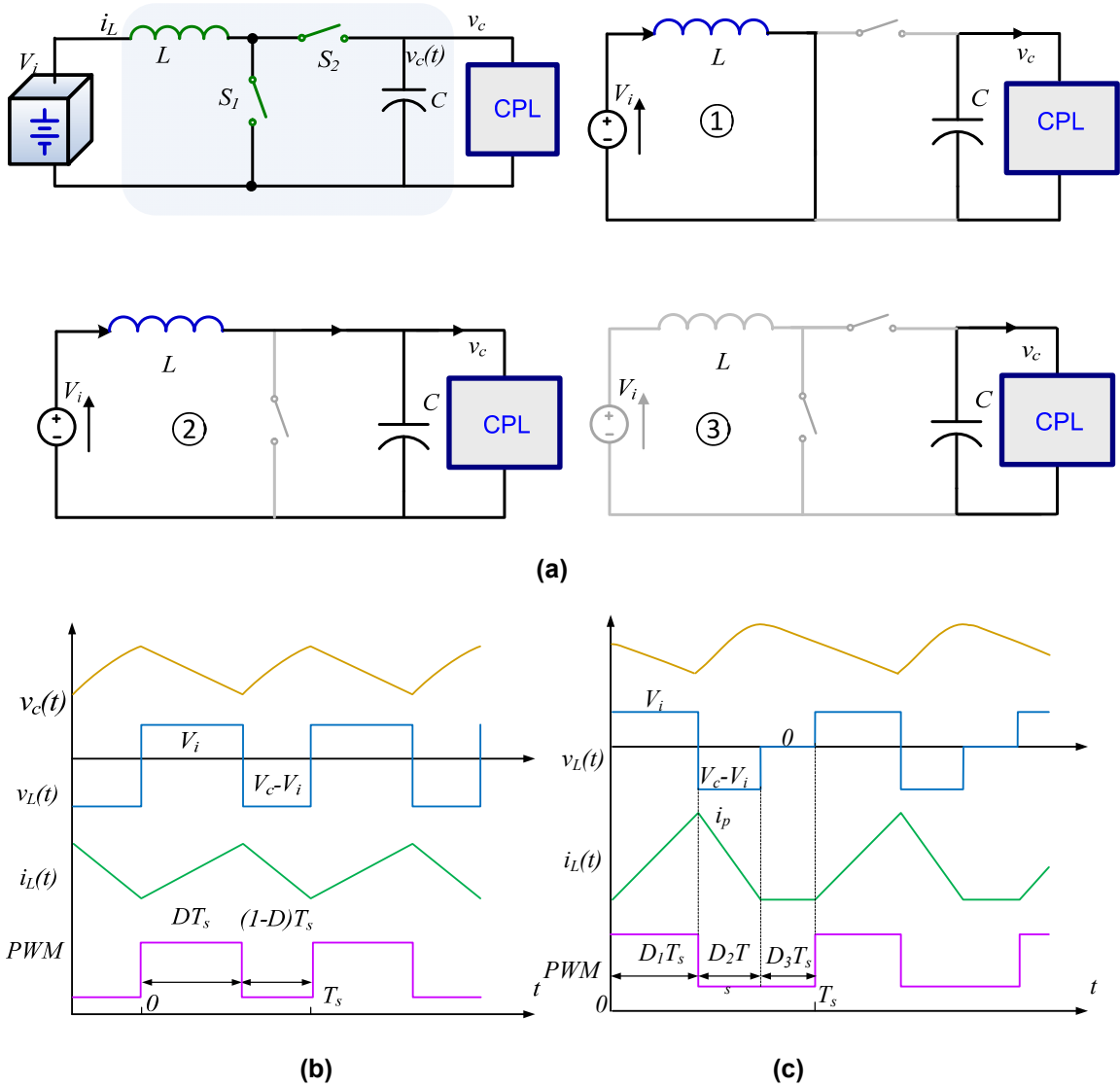
Figure 4.4 (a) Operation states of bidirectional boost converter with CPLs; (b) Key waveforms in CCM operation; (c) Key waveforms in DCM operation

By substituting D into equation 4.4, the output power P needs to satisfy the following expression for CCM operation:

$$D = (1 - \frac{V_i}{V_c})P \geq \frac{\mu V_i^2 (V_c - V_i)T_s}{2V_c L} \tag{4.7}$$

For the given parameters, the power boundary curve between the CCM and DCM can be drawn as shown in Figure 4.5:

In the DCM operation, employing the principles of volt-second balance and capacitor charge balance at the steady state, the following expressions can be obtained:

$$\begin{cases} D_1 T V_i + D_2 T (V_i - V_c) + D_2 T(0) = 0 \\ \int_{D_1 T_s}^{(D_1 + D_2)T_s} i_{ch}(t) = \int_{0_s}^{T_s} i_{dch}(t) \end{cases} \tag{4.8}$$
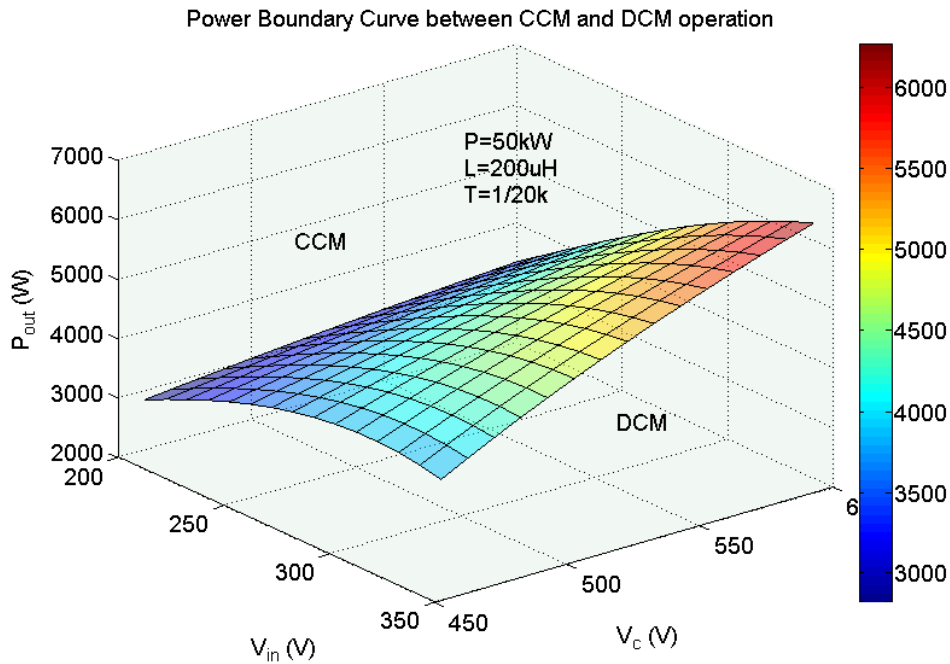
Figure 4.5 Example of power boundary curve between CCM and DCM (μ=1)

The charge input to the capacitor must be equal to the charge output in one period at the steady state. The charging current $i_{ch}(t)$ works at the second subintervals and the discharging current $i_{dch}(t)$ exists over the whole period. Hence, the following equations can be obtained:

$$\begin{cases} i_{ch}(t) = i_L(t) \ t \subset [D_1 T_s, (D_1 + D_2)T_s] \\ i_{dch}(t) = \frac{P}{V_c} \ t \subset [0, T_s] \end{cases} \tag{4.9}$$

The solution for the duty cycle yields:

$$\begin{cases} D_1 = \dfrac{V_c - V_i}{V_i} D_2 \\[3mm] D_1 D_2 = \dfrac{2PLT_s}{V_c V_i} \end{cases}$$

(4.10)

The substitution of D_2 into the second equation leads to the expression for duty cycle D_1:

$$D_1 = \sqrt{\frac{2PL(V_c - V_i)}{T_s V_i^2 V_c}}$$

(4.11)

Hence the expression of duty cycle D at the different operation modes can be obtained:

$$\begin{cases} D = 1 - \dfrac{V_i}{V_c} & CCM \\[3mm] D_1 = \sqrt{\dfrac{2PL(V_c - V_i)}{T_s V_i^2 V_c}} & DCM \end{cases}$$

(4.12)

For the given parameters, the duty cycle under the different operation modes can be illustrated as shown in Figure 4.6:
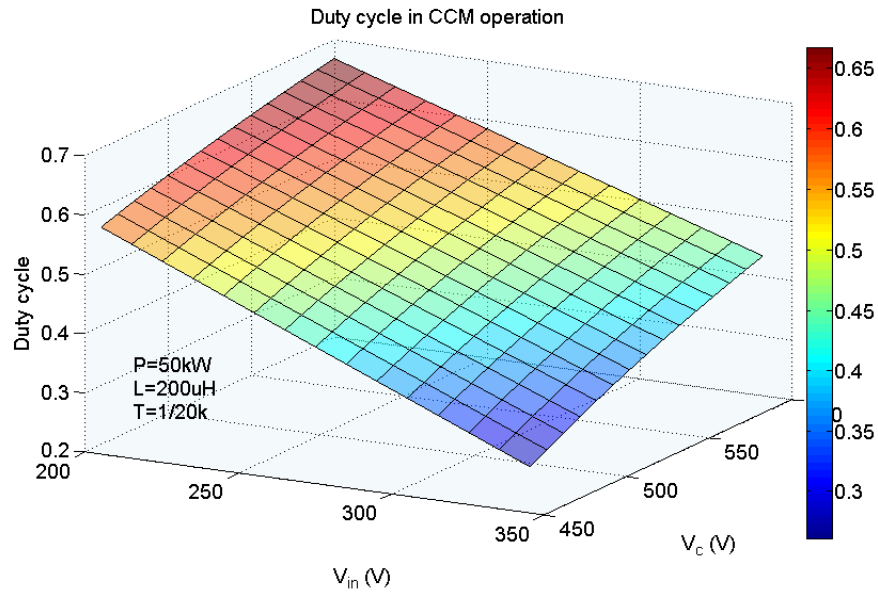
(a)
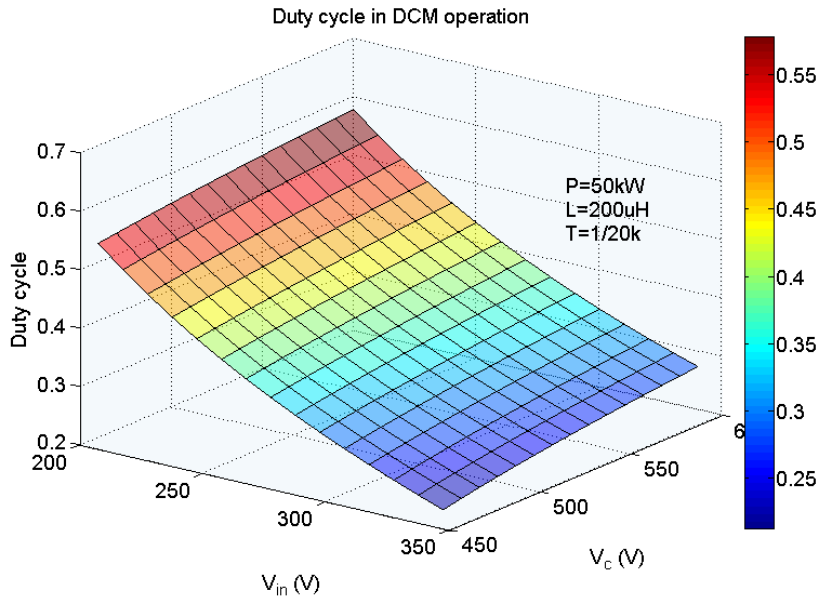
(b)

**Figure 4.6 Example of duty cycle in CCM and DCM operation: (a) CCM operation
(b) DCM operation**

4.4   Calculation of the Monodromy matrix
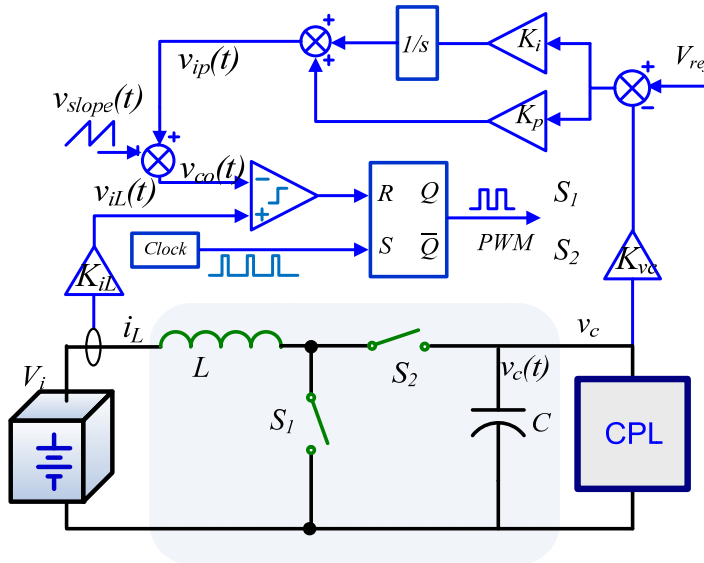
Figure 4.7 Boost converter with constant power load with close loop control

As discussed in the previous chapters, a DC-DC boost converter with the resistive load is a nonlinear system that can be described as an LTI system when the switch is in the on and off state. For a DC-DC boost converter powering a CPL the state matrices are not independent of time, and thus it becomes a linear time variant (LTV) system. Because of the nonlinear characteristics of CPL, the analytical expressions of the state transition matrices cannot be derived from the differential equations in the closed form. Based on the observation of the calculation results from the state

58

transition matrices, the voltage ripple slightly affects the fast-scale instability of the system, and thus the approximation method of neglecting the output ripple voltage could be employed to transform the original system to the LTI system. Consequently, the characteristic of constant power load is changed as a constant current load in the following analysis.

A diagram of a bidirectional boost converter loaded by CPL with peak current control and voltage feedback is illustrated in Figure 4.7. K_p and K_i represent the coefficients of the proportion and integrator; K_{vc} and K_{il} are the gains, which are from the sampled values of output voltage v_c and the inductor current i_L to the signals fed to the controller. As discussed at section of 3.4 in the last chapter, although the integrator in the feedback path introduces only an extra dimension in the state matrices, its associated eigenvalues have a slight effect in deciding the fast-scale stability of the system. The duty cycle of the switches is determined by the output of the integrator, and hence it needs to be considered when computing the instants of switching. Three state vectors x_1, x_2, x_3 are used to represent the capacitor voltage v_c, the inductor current i_L , and the output of the integrator in the feedback loop v_{ip} respectively. The switches S_1 and S_2 are operating complementarily with the PWM control algorithm and thus the corresponding differential equations and the approximated linear vector fields are given as follows according to the different operational conditions:

	subinterval 1	subinterval 2	subinterval 3
Differential equations	$$\begin{cases} \dfrac{dv_c}{dt} = -\dfrac{P}{Cv_c} \\ \dfrac{di_L}{dt} = \dfrac{V_i}{L} \\ \dfrac{dv_{ip}}{dt} = K_I(V_{ref}\text{-}K_{vc}v_c) \end{cases}$$ (4.13)	$$\begin{cases} \dfrac{dv_c}{dt} = \dfrac{i_L}{C} - \dfrac{P}{Cv_c} \\ \dfrac{di_L}{dt} = \dfrac{V_i - v_c}{L} \\ \dfrac{dv_{ip}}{dt} = K_I(V_{ref}\text{-}K_{vc}v_c) \end{cases}$$ (4.14)	$$\begin{cases} \dfrac{dv_c}{dt} = -\dfrac{P}{Cv_c} \\ \dfrac{di_L}{dt} = 0 \\ \dfrac{dv_{ip}}{dt} = K_I(V_{ref}\text{-}K_{vc}v_c) \end{cases}$$ (4.15)
Approximated linear vector fields	$$f_1 = \begin{bmatrix} -\dfrac{P}{CV_c} \\ \dfrac{V_i}{L} \\ K_I(V_{ref}\text{-}K_{vc}x_1) \end{bmatrix}$$ (4.16)	$$f_2 = \begin{bmatrix} \dfrac{x_2}{C} - \dfrac{P}{CV_c} \\ \dfrac{V_i - x_1}{L} \\ K_I(V_{ref} - K_{vc}x_1) \end{bmatrix}$$ (4.17)	$$f_3 = \begin{bmatrix} -\dfrac{P}{CV_c} \\ 0 \\ K_I(V_{ref} - K_{vc}x_1) \end{bmatrix}$$ (4.18)

The state matrices for every subinterval are given in the following:

$$\mathbf{A}_1 = \begin{bmatrix} 0 & 0 & 0 \\ 0 & 0 & 0 \\ -K_i K_{vc} & 0 & 0 \end{bmatrix} \tag{4.19}$$

$$\mathbf{A}_2 = \begin{bmatrix} 0 & \dfrac{1}{C} & 0 \\ -\dfrac{1}{L} & 0 & 0 \\ -K_i K_{vc} & 0 & 0 \end{bmatrix} \tag{4.20}$$

$$\mathbf{A}_3 = \begin{bmatrix} 0 & 0 & 0 \\ 0 & 0 & 0 \\ -K_i K_{vc} & 0 & 0 \end{bmatrix} \tag{4.21}$$

$$\mathbf{B}_1 = \mathbf{B}_2 = \begin{bmatrix} -\dfrac{P}{C} & 0 & 0 \\ 0 & \dfrac{1}{L} & 0 \\ 0 & 0 & K_I \end{bmatrix} \tag{4.22}$$

$$\mathbf{B}_3 = \begin{bmatrix} -\dfrac{P}{C} & 0 & 0 \\ 0 & 0 & 0 \\ 0 & 0 & K_I \end{bmatrix} \tag{4.23}$$

$$\mathbf{u} = \begin{bmatrix} \dfrac{1}{V_c} \\ V_i \\ V_{ref} \end{bmatrix} \tag{4.24}$$

From the diagram of the control algorithm displayed in Figure 4.7, the switching action of S_1 that changing from the on state to the off state happens when signal v_{iL} is equal to v_{con}. In other words, it is the moment that the inductor current equals the output value of the PI controller. This switching event exists in both CCM and DCM operation as shown in Figure 4.8.
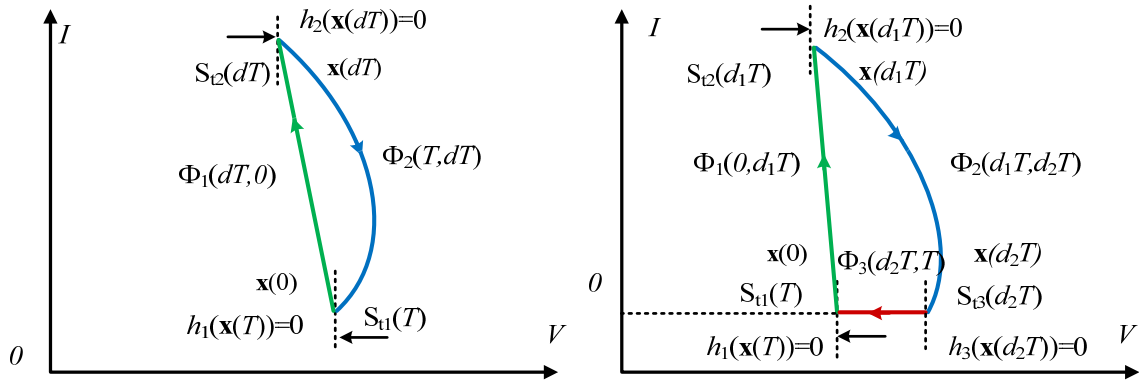
Figure 4.8 Phase portrait of inductor current and output voltage in CCM (left) and DCM operation (right).

If the switching condition is defined as $h_2(x, t)$, it is specified as follows:

$$h_2(x,t) = K_p(V_{ref} - K_{vc}x_1) + x_3 + m_c t - K_{iL}x_2 \qquad (4.25)$$

Hence, its normal vector can be obtained as:

$$\mathbf{n}_2 = \begin{bmatrix} \partial h_2 / \partial x_1 \\ \partial h_2 / \partial x_2 \\ \partial h_2 / \partial x_3 \end{bmatrix} = \begin{bmatrix} -K_p K_{vc} \\ -K_{iL} \\ 1 \end{bmatrix} \qquad (4.26)$$

And its rate of change is given by:

$$\frac{\partial h}{\partial t} = m_c \qquad (4.27)$$

The other terms involved in equation 2.17 can be expressed as follows:

$$(f_2 - f_1)\mathbf{n}_2^T = \begin{bmatrix} \dfrac{x_2}{C} \\ -\dfrac{x_1}{L} \\ 0 \end{bmatrix} \begin{bmatrix} -K_p K_{vc} & -K_{iL} & 1 \end{bmatrix} = \begin{bmatrix} -\dfrac{K_p K_{vc}x_2}{C} & -\dfrac{K_{iL}x_2}{C} & \dfrac{x_2}{C} \\ \dfrac{K_p K_{vc}x_1}{L} & \dfrac{K_{iL}x_1}{L} & -\dfrac{x_1}{L} \\ 0 & 0 & 0 \end{bmatrix} \qquad (4.28)$$

$$\mathbf{n}_2^T f_1 = \begin{bmatrix} -K_p K_{vc} & -K_{iL} & 1 \end{bmatrix} \begin{bmatrix} -\dfrac{P}{Cx_1} \\ \dfrac{V_i}{L} \\ K_I(V_{ref} - K_{vc}x_1) \end{bmatrix} = \dfrac{K_p K_{vc}P}{Cx_1} - \dfrac{K_{iL}V_i}{L} + K_I(V_{ref} - K_{vc}x_1) = s_p \qquad (4.29)$$

Hence the saltation matrix S_{t2} can be obtained as:

$$S_{t2} = \begin{bmatrix} 1 - \dfrac{K_p K_{vc} x_2}{C(s_p + \dfrac{m_c}{T})} & -\dfrac{K_{iL} x_2}{C(s_p + \dfrac{m_c}{T})} & \dfrac{x_2}{C(s_p + \dfrac{m_c}{T})} \\[3ex] \dfrac{K_p K_{vc} x_1}{L(s_p + \dfrac{m_c}{T})} & 1 + \dfrac{K_{iL} x_1}{L(s_p + \dfrac{m_c}{T})} & -\dfrac{x_1}{L(s_p + \dfrac{m_c}{T})} \\[3ex] 0 & 0 & 1 \end{bmatrix} \tag{4.30}$$

As mentioned in chapter 3, the periodical clock signals make the corresponding saltation matrix an identity matrix, and thus both the first saltation matrix in the CCM and DCM operation are given as identity matrices. If the third switching function is defined as h₃(x,t), the following is obtained

$$h_3(x,t) = x_2 = 0 \tag{4.31}$$

Thus :

$$\mathbf{n} = \begin{bmatrix} \partial h_3 / \partial x_1 \\ \partial h_3 / \partial x_2 \\ \partial h_3 / \partial x_3 \end{bmatrix} = \begin{bmatrix} 0 \\ 1 \\ 0 \end{bmatrix} \tag{4.32}$$

and:

$$\frac{\partial h}{\partial t} = 0 \tag{4.33}$$

$$(f_3 - f_2)\mathbf{n}^T = \begin{bmatrix} -\dfrac{x_2}{C} \\[2ex] \dfrac{x_1 - V_i}{L} \\[2ex] 0 \end{bmatrix} \begin{bmatrix} 0 & 1 & 0 \end{bmatrix} = \begin{bmatrix} 0 & -\dfrac{x_2}{C} & 0 \\[2ex] 0 & \dfrac{x_1 - V_i}{L} & 0 \\[2ex] 0 & 0 & 0 \end{bmatrix} \tag{4.34}$$

$$\mathbf{n}_3^T f_2 = \begin{bmatrix} 0 & 1 & 0 \end{bmatrix} \begin{bmatrix} \dfrac{x_2}{C} - \dfrac{P}{Cx_1} \\[2ex] \dfrac{V_i - x_1}{L} \\[2ex] K_I(K_{vc} x_1 - V_{ref}) \end{bmatrix} = \frac{V_i - x_1}{L} \tag{4.35}$$

$$\mathbf{S}_{t3} = \begin{bmatrix} 1 & -\dfrac{x_2 L}{(V_i - x_1)C} & 0 \\ 0 & 0 & 0 \\ 0 & 0 & 1 \end{bmatrix} \qquad (4.36)$$

By applying the following equations, the Mondromy matrix **M,** which is the state transition matrix of the whole clock period, can be calculated:

$$\begin{cases} \mathbf{M} = \mathbf{S}_{t1} \times \mathbf{\Phi}_1 \times \mathbf{S}_{t2} \times \mathbf{\Phi}_2 & \mathrm{C\,C\,M} \\ \mathbf{M} = \mathbf{S}_{t1} \times \mathbf{\Phi}_1 \times \mathbf{S}_{t2} \times \mathbf{\Phi}_2 \times \mathbf{S}_{t3} \times \mathbf{\Phi}_3 & \mathrm{D\,C\,M} \end{cases} \qquad (4.37)$$

4.5   Simulation results

4.5.1   CCM operation

The bifurcation diagram of the boost converter with constant power load at the different input voltages in CCM operation is shown in Figure 4.9(a). It can be seen that the bifurcation happens at the condition when the input voltage equals 308V, and the associated eigenvalues (eigenvalue 1) move to the unit circle along the negative real line as illustrated in Figure 4.9(b), which demonstrates that the system will exhibit the period-doubling bifurcation beyond this point.

(a)

(b)
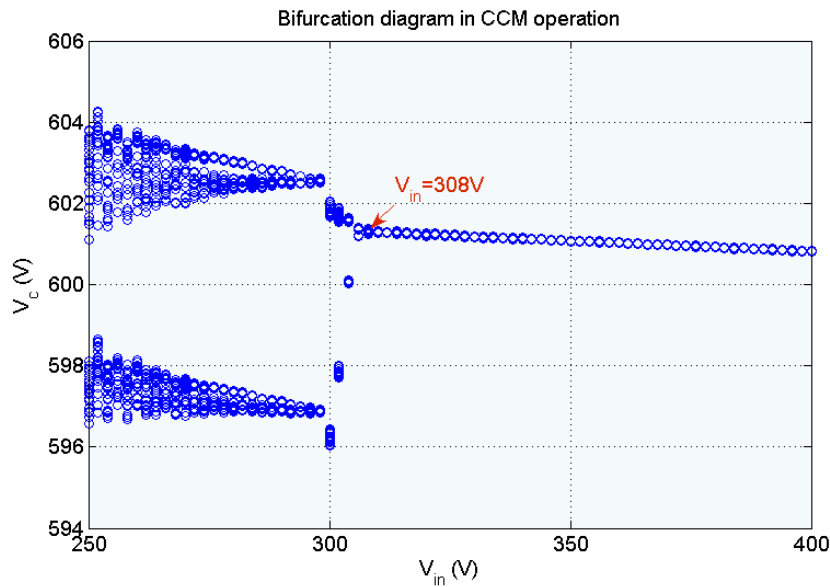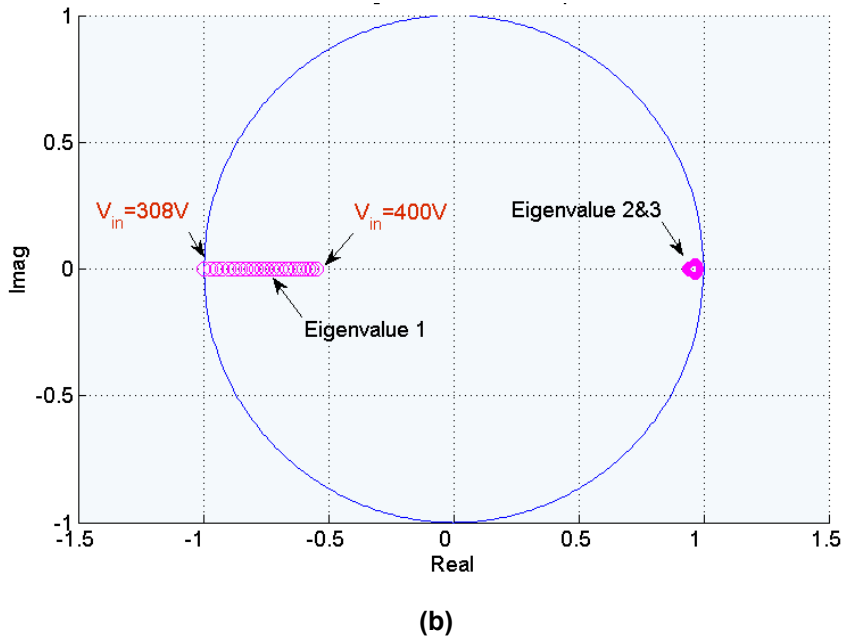
Figure 4.9 (a) Bifurcation diagram of boost converter with constant power load (50kW) in CCM operation
(b) Corresponding plotted eigenvalues of Monodromy matrix

Compared with this, the eigenvalues related to the state vectors of the output voltage and integrator (eigenvalue 2 and 3) see a slight change under the condition of varying input voltages. It turns out that they are not the strong relevant elements for fast-scale instability.
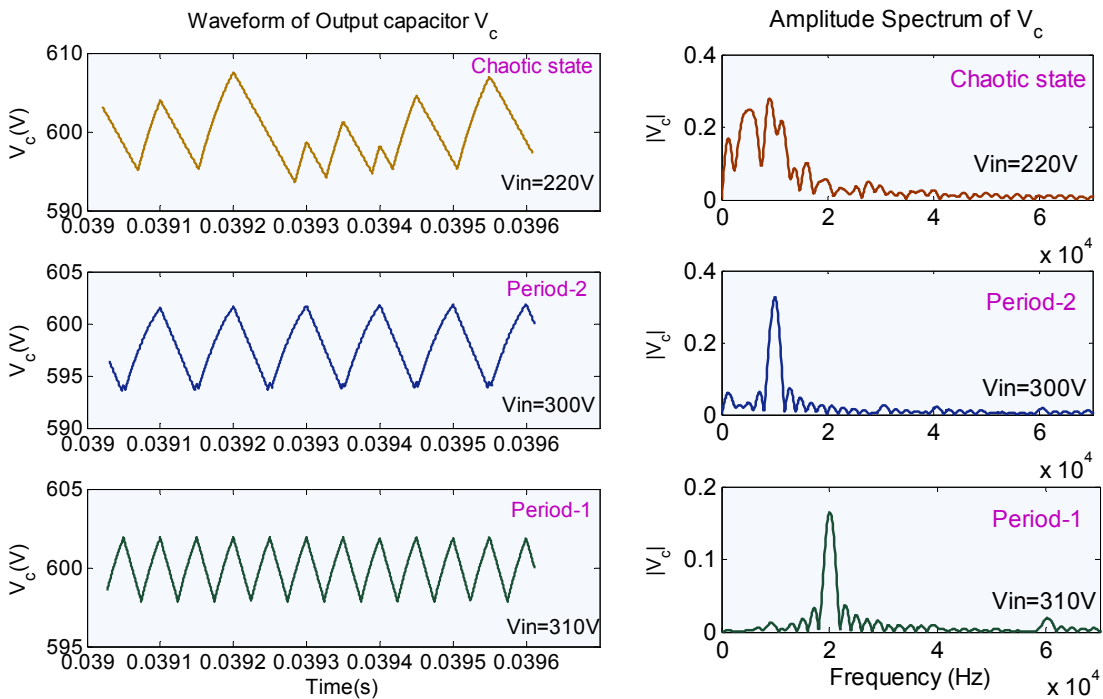
Figure 4.10 The waveform of output capacitor V_c and its power spectrum

The waveforms of output voltage v_c and the corresponding power spectrum under

three different input voltages are shown in Figure 4.10. The bottom row of the figure shows that the system is operating in the expected stable period-1 and the related curve of power spectrum demonstrates that the switching frequency is operating at 20kHz. The middle row of the figure illustrates the system changing to operate in period-2 when the input voltage is varied from 310V to 300V. The associated power spectrum shows that the frequency of the maximum components in the measured waveforms varies from 20kHz to 10kHz. In the top figure, the waveform exhibits random-like behaviour; and the corresponding power spectrum indicates that the system is operating in a chaotic state.

(a)

(b)
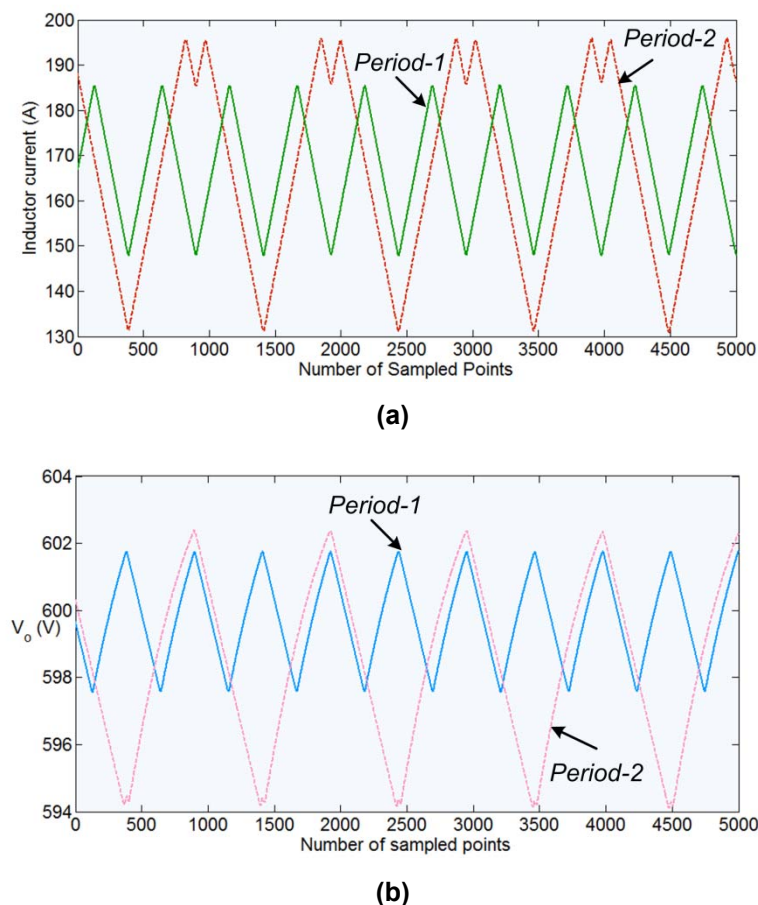
Figure 4.11 The comparison of waveforms of inductor current and output voltage in period-1 and period 2: (a) inductor current (b) output voltage

A comparison of voltage and current ripples in period-1 and period 2 is illustrated in Figure 4.11. This figure shows that both the voltage and current ripples nearly double in scale when changing from period-1 to period-2. Thus, although the period-2 is a kind of stable operation mode, it should be inhibited in practical applications. In addition, these ripples can become much larger when entering the chaotic state. Consequently, increased ripples cause not only higher losses across components,

but also produce potential EMI issues.

(a)

(b)
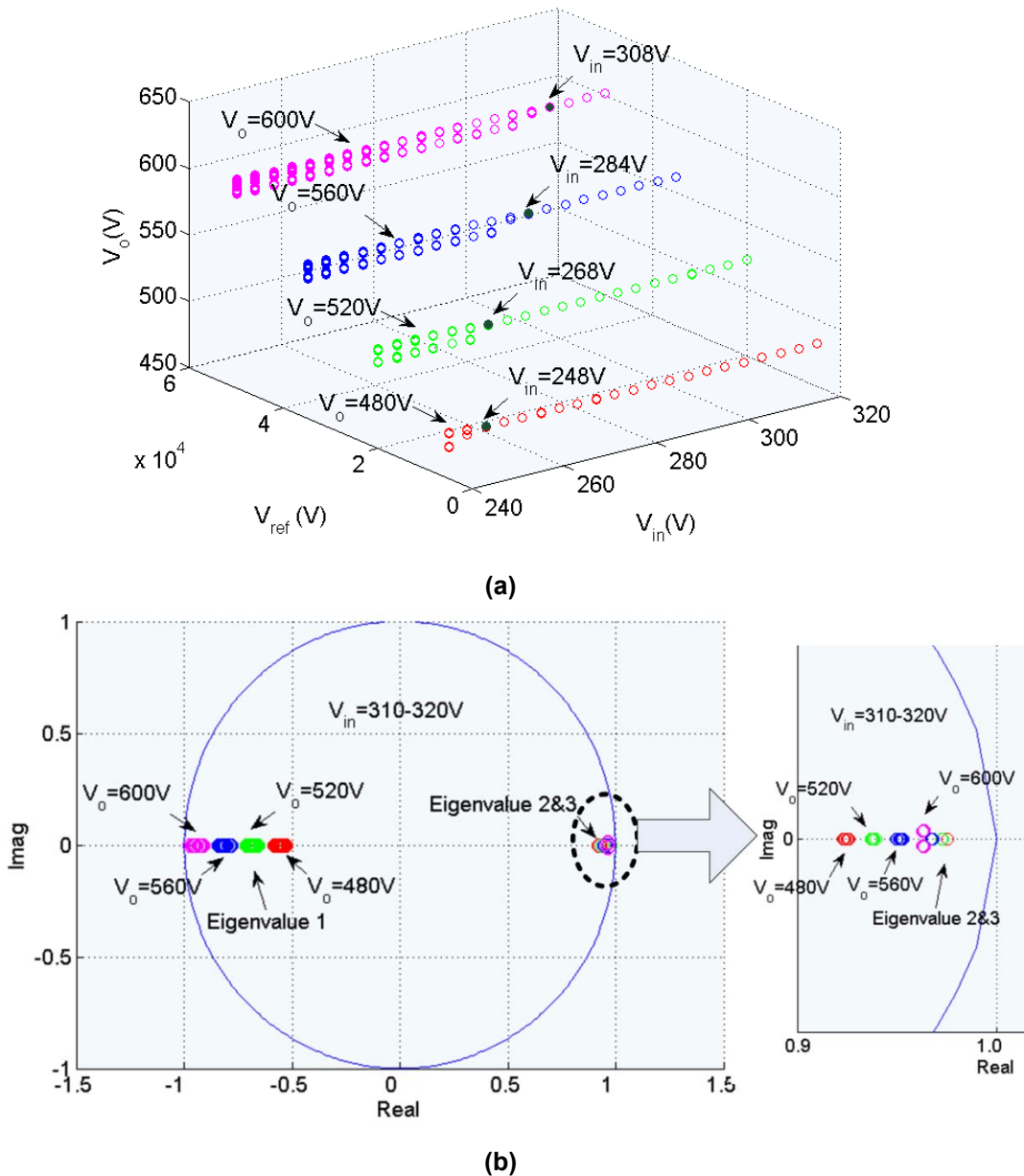
Figure 4.12 (a) Bifurcation diagram of boost converter with CPL at different output voltages (b) Corresponding eigenvalues of Monodromy matrix

In some specific applications, the systems are permitted a degree of voltage fluctuation at the output terminals. The bifurcation diagram of a boost converter with the different output voltage levels at the same load conditions is shown in Figure 4.12 (a). The output voltage is set at 480V, 520V, 560V, 600V at 50kW constant power load. The simulation results show that the bifurcation point varies from the input voltage of 248V to 308V accordingly. By setting the range of the input voltage from 310V to 320V, the calculated eigenvalues at the different output voltages are plotted in the diagram of the unit circle as illustrated in Figure 4.12 (b).

It is evident that eigenvalue 1 plays the most significant role in determining the fast-scale stability of the system. In contrast, eigenvalues 2 and 3 do not change dramatically during the variation of the different outputs. Moreover, the information of the stable margin can be obtained from the diagram generated, which can be employed for parameter evaluation and the optimal design of the DC-DC converters.

4.5.2 DCM operation

(a)

(b)
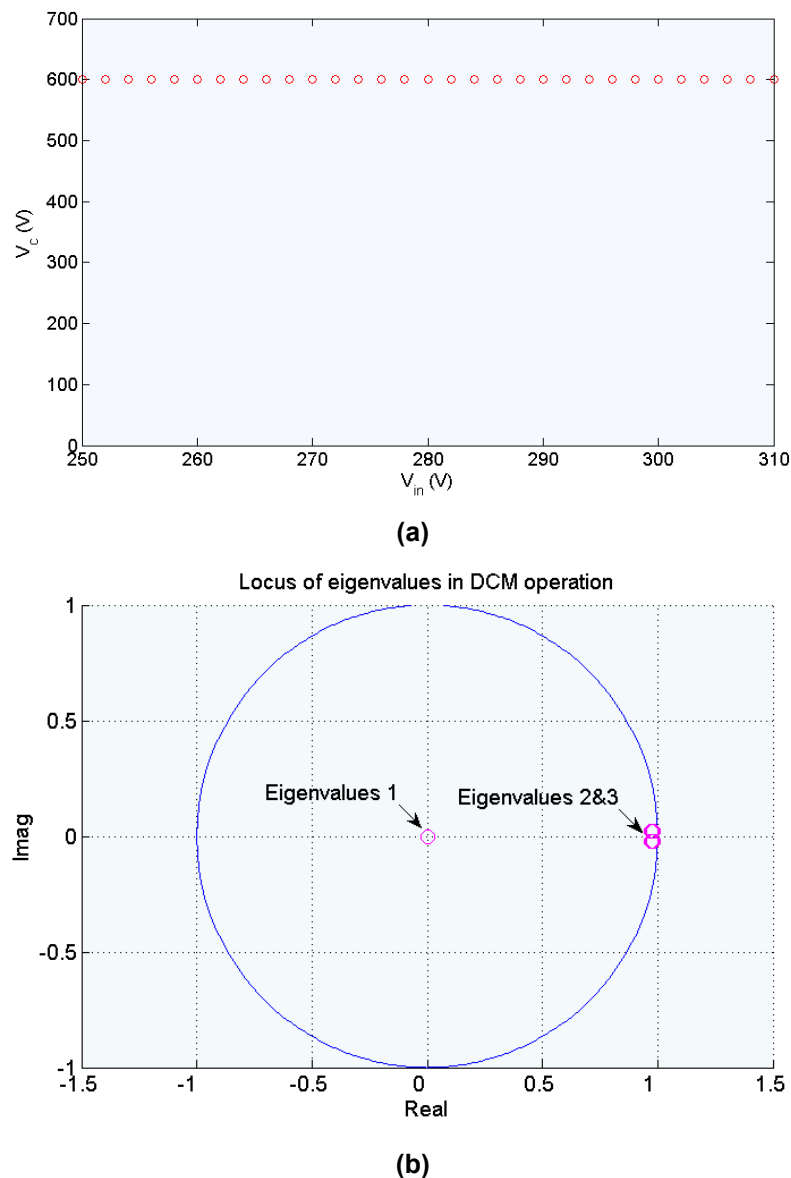
**Figure 4.13(a) Output performance of boost converter with CPLs in DCM operation
(b) Corresponding eigenvalues of Monodromy matrix**

Figure 4.13 presents the system performance in DCM operation. According to the boundary curve between the CCM and DCM in Figure 4.5, the output power is set to 4kW to guarantee that converter operates in the DCM mode, under the conditions of the input voltages varying from 250V to 310V. Compared with the bifurcation diagram

of the boost converter operating in the CCM mode, the system remains in the stable period-1 within this input range at the same given conditions. It can be seen that eigenvalue 1 comes out of zero under all inputs, since it is related to the inductor current which goes to zero at the end of every switching period.

It should be noted that the other eigenvalues show only a little change at the variation of the external parameters, which implies that the system is relatively more stable in the DCM operation than in the CCM operation from the perspective of fast-scale stability.

4.6   Averaged current control with voltage feedback

The cascaded control algorithm consisting of inner averaged current and outer voltage loop is widely used in many industrial applications and is illustrated in Figure 4.14. The approach of the averaging and small signal perturbation is employed to obtain the system transfer functions at the steady-state operating point. The gains of the PI-controller can be calculated by specifying the damping factor and natural frequency of the system. This is an effective method for the optimized design of converters in terms of dynamical responses in the slow-scale frequency domain but it cannot be used to study the fast-scale performance of the system. The following section adopts the presented nonlinear method of analysis to investigate the performance of the boost converter with CPL under the cascaded control algorithm.
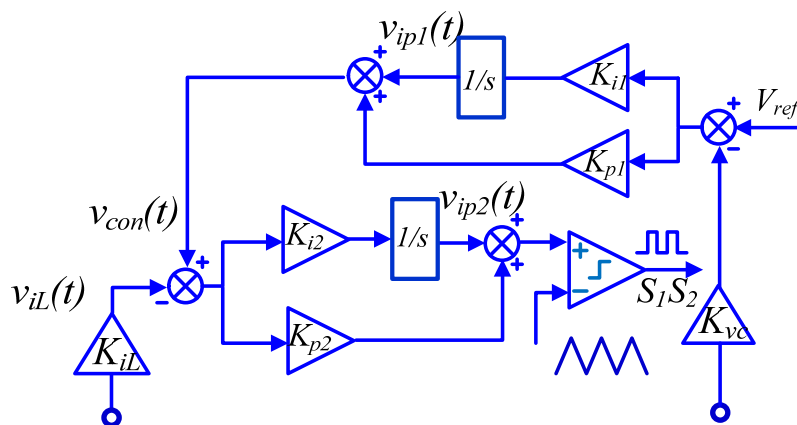
Figure 4.14 Diagram of cascaded control algorithm

The inductor current i_L, capacitor voltage v_c and the output of the integrator in the feedback loop v_{ip} are chosen as state variables. When the switch is ON, the state equations can be expressed as:

$$\begin{cases} \dfrac{dv_c}{dt} = -\dfrac{P}{Cv_c} \\[2mm] \dfrac{di_L}{dt} = \dfrac{V_i}{L} \\[2mm] \dfrac{dv_{ip1}}{dt} = K_{i1}(V_{ref} - K_{vc}v_c) \\[2mm] \dfrac{dv_{ip2}}{dt} = K_{i2}((v_{ip1} + K_{p1}(V_{ref} - K_{vc}v_c)) - K_{iL}i_L) \end{cases} \tag{4.38}$$

When the switch is OFF, the state equations are obtained as follows:

$$\begin{cases} \dfrac{dv_c}{dt} = \dfrac{i_L}{C} - \dfrac{P}{Cv_c} \\[2mm] \dfrac{di_L}{dt} = \dfrac{V_i - v_c}{L} \\[2mm] \dfrac{dv_{ip1}}{dt} = K_{i1}(V_{ref} - K_{vc}v_c) \\[2mm] \dfrac{dv_{ip2}}{dt} = K_{i2}((v_{ip1} + K_{p1}(V_{ref} - K_{vc}v_c)) - K_{iL}i_L) \end{cases} \tag{4.39}$$

If the state vector **x** is used to represent the above equations, the right-hand side state equations are expressed as:

$$f_{on} = \begin{bmatrix} -\dfrac{P}{CV_c} \\[3mm] \dfrac{V_i}{L} \\[3mm] K_{i1}(V_{ref} - K_{vc}x_1) \\[3mm] K_{i2}((x_3 + K_{p1}(V_{ref} - K_{vc}x_1)) - K_{iL}x_2) \end{bmatrix} \tag{4.40}$$

$$f_{off} = \begin{bmatrix} \dfrac{x_2}{C} - \dfrac{P}{CV_c} \\[3mm] \dfrac{V_i - x_1}{L} \\[3mm] K_{i1}(V_{ref} - K_{vc}x_1) \\[3mm] K_{i2}((x_3 + K_{p1}(V_{ref} - K_{vc}x_1)) - K_{iL}x_2) \end{bmatrix} \tag{4.41}$$

where x_1 is the capacitor voltage v_c, x_2 is the inductor current i_L. and x_3 and x_4 are the outputs of the integrator in the outer and inner feedback loops v_{ip1} and v_{ip2} respectively. Thus, the state matrices for the ON and OFF periods are given as:

$$
\mathbf{A}_{on} = \begin{bmatrix} 0 & 0 & 0 & 0 \\ 0 & 0 & 0 & 0 \\ -K_{i1}K_{vc} & 0 & 0 & 0 \\ -K_{vc}K_{i2}K_{p1} & -K_{iL}K_{i2} & K_{i2} & 0 \end{bmatrix} \tag{4.42}
$$

$$
\mathbf{A}_{off} = \begin{bmatrix} 0 & \dfrac{1}{C} & 0 & 0 \\ -\dfrac{1}{L} & 0 & 0 & 0 \\ -K_{i1}K_{vc} & 0 & 0 & 0 \\ -K_{i2}K_{p1}K_{vc} & -K_{i2}K_{iL} & K_{i2} & 0 \end{bmatrix} \tag{4.43}
$$

$$
\mathbf{B}_{on} = \mathbf{B}_{off} = \begin{bmatrix} -\dfrac{P}{C} & 0 & 0 & 0 \\ 0 & 0 & \dfrac{1}{L} & 0 \\ 0 & 0 & 0 & K_{i1} \\ 0 & 0 & 0 & K_{i2}K_{p1} \end{bmatrix} \tag{4.44}
$$

$$
\mathbf{u} = \begin{bmatrix} \dfrac{1}{V_c} \\ 0 \\ V_i \\ V_{ref} \end{bmatrix} \tag{4.45}
$$

The control signal obtained from the output of the PI controller is expressed as

$$
v_{con} = K_{p2}((x_3 + K_{p1}(V_{ref} - K_{vc}x_1)) - K_{iL}x_2) + x_4 \tag{4.46}
$$

This is used for comparison with the produced triangular signal to generate the PWM signals. Therefore, the switching condition can be defined as $h_1(x, t) = 0$, where:

$$
h_1(x,t) = K_{p2}((x_3 + K_{p1}(V_{ref} - K_{vc}x_1)) - K_{iL}x_2) + x_4 - \frac{V_p \cdot t}{T} \tag{4.47}
$$

Hence, its normal vector and the rate of change are given by:

$$
\mathbf{n} = \begin{bmatrix} \partial h_1 / \partial x_1 \\ \partial h_1 / \partial x_2 \\ \partial h_1 / \partial x_3 \\ \partial h_1 / \partial x_4 \end{bmatrix} = \begin{bmatrix} -K_{p1}K_{p2}K_{vc} \\ -K_{iL}K_{p2} \\ K_{p2} \\ 1 \end{bmatrix} \tag{4.48}
$$

$$
\frac{\partial h}{\partial t} = -\frac{V_p}{T} = s_a \tag{4.49}
$$

The other terms in calculating the saltation matrix can be obtained as follows:

$$(f_{off} - f_{on})\mathbf{n}^T = \begin{bmatrix} -\dfrac{K_{P2}K_{P1}K_{vc}x_2}{C} & -\dfrac{K_{P2}K_{iL}x_2}{C} & \dfrac{K_{P2}x_2}{C} & \dfrac{x_2}{C} \\[2mm] \dfrac{K_{P2}K_{P1}K_{vc}x_1}{L} & \dfrac{K_{P2}K_{iL}x_1}{L} & -\dfrac{K_{P2}x_1}{L} & -\dfrac{x_1}{L} \\[2mm] 0 & 0 & 0 & 0 \\[1mm] 0 & 0 & 0 & 0 \end{bmatrix} \tag{4.50}$$

$$\mathbf{n}_1^T f_{on} = \frac{K_{P2}K_{P1}K_{vc}\mathbf{P}}{Cx_1} - \frac{K_{P2}K_{iL}V_i}{L} + K_{P2}K_{i1}(V_{ref} - K_{vc}x_1) + K_{i2}((x_3 + K_{p1}(V_{ref} - K_{vc}x_1)) - K_{iL}x_2) = s_p \tag{4.51}$$

Substituting these results into the expression of the saltation matrix S₁, we obtain:

$$\mathbf{S}_1 = \begin{bmatrix} 1 - \dfrac{K_{P2}K_{P1}K_{vc}x_2}{C(s_p + s_a)} & -\dfrac{K_{P2}K_{iL}x_2}{C(s_p + s_a)} & \dfrac{K_{P2}x_2}{C(s_p + s_a)} & \dfrac{x_2}{C(s_p + s_a)} \\[3mm] \dfrac{K_{P2}K_{P1}K_{vc}x_1}{L(s_p + s_a)} & 1 + \dfrac{K_{P2}K_{iL}x_1}{L(s_p + s_a)} & -\dfrac{K_{P2}x_1}{L(s_p + s_a)} & -\dfrac{x_1}{L(s_p + s_a)} \\[3mm] 0 & 0 & 1 & 0 \\[1mm] 0 & 0 & 0 & 1 \end{bmatrix} \tag{4.52}$$

The specification of simulation parameters is given in Table 4.1.

Table 4.1 Specification of simulation parameters

parameters	value	parameters	value
Input voltage （V）	250~400	Frequency （kHz）	20
Output voltage （V）	600	K_{iL}	1/100
Power rating （kW）	50	K_{p1}	0.5
Inductance （uH）	200	K_{i1}	500
Output capacitance (uF)	500	K_{p2}	5
K_{vc}	1/120	K_{i2}	200

A diagram of plotted eigenvalues under the cascaded control method is presented in Figure 4.15. Compared with the bifurcation diagram of the boost converter under the peak current control in Figure 4.9(a), it is clear that, for the same given system parameters and input conditions, the system can remain stable and no bifurcation phenomena occur under averaged current control with voltage feedback. All the eigenvalues are located at the right hand side of unit circle and moving towards the centre of the circle with increasing of input voltage, which indicates that the system is becoming more stable and exhibiting the same trend as the results from peak current control. Furthermore, this also proves that the system is hardly prone at all to the

fast-scale instability under the averaged current control with voltage feedback control algorithm, compared with peak current control. However, although averaged current based controllers are commonly used in practical applications due to its characteristics to stability, peak current control is still popular in applications that require fast dynamic responds speed.
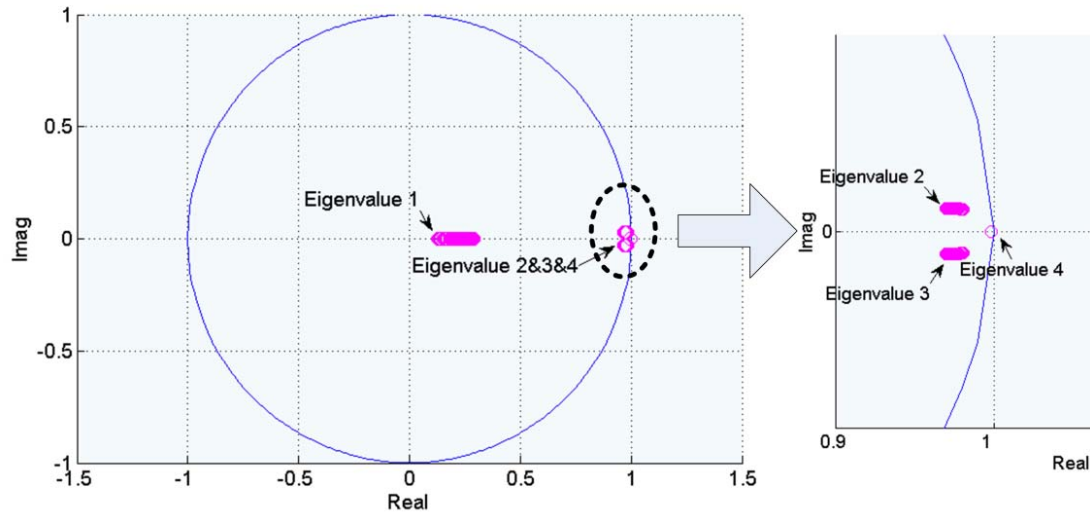
Figure 4.15 The eigenvalues of boost converter with CPLs under cascaded control

4.7 Summary

In this chapter, the nonlinear analysis method based on the Monodromy matrix is applied to the boost converter with CPL. Characteristic of the constant power load is transformed as a constant current load by using approximation method. This relevant investigation has not been reported before and is seen as a contribution to knowledge. The influence of the characteristics of the CPL on system stability in different operation modes (CCM and DCM) is fully studied. Based on the novel work two fundamental observations have been made. First results show that the system is relatively more stable in DCM operation than in CCM operation from the point of view of fast-scale stability. Second a comparison of peak current and averaged current cascaded control reveals that averaged current based controllers are very stable controller types under CPL.

5   Nonlinear analysis and control of interleaved boost converters

This chapter presents a nonlinear analysis of interleaved boost converters. Compared with single phase boost converters, interleaved type converters bring the advantages of reduced input current ripples and requiring less inductance levels. In this chapter, the interaction effect of the interleaved switching operation on the stability of the system is successfully investigated. The derivation of the Monodromy matrix at the different operational conditions is presented in detail and the study of the control loop is illustrated accordingly. Finally, the simulation results verify the theoretical analysis. To the knowledge of the author the full use of the Monodromy matrix applied to the interleaved boost converters is here reported for the first time.

5.1   Background

The study of the stability analysis and control of the nonlinear phenomena of the single-phase boost converters with different types of loads has been presented in previous chapters. Compared with single-phase boost converters, for the given inductance and load conditions, the current ripples to the power supply can be significantly reduced by using the interleaved boost converters. Figure 5.1 demonstrates the relationship between the percentage of ripple current to averaged current and duty cycle in the single-stage and the interleaved boost converters respectively. It shows that the percentage of ripple current in the interleaved boost converters is nearly half of that in the single phase converter, given the same operational range of the duty cycle. Because of this merit, interleaved boost converters have been widely used in recent years in renewable energy powered systems, such as fuel cells [134], PV power generation [135] and thermoelectric generator systems [136].

With the development of control techniques in power electronics, many effective control algorithms have been proposed to meet the demands of different applications. But most of the controllers are designed to regulate and control the system's dynamic behaviour based on the state-space averaging technique [137]. In this method, the actual nonlinear system is linearized around a steady-state operating point to yield a

linear model. A simple and accurate model at slow timescale can then be obtained, but it fails to predict nonlinear behaviour at a fast timescale. All power converters are inherently nonlinear and piecewise smooth systems because of the utilization of the nonlinear components such as switches and diodes. As a result, a variety of nonlinear phenomena such as bifurcation and chaos can be observed in the operation of power converters, which adversely affect their performance [138-140]. To study and reveal these fast-scale nonlinearities, the control methods mentioned in the first chapter, such as the nonlinear map-based methods [17], discrete-time modelling approaches [111, 139] and other individual control approaches [56, 65] are proposed in the literatures. Based on these discrete nonlinear modelling approaches, various control techniques [68, 94, 96, 141] are proposed to tackle these nonlinear behaviours and improve system performance.
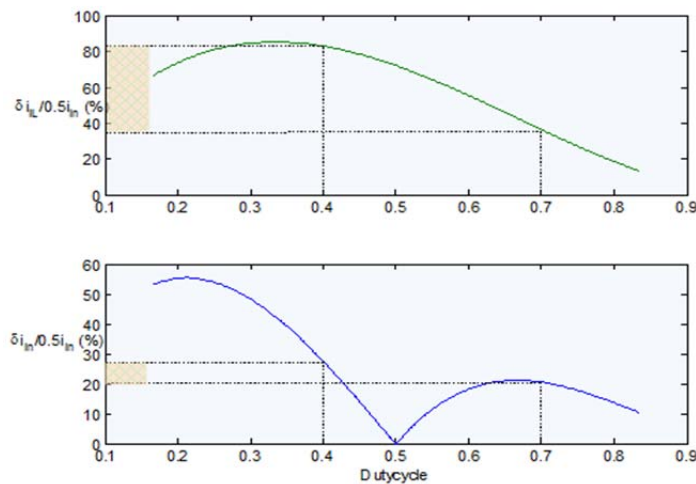
Figure 5.1 Percentage of ripple current to averaged current vs. duty cycle d in single-stage boost converter (upper) and interleaved boost converter (lower)

The Poincaré map [1, 17] approach is one of the most common and popular methods for studying the stability of the power converter systems. In this method, the eigenvalues of the Jacobian of the map computed at a fixed point are used to indicate the system stability; while the transcendental form of the system's equations mean that the Jacobian matrix cannot always be derived in the closed form. Other alternative approaches such as Floquet theory [56] and the trajectory sensitivity approach [64] can be applied effectively to the nonlinear analysis of power converters. The adopted methodology has previously been used with single-stage DC-DC converters [141], but now it can be expanded to apply to interleaved boost converters, which have a more complex topology and control sequence. In this

chapter, by applying Floquet theory and Filippov's method, the Monodromy matrix is presented to further study the interaction effect of the switching operation on the system's behaviour. All the comprehensive system information is introduced in the derivation of the Monodromy and saltation matrices, and the influence of various parameters on overall system stability can be investigated intuitively. The simulation results show the effectiveness of this method.

5.2 Matrix derivation

(a)

(b)
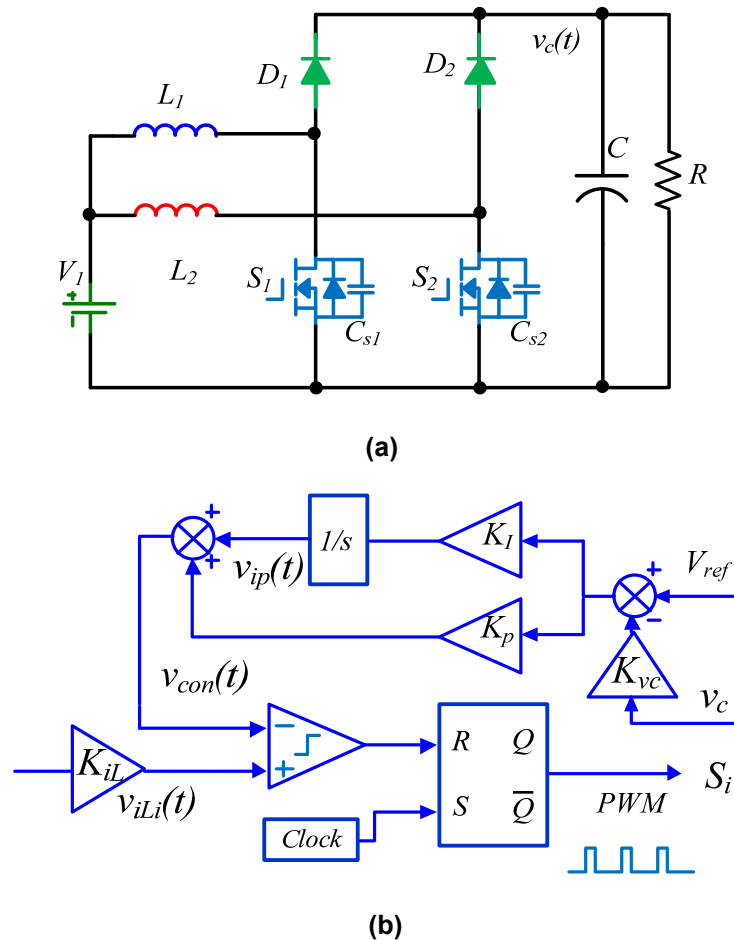
Figure 5.2 (a) Topology of interleaved boost converter
(b) diagram of control strategy for interleaved boost converter

The topology of a interleaved boost converter and the diagram of a control strategy for it are shown in Figure 5.2, K_i and K_p represent the gains of the PI controller; K_{vc} and K_{il} are the gain of signals from the practical sampled output voltage v_c and inductor current i_{Li} to the controller respectively. The inductor current i_{L1} , i_{L2}, capacitor voltage v_c and the output of the integrator in the feedback loop v_{ip} are chosen as the state variables. S_1 and S_2 are the switches employing the interleaved PWM control technique, which means that there is a 180 degree phase shift between

75

them as demonstrated in Figure 5.3(a).

The key waveforms of the converter in the steady state operation (when d>0.5) are illustrated in Figure 5.3. It can be seen that there are four subintervals in one period. The actions of on and off switches make the system evolve through different LTI subsystems, and therefore each subsystem can be described by a linear state space equation:

$$\dot{\mathbf{x}} = \mathbf{A}\mathbf{x} + \mathbf{B}\mathbf{u} \tag{5.1}$$

The state transition matrix can be represented as $\Phi_1 \sim \Phi_4$, which is a function of the initial state and time in term of the state matrix A that appears in the state equation. B is the matrix related to the external input conditions.

(a)

(b)
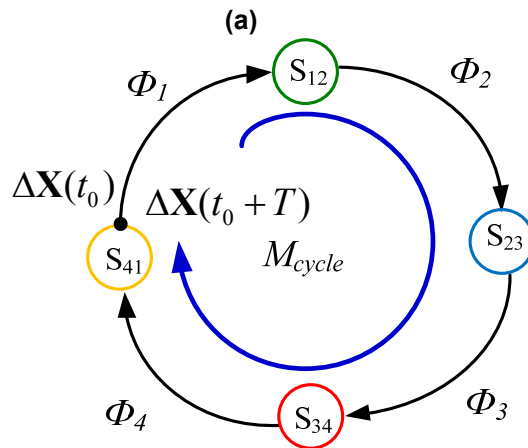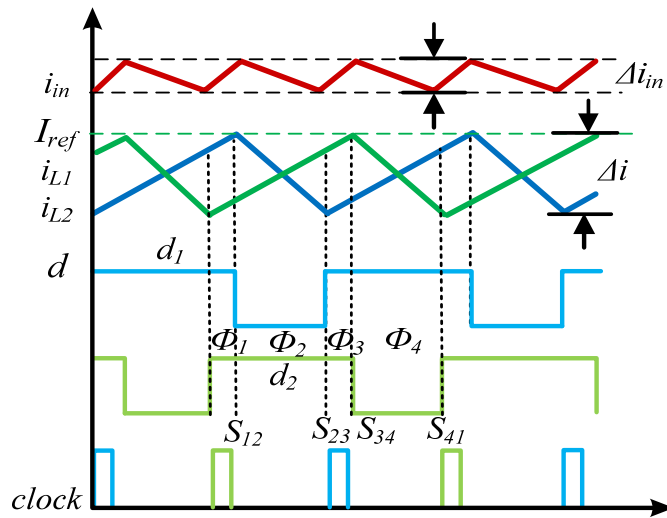
Figure 5.3 (a) Key operation waveforms in steady state (d>0.5)
(b) diagram of derivation of Monodromy matrix

The concept of Floquet theory (combined with Fillipov method) is to deduce the stability of a periodic solution by linearizing the system around the whole periodic

orbit. This can be obtained by calculating the state transition matrices before and after each switching and the saltation matrix that describes the behaviours of the solution during switching. The diagram of derivation of the Monodromy matrix is shown in Figure 5.3(b).

The system states at different switching sequences can be described by the following state equations:

$$\dot{x} = \begin{cases} ①\mathbf{A_1}x + \mathbf{B_1}E & S_1 \; and \quad S_2 \; on \\ ②\mathbf{A_2}x + \mathbf{B_2}E & S_1 \; on \quad and \quad S_2 \; off \\ ③\mathbf{A_3}x + \mathbf{B_3}E & S_1 \; off \quad and \quad S_2 \; on \\ ④\mathbf{A_4}x + \mathbf{B_4}E & S_1 \; and \quad S_2 \; off \end{cases} \tag{5.2}$$

When the switches S_1 and S_2 are ON, the state equations can be expressed as:

$$\frac{dv_c}{dt} = -\frac{v_c}{RC} \tag{5.3}$$

$$\frac{di_{L1}}{dt} = \frac{V_i}{L_1} \tag{5.4}$$

$$\frac{di_{L2}}{dt} = \frac{V_i}{L_2} \tag{5.5}$$

$$\frac{dv_{ipi}}{dt} = K_I(K_{vc}v_c - V_{ref}) \tag{5.6}$$

When the switch S_1 is ON and S_2 is OFF, the state equations are:

$$\frac{dv_c}{dt} = \frac{i_{L2}R - v_c}{RC} \tag{5.7}$$

$$\frac{di_{L1}}{dt} = \frac{V_i}{L_1} \tag{5.8}$$

$$\frac{di_{L2}}{dt} = \frac{V_i - v_c}{L_2} \tag{5.9}$$

$$\frac{dv_{ip}}{dt} = K_I(K_{vc}v_c - V_{ref}) \tag{5.10}$$

When the switch S_1 is OFF and S_2 is ON, the state equations are:

$$\frac{dv_c}{dt} = \frac{i_{L1}R - v_c}{RC} \tag{5.11}$$

$$\frac{di_{L1}}{dt} = \frac{V_i - v_c}{L_1} \tag{5.12}$$

$$\frac{di_{L2}}{dt} = \frac{V_i}{L_2} \tag{5.13}$$

$$\frac{dv_{ip}}{dt} = K_I(K_{vc}v_c - V_{ref}) \tag{5.14}$$

When the switch S_1 and S_2 are OFF, the state equations are obtained as:

$$\frac{dv_c}{dt} = \frac{(i_{L1} + i_{L2})R - v_c}{RC} \tag{5.15}$$

$$\frac{di_{L1}}{dt} = \frac{V_i - v_c}{L_1} \tag{5.16}$$

$$\frac{di_{L2}}{dt} = \frac{V_i - v_c}{L_2} \tag{5.17}$$

$$\frac{dv_{ipi}}{dt} = K_I(K_{vc}v_c - V_{ref}) \tag{5.18}$$

The state equations above can be represented using vector "x". Where x_1 is the capacitor voltage v_c, x_2 is the inductor current i_L, and x_3 the output of the integrator in the feedback loop v_{ip}, and the right-hand side state equations are expressed as:

$$f_1 = \begin{bmatrix} -\dfrac{x_1}{RC} \\ \dfrac{V_i}{L_1} \\ \dfrac{V_i}{L_2} \\ K_I(K_{vc}x_1 - V_{ref}) \end{bmatrix} \tag{5.19}$$

$$f_2 = \begin{bmatrix} \dfrac{x_3 R - x_1}{RC} \\ \dfrac{V_i}{L_1} \\ \dfrac{V_i - x_1}{L_2} \\ K_I(K_{vc}x_1 - V_{ref}) \end{bmatrix} \tag{5.20}$$

$$f_3 = \begin{bmatrix} \dfrac{x_2 R - x_1}{RC} \\[2mm] \dfrac{V_i - x_1}{L_1} \\[2mm] \dfrac{V_i}{L_2} \\[2mm] K_I(K_{vc}x_1 - V_{ref}) \end{bmatrix}$$
(5.21)

$$f_4 = \begin{bmatrix} \dfrac{(x_2 + x_3)R - x_1}{RC} \\[2mm] \dfrac{V_i - x_1}{L_1} \\[2mm] \dfrac{V_i - x_1}{L_2} \\[2mm] K_I(K_{vc}x_1 - V_{ref}) \end{bmatrix}$$
(5.22)

Thus, the corresponding state matrices for these four subintervals are shown in the following:

$$\mathbf{A}_1 = \begin{bmatrix} -\dfrac{1}{RC} & 0 & 0 & 0 \\[2mm] 0 & 0 & 0 & 0 \\[2mm] 0 & 0 & 0 & 0 \\[2mm] K_I K_{vc} & 0 & 0 & 0 \end{bmatrix}$$
(5.23)

$$\mathbf{A}_2 = \begin{bmatrix} -\dfrac{1}{RC} & 0 & \dfrac{1}{C} & 0 \\[2mm] 0 & 0 & 0 & 0 \\[2mm] -\dfrac{1}{L_2} & 0 & 0 & 0 \\[2mm] K_I K_{vc} & 0 & 0 & 0 \end{bmatrix}$$
(5.24)

$$\mathbf{A}_3 = \begin{bmatrix} -\dfrac{1}{RC} & \dfrac{1}{C} & 0 & 0 \\[2mm] -\dfrac{1}{L_1} & 0 & 0 & 0 \\[2mm] 0 & 0 & 0 & 0 \\[2mm] K_I K_{vc} & 0 & 0 & 0 \end{bmatrix}$$
(5.25)

$$\mathbf{A}_4 = \begin{bmatrix} -\dfrac{1}{RC} & \dfrac{1}{C} & \dfrac{1}{C} & 0 \\ -\dfrac{1}{L_1} & 0 & 0 & 0 \\ -\dfrac{1}{L_2} & 0 & 0 & 0 \\ K_I K_{vc} & 0 & 0 & 0 \end{bmatrix} \tag{5.26}$$

$$\mathbf{B}_1 = \mathbf{B}_2 = \mathbf{B}_3 = \mathbf{B}_4 = \begin{bmatrix} 0 & 0 & 0 & 0 \\ 0 & 0 & \dfrac{1}{L_1} & 0 \\ 0 & 0 & \dfrac{1}{L_2} & 0 \\ 0 & 0 & 0 & -K_I \end{bmatrix} \tag{5.27}$$

$$\mathbf{u} = \begin{bmatrix} 0 \\ 0 \\ V_i \\ V_{ref} \end{bmatrix} \tag{5.28}$$

According to the control strategy of peak current control, the switching transients occur at the beginning of each switching period and the moment when the value of inductor current i$_{Li}$ equals the reference signal. Therefore, the switching conditions from the ON to OFF state can be expressed as $h_i(x,t) = 0$ (i=1,2),where

$$h_i(x,t) = K_p(V_{ref} - K_{vc}v_c) + v_{ip} - K_{iL}i_{Li} \tag{5.29}$$

Hence, its normal vector can be given by:

$$\mathbf{n}_{12} = \begin{bmatrix} \partial h_1 / \partial x_1 \\ \partial h_2 / \partial x_2 \\ \partial h_3 / \partial x_3 \\ \partial h_4 / \partial x_4 \end{bmatrix} = \begin{bmatrix} -K_p K_{vc} \\ -K_{iL} \\ 0 \\ 1 \end{bmatrix} \tag{5.30}$$

$$\mathbf{n}_{34} = \begin{bmatrix} \partial h_1 / \partial x_1 \\ \partial h_2 / \partial x_2 \\ \partial h_3 / \partial x_3 \\ \partial h_4 / \partial x_4 \end{bmatrix} = \begin{bmatrix} -K_p K_{vc} \\ 0 \\ -K_{iL} \\ 1 \end{bmatrix} \tag{5.31}$$

The saltation matrices S$_{23}$ and S$_{41}$ turn out to be identity matrices, since they are related to the switching event from the OFF state to the ON state for S_1 and S_2 at the initial instant of every clock cycle respectively, which means that the rising edge of the ramp causes the term of $\partial h / \partial t$ in equation 2.17 to be infinity.

When the duty cycle d is bigger than 0.5, the system states evolve from the following sequence as illustrated in Figure 5.3(a):

$$①→③→①→②$$

The other relevant terms in the saltation matrix can be calculated as:

$$(f_{off} - f_{on})\mathbf{n}^T = (f_2 - f_1)\mathbf{n}^T = \begin{bmatrix} \dfrac{x_3}{C} \\ 0 \\ -\dfrac{x_1}{L_2} \\ 0 \end{bmatrix} \begin{bmatrix} -K_p K_{vc} & 0 & -K_{iL} & 1 \end{bmatrix} = \begin{bmatrix} -\dfrac{K_p K_{vc} x_3}{C} & 0 & -\dfrac{K_{iL} x_3}{C} & \dfrac{x_3}{C} \\ 0 & 0 & 0 & 0 \\ \dfrac{K_p K_{vc} x_1}{L_2} & 0 & \dfrac{K_{iL} x_1}{L_2} & -\dfrac{x_1}{L_2} \\ 0 & 0 & 0 & 0 \end{bmatrix}$$

$$(5.32)$$

$$s_p = \mathbf{n}_{34}^T f_{on} = \mathbf{n}_{34}^T f_1 = \begin{bmatrix} -K_p K_{vc} & 0 & -K_{iL} & 1 \end{bmatrix} \begin{bmatrix} -\dfrac{x_1}{RC} \\ \dfrac{V_i}{L_1} \\ \dfrac{V_i}{L_2} \\ K_I(K_{vc} x_1 - V_{ref}) \end{bmatrix} \quad (5.33)$$

$$= \dfrac{K_P K_{vc} x_1}{RC} - \dfrac{K_{iL} V_i}{L_2} + K_I(K_{vc} x_1 - V_{ref})$$

Substituting these into the expression of the saltation matrix **S₁₂ₐ** can be obtained as follows:

$$\mathbf{S}_{12a} = \begin{bmatrix} 1 - \dfrac{K_p K_{vc} x_3}{C(s_p + s_a)} & 0 & -\dfrac{K_{iL} x_3}{C(s_p + s_a)} & \dfrac{x_3}{C(s_p + s_a)} \\ 0 & 1 & 0 & 0 \\ \dfrac{K_p K_{vc} x_1}{L_2(s_p + s_a)} & 0 & 1 + \dfrac{K_{iL} x_1}{L_2(s_p + s_a)} & -\dfrac{x_1}{L_2(s_p + s_a)} \\ 0 & 0 & 0 & 1 \end{bmatrix} \quad (5.34)$$

Similarly, the saltation matrix S₃₄ₐ can be derived as:

$$\mathbf{S}_{34a} = \begin{bmatrix} 1 - \dfrac{K_p K_{vc} x_2}{C(s_p + s_a)} & -\dfrac{K_{iL} x_2}{C(s_p + s_a)} & 0 & \dfrac{x_2}{C(s_p + s_a)} \\[3mm] \dfrac{K_p K_{vc} x_1}{L_1(s_p + s_a)} & 1 + \dfrac{K_{iL} x_1}{L_1(s_p + s_a)} & 0 & -\dfrac{x_1}{L_1(s_p + s_a)} \\[3mm] 0 & 0 & 1 & 0 \\[2mm] 0 & 0 & 0 & 1 \end{bmatrix} \qquad (5.35)$$
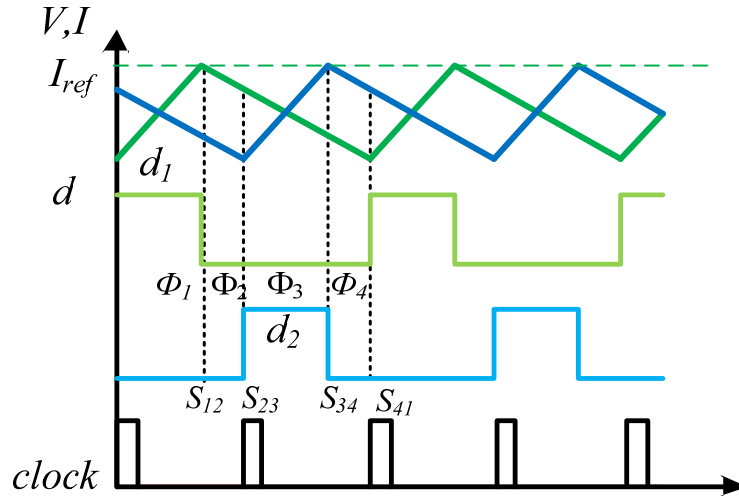
Figure 5.4 Key operation waveforms in steady state (d<0.5)

When duty cycle d is less than 0.5, the evolution of system states can be expressed in the following sequence:

$$②→④→③→④$$

Figure 5.4 presents the key operation waveforms in steady state at this condition. The saltation matrices $\mathbf{S}_{12b}$ and $\mathbf{S}_{34b}$ can be calculated as follows:

$$\mathbf{S}_{12b} = \begin{bmatrix} 1 - \dfrac{K_p K_{vc} x_2}{C(s_p + s_a)} & -\dfrac{K_{iL} x_2}{C(s_p + s_a)} & 0 & \dfrac{x_2}{C(s_p + s_a)} \\[3mm] \dfrac{K_p K_{vc} x_1}{L_1(s_p + s_a)} & 1 + \dfrac{K_{iL} x_1}{L_1(s_p + s_a)} & 0 & -\dfrac{x_1}{L_1(s_p + s_a)} \\[3mm] 0 & 0 & 1 & 0 \\[2mm] 0 & 0 & 0 & 1 \end{bmatrix} \qquad (5.36)$$

$$\mathbf{S}_{34b} = \begin{bmatrix} 1 - \dfrac{K_p K_{vc} x_3}{C(s_p + s_a)} & 0 & -\dfrac{K_{iL} x_3}{C(s_p + s_a)} & \dfrac{x_3}{C(s_p + s_a)} \\[3mm] 0 & 1 & 0 & 0 \\[3mm] \dfrac{K_p K_{vc} x_1}{L_2(s_p + s_a)} & 0 & 1 + \dfrac{K_{iL} x_1}{L_2(s_p + s_a)} & -\dfrac{x_1}{L_2(s_p + s_a)} \\[2mm] 0 & 0 & 0 & 1 \end{bmatrix} \qquad (5.37)$$

where

$$s_p = \frac{-K_P K_{vc}(x_2 R - x_1)}{RC} - \frac{K_{iL} V_i}{L_1} + K_I(V_{ref} - K_{vc} v_c) \tag{5.38}$$

$$s_a = \frac{\partial h}{\partial t} = 0 \tag{5.39}$$

For the interleaved control algorithm, the time of each subinterval can be represented in terms of d and T. The state transition matrices are given by the matrix exponential, hence

$$\boldsymbol{\Phi}_1 = e^{\mathbf{A}t} = e^{\mathbf{A}_1 d\,\mathrm{T}} \tag{5.40}$$

$$\boldsymbol{\Phi}_2 = e^{\mathbf{A}t} = e^{\mathbf{A}_2(0.5-d)\mathrm{T}} \tag{5.41}$$

$$\boldsymbol{\Phi}_3 = e^{\mathbf{A}t} = e^{\mathbf{A}_3 d\,\mathrm{T}} \tag{5.42}$$

$$\boldsymbol{\Phi}_4 = e^{\mathbf{A}t} = e^{\mathbf{A}_4(0.5-d)\mathrm{T}} \tag{5.43}$$

Thus, the Monodromy matrix **M** as illustrated in Figure 5.3(b) can be calculated by the following expression:

$$\mathbf{M} = \boldsymbol{\Phi}_{cycle} = \boldsymbol{\Phi}_1 \times \mathbf{S}_{12} \times \boldsymbol{\Phi}_2 \times \mathbf{S}_{23} \times \boldsymbol{\Phi}_3 \times \mathbf{S}_{34} \times \boldsymbol{\Phi}_4 \times \mathbf{S}_{41} \tag{5.44}$$

This contains all of the information about the system input and load conditions, the parameters of the converter and the coefficients of the control loop, and therefore the influence of any system parameter on system stability can be analysed using this matrix.

5.3   Study on the control loop
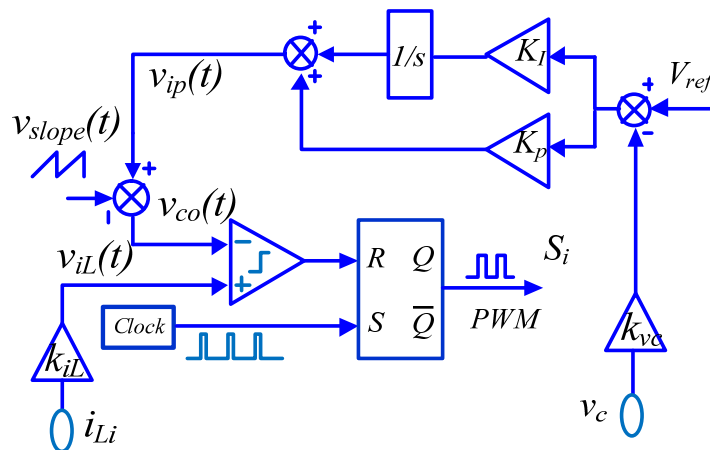
(a)
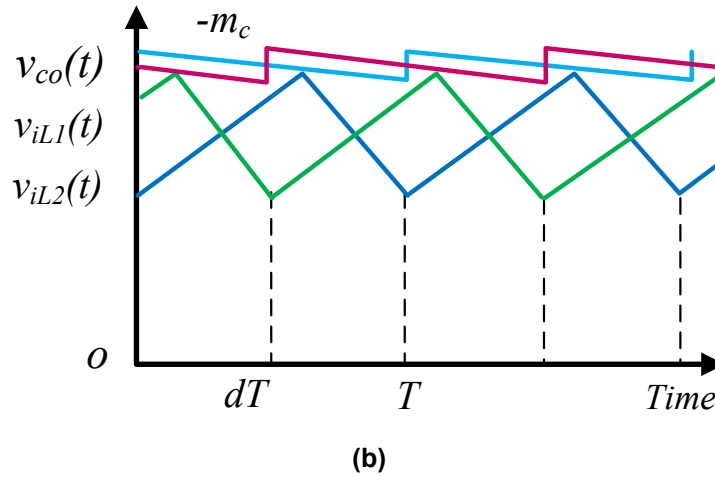
(b)

**Figure 5.5 (a) Diagram of conventional peak current control with slope compensation;
(b) illustration of slope compensation in interleaved boost converters**

The diagram of peak current control with slope compensation is illustrated in Figure 5.5(a). Slope compensation is widely adopted in many different kinds of converters employing peak current mode control to avoid unstable phenomenon when the duty cycle d is bigger than 0.5. However, the influence of the slope parameter m_c cannot be investigated theoretically in most state-space averaging-based methods. In this Monodromy matrix approach, the slope parameter m_c can be introduced in the derived saltation matrices $\mathbf{S_{12}}$ and $\mathbf{S_{34}}$ and a_c represents its amplitude at the end of each period. Specifically, it changes the switching manifold as shown in Figure 5.5(b) and then the switching condition becomes:

$$h_i(x,t) = K_p(V_{ref} - K_{vc}v_c) + v_{ip} + m_c t - K_{iL}i_{Li} \tag{5.45}$$

The term $\partial h / \partial t$ changes from 0 to the expression below:

$$\frac{\partial h}{\partial t} = m_c \tag{5.46}$$

By choosing the proper parameter mc in the new Monodromy matrix, the eigenvalues of this Monodromy matrix can be placed within the unit circle which make stable period-1 operation in that case.

5.4 Simulation Verifications

The specification of simulation parameters is shown as follows: V_i=80V~125V, V_{out}=240V, L=L_1=L_2=200µH, C=20µF, R=28.8Ω, f=100kHz, K_i=500, K_p=5, K_{vc}=5/240, K_{iL}=1/4, V_{ref}=5V. P_{out}=2kW.
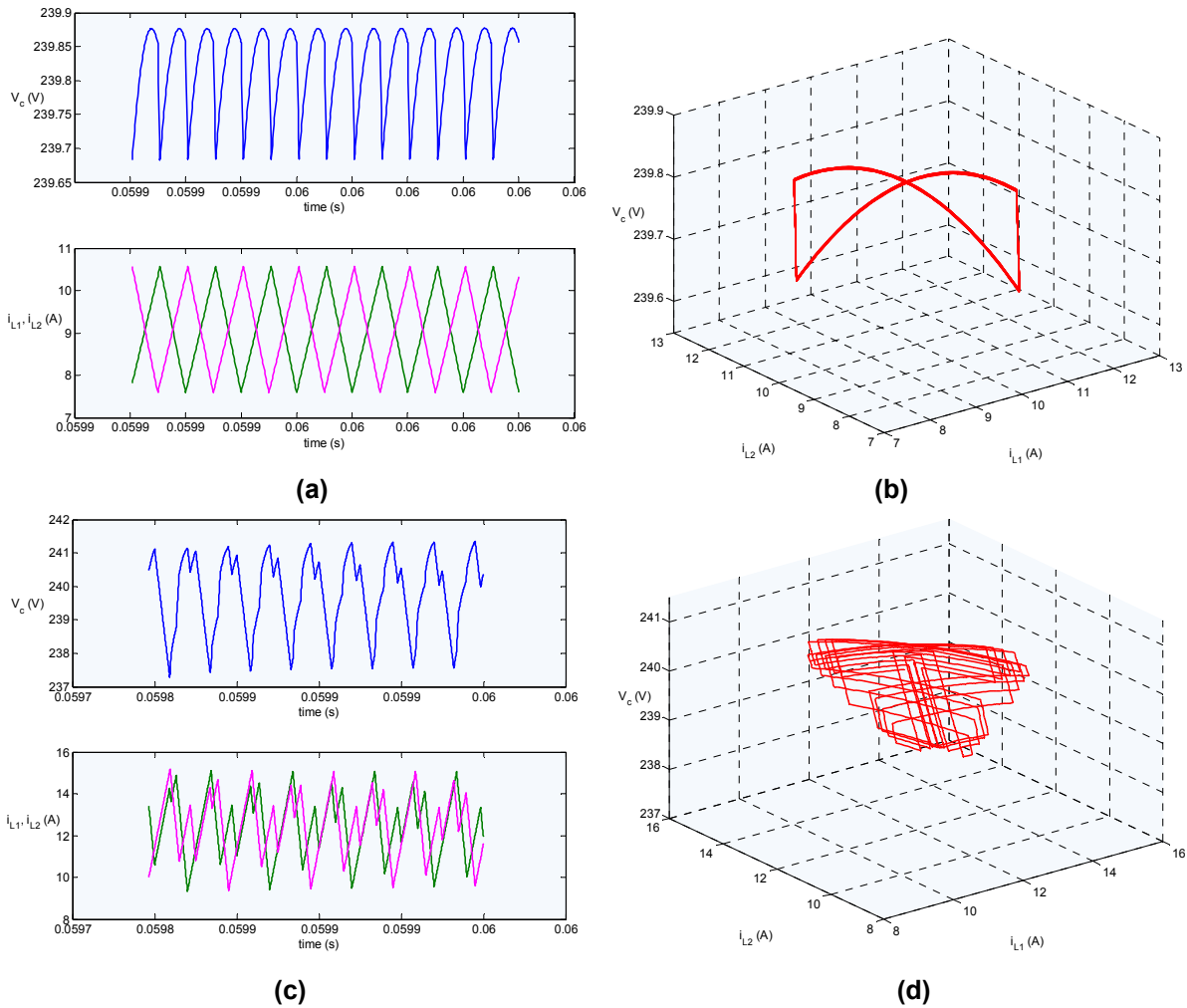
Figure 5.6 (a) (b) Waveforms of output voltage and inductor current at time domain and the corresponding phase portrait in period-1 (stable state); (c) (d) the waveforms in chaotic state

The waveforms of the output voltage and inductor current in the time domain and the corresponding phase portrait in the stable steady state are presented in Figure 5.6(a) and (b). With the variation of some parameters, the system may operate in the chaotic state as shown in Figure 5.6(c) and (d). We can see that the ripples of voltage and current increase dramatically in chaotic operation, which causes more losses and degrades the performance of the converter. The Monodromy matrix can be calculated numerically in Matlab/Simulink. The codes that show the process of calculation according to the theoretical derivation are presented in Appendix 5.

The bifurcation points of the system at different input voltages can be indicated by the locus of the eigenvalues in the Monodromy matrix. Setting the amplitude of the slope a_c to 0.3, the system jumps out of the stable period-1 when the input voltage is less than 118V as shown in Figure 5.7(a); meanwhile, one of the corresponding eigenvalues reaches the border of the unit circle in Figure 5.7(b), which means that

85

the system becomes unstable at this moment.

(a)

(b)

(c)

86
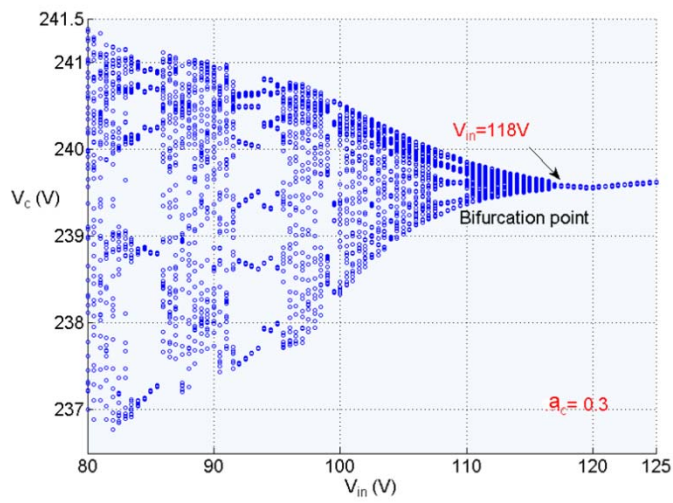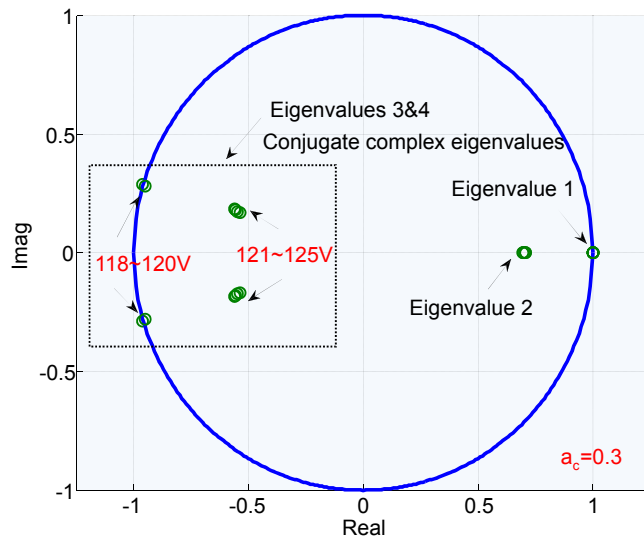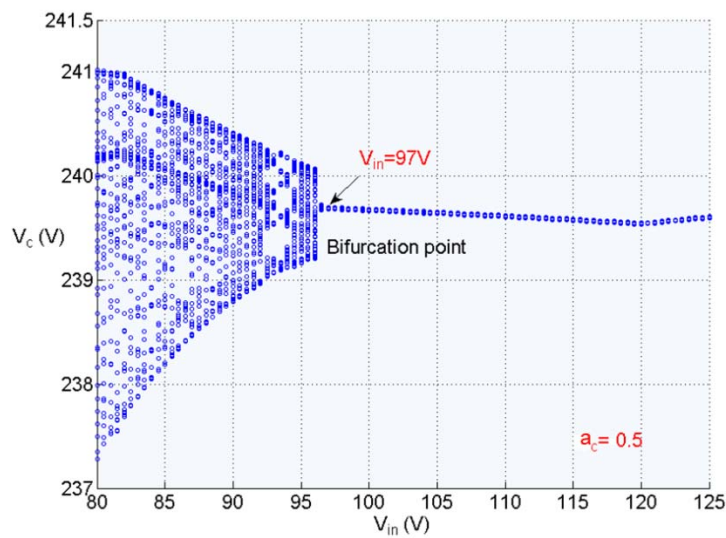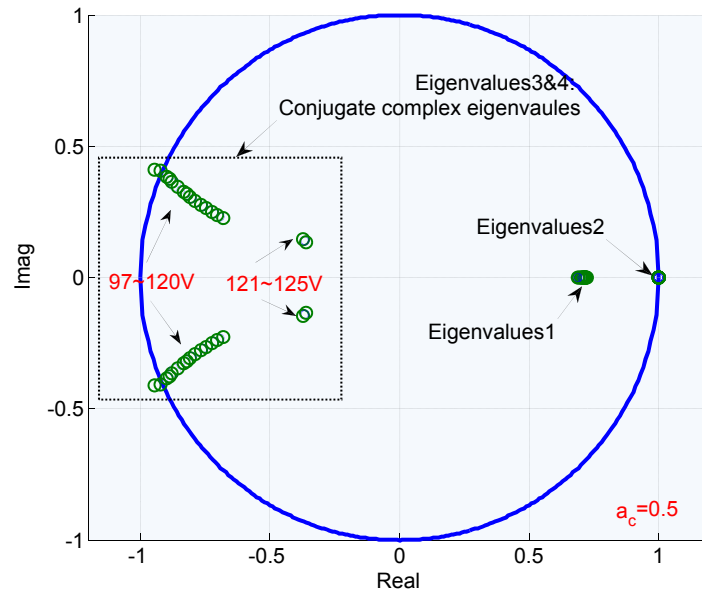
(d)

Figure 5.7 (a)~(d) Bifurcation diagram and corresponding locus of eigenvalues at a$_c$=0.3&0.5

In contrast, when a_c is set to 0.5, the system can remain stable when the input voltage is bigger than 97V as illustrated in Figure 5.7 (c). The corresponding locus of the eigenvalues in Figure 5.7(d) indicates the extended range of the input voltage, which can make system stable at the given conditions.
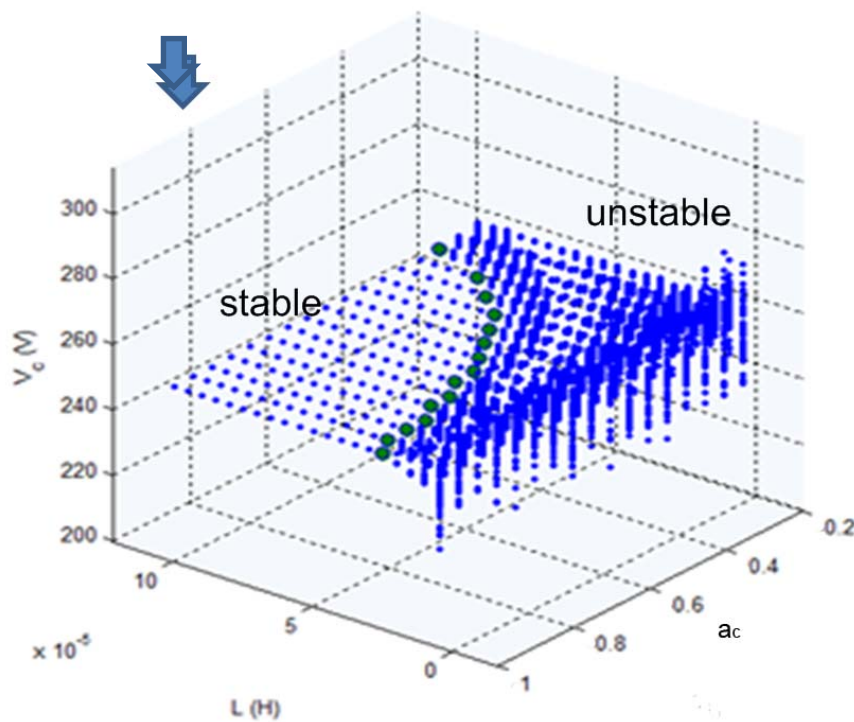
(a)
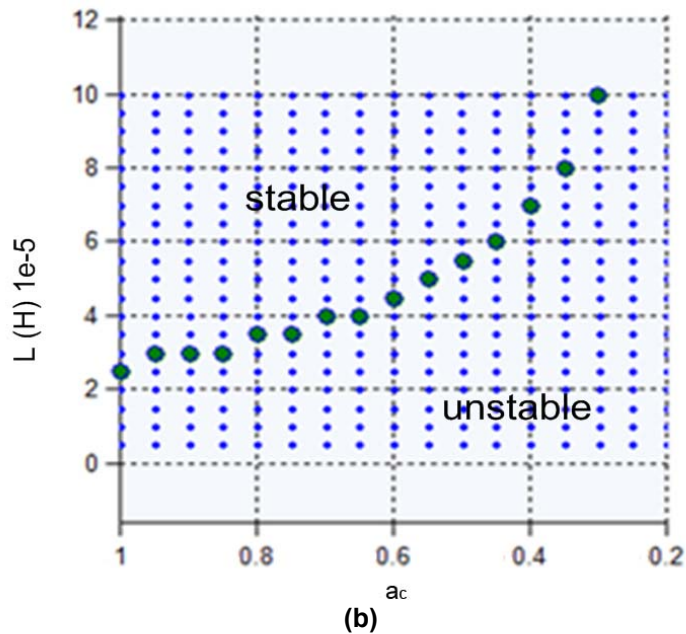
Figure 5.8 (a) Bifurcation diagram at different inductance L and slope a$_c$ (3-D)
(b) X-Y view

In order to further study the relationship between system stability and parameters such as inductance *L* and slope amplitude *a$_c$*, the bifurcation diagram at the different values of *L* and *a$_c$* is demonstrated in Figure 5.8 (a) and (b). It shows that the system becomes more stable with an increase in inductance *L* and amplitude *a$_c$*. The Monodromy matrix can be expressed as a function in terms of a$_c$ and L:

$$\mathbf{M} = M(a_c, L) \tag{5.47}$$

The border curve of the stable operating region can be calculated using the derived Monodromy matrix, which provides the design guidance for the given system.

5.5   Summary

Interleaved boost converters have the advantages of reducing the ripple current, compared to single phase converters. In this chapter, the method of analysis based on Monodromy matrix is extended to the investigation of a higher-order topology with an interleaving control sequence. The complete derivation of the Monodromy matrix for an interleaved boost converter at the different operation conditions is presented in this study. All of the circuit parameters and control coefficients can be included in the matrix obtained, which enables us to effectively investigate the influences of different input and load conditions or other parameters on system performance. The simulation results validate the effectiveness of this method.

6 Design and implementation of mixed-signal controller-based test system

This chapter provides an overview of techniques for peak current control, including traditional analogue techniques, fully digital and mixed-signal techniques. The features of the three main types of techniques are presented for comparison and the latest peak digital current control algorithms are reviewed and discussed. A new mixed signal technique containing a DSP controller with an external high performance waveform generator is proposed and demonstrated. This proposed controller does not only has the flexibility to change control algorithms quickly due to changes in coding, but also retains the unique characteristic of a real time cycle-by-cycle current limiter allowing quantisation errors to be offset which are common in digital comparators. The design of the hardware and software is presented and test results show that the new proposed controller works effectively. Finally, for the first time, the Monodromy matrices of the interleaved boost converter using digital peak current method are derived and corresponding simulation and experimental results are used to verify the analysis.

6.1 Introduction

The control algorithm employed in the previous chapters is mainly focused on the technique of peak current mode (PCM) control. This is a widely used current mode control (CMC) method for switching power converters, offering a number of benefits such as inherent cycle-by cycle current limiting, good current sharing of paralleled converters, and better load regulation compared to voltage mode control [142-144]. As illustrated in Figure 6.1, the inductor current linearly increases when the switch turns on at the initial instant of one switching period and the switch turns off when the instantaneous inductor current reaches the reference level. However, converters controlled by PCM suffer from subharmonic oscillations in CCM operation, exhibiting period-doubling bifurcation. DC-DC converters will lose stable operation from period-1 to period-2, when the duty cycle exceeds 50%. This phenomenon can be explained using a graphical approach as shown in Figure 6.1(a). Assuming that there is a current perturbation $\Delta iL(0)$ at the initial instant of one clock period, the value of this perturbation at the end of the switching period can be expressed by the following

equation:

$$\Delta i_L(T) = -\frac{m_2}{m_1}\Delta i_L(0)$$ (6.1)

Here m_1 and m_2 represent the slopes of inductor current when the switch is on and off respectively. This perturbation will be amplified and subharmonic oscillation will occur if the value of m_2 is larger than the value of m_1. It can be proven that this phenomenon happens when duty cycle is bigger than 0.5. To address this issue and regain stability, the approach of slope compensation is commonly applied as shown in Figure 6.1(b). The following expression can be derived using peak current control with conventional slope compensation [142]:

$$\Delta i_L(T) = -\frac{m_2 - m_{ca}}{m_1 + m_{ca}}\Delta i_L(0)$$ (6.2)

(a)

(b)
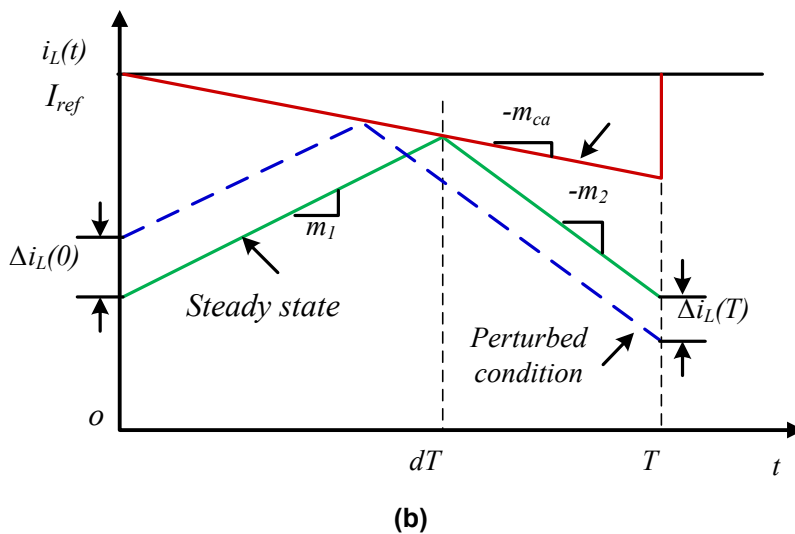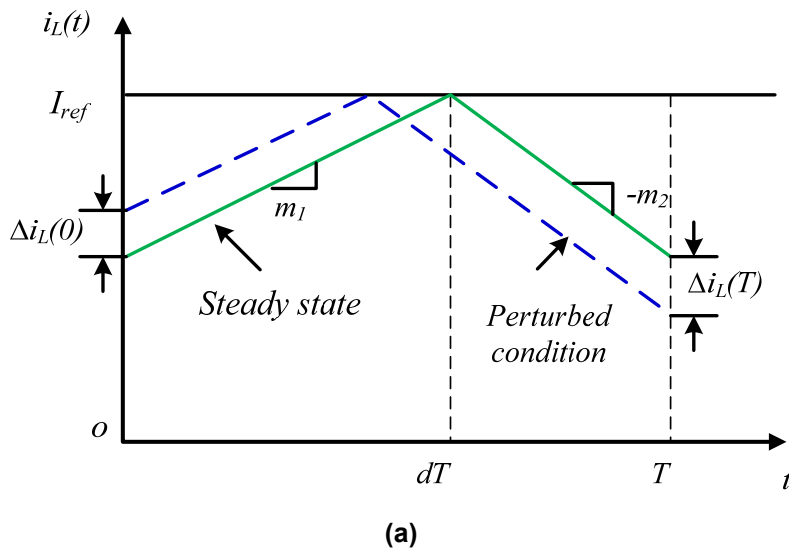
Figure 6.1 (a) Peak current control without slope compensation

(b) Peak current control with conventional slope compensation

90

For stable operation, following relations must be satisfied:

$$\left| \frac{m_2 - m_{ca}}{m_1 + m_{ca}} \right| < 1 \tag{6.3}$$

and the required slope of compensation ramp can be obtained as:

$$m_{ca} > \frac{1}{2}(m_2 - m_1) \tag{6.4}$$

In boost converters, m_2 and m_1 can be calculated by the following expressions:

$$\begin{cases} m_1 = \dfrac{V_{in}}{L} \\ m_2 = \dfrac{V_c - V_{in}}{L} \end{cases} \tag{6.5}$$

Equation 6.4 only shows the minimum value of the slope required to cope with the subharmonic oscillations; however, it cannot give the information about how the input and output voltages, inductance and other system parameters affect the stable margin of a system. By contrast, a Monodromy matrix-based approach can provide better insight for slope compensation. It can not only be applied in the analysis of conventional saw-tooth type compensation but can also be used in developing other types of compensation, as shown in the next chapter.

6.2   Overview of implementation for peak current control

Until recently, most practical applications still employed analogue implementations due to cost considerations. The typical analogue PCM controller is illustrated in Figure 6.2. In this circuit, a network of analogue operational amplifiers, capacitors and resistors is utilized to constitute the compensator. An internal voltage source is generated to mimic a current compensation ramp. Thanks to the evolution of low-cost, high performance digital signal processors (DSP) and other microcontrollers, the digital control of power switching converters is gradually demonstrating its advantages compared to analogue counterparts. Digital controllers feature improved reliability, greater design flexibility, and low sensitivity to environmental conditions. These attributes bring digital controllers closer to sophisticated and enhanced control methods such as adaptive and advanced nonlinear control to enhance the converter's static and dynamic performance. Therefore, digital peak current control has attracted the interests of many engineers and recent research is showing promising results [144-146].
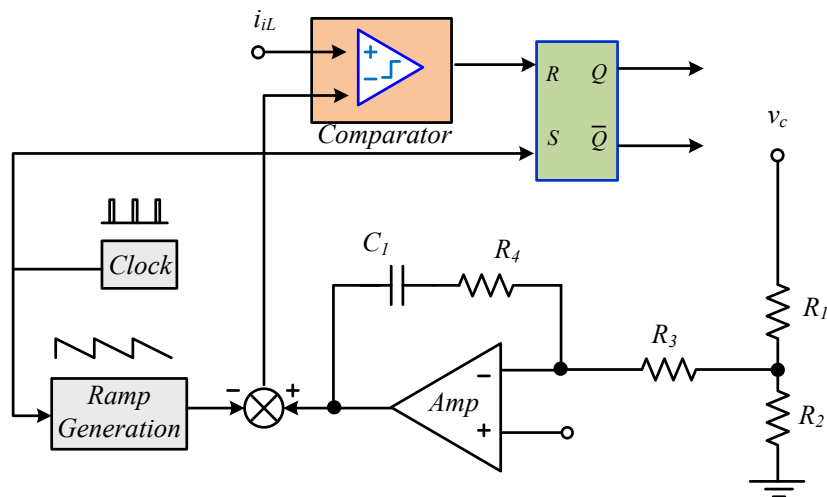
Figure 6.2 Analogue peak current mode (PCM) control

According to the principle of peak current control, the duty cycle is determined by the moment when the inductor current reaches a threshold value. The threshold value is mostly generated by the addition of the outer voltage control loop and a ramp generator signal. In digital control, the instantaneous waveform of inductor current is digitalized by high-speed analogue-to-digital converters (ADCs), while without appropriate means to accurately measure current at the desired point, the controller has to constantly monitor the inductor current during the PWM cycle in order to capture the moment when the inductor current reaches the reference signals. However, given the rapidly varying changes in inductor current, this concept of implementation using a full digital platform is difficult to realize and requires extremely high sampling and conversion rates of ADCs and high performance processors, especially when the power device switching frequency exceeds a few hundreds of kHz. A field programmable gate array (FPGA)-based implementation of digital peak current control has been proposed to achieve the digitalization. Two 10-bit differential pipeline ADCs are employed for sampling the error voltage and the inductor current. A compensating ramp is added with the sampled inductor current, which is implemented using a counter-based digital pulse-width-modulator (DPWM). However, this is not cost-effective and achieves low execution times since the converted results need to be compared with the reference signal after each conversion. Additionally, the staircase effect generated by the digitally compensating ramp may lead to sub-harmonic oscillations [145].

To avoid the need to sample the inductor current constantly during the switching period, a feasible alternative to the fully digital peak current solution is to use mixed

signal microcontrollers containing analogue comparators. Thereby the discrete threshold value is converted into an analogue voltage by an internal digital-to-analogue converter (DAC), to represent the current threshold level for the on-chip comparator as shown in Figure 6.3. Some relevant products have appeared in the markets (e.g. PIC, dsPIC, Piccolo) [147, 148] and a number of digital peak current control algorithms have been implemented based on these types of microcontrollers [143, 144, 146].
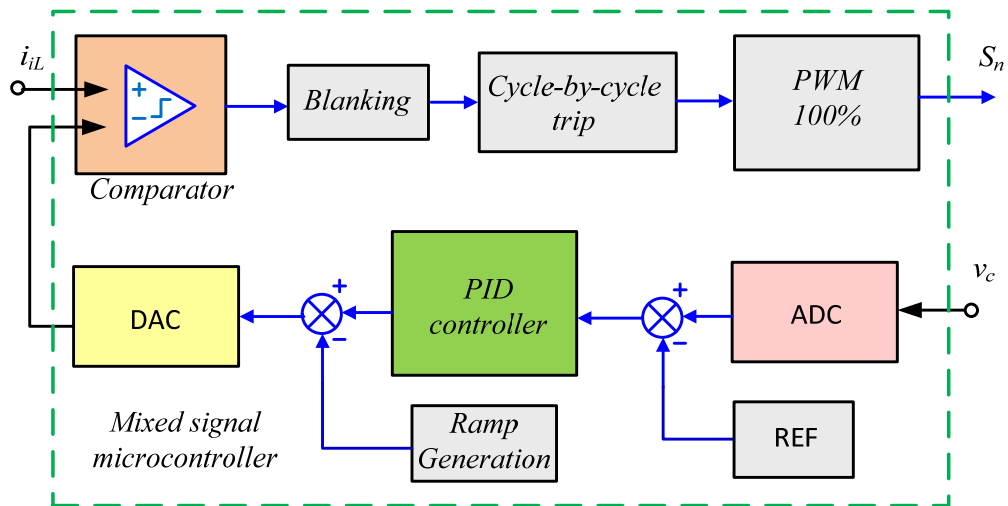
Figure 6.3 Digital peak current control by mixed signal microcontroller

6.3   Implementation of the mixed controller

As discussed above, although the analogue controller will certainly be more cost-effective than a digital solution in simple and low-cost DC-DC converter applications, in more complex systems that require advanced control features the digital controller is the better choice. The solution proposed in this thesis employs a DSP controller with an external high performance waveform generator, which has more flexibility in applying various control algorithms and allowing real-time comparisons of the inductor current to achieve real-time cycle-by-cycle current limiting. Control commands are sent at each switching period via an SPI communication interface. This is similar to the mixed-signal implementation in which the voltage controller utilizes digital implementation and the current loop remains in the analogue domain, but it provides more efficient configuration, since the processor only needs to send control commands to the waveform generator and the remaining processing capability of processor can be used to handle other computing task. Moreover, this external independent high-frequency waveform generator offers better resolution, and flexible compensation signal generation.

6.3.1   Hardware implementation
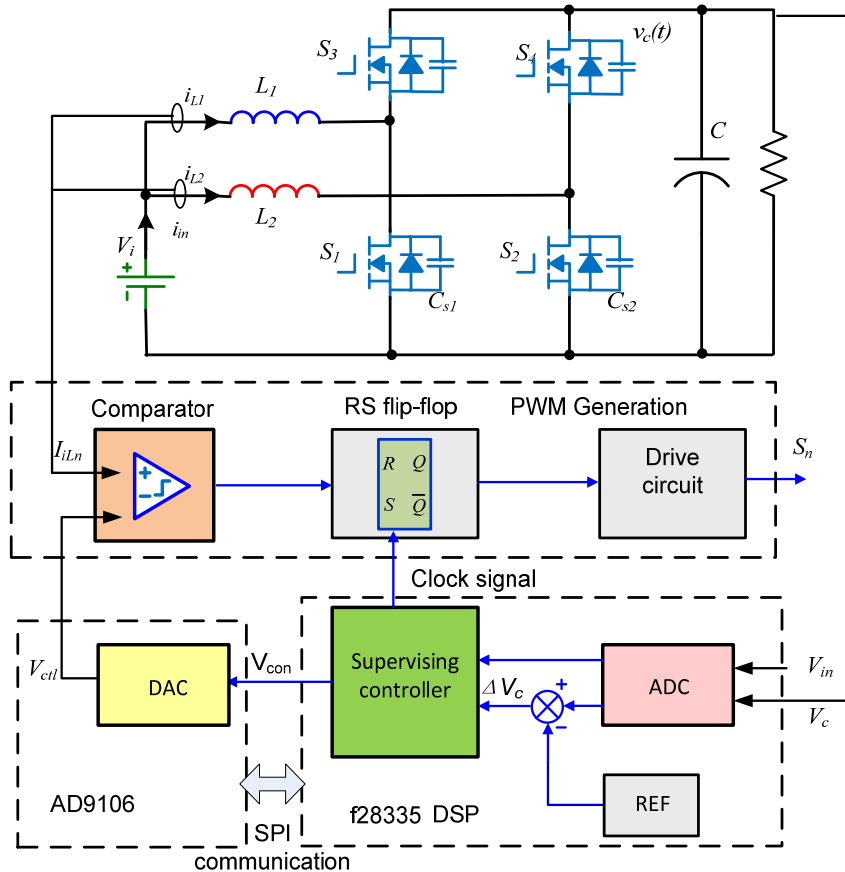
Figure 6.4 Interleaved boost converter with the diagram of digital peak current control

The interleaved boost converter with digital peak current control is illustrated in Figure 6.4. A Texas Instruments TMS320F28335 based-DSP controller is used as the core processor to achieve the functions of voltage signal sampling, digital proportional-integral-derivative (DPID) and sending commands to the external waveform generator AD9106 to produce the current reference. The analogue interface board is designed for PWM signal generation with comparator and RS flip-flop chips as shown in

Figure *6.5*. Two continious time inductor currents are sampled and scaled by Hall current sensors, and the signals are fed into the postive pins of the comparators to be compared with the output of the waveform generation board. Because of the interleaved configuration, the ripples of output voltage are at twice the switching frequency. Thus the sampling frequency of output voltage should be set as twice per period, which can be accomplished in the programming.

The TI f28335-based digital signal controller (DSC) is employed as the main controller. It is has many useful peripheral modules, including a general purpose

94

input and output (GPIO) module, an enhanced pulse width modulator (ePWM), a built-in ADC Module and serial peripheral interface (SPI) to name a few. Its flexibility of configuration and programmability make it popular in applications with power switching converters using digital control solutions. With the employment of the software Code Composer Studio (CCS), programs can be developed to serve many functions, meeting the demands of various advanced control algorithms such as the supervisory controller which plays a key role in this work and is discussed later in the thesis.

Figure 6.5 PWM generation board
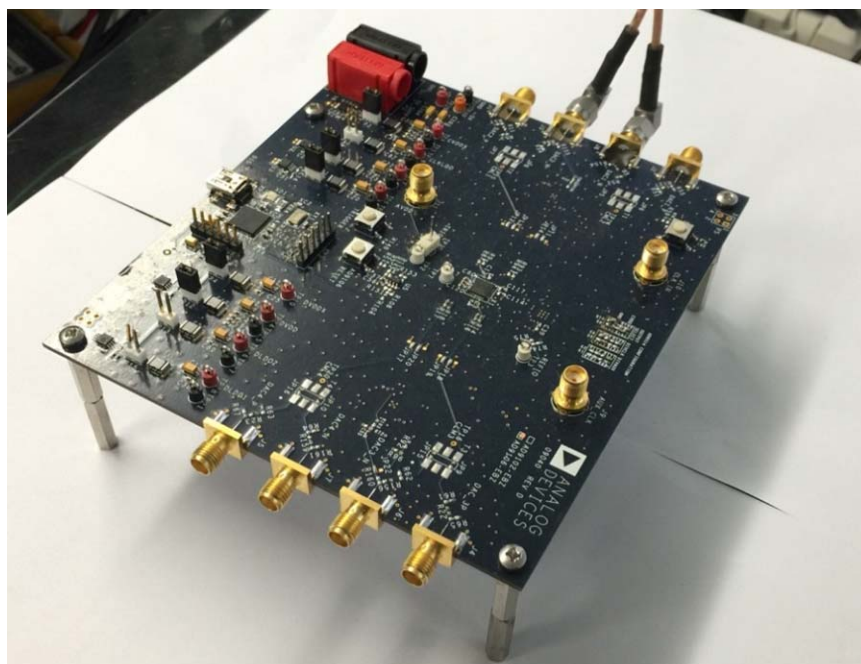
Figure 6.6 AD9106 evaluation board

The AD9106 evaluation board is a high-performance DAC integrating on-chip pattern memory, which can be used to generate complex waveforms with a direct digital synthesizer (DDS). Figure 6.6 shows a photograph of the board. Its internal static random-access memory (SRAM) provides the function of direct waveform generation based on stored data, with flexible gain and offset adjustments. In addition, an internal pattern control state machine allows the user to program the start delay and end time of the pattern. Configuration can be achieved via SPI communication with the master processor. Figure 6.7(a) shows a photograph of the SPI interface from the processor and Figure 6.7(b) demonstrates an example of captured waveforms of SPI communication. The waveforms from top to bottom are signals for chip selection, command words, the data clock and switching clock.
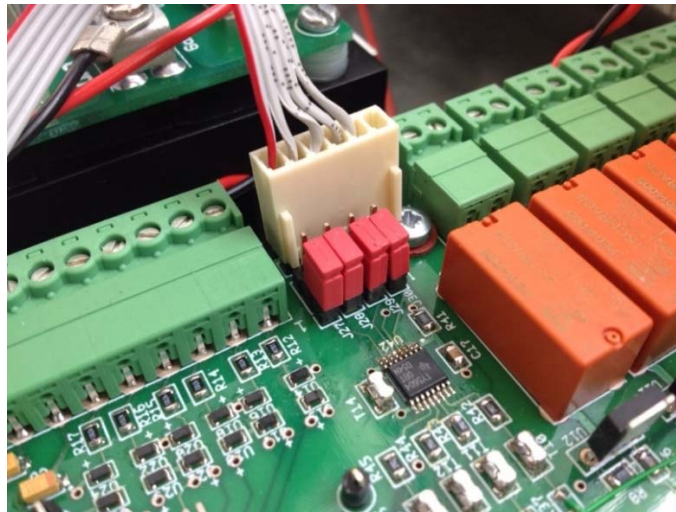
(a)
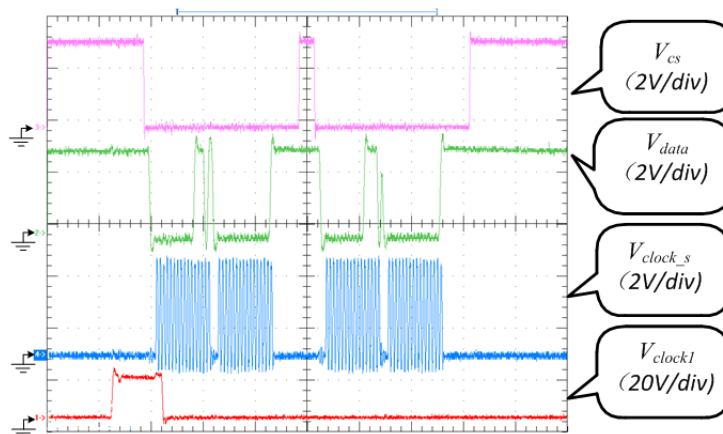
(b)

Figure 6.7 (a) SPI interface
(b) Operational waveforms of SPI communication

All of the components mentioned above were assembled into a power case for safety and a photograph of the full prototype is given in Figure 6.8. The whole test system

contains a front control and display panel, auxilary power supply and relays, an interleaved boost converter with an analogue PWM generation board, the DSP controller and waveform generation board.
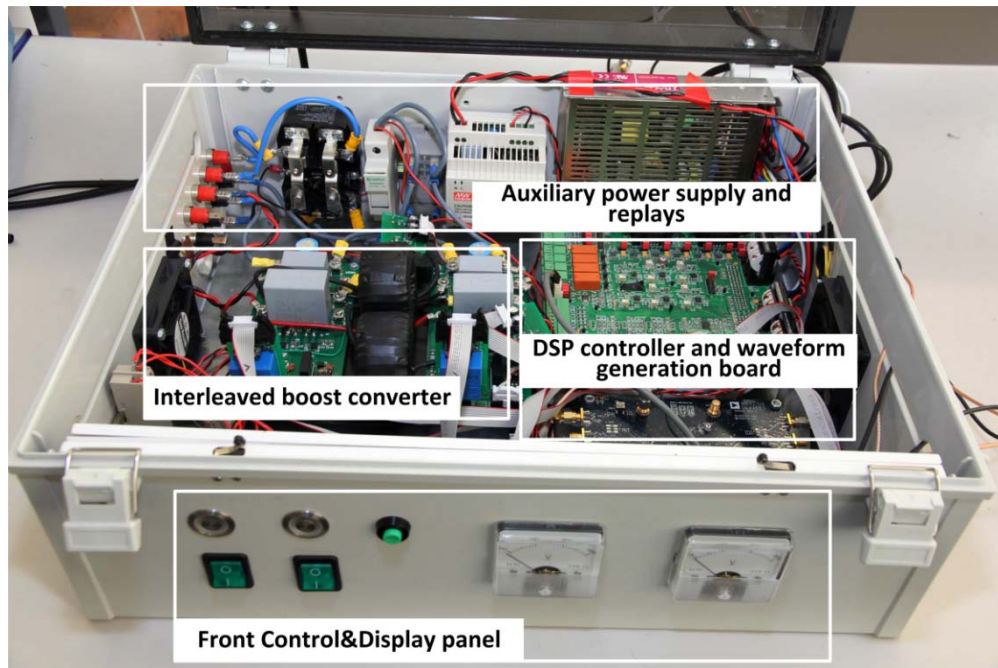
Figure 6.8 Photograph of prototype

6.3.2 Software implementation

Figure 6.9 presents the flow charts of programmed codes. The program starts with the initialisation code, which includes variable definition and configurations for all relevant registers. Then the program executes the Labview data exchange loop. The function of this loop is to continuously communicate with the Labview user control panel via the RS232 interface, receiving commands from the user and sending back the sampled data to the control panel. For each switching period, the code is set to jump into the subfunction of the interrupt service routine (ISR) which contains the ADC sampling, implementation of Digital PI and updating the output of external waveform generators. The present sampled values after ADC conversion are fed into the subfunction of the control algorithm block. This block achieves the functions of the calculation of the digital PI for current reference and the proper values of the compensation ramp to guarantee the stable operation of the converter. Main codes programmed in the DSP controller is attached in Appendix 5. Part of the user's Labview control panel is shown in Figure 6.10. States of input and output voltages, two inductor currents and calculated values of digital PID are monitored and displayed in this panel. Some parameters can be adjusted manually to change the

operation conditions of the converter.
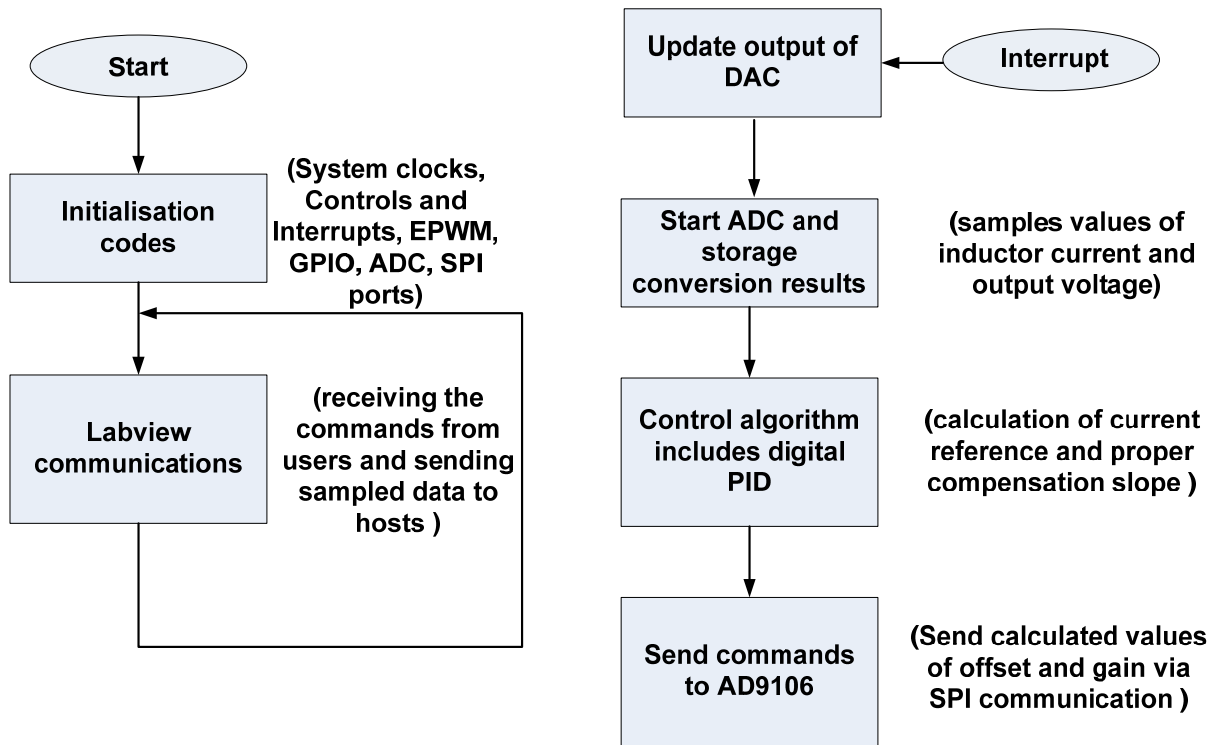
Figure 6.9 Flow charts of program

Figure 6.10 Part of the user's control panel in Labview

In order to reconstruct the bifurcation diagram, the output voltage and inductor currents are continuously sampled for 30 switching periods for each given operational condition, and the sampling results are transferred and generated as a

date file which is stored in the user's laptop. The process of sampled data collection is controlled by the acquire and save button as illustrated in Figure 6.11(a), and the corresponding diagram of graphical programming to achieve this function is presented in Figure 6.11(b).
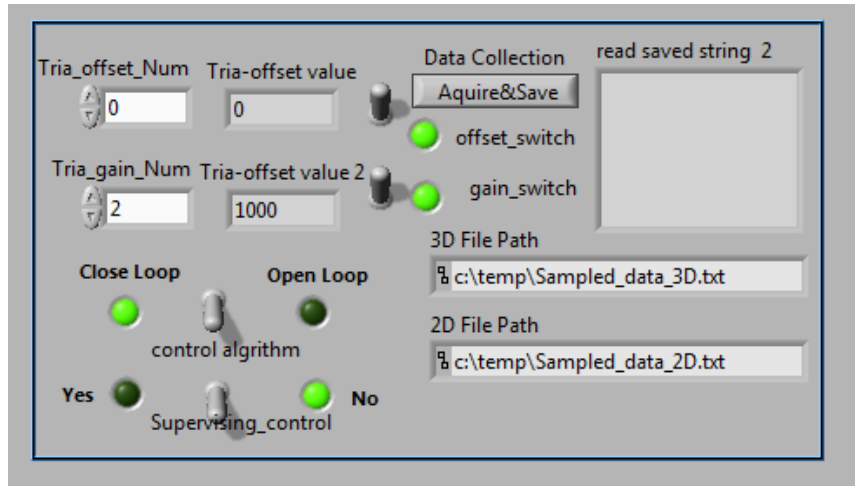
(a)
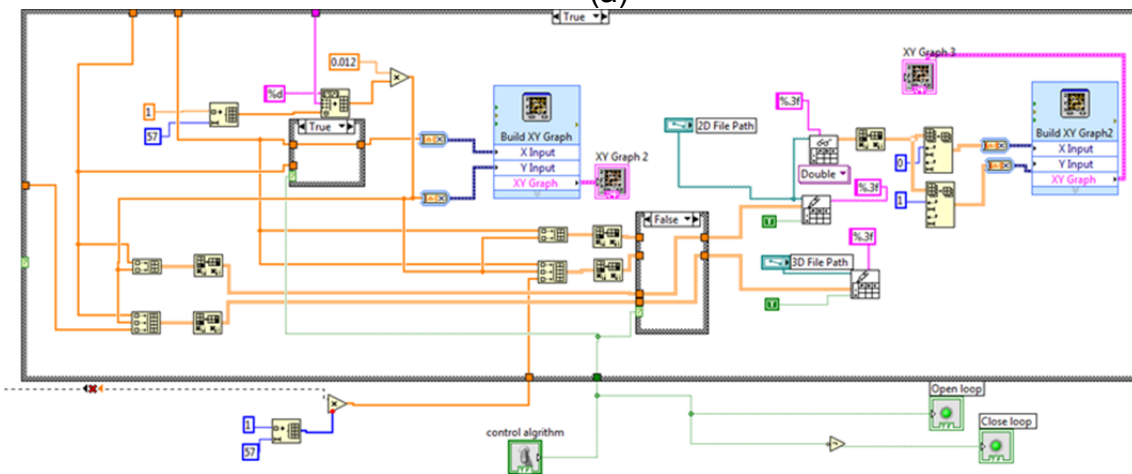
Figure 6.11 (a) Function block of data acquire and save

(b) Corresponding diagram of graphical programming

6.4　Experimental results

The interleaved boost converter used has the following specifications: V_{in}=14V, V_{out}=42V, P_o=200W, f_s=50kHz, and L_1=L_2=150µH. Figure 6.12(a) shows the two current references V_{com1} and V_{com2} generated from the AD9106 with a slope amplitude of a_c=0.1. In addition, the figure shows the two clock signals V_{clock1} and V_{clock2} with a 180 degrees phase shift both feeding RS flip-flops. The corresponding waveforms of the output voltage V_{out}, two inductor currents i_{L1}, i_{L2}, PWM drive signals V_{g1},V_{g2} and swtiching clocks are presented in Figure 6.12(b). All of the waveforms demonstrate that the system is in stable operation of period-1 under the given

conditions.
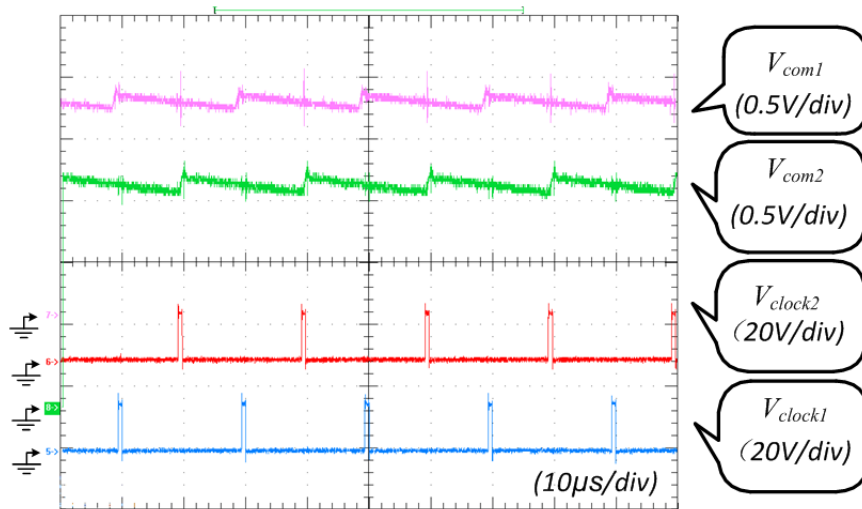
(a)
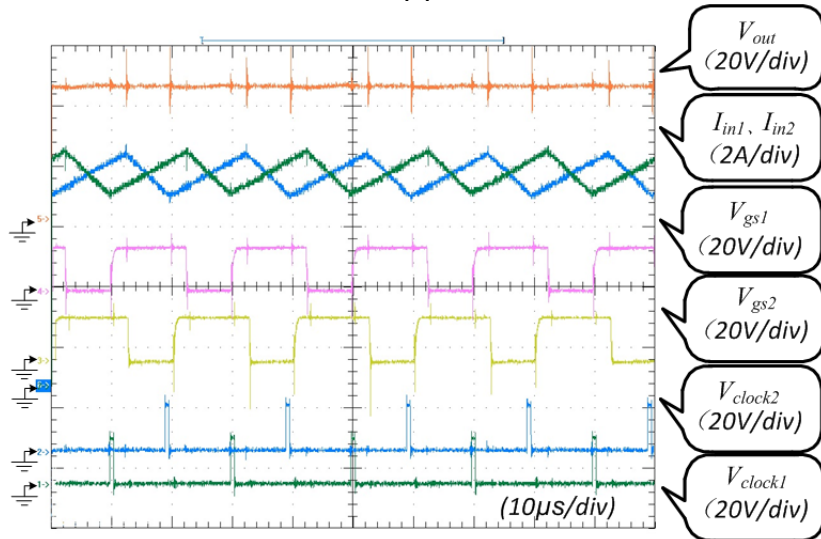
(b)

Figure 6.12 (a) Current references V_{com1} and V_{com2} and corresponding clock signals

(2) Waveforms at $a_c=0.1$

(a)

(b)
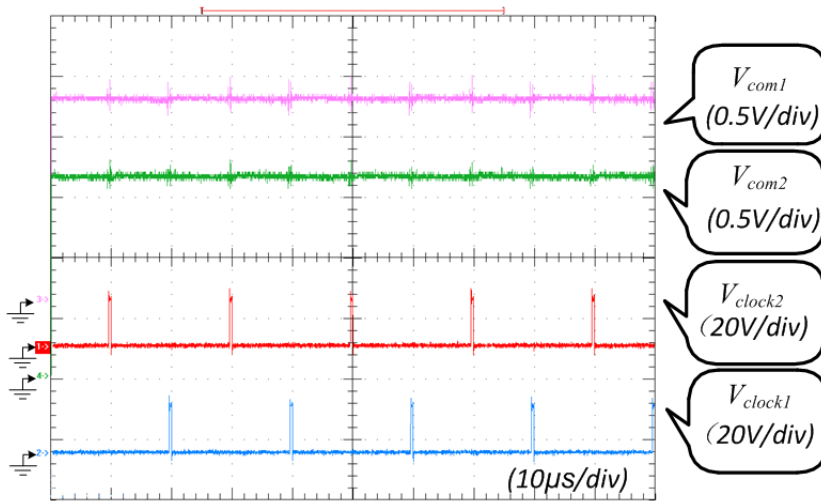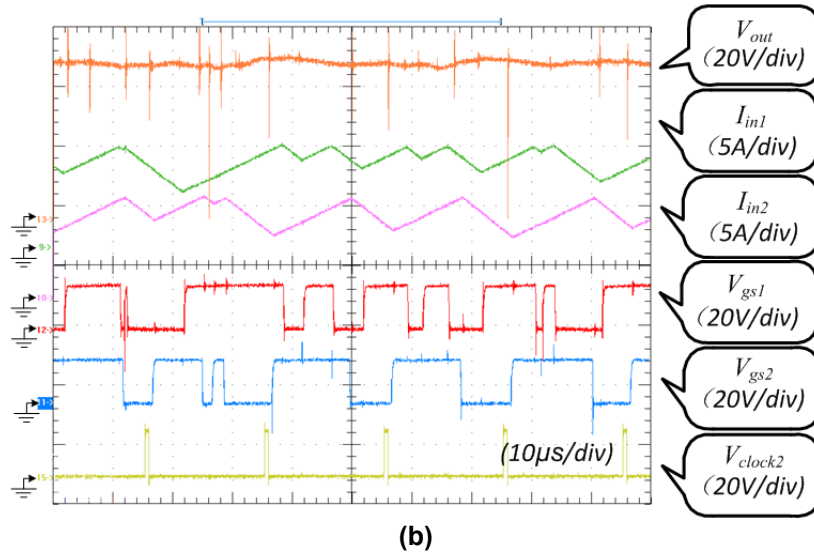
Figure 6.13 (a) Current references V_com1 and V_com2 and corresponding clock signals

(2) Waveforms at a_c=0.01

In contrast, when the amplitude of the compensation slope is set to a_c=0.01, as illutrated in Figure 6.13(a), the system becomes unstable, operating in chaotic mode which can be seen in Figure 6.13(b).

6.5 Digital controller
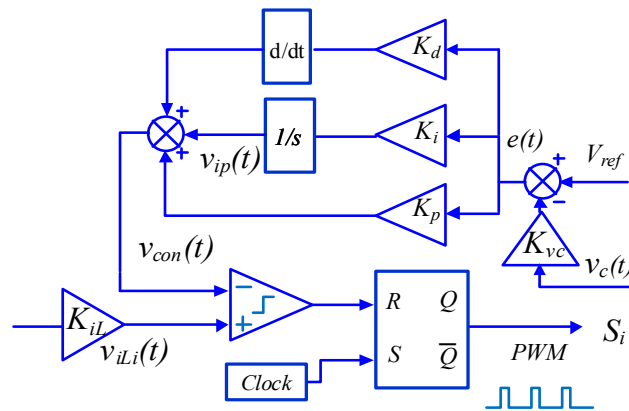
Figure 6.14 Diagram of the analogue PID controller

An analogue PID controller in the continuous time domain is illustrated in Figure 6.14. The output of the ideal PID controller *u(t)* can be expressed as:

$$u(t) = K_p(e(t) + \frac{1}{T_i}\int_0^t e(\tau)d\tau + T_d\frac{d}{dt}e(t)) \tag{6.6}$$

where

$$e(t) = K_{vc}(v_c(t) - V_{ref}) \tag{6.7}$$

Here e(t) is the error signal, K_p is the proportional coefficient, T_i and T_d represent integral time and derivative time respectively.

101

By applying Laplace transforms to equation 6.6, the relations of output voltage and error in the s domain can be expressed as:

$$D(s) = \frac{V(s)}{E(s)} = K_p(1 + \frac{1}{T_i s} + T_d s) = K_p + K_i \frac{1}{s} + K_d s \qquad (6.8)$$

Here, K_i and K_d are the integral and derivative coefficient respectively in the s-domain. In digital systems, the discrete sampling method is used to digitalize the original analogue system. The expression of PID control can be transformed from the s-domain into the z-domain as follows:

$$D(z) = D(s)|_{s = 1 - \frac{z^{-1}}{T}} = K_p(1 + \frac{T}{T_i}\frac{1}{1 - z^{-1}} + T_d(1 - z^{-1})) = K_P + K_I' \frac{1}{1 - z^{-1}} + K_D(1 - z^{-1}) \quad (6.9)$$

$$\begin{cases} K_I = \dfrac{K_p T_s}{T_i} = K_i T_s \\[3mm] K_D = \dfrac{K_p T_d}{T_s} \end{cases} \qquad (6.10)$$

where T_s is the sampling time and K_I and K_D are the integral and derivative coefficients respectively in the z-domain. The difference equation can be obtained from equation 6.9:

$$u(k) = K_p e(k) + K_I \sum_{i=0}^{k} e(i) + K_D[e(k) - e(k-1)] \qquad (6.11)$$

Thus, the output of a digitalised incremental PID control algorithm is:

$$\begin{aligned} \Delta u(k) &= K_p \Delta e(k) + K_I \sum_{i=0}^{k} \Delta e(i) + K_D[\Delta e(k) - \Delta e(k-1)] \\ &= K_p[e(k) - e(k-1)] + K_I e(k) + K_D[e(k) - 2e(k-1) + e(k-2)] \end{aligned} \qquad (6.12)$$

$$u(k) = u(k-1) + \Delta u(k) = u(k-1) + (K_p + K_I + K_D)e(k) - (K_p + 2K_D)e(k-1) + K_D e(k-2)$$
$$(6.13)$$

For the digital PI controller, the expression can be simplified to:

$$u(k) = u(k-1) + \Delta u(k) = u(k-1) + (K_p + K_I)e(k) - K_p e(k-1) \qquad (6.14)$$

From the programming point of view, the current output voltage u(k) can be expressed by the previous calculated output voltage u(k-1), current error e(k) and previous error e(k-1). For simulation in Matlab/Simulink, the diagram of incremental PI control is illustrated in Figure 6.15.
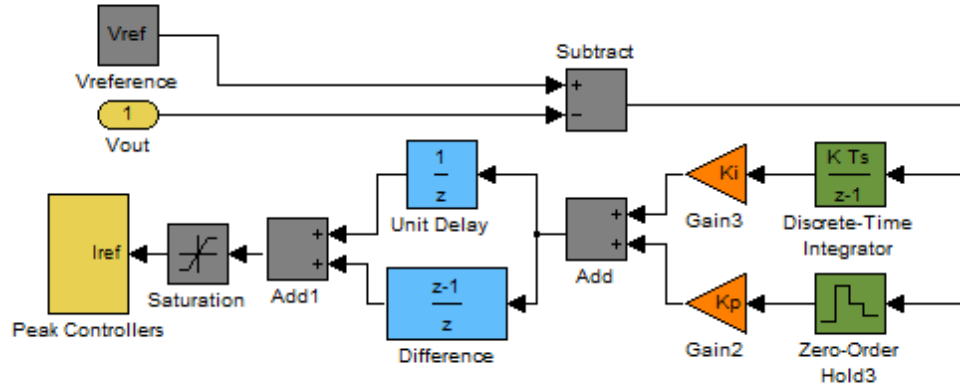
Figure 6.15 Diagram of incremental PI control in Matlab/Simulink

6.6   Monodromy matrix applied in digital control

In digital control, the effect of sampling and zero-order hold changes the derivation of the Monodromy matrix compared to the Monodromy matrix describing analogue control. For example, the original expression of PI output v$_{ipi}$ in analogue control relates to the instantaneous output voltage v$_c$ as shown below:

$$\frac{dv_{ipi}}{dt} = K_I(V_{ref} - K_{vc}v_c) \qquad (6.15)$$

In digital control, the output voltage v$_c$ is sampled and therefore constant for one switching period. Thus, v$_c$ is replaced with V$_{cs}$ and V$_{ipi}$ in digital control can be obtained as:

$$V_{ipi} = K_I(K_{vc}V_{cs} - V_{ref})T_s \qquad (6.16)$$

The sampled value of V$_{cs}$ depends on the ADC sampling time. Sampling mostly occurs at the beginning of the switching period after a slight delay, in order to avoid sampling the noise signals which take place in the switching instants. The control voltage obtained from the output of the PI controller is then obtained as follows:

$$v_{con} = K_p(V_{ref} - K_{vc}V_{cs}) + m_c t + K_I(V_{ref} - K_{vc}V_{cs})T_s \qquad (6.17)$$

This can be simplified as

$$v_{con} = (K_p + K_I T_s)(V_{ref} - K_{vc}V_{cs}) + m_c t \qquad (6.18)$$

103
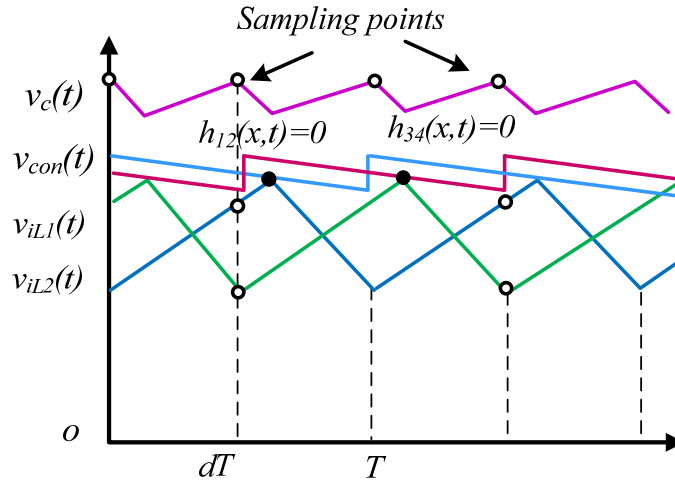
Figure 6.16The sampling points and switching conditions

Since the output of PI v_{ipi} is not related to the instantaneous value in digital control, capacitor voltage v_c and the two inductor currents i_{L1} and i_{L2} are chosen as state vectors, represented by variables x_1,x_2,x_3 respectively. In the peak current control algorithm, the switches of the DC-DC converter will turn off when the outputs of the PI controller v_{con1} and v_{con2} equal the values of the inductor current x_2 and x_3, which is illustrated in Figure 6.16. Therefore, when the duty cycle d is bigger than 0.5, the switching functions can be defined as $h(x, t)$ and these are displayed in equations 6.19 and 6.20 below:

$$h_{12}(x,t) = (K_p + K_I T_s)(V_{ref} - K_{vc}V_{cs}) + m_c t - K_{iL}x_3 \tag{6.19}$$

$$h_{34}(x,t) = (K_p + K_I T_s)(V_{ref} - K_{vc}V_{cs}) + m_c(t - \frac{T}{2}) - K_{iL}x_2 \tag{6.20}$$

And:

$$\frac{\partial h_{34}}{\partial t} = \frac{\partial h_{12}}{\partial t} = m_c = S_a \tag{6.21}$$

Its normal vector and the rate of change are given by

$$\mathbf{n}_{12} = \begin{bmatrix} \partial h_1 / \partial x_1 \\ \partial h_2 / \partial x_2 \\ \partial h_3 / \partial x_3 \end{bmatrix} = \begin{bmatrix} 0 \\ 0 \\ -K_{iL} \end{bmatrix} \tag{6.22}$$

$$\mathbf{n}_{34} = \begin{bmatrix} \partial h_1 / \partial x_1 \\ \partial h_2 / \partial x_2 \\ \partial h_3 / \partial x_3 \end{bmatrix} = \begin{bmatrix} 0 \\ -K_{iL} \\ 0 \end{bmatrix} \tag{6.23}$$

The Saltation matrices S_{12a} and S_{34a} can be obtained as:

$$\mathbf{S}_{12a} = \begin{bmatrix} 1 & 0 & -\dfrac{K_{iL}x_3}{C(s_{pa1}+s_a)} \\[2mm] 0 & 1 & 0 \\[2mm] 0 & 0 & 1+\dfrac{K_{iL}x_1}{L_2(s_{pa1}+s_a)} \end{bmatrix} \tag{6.24}$$

$$\mathbf{S}_{34a} = \begin{bmatrix} 1 & -\dfrac{K_{iL}x_2}{C(s_{pb2}+s_a)} & 0 \\[2mm] 0 & 1+\dfrac{K_{iL}x_1}{L_1(s_{pb2}+s_a)} & 0 \\[2mm] 0 & 0 & 1 \end{bmatrix} \tag{6.25}$$

Where

$$s_{pa1} = \mathbf{n}_{12}^T f_{on} = \mathbf{n}_{12}^T f_1 = \begin{bmatrix} 0 & 0 & -K_{iL} \end{bmatrix} \begin{bmatrix} -\dfrac{x_1}{RC} \\[2mm] \dfrac{V_i}{L_1} \\[2mm] \dfrac{V_i}{L_2} \end{bmatrix} = -\dfrac{K_{iL}V_i}{L_2} \tag{6.26}$$

$$s_{pa2} = \mathbf{n}_{34}^T f_{on} = \mathbf{n}_{34}^T f_1 = \begin{bmatrix} 0 & -K_{iL} & 0 \end{bmatrix} \begin{bmatrix} -\dfrac{x_1}{RC} \\[2mm] \dfrac{V_i}{L_1} \\[2mm] \dfrac{V_i}{L_2} \end{bmatrix} = -\dfrac{K_{iL}V_i}{L_1} \tag{6.27}$$

$$\mathbf{S}_{23a} = \mathbf{S}_{41a} = \mathbf{I} \tag{6.28}$$

6.7   Peak current control and voltage feedback control

Figure 6.17 shows the bifurcation diagram of one phase inductor current at different current references. It is reconstructed from the sampled data of 32 consecutive switching periods under about 45 different given current references. From the figure, it can be seen that, when the amplitude of the compensation slope is set as a_c=0.01, the inductor current experiences three different operational states from period-1, period-2 to the chaotic state during the increase of input current reference. Bifurcation behaviour occurs when the current reference is equal to 1.15. Figure 6.18 demonstrates the key operational waveforms of the DC-DC converter, which are the

output voltage, inductor current fast Fourier transform (FFT) curve, current reference and gate drive signals from top to bottom.
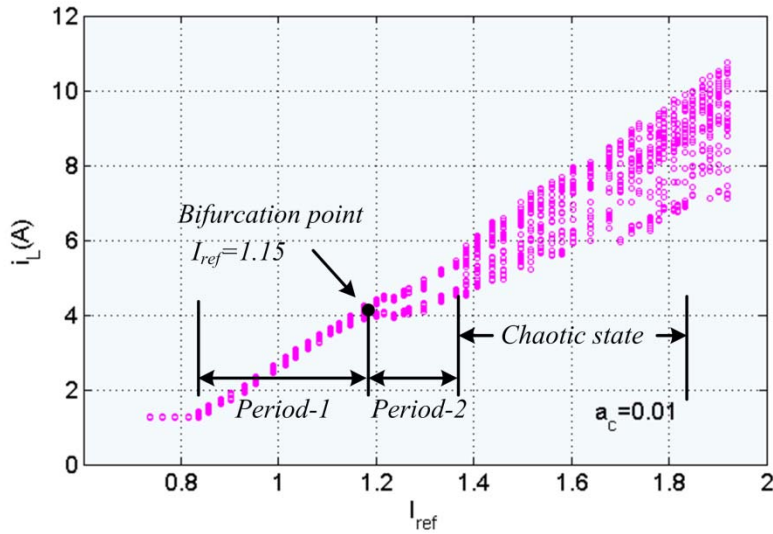
Figure 6.17 Bifurcation diagram of input current under different current reference (a_c=0.01)

Figure 6.18(a) presents the waveforms when I_{ref} is equal to 1and the converter is in a stable operation of period-1.The FFT spectrum curve shows a maximum high frequency amplitude at 50kHz. This is the same frequency as the switching frequency. When the current reference is increased to I_{ref}=1.2, the converter exhibits the behaviour of period-2 as illustrated in Figure 6.18(b). In this state, the duty cycle of the gate drive repeats between two alternate different values and the corresponding FFT spectrum shows the frequency of the measured inductor current to become 25kHz, which is half of the switching frequency. Chaotic behaviour occurs when the reference current is bigger than 1.4, which is indicated by the non-periodic duty cycle and corresponding FFT spectrum curve shown in Figure 6.18(c).

(a)

106

(b)

(c)
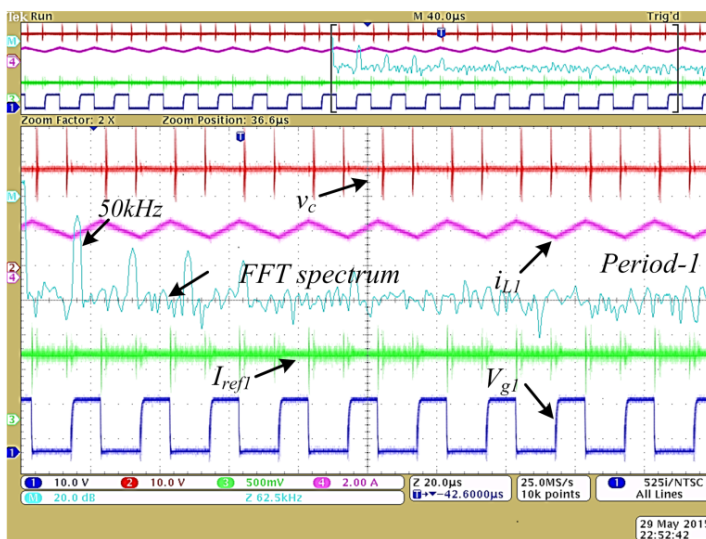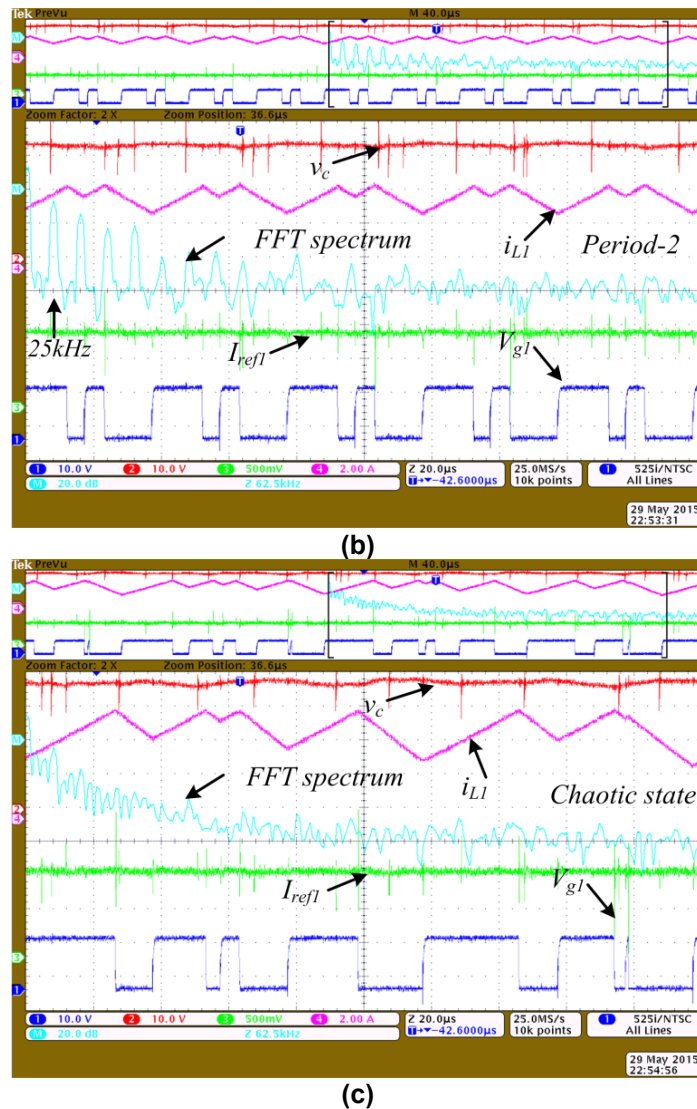
Figure 6.18 Key operational waveforms of converter at different states: (a) period-1 (b) period-2 (c) chaotic state

Figure 6.19 demonstrates the bifurcation diagram of the inductor current at a different a_c which equals 0.1. It can be seen that the range of the stable period-1 is extended compared with that in Figure 6.17, and the bifurcation point is increased to 1.4. Likewise, the region of period-2 is changed and extended to a wider range. In addition, the operation of period-3 occurs when the current reference exceeds 1.75, which cannot be found at all in Figure 6.18(a). From the experimental results, it is evident that the small change in the magnitude of the compensation slope brings about the large influence on the operation of the converter. In order to verify the effectiveness of the simulation, the converter was tested with the conditions shown in Table 4.1. The outer voltage close loop with digital PI and inner current loop were employed in the simulation, and the same control algorithm was implemented in the DSP control for the comparison.
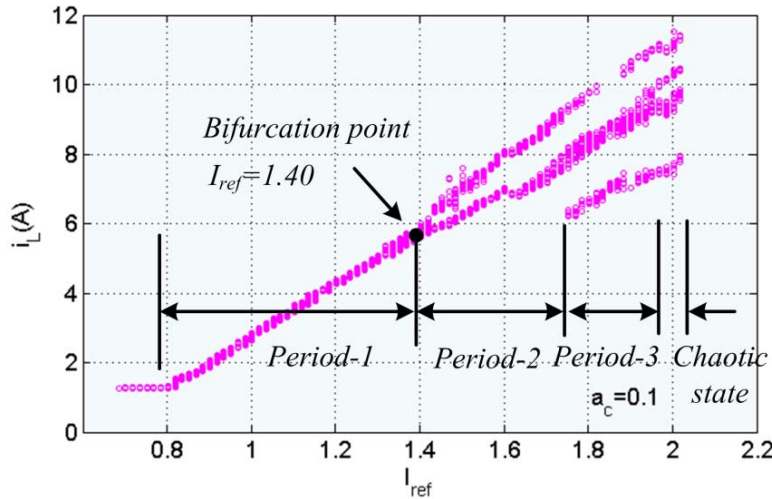
Figure 6.19 Bifurcation diagram of input current under different current reference (a_c=0.1)

Table 6.1 Specifications of testing conditions

Parameters	Value	Parameters	Value
Input voltage （V）	5~18,	Frequency （kHz）	50
Output voltage （V）	24,	K_{iL}	1/8.5
Power rating （W）	60	K_{p1}	0.5
Inductance （uH）	150	K_{i1}	2000
Output capacitance (uF)	40	a_c	0.05
K_{vc}	1/120		

Figure 6.20(a) shows the bifurcation diagram of output voltage v_c and inductor current i_{L1} in simulation at different input voltages. In contrast, the corresponding experimental results are displayed in Figure 6.20(b). It can be seen that they are quite close but with some differences in terms of profile and bifurcation point. The main difference is caused by the varying steps of input voltage in the experiment and the constant step setting in the simulation. The simulation results are from the ideal model-based calculation, and thus the sampled points generated for constant values are exactly located at one point. In contrast, errors in the experimental results are caused by the sampling resolution and quantization effect, and thus the constant values to sample will be transferred as values with some errors in the DSP controller. The errors are also related to settings of the zero-order hold and capture window in relevant registers, and this is normally set within a certain acceptable range to guarantee accuracy. In general, the simulation results are reliable enough so as to be used to facilitate the practical circuit design.
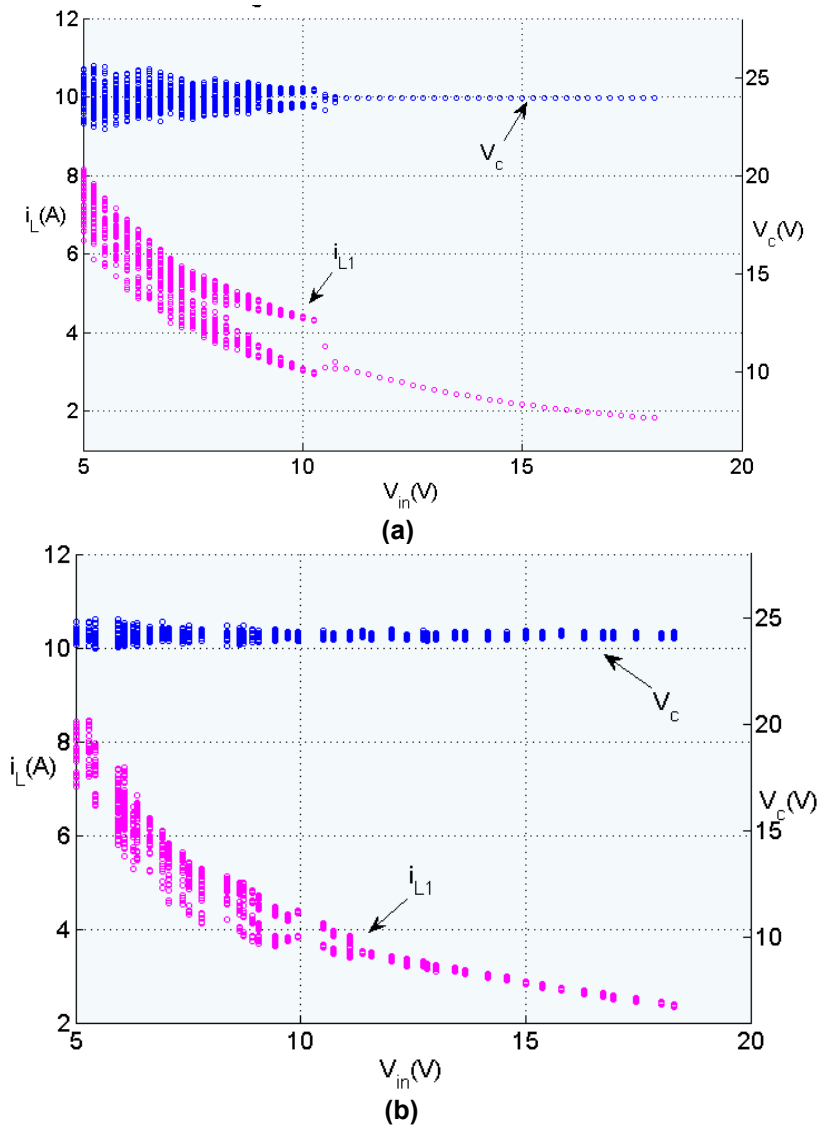
Figure 6.20 Bifurcation diagram of output voltage and inductor current in simulation at different input voltages: (a) simulation results (b) experimental results

Figure 6.21 shows the performance of interleaved boost converter at different input voltages. When the input voltage V_{in} is set at 17 volts, the waveforms indicate that the system is in the stable operation of period-1 as illustrated in Figure 6.21 (a). Until the input voltage is reduced to the bifurcation point when V_{in} equals 10.5 volts, the converter exhibits the behaviour of period doubling bifurcation in the operation of period-2, where the switching frequency is still 50kHz as in period-1 but the frequency of the inductor current becomes half of the switching frequency as shown in Figure 6.21(b).

When V_{in} is set from 10.5V to 10V, the converter is in another period-2 mode, and the switching frequency is changed to 25kHz as displayed in Figure 6.21(c). According to the bifurcation diagram illustrated in Figure 6.20, the converter will exhibit chaotic

behaviour when V_{in} is less than 7.5V. Figure 6.21(d) presents the waveforms of the converter when V_{in} equals 6.5V, and the FFT spectrum curve indicates that the converter is operating in the chaotic state.

(a)

(b)

(c)

110
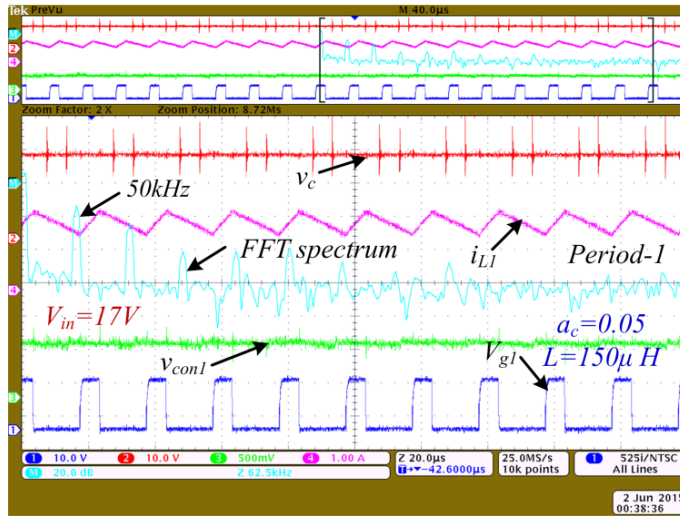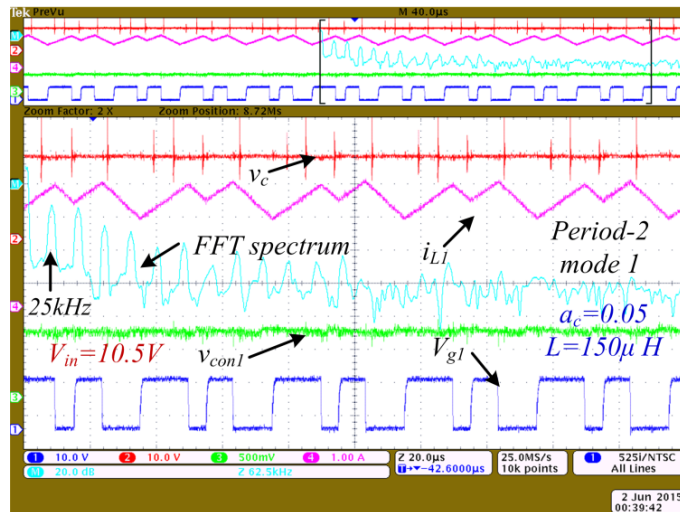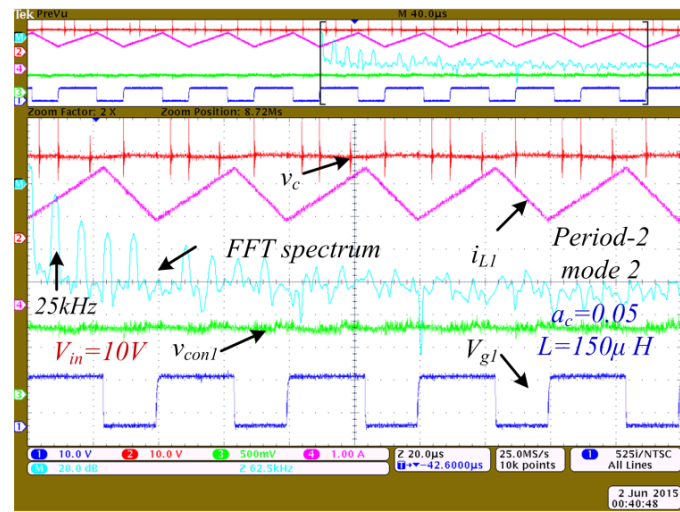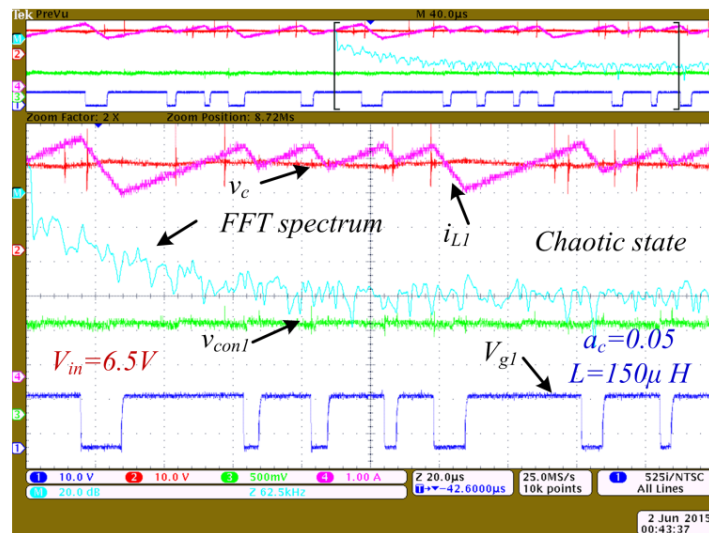
(d)

Figure 6.21 Key operational waveforms at different input voltages: (a) V_{in}=17V (b) V_{in}=10.5V (c) V_{in}=10V (d) V_{in}=6.5V

6.8 Summary

A new mixed signal technique is proposed to achieve digital peak current control. Experimental results demonstrate that the test system works effectively, and can be used for the nonlinear analysis and control of DC-DC converters. In addition, a derivation of Monodromy matrices of the interleaved boost converter under digital peak current control is presented for the first time, and this is also validated numerically and experimentally.

7 Control of nonlinear behaviour and applications

This chapter tackles the control of nonlinear behaviour in power switching converters, especially focusing on digital slope compensation. Some control algorithms for current mode control in digital implementations that have been proposed in recent years are compared and discussed. The influence of slope amplitude in conventional fixed slope compensation and sinewave compensation is investigated theoretically and by experiments. Based on knowledge of the derived Monodromy matrix, a real time cycle to cycle variable slope compensation control method is proposed to control the nonlinearity in DC-DC converters. Moreover, an improved quadratic curve slope compensation (QCSC) control is proposed in this chapter, which can use a smaller amplitude of slope but provides a much better compensation effect compared to conventional slope compensation. Experimental results verify the effectiveness of the proposed methods. Finally, a case study of reduced inductance in an interleaved boost converter is presented to demonstrate the potential application of the proposed nonlinear analysis and control method.

7.1 Introduction

The final section of the previous chapter demonstrated the nonlinear behaviour of DC-DC switching converter under peak current mode control. As summarised in the chapter 1 in this thesis, various feedback and non-feedback control techniques have been proposed to eliminate undesired nonlinear phenomena in converters. They can be applied to different applications, meeting the demand to control nonlinearity but involving various advantages and disadvantages. However, some of them are highly dependent on the mathematical model used and therefore cannot easily be implemented in practical circuits. Among the proposed methods, ramp compensation is the most well-known approach and is widely applied in industrial applications. Some mature commercial analogue controllers with internal or external ramp compensation are available on the market. Nevertheless, due to the lack of a thorough understanding of the operation of converters, the compensated magnitude of the ramp is only set as a constant value in most of the practical applications, which is based on experience rather than analysis. In recent years, a few digital controllers with ramp compensation module using a built-in analogue comparator have emerged

[147, 148].

Since the development of digital controllers in power converters, many relevant control algorithms have been proposed to achieve current mode control. A predictive peak current control method has been presented [149] in which the inductor current is pre-calculated using knowledge of inductance. Inductor current and output voltage are sampled once per cycle and used to predict the desired comparator switch-off threshold. Another digital peak current technique introduces the calculation of the duty cycle of the next switching period by solving the instant at which the sampled current becomes equal to the compensated current reference from the outer voltage loop [150]. A technique of cycle-by-cycle duty ratio computation in real time has also been presented [151]. A time-to-digital converter translates information of the last duty ratio into digital code, and then reconstructs the next duty ratio by using a moving average filter. However, all of these methods predict future values of the duty cycle by employing a mathematical model, and these cannot be regarded as true examples of peak current mode control since the inherent characteristics of a real-time cycle-by-cycle current limiting ability are lost [152].

Figure 7.1 Adaptive digital slope compensation

In order to address the problem of excessive compensation and to improve the performance of peak current control, a piecewise linear slope compensation has been presented in [142]. The optimum value of slope over a wide range of duty cycle is here achieved by adding additional analogue circuitry. An adaptive digital slope compensation algorithm was then proposed to achieve optimal slope compensation over a wide operating range [143]. The structure of this digital control is shown in Figure 7.1. The sampled signals of input and output voltages and the minimum value

of the input current are required to generate the adequate threshold as reference for the inductor current. The appropriate amplitude of the slope is calculated according to a formula based on the type of converter.

However, despite the great effort over the last decade devoted to the implementation of and advanced algorithms for digital peak current control, the influence of compensation slope and digital control for the fast-scale stability issues of systems has not been thoroughly investigated. Knowledge of how slope compensation affects the system's stability and achieves a suitable stable margin cannot be studied effectively with the methods described so far, and in any case their only purpose is to limit oscillation. Moreover, according to the research findings presented in Chapter 3, the system stability in peak current control is strongly related to the rate of the slope itself, and not only to the absolute offset value of the reference current [143]. Thus the adopted Monodromy matrix-based nonlinear analysis method can be an effective tool for the full analysis of the influence of the compensated slope amplitude, and it also can provide the knowledge about the inherent characteristics of peak current control with slope compensation.

7.2   Conventional fixed slope compensation control

The interleaved boost converter with the specifications shown in Table 6.1 was utilized to investigate the conventional fixed slope compensation control. The influence of different amplitudes of compensation slope m_c, is demonstrated in Figure 7.2. The input voltage is set at 6V, and amplitude a_c is set from 0.1 to 0.25 with steps of 0.05. Figure 7.2(a) shows that the converter operates in the chaotic state when a_c equals 0.1; and when a_c is changed to 0.15, then the FFT spectrum indicates that the converter is operating in period-4 mode, with a fundamental frequency of 12.5kHz which is a quarter of period-1. The operation of the converter moves to period-2 when a_c is set to 0.20, and stable operation in period-1 occurs when a_c is decreased to - 0.25. The key operational waveforms are presented in Figure 7.2. It is evident that the values of the slope compensation dramatically affect the stability of converters operation and a larger amplitude (a_c) of compensation ramp can increase the stability of the system.
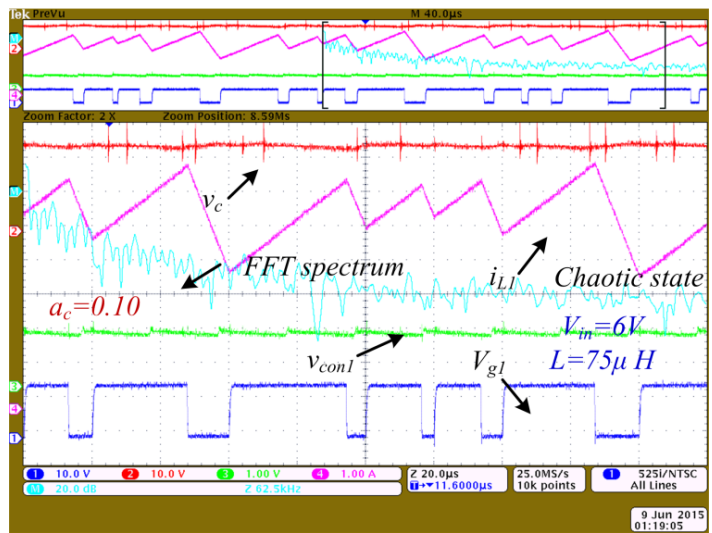
(a)
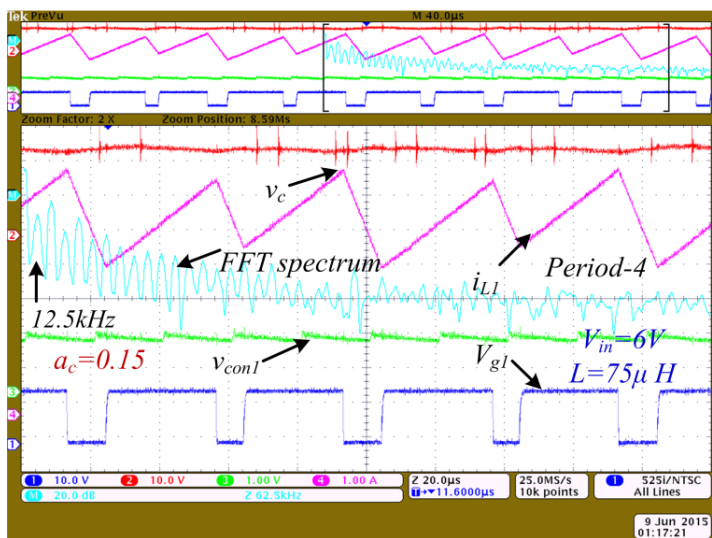
(b)
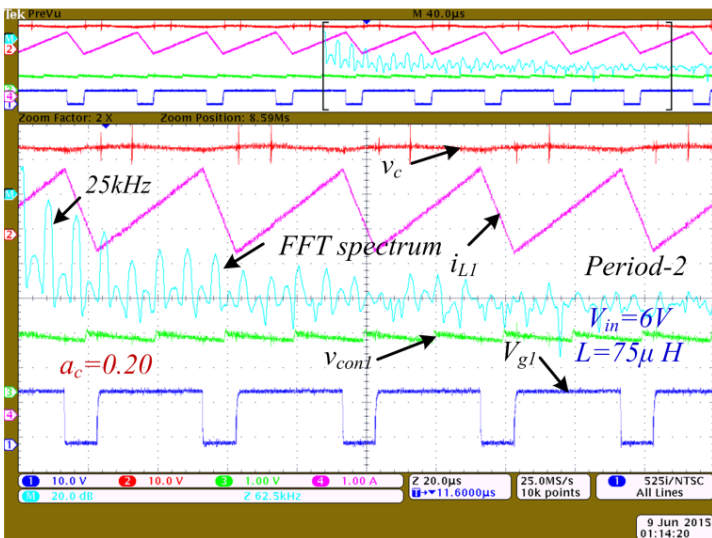
(c)
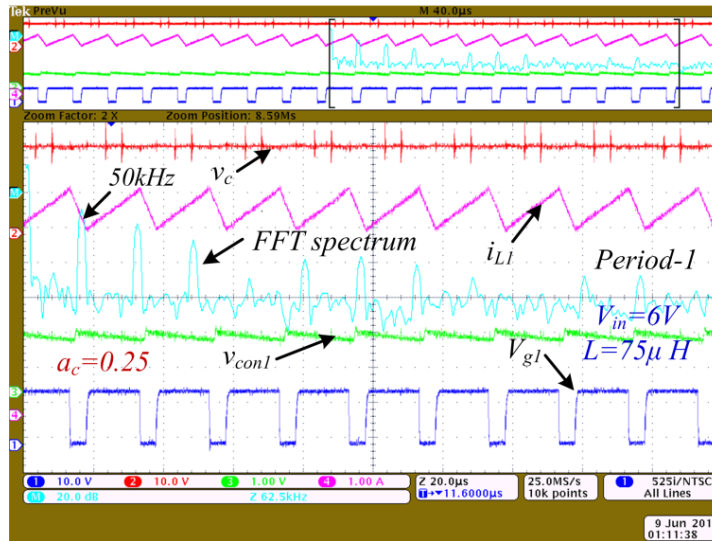
(d)

Figure 7.2 Key operational waveforms at different values of compensation amplitude a_c: (a) a_c=0.10; (b) a_c=0.15; (c) a_c=0.20; (d) a_c=0.25

Figure 7.3 presents a bifurcation diagram of output voltage and inductor current with conditions of different input voltages and slope compensations m_c. The graphs are reconstructed based on the sampled and stored data, which are from the file generated using Labview. It is clear that the bifurcation points vary at different values of a_c, exhibiting linear and non-linear relationships.

(a)

116

(b)
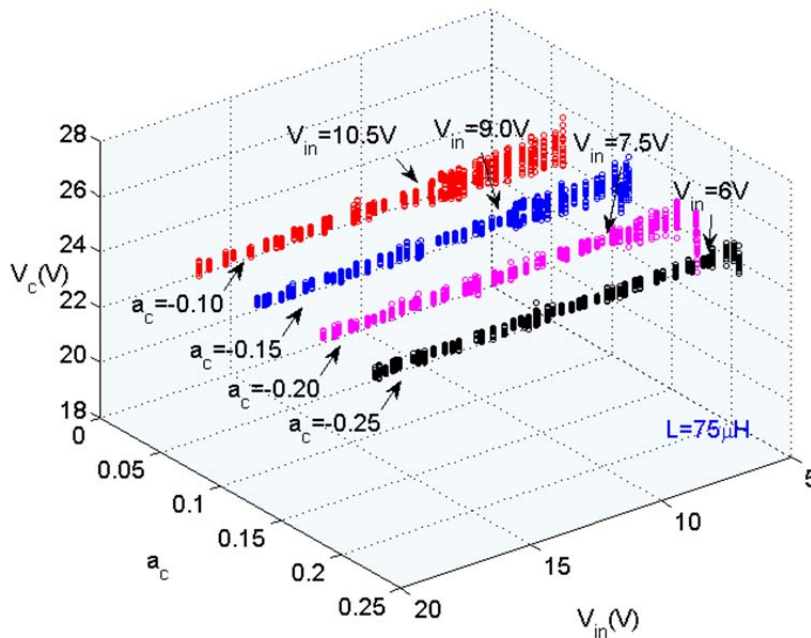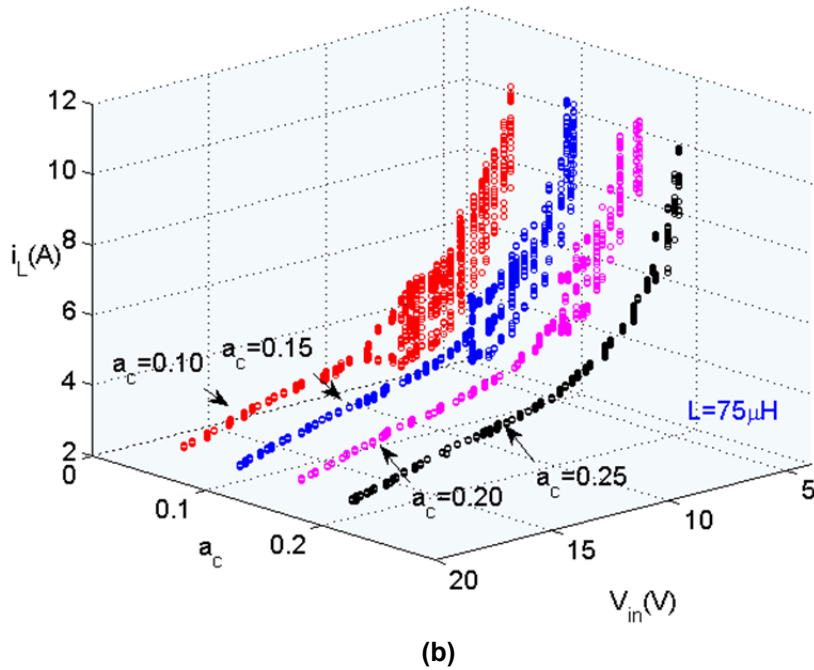
Figure 7.3 Bifurcation diagram of inductor current and output voltage at different input voltages and a_c by employing conventional slope compensation (L=75μH): (a) output voltage; (b) inductor current
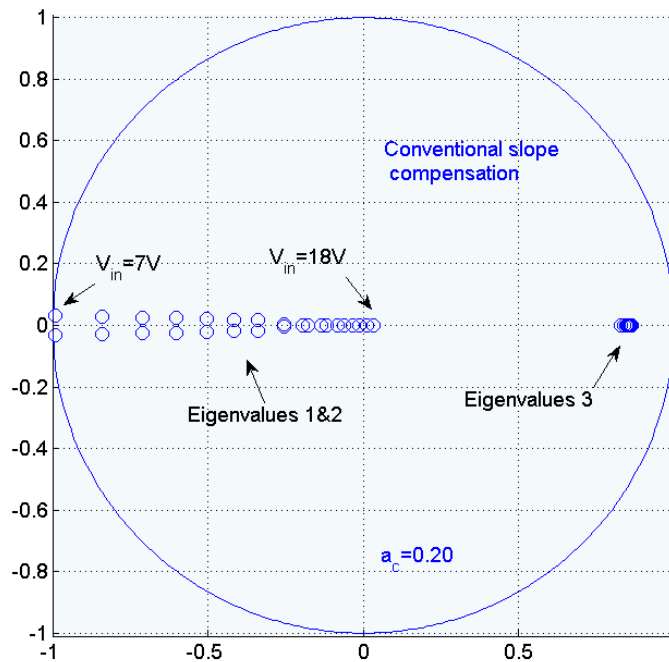
Figure 7.4 Locus of eigenvalues using conventional slope compensation when a_c=0.20

In order to compare the experimental results with the theoretical analysis, the practical parameters are used as input to the codes debugged in the Matlab. This can produce the locus of eigenvalues using slope compensation when a_c equals 0.20,

117

which is illustrated in Figure 7.4. It demonstrates that the converter will lose stability when input voltage is less than 7V, in contrast, the boundary value is 7.5V according to the experimental results shown in Figure 7.3. Thus, it proves that the calculated eigenvalues can be utilized to predict the operation boundary.

7.3 Real-time cycle-to-cycle variable slope compensation control

In order to control nonlinear behaviour and improve the performance of converters, an approach named real-time cycle-by-cycle variable slope compensation (VSC) is proposed in this section, which is based on knowledge of Monodromy matrix. The concepts and principles of this method are presented in section 3.5.1. As illustrated in Figure 7.5, the upper waveforms are two current references added by variable slope compensations with a 180 degree shift, which are generated by the programmable DAC, and the bottom waveforms are the corresponding clock signals. The amplitudes of the slopes are programmed to increase with given step, demonstrating the ability of cycle-by-cycle slope control.
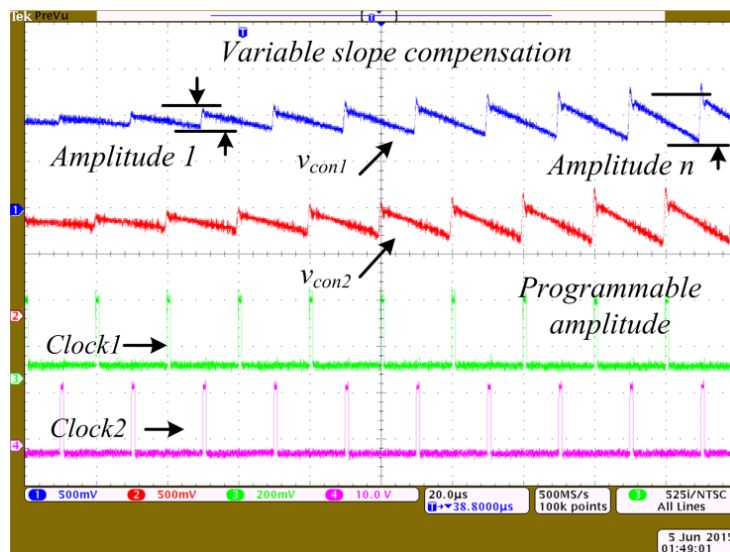
Figure 7.5 Variable slope compensation

Figure 7.6 presents the effect of the proposed method on the control of nonlinearity in converters. The waveforms of the output voltage, inductor current, feedback control signals and gate drives are displayed from the top to the bottom. Figure 7.6 (a) and (b) show the moments where the system loses stability from stable operation of period-1 to the chaotic state in Figure 7.5.(a) and to the period-2 state in Figure 7.5 (b). By employing VSC, the system can be kept in stable operation at certain operating conditions; in contrast, when the controller is switched to use conventional

fixed slope control, the converter loses stability immediately at one cycle time. Similarly, the system can regain stability by switching to the proposed method within a few cycles. Compared to the stable state, it can also be seen that the ripples of output voltage and inductor current increase markedly when the converter is in the unstable chaotic state.
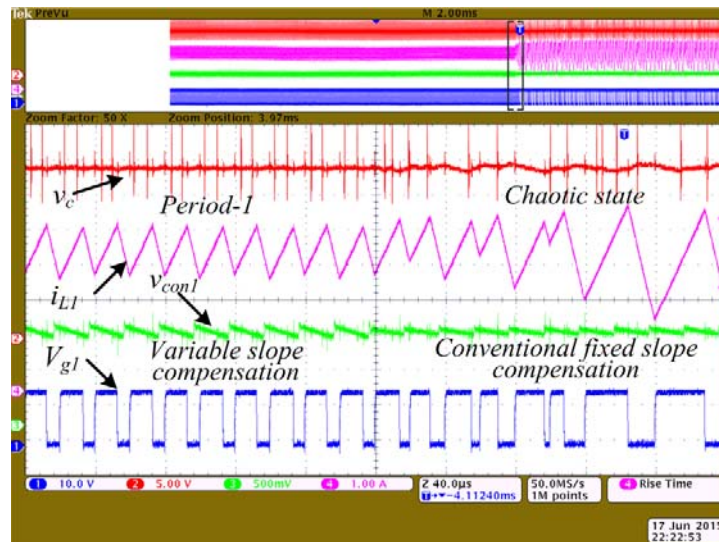
(a)
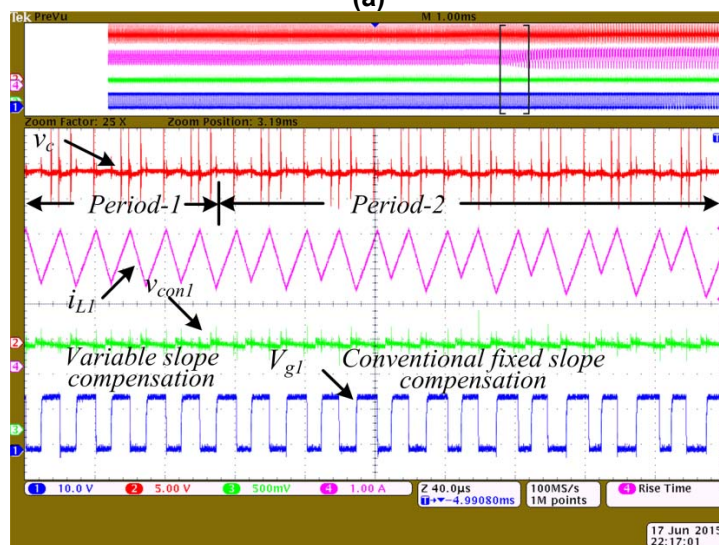
(b)

Figure 7.6 Control of nonlinearity in converters by employing cycle by cycle variable slope compensation: (a) period-1 state to chaotic state; (b) period-1 state to period-2

As discussed in Chapter 5, the eigenvalues in the Monodromy matrix can be used to predict the bifurcation points of the system at different input voltages and values of slope compensation. The locus of eigenvalues can indicate the margin of the stable range at different levels of variation in system parameters or external input and output conditions. In other words, if a specific margin is set, the corresponding compensation slope can be calculated by the given parameters. Here, if the eigenvalues are placed at the radius of 0.5 in the unit circle, for example, the

following nonlinear transcendental equation can be obtained which should be solved numerically:

$$|eig(\mathbf{M}(0,T))| = 0.5 \tag{7.1}$$

The relationship of input voltage and the required mc can be given in the form of a third order polynomial expression:

$$m_c \cdot T = -2.098 \times 10^{-5} \times V_{in}^3 + 7.832 \times 10^{-4} \times V_{in}^2 + 5.5 \times 10^{-3} \times V_{in} - 0.2561 \tag{7.2}$$
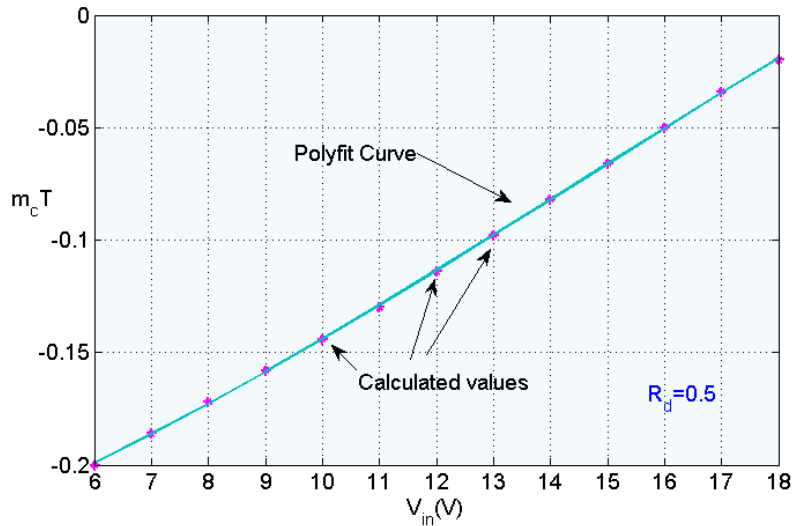
Figure 7.7 Polyfit curve and calculated values of m_c vs. input voltage

Figure 7.7 shows the polynomial fitting curve and the calculated values of a_c at different input voltages for the given radius of 0.5. Thus, in digital VSC, the amplitudes of the compensation slope are calculated from the input voltages according to the expression above.

(a)

120

(b)
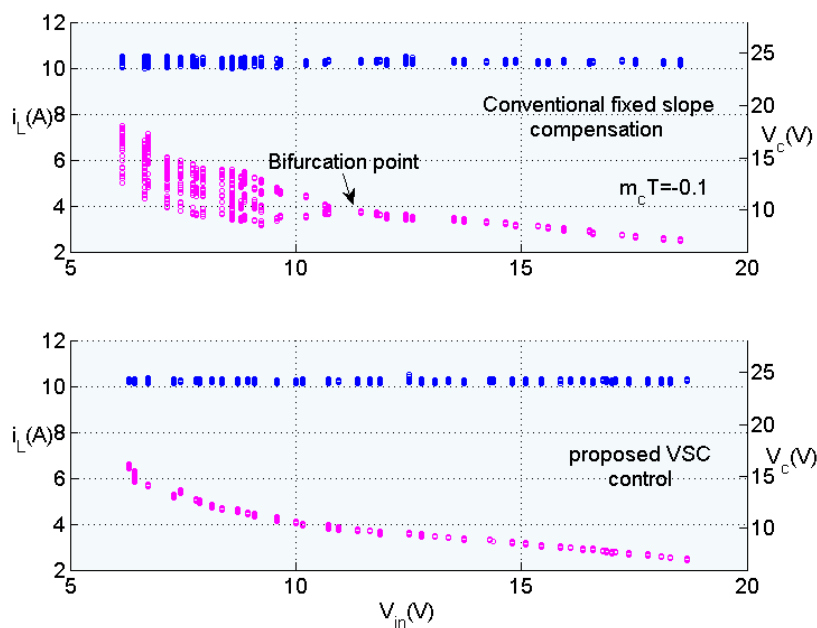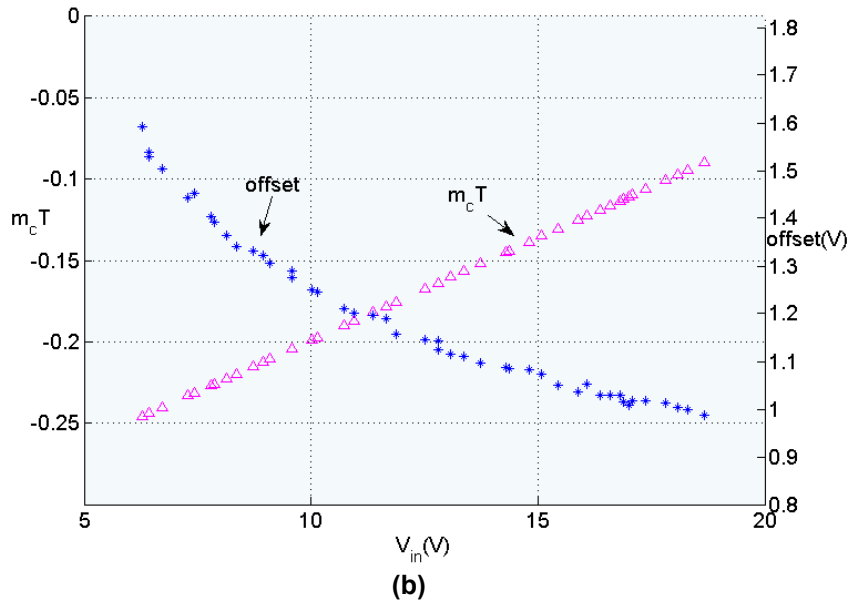
Figure 7.8 (a) Comparison of conventional fixed slope compensation and proposed method under digital control;

(b) calculated values of m$_c$ and offset in digital controller.

A comparison of conventional fixed slope compensation and the proposed method under digital control is presented in Figure 7.8(a). It can be seen that bifurcation occurs when the input voltage is around 12 volts with conventional fixed slope compensation; in contrast, the converter remains stable over the whole range of input voltage from 6 to 18 volts when employing VCS. Figure 7.8(b) demonstrates the calculated values of m$_c$ and the offset in the operation at different input voltages. With a linear increase in the ramp m$_c$, the offset falls exponentially.

7.4 Sinewave compensation control
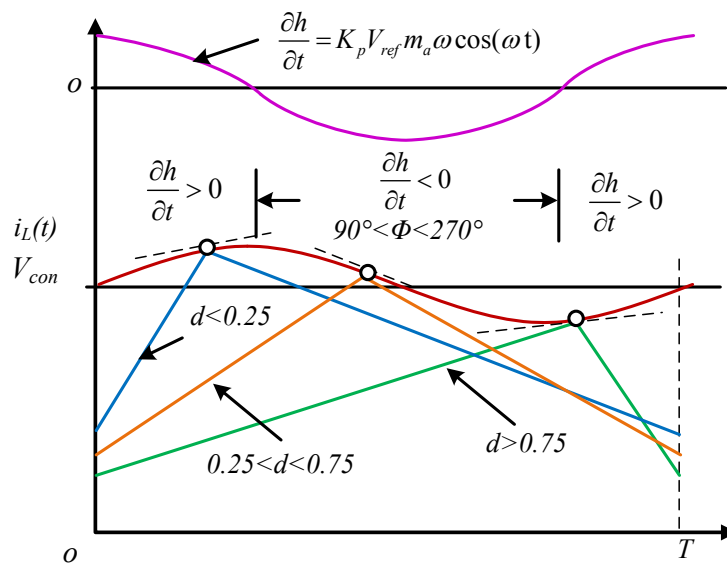
Figure 7.9 Diagram of peak current control with sinewave compensation at different duty cycles

Besides conventional slope compensation, some other studies propose the use of sinewave compensation. For example, a comparison of a non-smooth bifurcation in a ramp-controlled and sinewave-controlled buck converter is discussed in [101].

However, the generation of this type of compensation and synchronisation between signals is hard to implement without employing high-performance DAC. Thus, previous studies are only based on simulation results, and some discussions merely focus on descriptions of phenomena rather than investigating their inherent mechanisms. In addition, previous work has not determined the relationship between compensation effects and the duty cycle. By applying the Monodromy matrix-based method adopted here, more detailed knowledge of this compensation can be gained, which can be verified by experimental results.
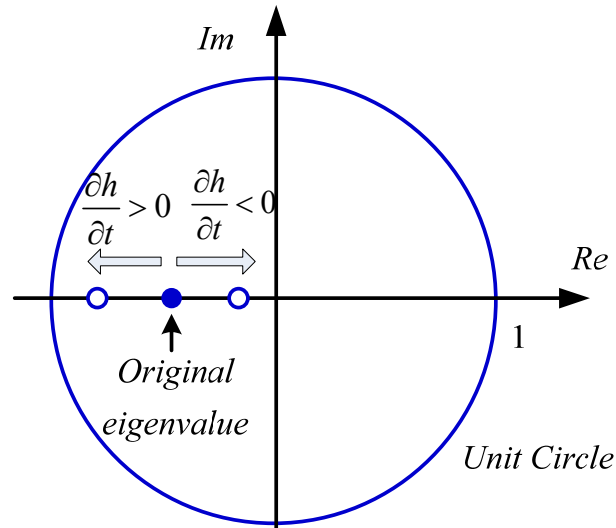
Figure 7.10 Movement track of corresponding eigenvalues with slope compensation

The switching condition of peak current control with sinewave compensation can be expressed as:

$$h(\mathrm{x,t}) = K_p(V_{ref}(1 + a_m \sin(\omega \mathrm{t})) - K_{vc}V_c) - K_{iL}i_L \qquad (7.3)$$

As discussed in previous chapters, the derivative of switching conditions with respect to time affects the terms of the saltation matrix, which is strongly related to the stability of the system. It can be expressed as follows:

$$\frac{\partial h}{\partial t} = K_p V_{ref} a_m \omega \cos(\omega \mathrm{t}) = \frac{2\pi K_p V_{ref} a_m}{T_s} \cos(2\pi d) \qquad (7.4)$$

According to equation 7.4, the derivative is dependent on the duty cycle d and the amplitude of the sinewave a_m. A diagram of peak current control with sinewave

compensation at different duty cycles is shown in Figure 7.9. It can be seen that the values of $\partial h / \partial t$ are less than 0 when the duty cycle is in the range of 0.25 to 0.75. Compared to the original system without compensation, stability is improved under this operational condition according to the calculation of eigenvalues. How the slope compensation affects the stability of system is illustrated in Figure 7.10. It shows the movement track of the corresponding eigenvalues with slope compensation. The locus of eigenvalues will move towards the core of the unit circle when the values of $\partial h / \partial t$ are negative, which results in a wider stable operational range. Similarly, system stability will decrease when d is less than 0.25 or larger than 0.75. Since values of $\partial h / \partial t$ are bigger than 0 and this results in the movement of eigenvalues towards -1 along the negative axis, as shown in Figure 7.10. For the given value of slope, when the duty cycle equals 0.5, this provides the best compensation effect in improving the system stability.
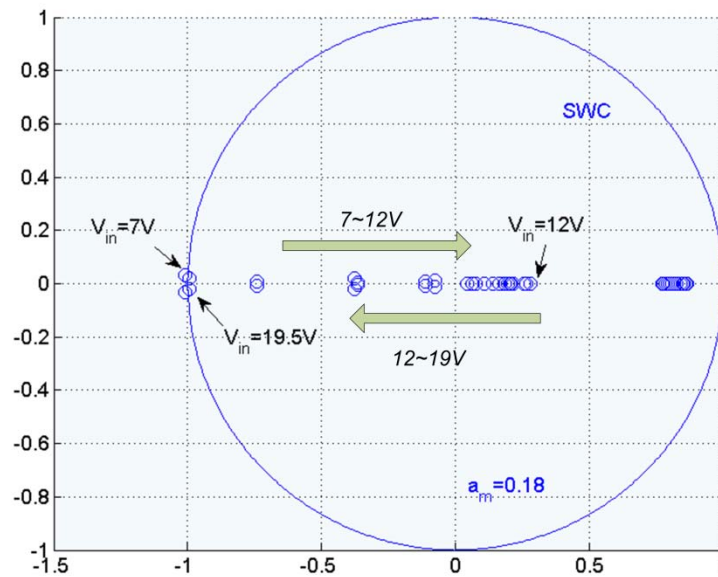
Figure 7.11 Locus of eigenvalues using sinewave slope compensation (a_m = 0.18)

A bifurcation diagram of voltage and current under peak current control with sinewave compensation (SWC) is illustrated in Figure 7.12. The value of a_m is set from 0.05 to 0.20 with steps of 0.05, and the bifurcation points are varied from 9.5V to 7.0V input accordingly. It can be noted that the curve of a_m equals 0.20 is different from all of the other curves. At a_m=0.20 another bifurcation occurs when the input voltage is increased above 18V. Because the duty cycle becomes less than 0.25, the larger amplitude leads to a negative compensation effect, which decreases the

stability of the original system. The locus of eigenvalues using SWC control (a_m =0.18) is shown in Figure 7.11, which is calculated and generated in Matlab. In this figure, the movement of the eigenvalues is indicated by arrows, and it shows that the system will exhibit bifurcations when input voltage is less than 7V or bigger than 19.5V. This result is very close to the experimental outcome when m_a equals 0.2. Therefore, the Monodromy matrix-based analysis method provides knowledge of how the duty cycle relates to system stability with sinewave compensation.

(a)

(b)
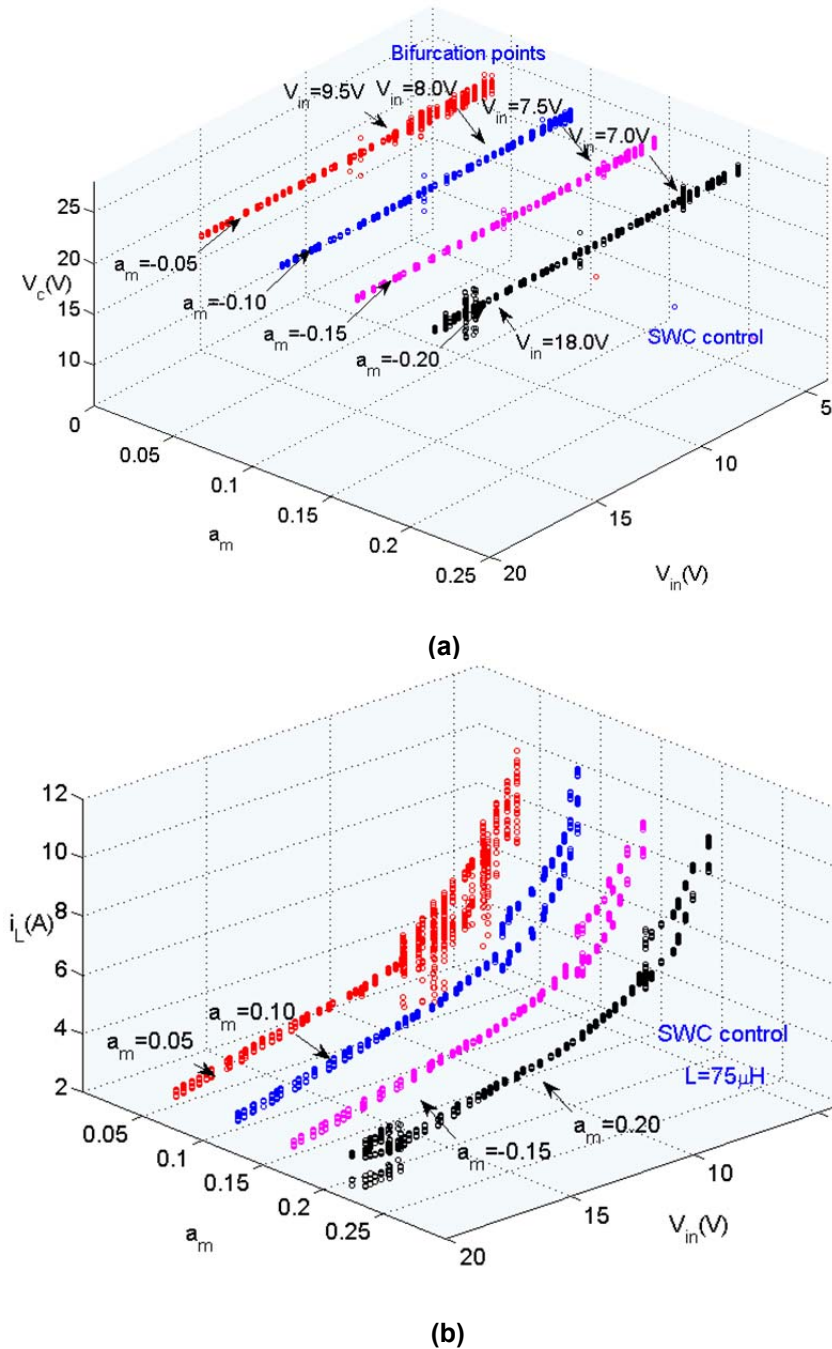
Figure 7.12 Bifurcation diagram of inductor current and output voltage at different input voltages and a_m when employing sinewave compensation (L=75μH): (a) output voltage; (b) inductor current

Figure 7.13 presents the operational waveforms of the converter under peak current control with sinewave compensation when a_m equals 0.2. The converter is operating in stable period-1 when the input voltage is set at 8.5 volts, which can be seen in Figure 7.13(a); Figure 7.13(b) and (c) show the converter in the operation of period-2 when the input voltages equal 7.5V and 18V respectively. Similarly, the amplitude of the sinewave can be set cycle-by-cycle to achieve an advanced control algorithm based on the Monodromy matrix as illustrated in Figure 7.14 . Besides, a method of varying-phase sinusoid injections is presented in Appendix 4, in which the appropriate phase of the sinusoid can be chosen in each clock cycle, to make the zero crossing coincide with the nominal steady-state switching instant.
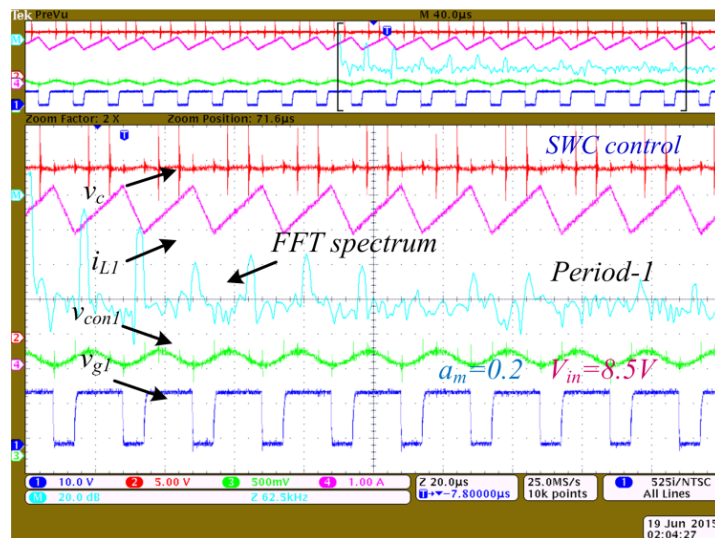
(a)
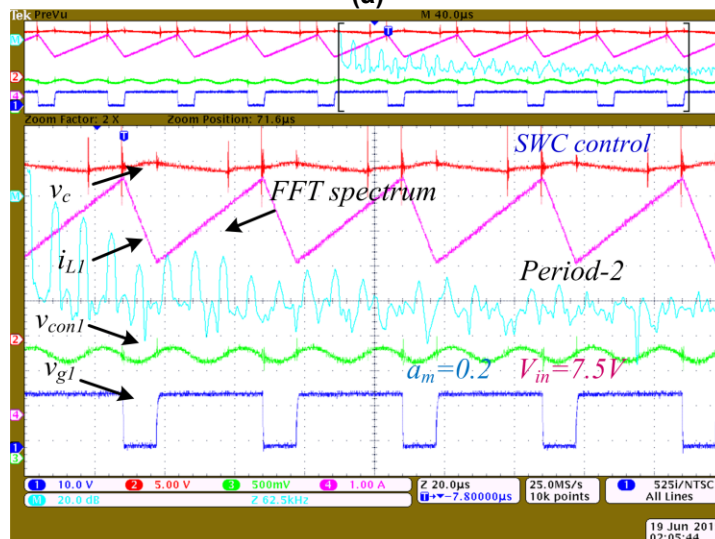
(b)
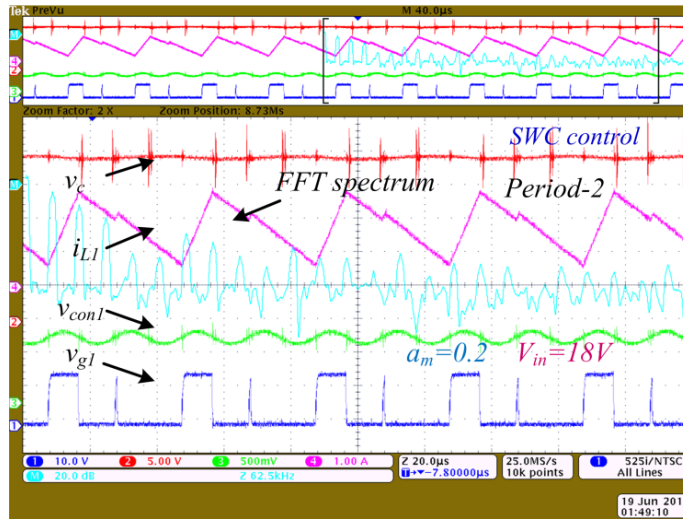
(c)

Figure 7.13 Key operational waveforms at different input voltages by using SWC control: (a) V_{in}=8.5V; (b) V_{in}=7.5V; (c) V_{in}=18V
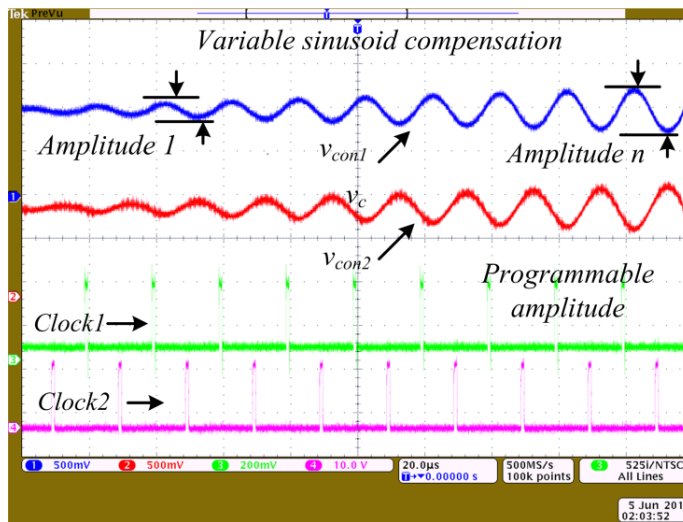
Figure 7.14 Variable amplitude of sinewave compensation

7.5   Improved quadratic curve slope compensation (QCSC) control
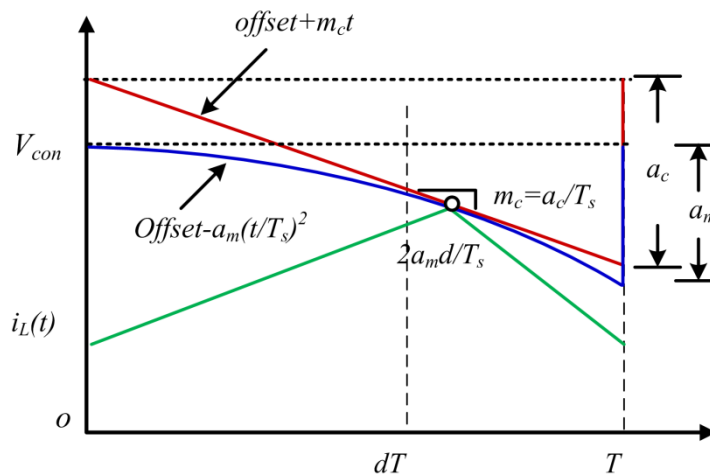
Figure 7.15 Proposed improved quadratic curve slope compensation

As discussed in the previous section, the bigger the amplitude of m_c in conventional

slope compensation, the better is the effect on improving the stability of the DC-DC converter. This is particularly true for cases of high voltage conversion ratios (which also means high duty cycles) where a bigger amplitude of m_c is required. However, the amplitude of m_c has its limitations. Specifically, the bigger amplitude of compensation slope m_c can degrade the dynamical response and the average output current will be limited due to the reduced current reference input which is driven by slope compensation [99]. As shown in Figure 7.15, for conventional slope compensation, if the amplitude of m_c is high enough, the values of peak current will be restrained far away from the offset value, which is illustrated as the waveform coloured in red. This offset value is determined by the output of the PI controller and its maximum value is limited by the waveform generator. To overcome this problem a new improved quadratic curve slope compensator (QCSC) is proposed in this section. The compensation slope is not a constant ramp but is constructed as a quadratic curve with regards with time t coloured in blue.

Employing this new compensation method, the switching condition and the derivative of switching conditions with respect to time becomes:

$$h(\mathrm{x},\mathrm{t}) = K_p (V_{ref} 1 - K_{vc} V_c) - a_m (\mathrm{t}/T_s)^2 - K_{iL} i_L \qquad (7.5)$$

$$\frac{\partial h}{\partial t} = -2 a_m t / T_s^2 = -2 a_m d / T_s \qquad (7.6)$$

The term $\partial h / \partial t$ becomes the expression that relates to the duty cycle d and amplitude a_m, which is different from the expression that only relates to the amplitude of slope m_c in conventional slope compensation. When the duty cycle is less than 0.5, only a small slope or even no compensation is required to guarantee the system's stability; but compensation is required for any duty cycle value over 0.5. Compared to conventional slope compensation, this can provide the same compensation effect when the following equation is applied:

$$-2 a_m d / T_s = -a_c / T_s \qquad (7.7)$$

It turns out that when the duty cycle is bigger than 0.5, the required a_m is less than a_c, and it is approaching half of a_c with increasing values of duty cycle. For instance, when the duty cycle is 0.75 and the calculated value of a_c equals 0.15, the required a_m is obtained as 0.1 according to equation 7.7. The comparison of QCSC method and conventional slope compensation is shown in Figure 7.16, which demonstrates that the system loses stability from period-1 to period-2 when the control algorithm is

switched from the QCSC method to conventional slope compensation. In addition, it is evident that the amplitude required (a_m=0.1) is nearly 33% less than conventional method in this case (a_c=0.15 is required for period-1 operation).
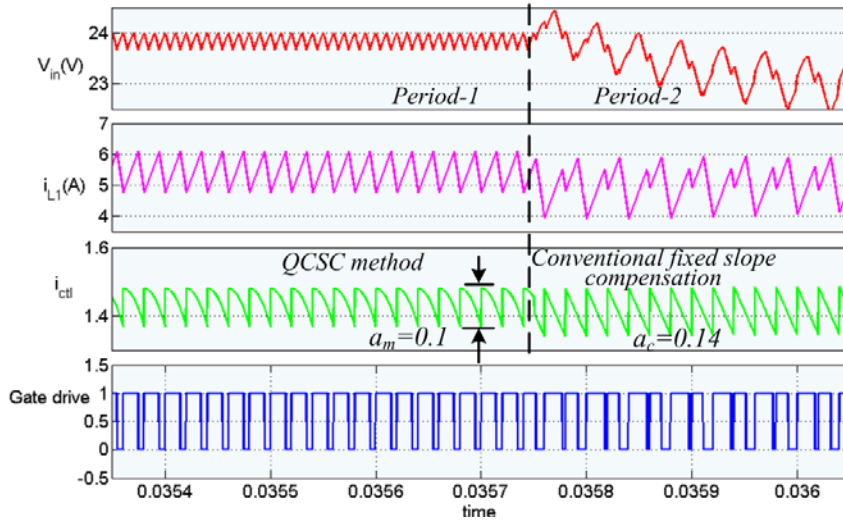
Figure 7.16 Comparison of QCSC method and conventional slope compensation

Figure 7.17 demonstrates the compensation effect of the proposed method. When the value of a_m is set at 0.15, the bifurcation point occurs at input voltage equalling 6V. This gives similar compensation results as conventional slope compensation with an a_c equals 0.25 as shown in Figure 7.3. When a_m is set at 0.20, the converter becomes stable over the whole input range from 6 to 18V. Figure 7.19 shows the operational waveforms when the input voltage equals 6V, 12V and 18V respectively. The figure proves that smaller slope amplitudes are required to yield better effects on compensation. This is the achievement of the new proposed control method.

(a)

(b)
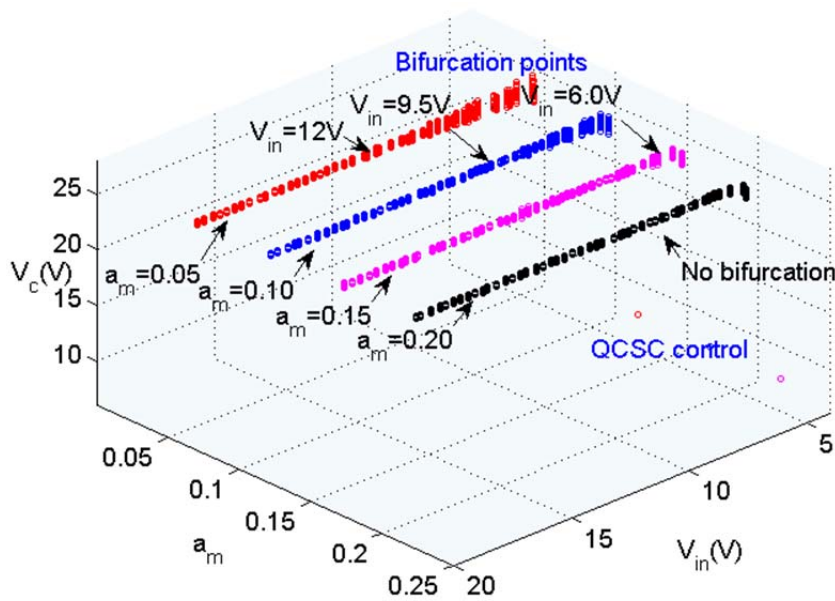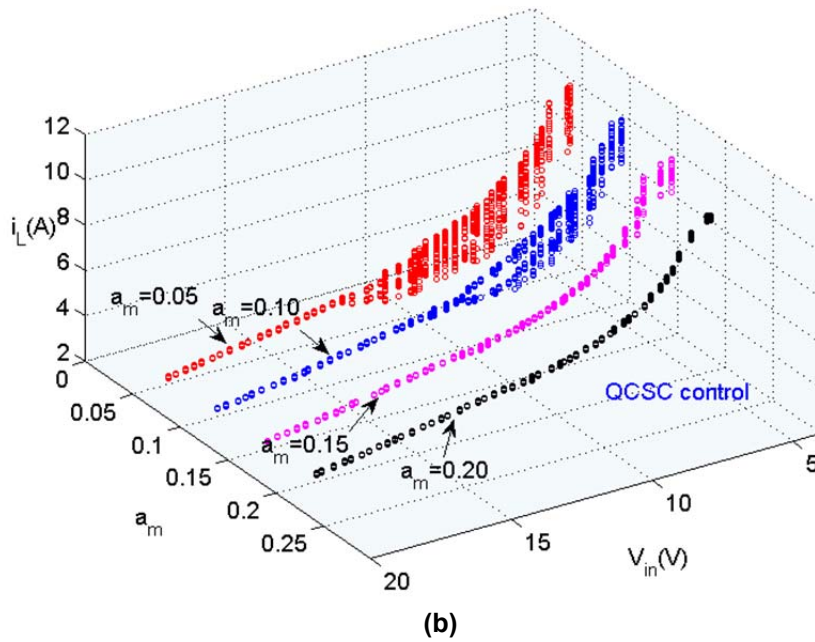
Figure 7.17 Bifurcation diagram of inductor current and output voltage at different input voltages and m$_c$ when employing QCSC control (L=75μH): (a) output voltage; (b) inductor current
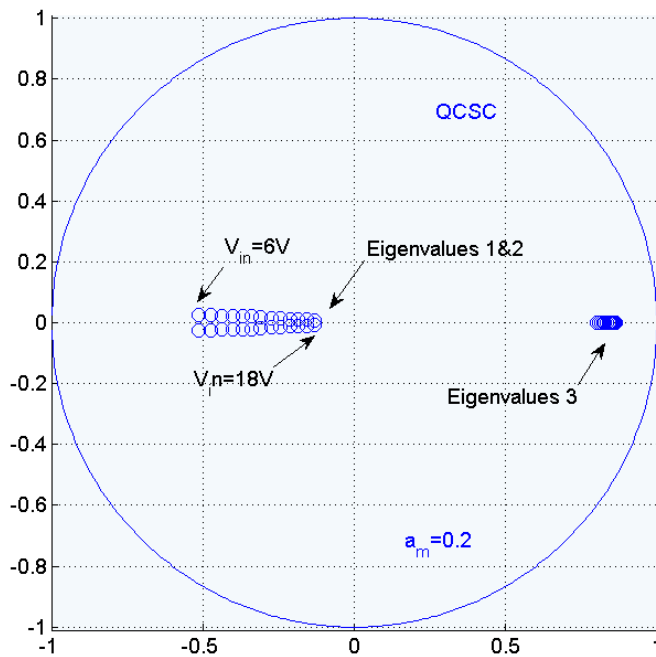
Figure 7.18 Locus of eigenvalues using QCSC control (a$_m$ = 0.2)

Figure 7.18 shows the locus of eigenvalues using QCSC control when am equals 0.2, and the margin of stable operation for the input conditions given can be indicated by this diagram.
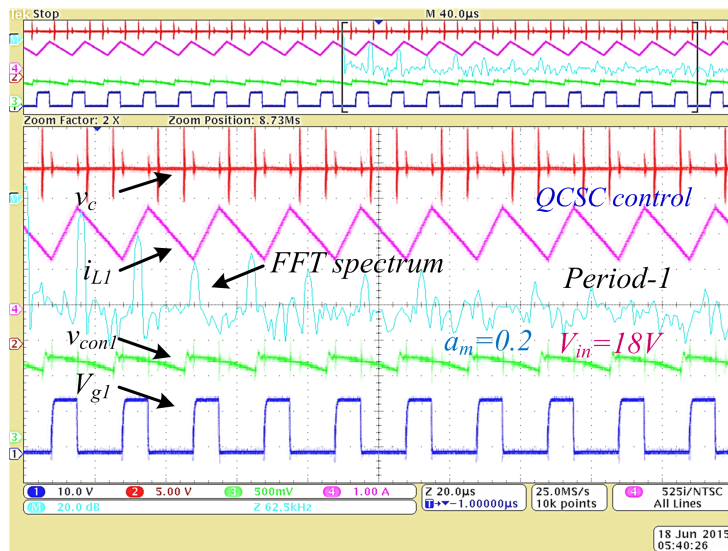
(a)
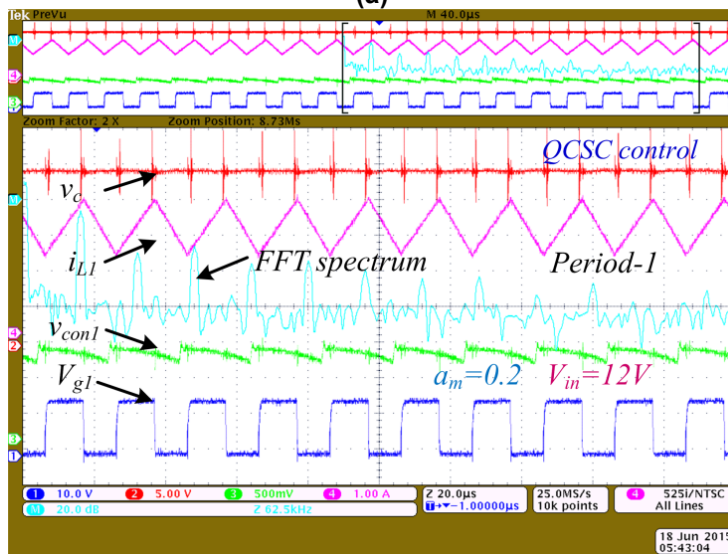
(b)
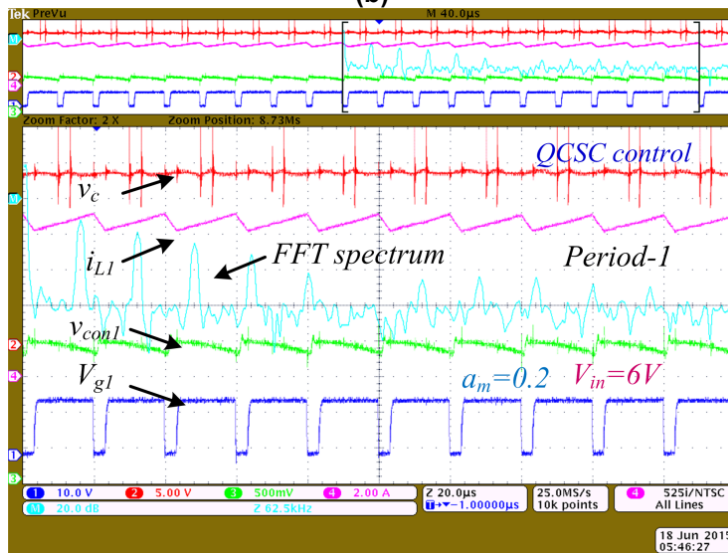
(c)

Figure 7.19 Key operational waveforms at different input voltages by using QCSC control:

(a) V_{in}=18V; (b) V_{in}=12V; (c) V_{in}=6V

130

7.6   Application for reduced inductance

The aforementioned practical work demonstrates the analysis and control of nonlinear behaviour for interleaved boost converters by applying the Monodromy matrix. This section focuses on the application of the Monodromy matrix in order to reduce the size of the converters.

Energy crises and low-carbon environmental requirements are leading more countries to invest a great deal of research funding in the development of the next generation of low-carbon vehicles. Therefore, the Hybrid Electric Vehicle (HEV) and Electric Vehicle (EV) have attracted the worldwide attention to the use of environmentally-friendly cars which are seen as clean. However, delivering the technology required to decarbonize road transport is a global challenge, and there are some key barriers to bringing EVs to the mass market. Two key issues are cost and power density.

Power electronics technologies play a significant role in the development of EVs. Many on-board converter systems, which are utilized as the interface among energy source storage elements and the traction machine, use a complicated, heavy, expensive and non-optimized solution. However, without in-depth knowledge, there is no appropriate way to further optimize and upgrade power electronics systems. To solve these issues and achieve compact, integrated and high-efficiency power conversion, more constructive basic research needs to be carried out. One of the challenges is to investigate appropriate approaches to reducing the size of DC-DC converters without increasing frequency.
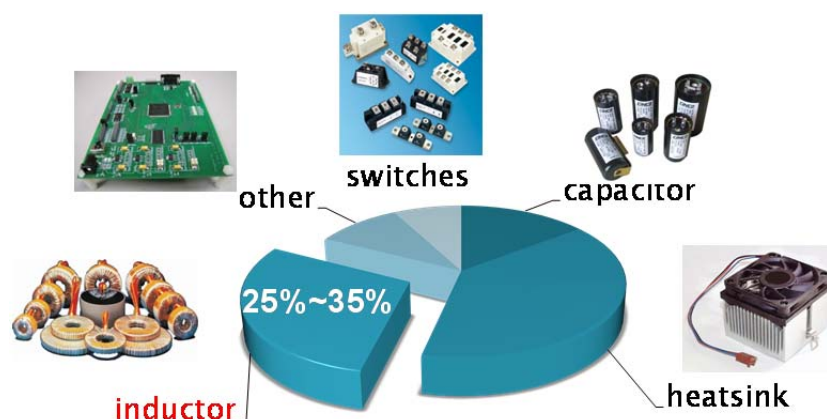
Figure 7.20 Volume distribution of typical non-isolated dc-dc converters

Normally, passive components such as inductors, transformers, and input and output filters represent 30%~40% of the mass of a power converter. Figure 7.20 shows the volume distribution of a typical non-isolated DC-DC converter. This shows that the inductor accounts for 25%~35% of the whole converter mass. Therefore, reducing the size of inductors is of great significance to achieve higher power density. Some feasible methods exist to address this issue, as shown in Figure 7.21. The most common way in reducing the size of the converter is by increasing the switching frequency, which is always inversely proportional to the required inductance. However, the switching and iron losses rise dramatically with increasing frequency. Meanwhile, faster active components, and advanced magnetic materials and control methods should be developed to satisfy the requirement of high frequency applications.

Without increasing frequency, there are still many possible approaches to reduce the size of magnetic components, and these can be classified into four categories using: state of the art materials; interleaved configuration; flexible inductor techniques; and improved control strategies, (see Figure 7.21). Different techniques can be applied in different types of converters, depending on the requirements of specific applications, and some techniques can also be adopted individually or in combination to achieve desired results.
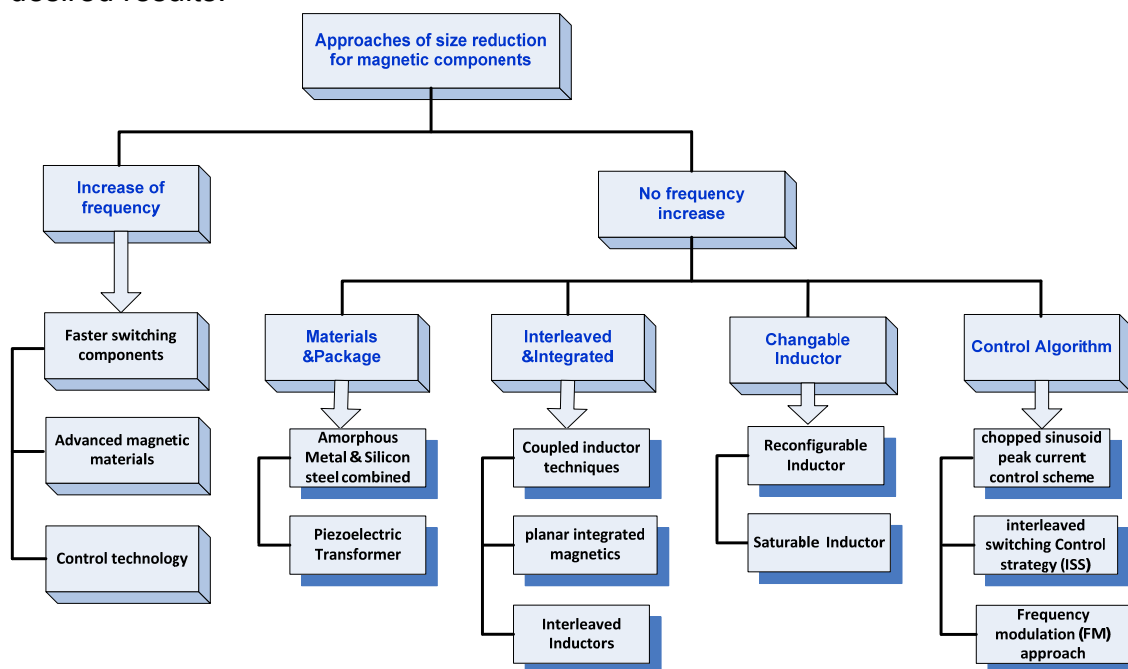
Figure 7.21 Present feasible methods to reduce the size of magnetic components

Nevertheless, most of the approaches are confined to a particular application. For instance: the new amorphous metal and silicon steel material is only used in low-

medium frequency converters [153]; integrated techniques can be applied only in low power application [154]; additional components are required to implement reconfiguration, which increases the complexity and adds extra losses [155, 156]; some techniques can only be utilized in particular converters [157, 158]. Therefore, in order to reduce the size of converters, one of the best solutions is to find a general control method applicable to a variety of converters without increasing frequency and circuit complexity. This thesis develops a control method that is addressing fast-scale instability phenomena, and the derived Mondomoy matrix contains comprehensive information about system parameters. Thus it has the potential to be used for stability analysis and advanced control of DC-DC converters applying reduced inductor values.
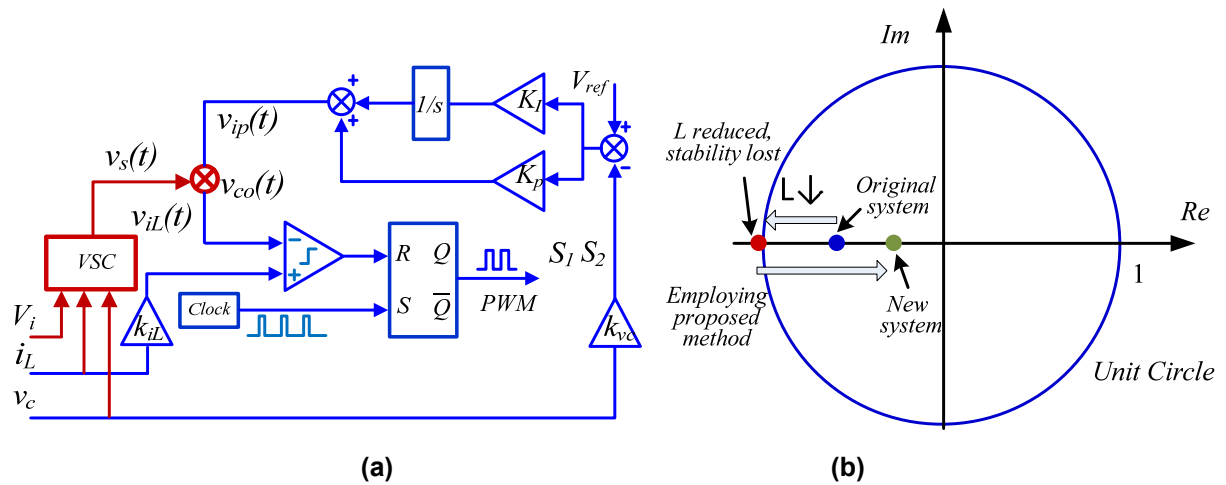
Figure 7.22 (a) Diagram of the proposed control method; (b) Locus of eigenvalues using the proposed method

The basic concept in employing the proposed method is illustrated in Figure 7.22. By using the conventional averaging method, the influence of a reduced inductor on fast-scale stability cannot be analysed, and the given system will lose stability to some extent when inductance is reduced. The most common solution to this is to utilize a bigger choke with higher inductance to guarantee stability, at the expense of cost and weight. In contrast, the proposed method takes information about the switching instant into account; and the impact of reduced inductance can be compensated for by manipulating the derived Saltation matrix S. Specifically, the original system will lose stability with the reduced inductance L, and the eigenvalue of Monodromy matrix moves outside of unit circle as shown in Figure 7.22(b). In order to regain system to be stable at the condition of inductance reduced, the compensation in the controller is implemented using the proposed method as illustrated in Figure 7.22(a). Information of input voltage, output voltage and inductor current are fed into the

133

advanced controller to generate the control signal and the terms of Monodromy matrix are affected accordingly. As a result, the corresponding eigenvalues are relocated within the unit circle, which means the new system remains stable using the proposed controller.
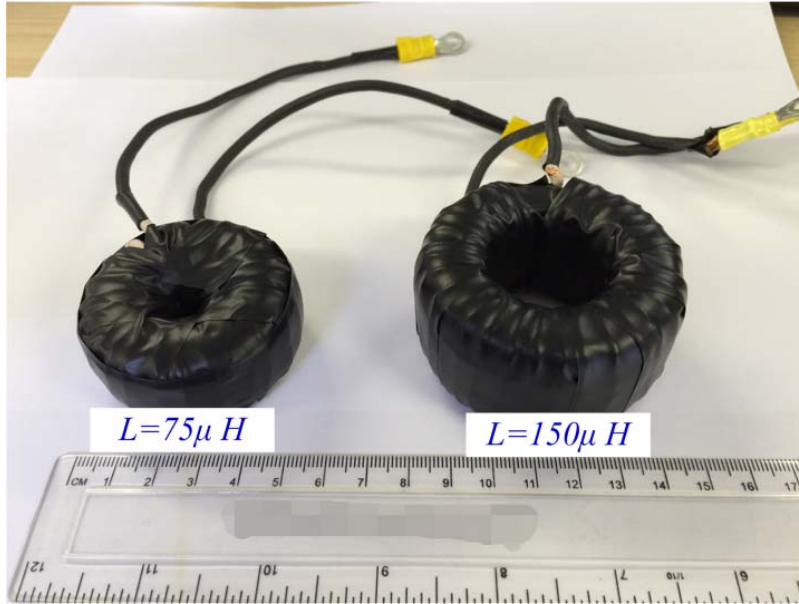
Figure 7.23 Comparison of two different inductors (75µH&150µH)

In order to study the influence of reduced inductance on the system's stability, two inductors with different inductances were designed for testing in experiments, as shown in Figure 7.23. Using a 150µH inductor, the bifurcation diagram of output voltage and inductor current at different slopes are presented in Figure 7.24 (a) and (b) separately.

(a)

(b)
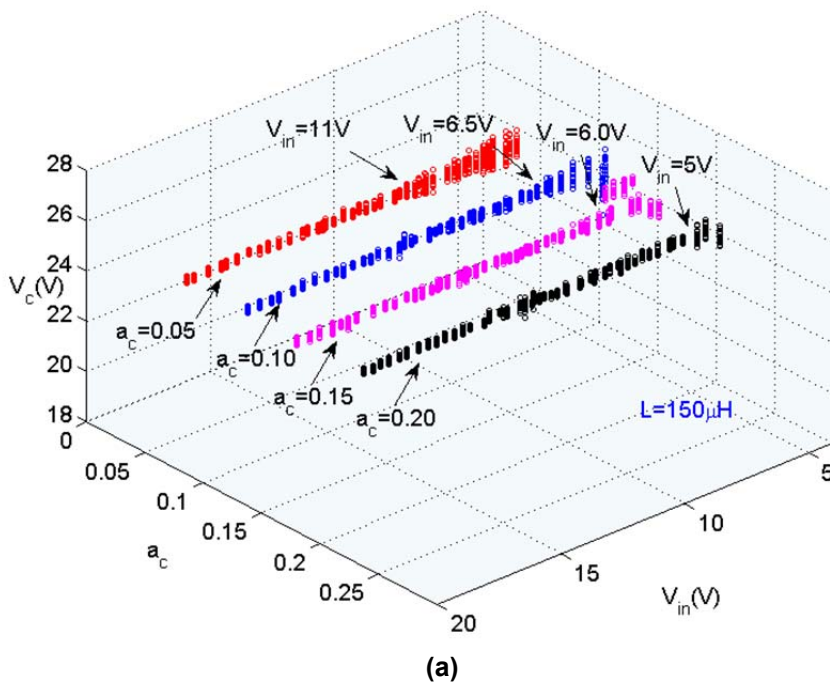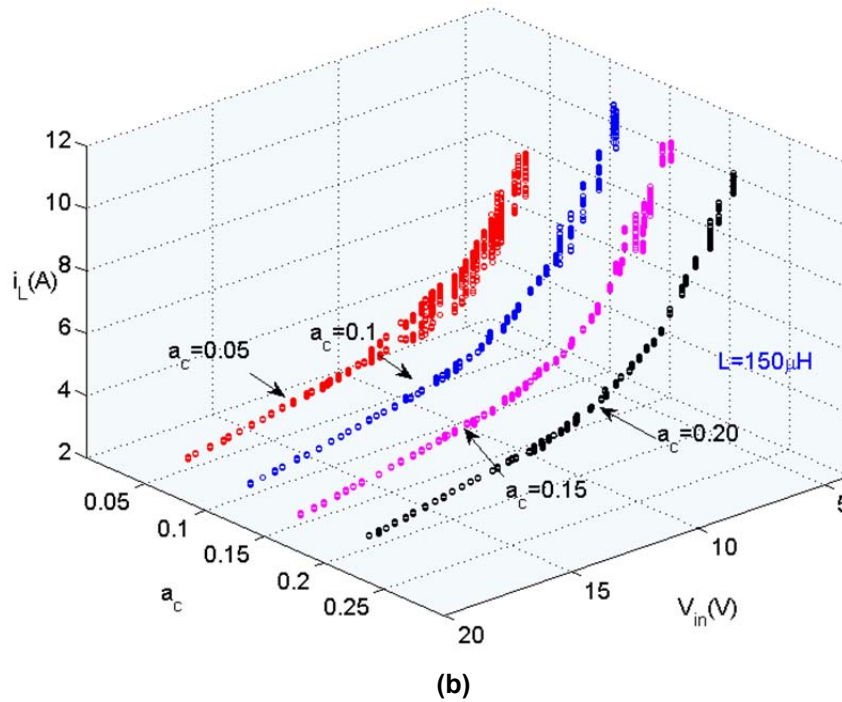
Figure 7.24 Bifurcation diagram of inductor current and output voltage at different input voltages: (a) output voltage; (b) inductor current
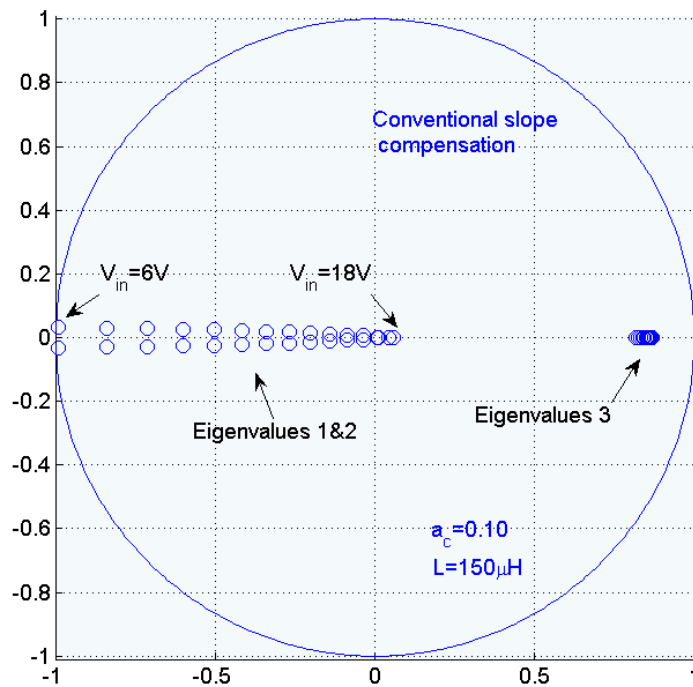
Figure 7.25 Locus of eigenvalues using conventional slope compensation (a_c=0.1,L=150 µH)

Compared to the results when employing 75µH inductors in section 7.2, it can be seen that the bifurcations points have changed significantly. For instance, when the amplitude a_c is 0.10, the bifurcation point is changed to 6.5V input from the 10.5V input when inductance equals 75µH. This indicates that the stable operational range

has been extended with the increase in inductance. The corresponding locus of eigenvalues using 150 µH inductor is calculated and generated in the Matlab as shown in Figure 7.25, which shows a good agreement between experimental and theoretical analysis.

Figure 7.26 presents the operational waveforms of the converter when input voltage equals 6V. If the original system is designed to use a 150µH inductor with a fixed a_c equals 0.15, the system is in stable operation of period-1 as shown in Figure 7.26(a). When the inductance is reduced to 75µH at the same given operational conditions, the system will lose stability as illustrated in Figure 7.26(b). In order to regain stable operation, the amplitude of ramp can be changed to 0.25 as shown in Figure 7.26(c).
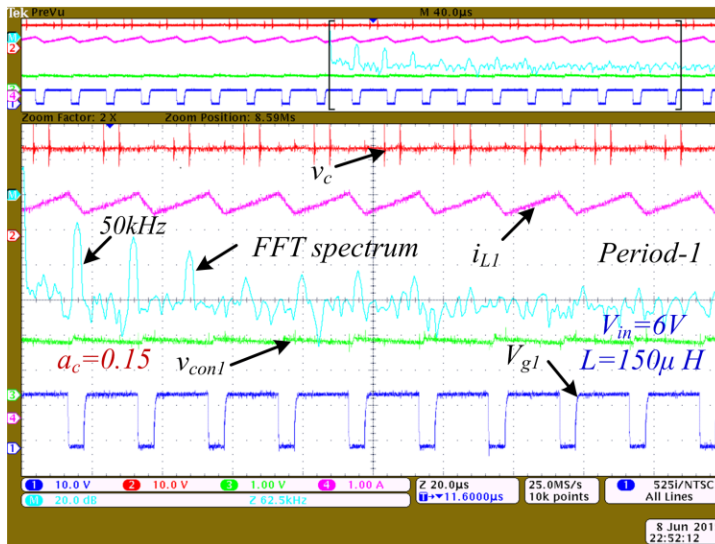
(a)
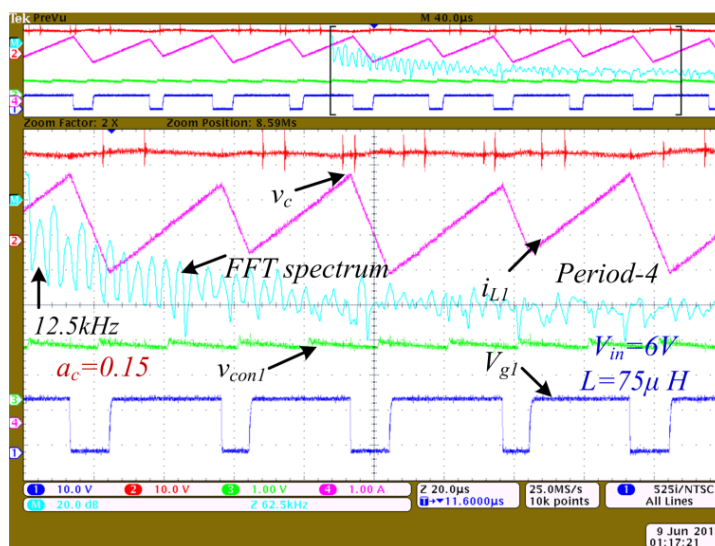
(b)
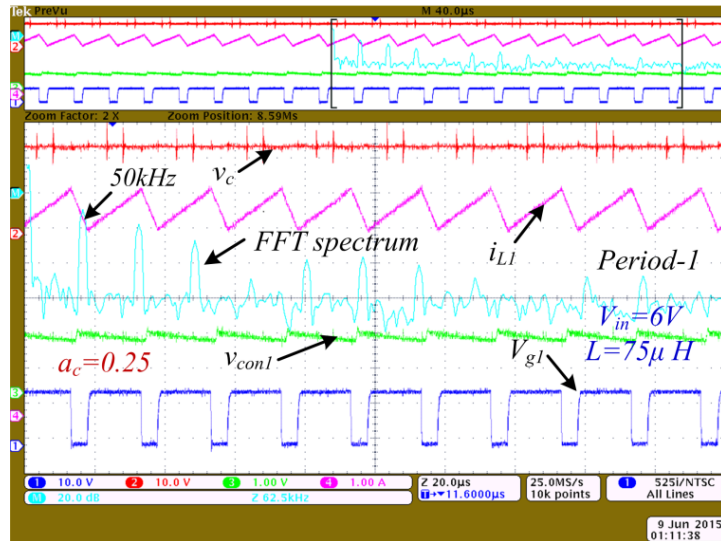
(c)

Figure 7.26 Key operational waveforms of the converter using different inductors at the same input voltage: (a) a_c=0.15, L=150µH; (b) a_c=0.15, L=75µH; (c) a_c=0.25, L=75µH

It is clear that the system remains in stable operation despite reduced inductance, when the compensating parameter is changed. The specific compensating value of m_c can be calculated using information from the Monodromy matrix. Therefore, the experimental results verify the concept of reducing the size of converters by using developed control methodology without increasing frequency.

7.7 Summary

In order to control the nonlinear behaviour of DC-DC converters, several control algorithms for current mode control in digital implementations are proposed and developed using the knowledge of the Monodromy matrix. In addition, a deeper understanding in the behaviour of the system, such as how system's stable operation is lost, can be gained by employing the adopted nonlinear analysis method, and it also provides a new perspective on control laws of designing the appropriate controllers to address the nonlinearities in DC-DC converters. This chapter introduced two new control laws: variable slope compensation and quadratic curve slope compensation. Finally, a successful application of a boost converter operating at reduced inductances has been demonstrated in this chapter.

8 Conclusion and future work

8.1 Conclusion

In this thesis, a nonlinear analytic methodology based on the Monodromy matrix has been employed for the stability analysis and control of DC-DC converters. This derived matrix contains all the circuit parameters and control coefficients, and this enables system performance with different input and output parameter to be evaluated. Specific derivations of the Monodromy matrix have been presented in the thesis. In addition, based on the knowledge gained from the Monodromy matrix, new advanced control techniques have been proposed and developed to improve the stability performance of DC-DC converters. The new proposed schemes allow DC-DC converters to operate at extended input voltage ranges, and the techniques proposed here can be applied to other switching converters such as interleaved or multiphase converters. Moreover, the proposed control algorithm has been implemented in a mixed-signal digital controller to maximise the impact of the control parameters. This approach has not been previously reported. Finally, the Monodromy matrix was also applied to help with the reduction of the inductor size of DC-DC converters. Simulation and experimental results have validated the theoretical analysis and the effectiveness of the methods developed.

The periodic solution for bidirectional DC-DC boost converters with current mode control is presented analytically and validated numerically. Parasitic elements such as resistance of the inductor and capacitor are considered in the derivation of the Monodromy matrix, which is proven to affect the fast-scale stability of converters to some extent at the given operation conditions. Quantitative analysis of this influence was carried out numerically using the derived matrix.

The adopted analytical method is then applied to the boost converter with constant power loads (CPL). Characteristic of CPL is transformed to constant current using approximation method in the analysis and the stability of system is fully unfolded analytically and numerically in the examples of boost converters employing CCM and DCM operation modes. The results show that the system is relatively more stable during DCM than in CCM operation from the perspective of fast-scale stability. In

addition, cascading with outer voltage loop, the comparison of inner peak current mode control and averaged current control is presented using the locus of eigenvalues. The results prove that the system is less prone to the fast-scale instability under the averaged current control algorithm compared to peak current control.

The thesis also shows for the first time that the nonlinear analysis of interleaved boost converters demonstrates that the Monodromy matrix-based method can be successfully applied in higher order switching converters with interleaved operation. The switching events are treated independently and the interaction effect of interleaving on the stability of the system is introduced into the procedure of matrices derivation. The theoretical analysis is verified by the simulation results, and the numerical results of the interleaved boost converter are validated by experimental outcomes from the prototype, which is controlled by the proposed mixed signal controller. The new implementation of the digital controller does not only exhibit flexibility in implementing various control algorithms quickly, but also retains the inherent characteristics of real-time cycle-by-cycle current limiting experienced using analogue comparators. It works effectively to capture the variety of nonlinear phenomena exhibited by the interleaved converter.

Based on the information in the derived Monodromy matrix, several control algorithms for current mode control in digital implementations are proposed and developed to enhance system performance. It has been shown that the adopted nonlinear analysis method can not only provide valuable insights into the behaviour of the system, including revealing how its stable operation is lost, but also a new perspective is developed on the design of control laws to cope with nonlinear behaviour in DC-DC converters. Two new control laws were developed: variable slope compensation and quadratic curve slope compensation. The thesis ends with a study of reduced inductances in boost converters using the analytical work developed which have a wide practical application.

8.2 Future work

Based on the work presented in this thesis, some potential further research areas can be suggested as follows. The methods described here can be applied to the nonlinear analysis of other types of non-isolated or isolated converters with higher

order. For example, how to develop the Monodromy matrix including the nonlinearities of transformers. In addition, based on the new control laws established how many other control techniques can be generated with the proposed methods? For example, the relationship between switching conditions and different control algorithms, and corresponding changes in the Monodromy matrix can be studied. In terms of the practical implementation at the test bench, the existing platform can be enhanced in order to achieve more functions and to make it universal for the testing other types of converters at different power ratings. Finally, the visualization of the stability of systems with comprehensive information about all the system parameters and external conditions can be developed to aid product design.

References

[1]   C. K. Tse, *Complex behavior of switching power converters*: CRC press, 2003.

[2]   Brockeet.R.W. and W. J.R., "Understanding power converter chaotic behaviour mechanisms in protective and abnormal modes," in *POWERCON'11, Eleventh Annual International Power Electronics Conference*, 1984, pp. E-4 1 to 15.

[3]   D. C. Hamill and D. J. Jeffries, "Subharmonics and chaos in a controlled switched-mode power converter," *Circuits and Systems, IEEE Transactions on,* vol. 35, pp. 1059-1061, 1988.

[4]   D. C. Hamill, J. H. B. Deane, and D. J. Jefferies, "Modeling of chaotic DC-DC converters by iterated nonlinear mappings," *Power Electronics, IEEE Transactions on,* vol. 7, pp. 25-36, 1992.

[5]   P. Krein and R. Bass, "Types of instability encountered in simple power electronic circuits: unboundedness, chattering, and chaos," in *Applied Power Electronics Conference and Exposition, 1990. APEC '90, Conference Proceedings 1990., Fifth Annual*, 1990, pp. 191-194.

[6]   J. H. B. Deane, "Chaos in a Current-Mode Controlled Boost Dc-Dc Converter," *Ieee Transactions on Circuits and Systems I-Fundamental Theory and Applications,* vol. 39, pp. 680-683, Aug 1992.

[7]   V. S. Baushev, Z. T. Zhusubaliev, Y. V. Kolokolov, and I. V. Terekhin, "Local Stability of Periodic-Solutions in Sampled-Data Control-Systems," *Automation and Remote Control,* vol. 53, pp. 865-871, Jun 1992.

[8]   C. K. Tse, "Flip bifurcation and chaos in three-state boost switching regulators," *Circuits and Systems I: Fundamental Theory and Applications, IEEE Transactions on,* vol. 41, pp. 16-23, 1994.

[9]   E. Fossas and G. Olivar, "Study of chaos in the buck converter," *Circuits and Systems I: Fundamental Theory and Applications, IEEE Transactions on,* vol. 43, pp. 13-25, 1996.

[10]   S. Banerjee, "Coexisting attractors, chaotic saddles, and fractal basins in a power electronic circuit," *Circuits and Systems I: Fundamental Theory and Applications, IEEE Transactions on,* vol. 44, pp. 847-849, 1997.

[11]   M. diBernardo, F. Garofalo, L. Glielmo, and F. Vasca, "Analysis of chaotic buck, boost and buck-boost converters through switching maps," *Pesc'97: 28th Annual IEEE Power Electronics Specialists Conference - Record, Vols I and Ii,* pp. 754-760, 1997.

[12]   M. di Bernardo, F. Garofalo, L. Glielmo, and F. Vasca, "Switchings, bifurcations, and chaos in DC/DC converters," *IEEE Transactions on Circuits and Systems I-Regular Papers,* vol. 45, pp. 133-141, Feb 1998.

[13]   Y. Guohui, S. Banerjee, E. Ott, and J. A. Yorke, "Border-collision bifurcations in the buck converter," *Circuits and Systems I: Fundamental Theory and Applications, IEEE Transactions on,* vol. 45, pp. 707-716, 1998.

[14]   N. Zhu and W. L. Wu, "Two-parameter chaotic control in the voltage controlled buck converter," *Peds 2003 : Fifth International Conference on Power Electronics and Drive Systems, Vols 1 and 2, Proceedings,* 2003, pp. 1329-1333.

[15]   W. G. Lu, L. W. Zhou, and Q. M. Luo, "Notch filter feedback controlled chaos in buck converter," *Chinese Physics,* vol. 16, pp. 3256-3261, Nov 2007.

[16]   A. El Aroudi, L. Benadero, E. Toribio, and G. Olivar, "Hopf bifurcation and chaos from torus breakdown in a PWM voltage-controlled DC-DC boost converter," *IEEE Transactions on Circuits and Systems I-Regular Papers,* vol. 46, pp. 1374-1382, Nov 1999.

[17]   S. K. Mazumder, A. H. Nayfeh, and D. Boroyevich, "An investigation into the fast- and slow-scale instabilities of a single phase bidirectional boost converter," *IEEE*

Transactions on Power Electronics, vol. 18, pp. 1063-1069, Jul 2003.

[18] D. Giaouris, S. Banerjee, O. Imrayed, K. Mandal, B. Zahawi, and V. Pickert, "Complex Interaction Between Tori and Onset of Three-Frequency Quasi-Periodicity in a Current Mode Controlled Boost Converter," *IEEE Transactions on Circuits and Systems I-Regular Papers,* vol. 59, pp. 207-214, Jan 2012.

[19] L. Q. Wang and X. Y. Wei, "Computation of Lyapunov exponents for a current-programmed buck-boost converter," *Iwads: 2nd International Workshop on Autonomous Decentralized System, Proceedings,* 2002, pp. 273-276.

[20] C. D. Xu, K. W. E. Cheng, H. Zhang, X. K. Ma, and K. Ding, "Study of Intermittent Bifurcations and Chaos in Buck-Boost Converters with Input regulators," in *Power Electronics Systems and Applications, 2006. ICPESA '06. 2nd International Conference on*, 2006, pp. 268-272.

[21] W. Hen-Kung, C. Po-Lun, H. Fei-Hu, and H. Hsiang-Yan, "Nonlinear phenomenon in a current-mode controlled buck-boost converter with solar cell input via varying reference current," in *Machine Learning and Cybernetics (ICMLC), 2014 International Conference on*, 2014,pp. 632-637.

[22] W. Siu Chung, W. Xiaoqun, and C. K. Tse, "Sustained Slow-Scale Oscillation in Higher Order Current-Mode Controlled Converter," *Circuits and Systems II: Express Briefs, IEEE Transactions on,* vol. 55, pp. 489-493, 2008.

[23] X. Fan, Z. Bo, Q. Dongyuan, Y. Ru, and H. H. C. Iu, "Complex bifurcation and torus breakdown in higher order converters with an inductive impedance load," in *Industrial Electronics Society, IECON 2013 - 39th Annual Conference of the IEEE*, pp. 8362-8366, 2013.

[24] P. Deivasundari, G. Uma, and S. Ashita, "Chaotic dynamics of a zero average dynamics controlled DC-DC Cuk converter," *Power Electronics, IET,* vol. 7, pp. 289-298, 2014.

[25] H. Fei-Hu, W. Hen-Kung, C. Po-Lun, S. Ming-Hong, and Y. Ying-Kuei, "Study of nonlinear phenomena and chaotic control in current-programmed forward converters," in *Industrial Technology, 2009. ICIT 2009. IEEE International Conference on*, pp. 1-6. 2009.

[26] L. Premalatha and G. M. Sneha, "Experimental analysis of power density spectrums in a forward converter with nonlinear dynamics," in *Advances in Engineering, Science and Management (ICAESM), 2012 International Conference on*, 2012,pp. 553-557.

[27] H. H. C. Iu, C. K. Tse, V. Pjevalica, and Y. M. Lai, "Analysis of Hopf bifurcation in parallel-connected boost converters via averaged models," *2002 Ieee International Symposium on Circuits and Systems, Vol V, Proceedings,* pp. 305-308, 2002.

[28] H. H. C. Lu and C. K. Tse, "Study of low-frequency bifurcation phenomena of a parallel-connected boost converter system via simple averaged models," *IEEE Transactions on Circuits and Systems I-Fundamental Theory and Applications,* vol. 50, pp. 679-686, May 2003.

[29] A. Natsheh, "Chaotic behaviour in parallel-connected DC-DC buck-boost converters," in *Ecological Vehicles and Renewable Energies (EVER), 2014 Ninth International Conference on*, 2014,pp. 1-5.

[30] D. Giaouris, S. Banerjee, B. Zahawi, and V. Pickert, "Control of fast scale bifurcations in power-factor correction converters," *IEEE Transactions on Circuits and Systems Ii-Express Briefs,* vol. 54, pp. 805-809, Sep 2007.

[31] A. El Aroudi and M. Orabi, "Control of oscillations in PFC power supplies by Time Delay Feedback," in *Electric Power and Energy Conversion Systems, 2009. EPECS '09. International Conference on*, 2009, pp. 1-8.

[32] C. Weibin, S. Jiuxu, L. Hong, and G. Yingna, "Time-Varying Compensation for Peak

Current-Controlled PFC Boost Converter," *Power Electronics, IEEE Transactions on,* vol. 30, pp. 3431-3437, 2015.

[33]   O. Dranga, B. Buti, and I. Nagy, "Stability analysis of a feedback-controlled resonant DC-DC converter," *IEEE Transactions on Industrial Electronics,* vol. 50, pp. 141-152, Feb 2003.

[34]   K. Manda, S. Banerjee, and C. Chakraborty, "Symmetry-breaking bifurcation in load resonant dc-dc converters," in *Circuits and Systems (ISCAS), 2011 IEEE International Symposium on*, 2011, pp. 1327-1330.

[35]   A. El Aroudi, E. Alarcon, E. Rodriguez, and M. Orabi, "Modeling of switching frequency instabilities in buck-based DC-AC inverters by nonlinear time varying Poincaré; mappings," in *Power System Conference, 2008. MEPCON 2008. 12th International Middle-East*, 2008, pp. 354-359.

[36]   H. Fei-Hu, W. Hen-Kung, C. Po-Lun, and W. Hsuan-Chiang, "Nonlinear Dynamic Behaviors in Voltage-Mode Controlled Single-Phase Half-Bridge Inverters via Varying Input Voltage," in *Pervasive Computing Signal Processing and Applications (PCSPA), 2010 First International Conference on*, 2010, pp. 230-234.

[37]   D. P. Shankar, U. Govindarajan, and K. Karunakaran, "Period-bubbling and mode-locking instabilities in a full-bridge DC-AC buck inverter," *IET Power Electronics,* vol. 6, pp. 1956-1970, Nov 2013.

[38]   I. Daho, D. Giaouris, B. Zahawi, V. Pickert, and S. Banerjee, "Control of Nonlinear Instabilities in a System of Coupled Interleaved Buck Converters," *IEEE Region 10 Colloquium and Third International Conference on Industrial and Information Systems, Vols 1 and 2,* pp. 490-495, 2008.

[39]   H. Wu, V. Pickert, and D. Giaouris, "Nonlinear analysis for interleaved boost converters based on Monodromy matrix," in *Energy Conversion Congress and Exposition (ECCE), 2014 IEEE*, 2014, pp. 2511-2516.

[40]   P. Deivasundari, G. Uma, C. Vincent, and K. Murali, "Non-linear intermittent instabilities and their control in an interleaved DC/DC converter," *Power Electronics, IET,* vol. 7, pp. 1235-1245, 2014.

[41]   P. T. Krein, J. Bentsman, R. M. Bass, and B. C. Lesieutre, "On the Use of Averaging for the Analysis of Power Electronic Systems," *Pesc 89 Record, Vols 1 and 2,* pp. 463-467, 1989.

[42]   C. Jingquan, R. Erickson, and D. Maksimovic, "Averaged switch modeling of boundary conduction mode DC-to-DC converters," in *Industrial Electronics Society, 2001. IECON '01. The 27th Annual Conference of the IEEE*, 2001, pp. 844-849 vol.2.

[43]   B. Lehman and R. M. Bass, "Switching frequency dependent averaged models for PWM DC-DC converters," *Power Electronics, IEEE Transactions on,* vol. 11, pp. 89-98, 1996.

[44]   V. A. Caliskan, G. C. Verghese, and A. M. Stankovic, "Multifrequency averaging of DC/DC converters," *IEEE Transactions on Power Electronics,* vol. 14, pp. 124-133, Jan 1999.

[45]   P. Fei and A. M. Cramer, "Reduced-order multifrequency averaging in naturally sampled PWM converters," in *Energy Conversion Congress and Exposition (ECCE), 2014 IEEE*, 2014, pp. 3010-3015.

[46]   Y. Gao, Y. Wang, J. Huang, M. Li, and X. Yang, "Modeling of single-HB PWM modulated dual active bridge DC-DC converter with multifrequency average approach," in *Energy Conversion Congress and Exposition (ECCE), 2014 IEEE*, 2014, pp. 2588-2593.

[47]   S. R. Sanders, J. M. Noworolski, X. Z. Liu, and G. C. Verghese, "Generalized averaging method for power conversion circuits," *Power Electronics, IEEE*

Transactions on, vol. 6, pp. 251-259, 1991.

[48]   S. Jian and R. M. Bass, "A new approach to averaged modeling of PWM converters with current-mode control," in *Industrial Electronics, Control and Instrumentation, 1997. IECON 97. 23rd International Conference on*, 1997, pp. 599-604 vol.2.

[49]   M. di Bernardo and F. Vasca, "Discrete-time maps for the analysis of bifurcations and chaos in DC/DC converters," *IEEE Transactions on Circuits and Systems I-Regular Papers,* vol. 47, pp. 130-143, Feb 2000.

[50]   Y. Sun, A. P. Hu, X. Dai, and Y. G. Su, "Discrete time mapping modeling and bifurcation phenomenon study of a ZVS converter," *2004 International Conference on Power System Technology - POWERCON, Vols 1 and 2,* 2004, pp. 1015-1018.

[51]   Z. Suto, E. Masada, and I. Nagy, "Discontinuous iterated map model of bifurcation phenomena in DTC drives," in *Electrical Machines and Systems, 2009. ICEMS 2009. International Conference on*, 2009, pp. 1-6.

[52]   S. Almer, U. Jonsson, C. Y. Kao, and J. Mari, "Global stability analysis of DC-DC converters using sampled-data modeling," *Proceedings of the 2004 American Control Conference, Vols 1-6,* 2004, pp. 4549-4554.

[53]   C. C. Fang and E. H. Abed, "Sampled-data modelling and analysis of the power stage of PWM DC-DC converters," *International Journal of Electronics,* vol. 88, pp. 347-369, Mar 2001.

[54]   G. C. Verghese, C. A. Bruzos, and K. N. Mahabir, "Averaged and sampled-data models for current mode control: a re-examination," in *Power Electronics Specialists Conference, 1989. PESC '89 Record., 20th Annual IEEE*, 1989, pp. 484-491 vol.1.

[55]   D. Giaouris, A. Elbkosh, S. Banerjee, B. Zahawi, and V. Pickert, "Control of switching circuits using complete-cycle solution matrices," *2006 IEEE International Conference on Industrial Technology, Vols 1-6,* 2006, pp. 2935-2940.

[56]   D. Giaouris, S. Banerjee, B. Zahawi, and V. Pickert, "Stability Analysis of the Continuous-Conduction-Mode Buck Converter Via Filippov's Method," *Circuits and Systems I: Regular Papers, IEEE Transactions on,* vol. 55, pp. 1084-1096, 2008.

[57]   O. Imrayed, B. Zahawi, D. Giaouris, and V. Pickert, "Reduced Inductance in DC-DC Converter Circuits via the Application of Filippov's Method," in *IUTAM Symposium on Nonlinear Dynamics for Advanced Technologies and Engineering Design*, 2013, pp. 295-311.

[58]   K. Pyragas, "Control of Chaos Via Extended Delay Feedback," *Physics Letters A,* vol. 206, pp. 323-330, Oct 16 1995.

[59]   S. K. Mazumder and K. Acharya, "Multiple Lyapunov Function Based Reaching Condition for Orbital Existence of Switching Power Converters," *Power Electronics, IEEE Transactions on,* vol. 23, pp. 1449-1471, 2008.

[60]   M. Spinetti, E. Fossas, and D. Biel, "Stabilitiy analysis of a Lyapunov-based controlled boost converter," *Proceedings of the 48th Ieee Conference on Decision and Control, 2009 Held Jointly with the 2009 28th Chinese Control Conference (Cdc/Ccc 2009),* pp. 6544-6548, 2009.

[61]   T. S. Hu, "A Nonlinear-System Approach to Analysis and Design of Power-Electronic Converters With Saturation and Bilinear Terms," *Ieee Transactions on Power Electronics,* vol. 26, pp. 399-410, Feb 2011.

[62]   B. Grzesik and P. Siewniak, "Lyapunov Stability Analysis of DC-DC Power Electronic Converters: A Brief Overview," *Przeglad Elektrotechniczny,* vol. 88, pp. 162-166, 2012.

[63]   C. Yfoulis, D. Giaouris, S. Voutetakis, and S. Papadopoulou, "Constrained switching stabilization of a dc-dc boost converter using piecewise-linear Lyapunov functions," *2013 21st Mediterranean Conference on Control and Automation (Med),* pp. 814-823,

2013.

[64]   I. A. Hiskens and M. A. Pai, "Trajectory sensitivity analysis of hybrid systems," *IEEE Transactions on Circuits and Systems I-Regular Papers,* vol. 47, pp. 204-220, Feb 2000.

[65]   A. El Aroudi, E. Rodriguez, R. Leyva, and E. Alarcon, "A Design-Oriented Combined Approach for Bifurcation Prediction in Switched-Mode Power Converters," *IEEE Transactions on Circuits and Systems Ii-Express Briefs,* vol. 57, pp. 218-222, Mar 2010.

[66]   J. Reina, Rodri, x, E. guez, E. Alarcon, and A. El Aroudi, "Ripple-based approach for predicting fast-scale instability in multi-level converters," in *Control and Modeling for Power Electronics (COMPEL), 2010 IEEE 12th Workshop on,* 2010, pp. 1-8.

[67]   E. Rodriguez, A. El Aroudi, F. Guinjoan, and E. Alarcon, "A Ripple-Based Design-Oriented Approach for Predicting Fast-Scale Instability in DC-DC Switching Power Supplies," *Ieee Transactions on Circuits and Systems I-Regular Papers,* vol. 59, pp. 215-227, Jan 2012.

[68]   K. Mehran, D. Giaouris, and B. Zahawi, "Stability Analysis and Control of Nonlinear Phenomena in Boost Converters Using Model-Based Takagi-Sugeno Fuzzy Approach," *Ieee Transactions on Circuits and Systems I-Regular Papers,* vol. 57, pp. 200-212, Jan 2010.

[69]   K. H. Wong, "Output capacitor stability study on a voltage-mode buck regulator using system-poles approach," *IEEE Transactions on Circuits and Systems Ii-Express Briefs,* vol. 51, pp. 436-441, Aug 2004.

[70]   D. Dong, C. K. Tse, and M. Xikui, "Symbolic Analysis of Switching Systems: Application to Bifurcation Analysis of DC/DC Switching Converters," *Circuits and Systems I: Regular Papers, IEEE Transactions on,* vol. 52, pp. 1632-1643, 2005.

[71]   X. M. Wang, B. Zhang, and D. Y. Qiu, "The Quantitative Characterization of Symbolic Series of a Boost Converter," *Ieee Transactions on Power Electronics,* vol. 26, pp. 2101-2105, Aug 2011.

[72]   N. Quanmin, J. Zhizhong, Q. Chengchao, and W. Hengli, "Study on Bifurcation and Chaos in Boost Converter Based on Energy Balance Model," in *Power and Energy Engineering Conference, 2009. APPEEC 2009. Asia-Pacific,* 2009, pp. 1-5.

[73]   A. El Aroudi, D. Giaouris, H. Ho-Ching Iu, and I. A. Hiskens, "A Review on Stability Analysis Methods for Switching Mode Power Converters," *Emerging and Selected Topics in Circuits and Systems, IEEE Journal on,* vol. 5, pp. 302-315, 2015.

[74]   E. Ott, C. Grebogi, and J. A. Yorke, "Controlling chaos," *Physical review letters,* vol. 64, p. 1196, 1990.

[75]   K. Pyragas, "Continuous Control of Chaos by Self-Controlling Feedback - Stabilization of Unstable Periodic and Aperiodic Orbits," *Chaos/Nonlinear Dynamics: Methods and Commercialization,* vol. 2037, pp. 148-159, 1994.

[76]   R. S. Bueno and J. L. R. Marrero, "Application of the OGY method to the control of chaotic DC-DC converters: Theory and experiments," *Iscas 2000: Ieee International Symposium on Circuits and Systems - Proceedings, Vol II,* pp. 369-372, 2000.

[77]   C. Grebogi and L. Ying-Cheng, "Controlling chaos in high dimensions," *Circuits and Systems I: Fundamental Theory and Applications, IEEE Transactions on,* vol. 44, pp. 971-975, 1997.

[78]   C. Batlle, E. Fossas, and G. Olivar, "Time-delay stabilization of the buck converter," in *Control of Oscillations and Chaos, 1997. Proceedings., 1997 1st International Conference,* 1997, pp. 590-593 vol.3.

[79]   C. Liang and Y. Xinghuo, "On time-delayed feedback control of chaotic systems," *Circuits and Systems I: Fundamental Theory and Applications, IEEE Transactions on,*

vol. 46, pp. 767-772, 1999.

[80]   H. H. C. Iu and B. Robert, "Control of chaos in a PWM current-mode H-bridge inverter using time-delayed feedback," *Ieee Transactions on Circuits and Systems I-Fundamental Theory and Applications,* vol. 50, pp. 1125-1129, Aug 2003.

[81]   A. Yazdanpanah and A. Khaki-Sedigh, "Adaptive control of chaos in nonlinear discrete-time systems using time-delayed state feedback," *2005 International Conference on Physics and Control (Physcon),* pp. 908-912, 2005.

[82]   A. Y. Goharrizi, A. Khaki-Sedigh, and N. Sepehri, "Observer-based adaptive control of chaos in nonlinear discrete-time systems using time-delayed state feedback," *Chaos Solitons & Fractals,* vol. 41, pp. 2448-2455, Sep 15 2009.

[83]   A. Abbasi, M. Rostami, S. H. Fathi, J. Abdollahi, and H. R. Abbasi, "The TDFC method for control unstable chaotic behaviour in boost converter," in *Computer Applications and Industrial Electronics (ICCAIE), 2010 International Conference on,* 2010, pp. 110-114.

[84]   A. El Aroudi, J. Pelaez-Restrepo, K. Kaoubaa, M. Feki, and B. G. M. Robert, "Time Delay Feedback Control of a Two-cell DC-DC Buck converter," *Proceedings of 14th International Power Electronics and Motion Control Conference (Epe-Pemc 2010),* 2010.

[85]   N. Wang, G. N. Lu, X. Z. Peng, and Y. K. Cai, "A Research on Time Delay Feedback Control Performance in Chaotic System of Dc-Dc Inverter," *2013 IEEE International Conference on Vehicular Electronics and Safety (Icves),* pp. 215-218, 2013.

[86]   D. Chen, H. O. Wang, and G. R. Chen, "Anti-control of Hopf bifurcations through washout filters," *Proceedings of the 37th IEEE Conference on Decision and Control, 1998, Vols 1-4,* pp. 3040-3045.

[87]   W. Ma, M. Y. Wang, S. X. Liu, S. Li, and P. Yu, "Stabilizing the Average-Current-Mode-Controlled Boost PFC Converter via Washout-Filter-Aided Method," *Ieee Transactions on Circuits and Systems Ii-Express Briefs,* vol. 58, pp. 595-599, Sep 2011.

[88]   M. S. Saad, M. A. Hassouneh, E. H. Abed, and A. Edris, "Delaying instability and voltage collapse in power systems using SVCs with washout filter-aided feedback," in *American Control Conference, 2005. Proceedings of the 2005,* 2005, pp. 4357-4362 vol. 6.

[89]   M. A. Hassouneh, L. Hsien-Chiarn, and E. H. Abed, "Washout filters in feedback control: benefits, limitations and extensions," in *American Control Conference, 2004. Proceedings of the 2004,* 2004, pp. 3950-3955 vol.5.

[90]   W. G. Lu, L. W. Zhou, Q. M. Luo, and X. F. Zhang, "Filter based non-invasive control of chaos in Buck converter," *Physics Letters A,* vol. 372, pp. 3217-3222, Apr 28 2008.

[91]   A. El Aroudi, R. Haroun, A. Cid-Pastor, and L. Martinez-Salamero, "Suppression of Line Frequency Instabilities in PFC AC-DC Power Supplies by Feedback Notch Filtering the Pre-Regulator Output Voltage," *Circuits and Systems I: Regular Papers, IEEE Transactions on,* vol. 60, pp. 796-809, 2013.

[92]   L. Wei-Guo, Z. Luo-Wei, and W. Jun-Ke, "Self-Stable Chaos Control of dc—dc Converter," *Chinese Physics Letters,* vol. 26, p. 030503, 2009.

[93]   J. Xu, G. Zhou, and M. He, "Improved digital peak voltage predictive control for switching DC–DC converters," *Industrial Electronics, IEEE Transactions on,* vol. 56, pp. 3222-3229, 2009.

[94]   E. Rodriguez, E. Alarcon, H. H. C. Iu, and A. El Aroudi, "A Frequency Domain Approach for Controlling Chaos in Switching Converters," *2010 IEEE International Symposium on Circuits and Systems,* 2010, pp. 2928-2931.

[95]   E. Mirzaei and H. Mojallali, "Auto tuning PID controller using chaotic PSO algorithm

for a Boost converter," in *Fuzzy Systems (IFSC), 2013 13th Iranian Conference on*, 2013, pp. 1-6.

[96]   Y. F. Zhou, H. H. C. Iu, C. K. Tse, and J. N. Chen, "Controlling chaos in DC/DC converters using optimal resonant parametric perturbation," *2005 IEEE International Symposium on Circuits and Systems (Iscas), Vols 1-6, Conference Proceedings,* 2005 pp. 2481-2484.

[97]   A. Kavitha and G. Uma, "Control of chaos by resonant parametric perturbation in a current mode controlled buck-boost Dc-Dc converter," *Apec 2008: Twenty-Third Annual IEEE Applied Power Electronics Conference and Exposition, Vols 1-4,* 2008, pp. 323-327.

[98]   Y. Zhou, C. K. Tse, S.-S. Qiu, and F. C. M. Lau, "Applying resonant parametric perturbation to control chaos in the buck dc/dc converter with phase shift and frequency mismatch considerations," *International Journal of Bifurcation and Chaos,* vol. 13, pp. 3459-3471, 2003.

[99]   C. K. Tse, Y. M. Lai, and M. H. L. Chow, "Control of bifurcation in current-programmed DC/DC converters: an alternative viewpoint of ramp compensation," in *Industrial Electronics Society, 2000. IECON 2000. 26th Annual Conference of the IEEE*, 2000, pp. 2413-2418 vol.4.

[100]   B. Bocheng, Z. Guohua, X. Jianping, and L. Zhong, "Unified Classification of Operation-State Regions for Switching Converters with Ramp Compensation," *Power Electronics, IEEE Transactions on,* vol. 26, pp. 1968-1975, 2011.

[101]   J. Morcillo and G. Olivar, "Description and comparison of non-smooth bifurcations in a ramp-controlled and sine-controlled buck converter," in *Circuits and Systems (CWCAS), 2012 IEEE 4th Colombian Workshop on*, 2012, pp. 1-6.

[102]   N. Zamani, M. Niroomand, and M. Ataei, "Modeling and chaos control of current mode controlled switching converter with ramp compensation," in *Power Electronics, Drive Systems and Technologies Conference (PEDSTC), 2014 5th*, 2014, pp. 360-365.

[103]   K. Guesmi, A. Hamzaoui, and J. Zaytoon, "Control of nonlinear phenomena in DC–DC converters: Fuzzy logic approach," *International Journal of Circuit Theory and Applications,* vol. 36, pp. 857-874, 2008.

[104]   N. Inaba, T. Endo, T. Yoshinaga, and K. Fujimoto, "Collapse of mixed-mode oscillations and chaos in the extended Bonhoeffer-van Der pol oscillator under weak periodic perturbation," in *Circuit Theory and Design (ECCTD), 2011 20th European Conference on*, 2011, pp. 369-372.

[105]   H. Li, B. Zhang, Z. Li, W. A. Halang, and G. Chen, "Controlling DC–DC converters by chaos-based pulse width modulation to reduce EMI," *Chaos, Solitons & Fractals,* vol. 42, pp. 1378-1387, 2009.

[106]   L. Premalatha and A. Thanuja, "Generation of chaos and EMI reduction in current controlled boost converter using Random modulation," in *Recent Advancements in Electrical, Electronics and Control Engineering (ICONRAEeCE), 2011 International Conference on*, 2011, pp. 211-215.

[107]   N. Sudhakar, N. Rajasekar, V. T. Rohit, E. Rakesh, and J. Jacob, "EMI mitigation in closed loop boost converter using soft switching combined with chaotic mapping," in *Advances in Electrical Engineering (ICAEE), 2014 International Conference on*, 2014, pp. 1-6.

[108]   P. Aruna and L. Premalatha, "Investigation of EMI reduction in buck converter by using external chaos generator," in *Recent Advancements in Electrical, Electronics and Control Engineering (ICONRAEeCE), 2011 International Conference on*, 2011, pp. 520-525.

[109]   D. C. Hamill, J. H. B. Deane, and P. J. Aston, "Some applications of chaos in power

converters," in *Update on New Power Electronic Techniques (Digest No: 1997/091), IEE Colloquium on*, 1997, pp. 5/1-5/5.

[110] S. Wiggins, *Introduction to applied nonlinear dynamical systems and chaos* vol. 2: Springer Science & Business Media, 2003.

[111] S. Banerjee and G. C. Verghese, *Nonlinear phenomena in power electronics*: IEEE, 1999.

[112] R. I. Leine and H. Nijmeijer, *Dynamics and bifurcations of non-smooth mechanical systems* vol. 18: Springer Science & Business Media, 2013.

[113] S. H. Kellert, *In the wake of chaos: Unpredictable order in dynamical systems*: University of Chicago press, 1994.

[114] E. Ott, *Chaos in dynamical systems*: Cambridge university press, 2002.

[115] H. Shengzhong, W. Songrong, X. Yinglei, Y. Tiesheng, C. Yiming, and C. Li, "Nonlinear modeling and analysis of valley V^2 controlled buck converter," in *Microwave, Antenna, Propagation and EMC Technologies for Wireless Communications (MAPE), 2013 IEEE 5th International Symposium on*, 2013, pp. 659-663.

[116] J. Crutchfield, D. Farmer, N. Packard, R. Shaw, G. Jones, and R. Donnelly, "Power spectral analysis of a dynamical system," *Physics Letters A,* vol. 76, pp. 1-4, 1980.

[117] X. Fan, Z. Bo, Y. Ru, and Q. Dongyuan, "Quantifying the Complexity of DC–DC Switching Converters by Joint Entropy," *Circuits and Systems II: Express Briefs, IEEE Transactions on,* vol. 61, pp. 579-583, 2014.

[118] S. Banerjee and K. Chakrabarty, "Nonlinear modeling and bifurcations in the boost converter," *IEEE Transactions on Power Electronics,* vol. 13, pp. 252-260, Mar 1998.

[119] V. Grigore, J. Hatonen, J. Kyyra, and T. Suntio, "Dynamics of a buck converter with a constant power load," in *Power Electronics Specialists Conference, 1998. PESC 98 Record. 29th Annual IEEE*, 1998, pp. 72-78 vol.1.

[120] C. Rivetta and G. A. Williamson, "Global behaviour analysis of a DC-DC boost power converter operating with constant power load," in *Circuits and Systems, 2004. ISCAS '04. Proceedings of the 2004 International Symposium on*, 2004, pp. V-956-V-959 Vol.5.

[121] A. Emadi, A. Khaligh, C. H. Rivetta, and G. A. Williamson, "Constant power loads and negative impedance instability in automotive systems: Definition, modeling, stability, and control of power electronic converters and motor drives," *IEEE Transactions on Vehicular Technology,* vol. 55, pp. 1112-1125, Jul 2006.

[122] A. Khaligh and A. Emadi, "Power alignment, new digital control approach for a DC-DC flyback converter with constant power loads," *Iciea 2006: 1st IEEE Conference on Industrial Electronics and Applications, Vols 1-3, Proceedings,* pp. 606-611, 2006.

[123] A. Khaligh, A. M. Rahimi, and A. Emadi, "Negative impedance stabilizing pulse adjustment control technique for DC/DC converters operating in discontinuous conduction mode and driving constant power loads," *IEEE Transactions on Vehicular Technology,* vol. 56, pp. 2005-2016, Jul 2007.

[124] A. M. Rahimi and A. Emadi, "An Analytical Investigation of DC/DC Power Electronic Converters With Constant Power Loads in Vehicular Power Systems," *Vehicular Technology, IEEE Transactions on,* vol. 58, pp. 2689-2702, 2009.

[125] P. Liutanakul, A. B. Awan, S. Pierfederici, B. Nahid-Mobarakeh, and F. Meibody-Tabar, "Linear Stabilization of a DC Bus Supplying a Constant Power Load: A General Design Approach," *IEEE Transactions on Power Electronics,* vol. 25, pp. 475-488, Feb 2010.

[126] G. Zhaohui, Z. Xiaobin, and L. Hui, "Modeling and Nonlinear Control for the Boost Converter with Constant Power Loads," in *Power and Energy Engineering Conference*

(APPEEC), 2010 Asia-Pacific, 2010, pp. 1-4.

[127] A. Kwasinski and C. N. Onwuchekwa, "Dynamic Behavior and Stabilization of DC Microgrids With Instantaneous Constant-Power Loads," *IEEE Transactions on Power Electronics,* vol. 26, pp. 822-834, Mar 2011.

[128] D. Weijing, Z. Junming, Z. Yang, Q. Zhaoming, and P. Fangzheng, "Large signal stability analysis based on gyrator model with constant power load," in *Power and Energy Society General Meeting, 2011 IEEE*, 2011, pp. 1-8.

[129] L. Yushan, K. R. Vannorsdel, A. J. Zirger, M. Norris, and D. Maksimovic, "Current Mode Control for Boost Converters With Constant Power Loads," *Circuits and Systems I: Regular Papers, IEEE Transactions on,* vol. 59, pp. 198-206, 2012.

[130] X. Zhi-yu, Y. You-ling, X. Wei-sheng, and W. Qi-di, "Controllability of nonisolated DC-DC converters with constant-power-load," in *Control and Decision Conference (CCDC), 2012 24th Chinese*, 2012, pp. 669-673.

[131] D. Marx, P. Magne, B. Nahid-Mobarakeh, S. Pierfederici, and B. Davat, "Large Signal Stability Analysis Tools in DC Power Systems With Constant Power Loads and Variable Power Loads 2014;A Review," *Power Electronics, IEEE Transactions on,* vol. 27, pp. 1773-1787, 2012.

[132] C. H. Rivetta, A. Emadi, G. A. Williamson, R. Jayabalan, and B. Fahimi, "Analysis and control of a buck DC-DC converter operating with constant power load in sea and undersea vehicles," *Industry Applications, IEEE Transactions on,* vol. 42, pp. 559-572, 2006.

[133] A. Griffo, J. Wang, and D. Howe, "Large signal stability analysis of DC power systems with constant power loads," in *Vehicle Power and Propulsion Conference, 2008. VPPC '08. IEEE*, 2008, pp. 1-6.

[134] X. Haiping, W. Xuhui, Q. Ermin, G. Xin, and K. Li, "High Power Interleaved Boost Converter in Fuel Cell Hybrid Electric Vehicle," in *Electric Machines and Drives, 2005 IEEE International Conference on*, 2005, pp. 1814-1819.

[135] M. Veerachary, T. Senjyu, and K. Uezato, "Maximum power point tracking of coupled inductor interleaved boost converter supplied PV system," *Electric Power Applications, IEE Proceedings ,* vol. 150, pp. 71-80, 2003.

[136] N. Long-xian, S. Kai, Z. Li, X. Yan, C. Min, and L. Rosendahl, "A power conditioning system for thermoelectric generator based on interleaved Boost converter with MPPT control," in *Electrical Machines and Systems (ICEMS), 2011 International Conference on*, 2011, pp. 1-6.

[137] S. Kolluri and N. L. Narasamma, "Analysis, modeling, design and implementation of average current mode control for interleaved boost converter," in *Power Electronics and Drive Systems (PEDS), 2013 IEEE 10th International Conference on*, 2013, pp. 280-285.

[138] D. Giaouris, S. Banerjee, F. Stergiopoulos, S. Papadopoulou, S. Voutetakis, B. Zahawi, V. Pickert, A. Abusorrah, M. Al Hindawi, and Y. Al‑Turki, "Foldings and grazings of tori in current controlled interleaved boost converters," *International Journal of Circuit Theory and Applications,* vol. 42, pp. 1080-1091, 2014.

[139] Y. B. Zhao, J. C. Feng, and C. K. Tse, "Discrete-Time Modeling and Stability Analysis of Periodic Orbits With Sliding for Switched Linear Systems," *IEEE Transactions on Circuits and Systems I-Regular Papers,* vol. 57, pp. 2948-2955, Nov 2010.

[140] D. Giaouris, S. Maity, S. Banerjee, V. Pickert, and B. Zahawi, "Application of Filippov method for the analysis of subharmonic instability in dc–dc converters," *International Journal of Circuit Theory and Applications,* vol. 37, pp. 899-919, 2009.

[141] H. Wu and V. Pickert, "Stability analysis and control of nonlinear phenomena in bidirectional boost converter based on the Monodromy matrix," in *Applied Power*

Electronics Conference and Exposition (APEC), 2014 Twenty-Ninth Annual IEEE, 2014, pp. 2822-2827.

[142] J. Lu and X. Wu, "A Novel Piecewise Linear Slope Compensation Circuit in Peak Current Mode Control," in *Electron Devices and Solid-State Circuits, 2007. EDSSC 2007. IEEE Conference on*, 2007, pp. 929-932.

[143] T. Grote, F. Schafmeister, H. Figge, N. Frohleke, P. Ide, and J. Bocker, "Adaptive digital slope compensation for peak current mode control," in *Energy Conversion Congress and Exposition, 2009. ECCE 2009. IEEE*, 2009, pp. 3523-3529.

[144] M. Hallworth and S. A. Shirsavar, "Microcontroller-Based Peak Current Mode Control Using Digital Slope Compensation," *Power Electronics, IEEE Transactions on,* vol. 27, pp. 3340-3351, 2012.

[145] A. K. Singha; S. Kapat; S. Banerjee; J. Pal, "Nonlinear Analysis of Discretization Effects in a Digital Current Mode Controlled Boost Converter," *IEEE J. Emerg. Selected Topics Cir. Systs,* 2015.

[146] O. Trescases, Z. Lukic, N. Wai Tung, and A. Prodic, "A low-power mixed-signal current-mode DC-DC converter using a one-bit Delta; Sigma; DAC," in *Applied Power Electronics Conference and Exposition, 2006. APEC '06. Twenty-First Annual IEEE*, 2006, p. 5 pp.

[147] TI, "Piccolo Microcontrollers," *http://www.ti.com/lit/ds/symlink/tms320f28035.pdf,* 2013.

[148] Microchip, "MCP19110/11," *http://ww1.microchip.com/downloads/en/DeviceDoc/20002331B.pdf,* 2013.

[149] C. Jingquan, A. Prodic, R. W. Erickson, and D. Maksimovic, "Predictive digital current programmed control," *Power Electronics, IEEE Transactions on,* vol. 18, pp. 411-419, 2003.

[150] S. Chattopadhyay and S. Das, "A Digital Current-Mode Control Technique for DC–DC Converters," *Power Electronics, IEEE Transactions on,* vol. 21, pp. 1718-1726, 2006.

[151] S. Kapat, "Selectively Sampled Subharmonic-Free Digital Current Mode Control Using Direct Duty Control," *Circuits and Systems II: Express Briefs, IEEE Transactions on,* vol. 62, pp. 311-315, 2015.

[152] L. Yan-Fei, E. Meyer, and L. Xiaodong, "Recent Developments in Digital Control Strategies for DC/DC Switching Power Converters," *Power Electronics, IEEE Transactions on,* vol. 24, pp. 2567-2577, 2009.

[153] J. Diaz, F. Nuno, J. M. Lopera, and J. A. Martin-Ramos, "A new control strategy for an AC/DC converter based on a piezoelectric transformer," *IEEE Transactions on Industrial Electronics,* vol. 51, pp. 850-856, Aug 2004.

[154] M. Hirakawa, Y. Watanabe, M. Nagano, K. Andoh, S. Nakatomi, S. Hashino, and T. Shimizu, "High power DC/DC converter using extreme close-coupled inductors aimed for electric vehicles," in *Power Electronics Conference (IPEC), 2010 International*, 2010, pp. 2941-2948.

[155] Z. Ouyang, Z. Zhe, O. C. Thomsen, and M. A. E. Andersen, "Planar-Integrated Magnetics (PIM) Module in Hybrid Bidirectional DC 2013;DC Converter for Fuel Cell Application," *Power Electronics, IEEE Transactions on,* vol. 26, pp. 3254-3264, 2011.

[156] N. D. Benavides and P. L. Chapman, "Boost converter with a reconfigurable inductor," *2007 IEEE Power Electronics Specialists Conference, Vols 1-6,* 2007, pp. 1695-1700.

[157] L. L. Gu, J. L. Sun, M. Xu, Q. P. Zuo, and J. B. Fan, "Size Reduction of the Inductor in Critical Conduction Mode PFC Converter," *2011 Twenty-Sixth Annual Ieee Applied Power Electronics Conference and Exposition (APEC),* 2011,pp. 550-557.

[158] A. A. M. Bento, E. R. C. da Silva, and E. C. dos Santos, "Reducing inductor size and current ripple in an AC-AC converter by interleaved switching strategy," *2006 IEEE Power Electronics Specialists Conference, Vols 1-7,* 2006,pp. 1257-1263.

[159] A. O. Elbkosh, "Nonlinear Analysis and Control of DC-DC Converters," *PhD Thesis Newcastle University,* 2009.

Appendix 1

By differentiating equation 2.8 with respect to $\mathbf{x}_0$, this Jacobian matrix can be obtained from the following expression:

$$\frac{\partial \mathbf{x}(t_0+T)}{\partial \mathbf{x}_0} = \mathbf{I} + \int_{t_0}^{t_0+T} \mathbf{A}(\tau,\mathbf{x}_0)\frac{\partial \varphi(\tau,\mathbf{x}_0)}{\partial \mathbf{x}_0}d\tau \tag{A1.1}$$

where **I** is the identity matrix with the same order as the state variables and the term $\mathbf{A}(\tau,\mathbf{x}_0)$ is shown as follows:

$$\mathbf{A}(\tau,\mathbf{x}_0) = \frac{\partial f(\varphi(\tau,\mathbf{x}_0),\tau)}{\partial \varphi(\tau,\mathbf{x}_0)} \tag{A1.2}$$

The following differential equation can be derived by differentiating equation A1.1 with respect to time:

$$\frac{d}{dt}\left(\frac{\partial \mathbf{x}(t_0+T)}{\partial \mathbf{x}_0}\right) = \mathbf{A}(t,\mathbf{x}_0) \times \frac{\partial \mathbf{x}(t_0+T)}{\partial \mathbf{x}_0} \tag{A1.3}$$

The Jacobian matrix can be calculated from solving the equation above.

The following expression can be obtained by perturbing around this fixed point,

$$\Delta\mathbf{x}(t_0+T) = \frac{\partial \mathbf{x}(t_0+T)}{\partial \mathbf{x}_0}\Delta\mathbf{x}(t_0) \tag{A1.4}$$

Hence the stability of the fixed point of the Poincaré map, which represents the original periodic smooth system, can be studied using the eigenvalues of this obtained Jacobian matrix.

Appendix 2

Assume that there is a system which has a generic initial value:

$$\frac{dx(t)}{dt} = f(x(t), t)\big|_{x(t)=\phi(t,t_0,x_0)}, \qquad x(t_0) = x_0 \tag{A2.1}$$

Then, according to the theory of trajectory sensitivity, the system's stability can be analysed using the solution $\phi(t,t_0,x_0)$ by adding a small perturbation δ and observing its evolution. In addition, by employing the linearization approach of the Taylor series around the periodic orbit, the following equation can be obtained:

$$\frac{d}{dt}\Delta\phi(t,t_0,x_0) = \frac{\partial f(x(t),t)}{\partial x(t)}\big|_{x(t)=\phi(t,t_0,x_0)} \Delta\phi(t,t_0,x_0) + \text{higher order terms} \tag{A2.2}$$

Since the perturbation is small enough, the higher order terms can be neglected. Here:

$$\delta = \Delta\phi(t_0,t_0,x_0) = \phi(t_0,t_0,x_0+\delta) - \phi(t_0,t_0,x_0) \tag{A2.3}$$

$$\Delta\phi(t,t_0,x_0) = \phi(t,t_0,x_0+\delta) - \phi(t,t_0,x_0) \tag{A2.4}$$

The solution to equation A2.2 reveals the relationship between the perturbation $\Delta\phi(t,t_0,x_0)$ and the original one at time t_0, which is written as follows:

$$\Delta\phi(t,t_0,x_0) = \frac{\partial\phi(t,t_0,x_0)}{\partial x_0}\Delta\phi(t_0,t_0,x_0) = \Phi(t,t_0)\Delta\phi(t_0,t_0,x_0) \tag{A2.5}$$

where $\Phi(t,t_0)$ represents the state transition matrix of the system. This system can be regarded as stable if the perturbation tends to zero when t→∞. For a periodic orbit with a period of T, the following equation can be proved:

$$\Delta\phi(kT+t_0,t_0,x_0) = \Phi^k(T+t_0,t_0)\Delta\phi(t_0,t_0,x_0) \tag{A2.6}$$

where $\Phi(T+t_0,t_0)$ is named as the Mondromy matrix, which is the state transition matrix over a whole period T. This equation can be written in the following form:

$$\Delta\phi(kT+t_0,t_0,x_0) = E\Lambda^k E^{-1}\Delta\phi(t_0,t_0,x_0) \tag{A2.7}$$

where E is the eigenmatrix of this Monodromy matrix. The stability of the system can be determined from the magnitudes of the eigenvalues of the Monodromy matrix (also named the Floquet multipliers).

Appendix 3

The theory of Filippov provides a generalised definition of system solutions with switching behaviour [56, 112, 159]. Such systems can be described as:

$$\dot{\mathbf{x}}(t) = \begin{cases} f_-(\mathbf{x}(t),t) & \mathbf{x} \in V_- \\ f_\Sigma(\mathbf{x}(t),t) & \mathbf{x} \in \Sigma \\ f_+(\mathbf{x}(t),t) & \mathbf{x} \in V_+ \end{cases} \tag{A3.1}$$

where $f_-(\mathbf{x}(t),t)$ and $f_+(\mathbf{x}(t),t)$ represent the smooth vector fields before and after switching respectively. V- and V+ are two different regions in state space and the switching manifold Σ separates them as shown in Figure A3.1
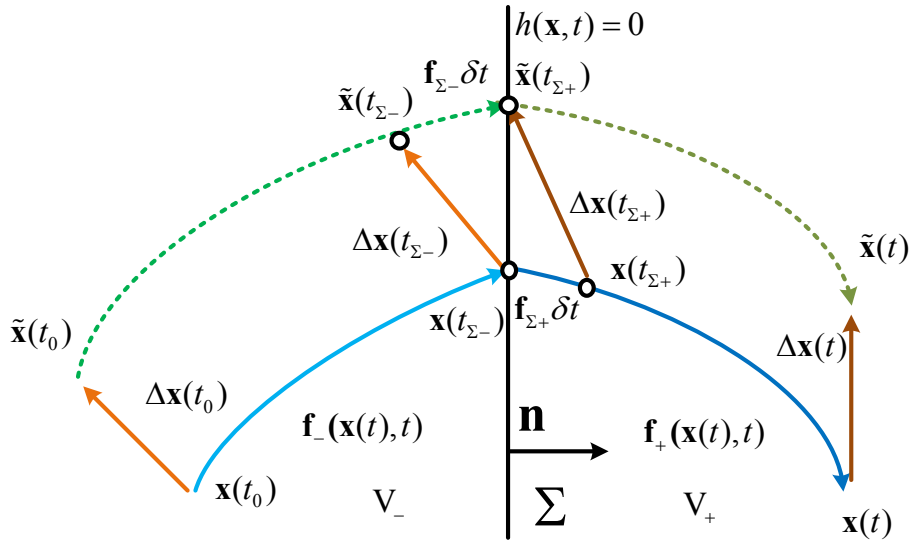
Figure.A3.1 Solution of nonsmooth system and its perturbed solution

In smooth systems, the evaluation of perturbation from the initial condition to the end of the period can be mapped by the fundamental matrix. In nonsmooth systems, however, the switching instant makes the vector field discontinuous. As a result, the fundamental matrix breaks down and the information of the switching instant needs to be taken into account. The relations of perturbation vectors $\Delta\mathbf{x}(t_{\Sigma-})$ and $\Delta\mathbf{x}(t_{\Sigma+})$ which are before and after the switching respectively, can be described using the saltation matrix

$$\Delta\mathbf{x}(t_{\Sigma+}) = \mathbf{S}\,\Delta\mathbf{x}(t_{\Sigma-}) \tag{A3.2}$$

The following equations can be obtained:

$$\begin{cases} \Delta\mathbf{x}(t_0) = \tilde{\mathbf{x}}(t_0) - \mathbf{x}(t_0) \\ \Delta\mathbf{x}(t) = \tilde{\mathbf{x}}(t) - \mathbf{x}(t) \\ \tilde{\mathbf{x}}(t_{\Sigma-}) = \mathbf{x}(t_{\Sigma-}) + \Delta\mathbf{x}(t_{\Sigma-}) \\ \tilde{\mathbf{x}}(t_{\Sigma+}) = \mathbf{x}(t_{\Sigma+}) + \Delta\mathbf{x}(t_{\Sigma+}) \\ t_{\Sigma+} = t_{\Sigma-} + \delta t \end{cases} \tag{A3.3}$$

δt represents the time difference before and after the switching instant, which is small enough. By employing Taylor series expansion, the relationship of the state vectors can be expressed as follows:

$$\tilde{\mathbf{x}}(t_{\Sigma+}) = \tilde{\mathbf{x}}(t_{\Sigma-} + \delta t) = \tilde{\mathbf{x}}(t_{\Sigma-}) + f_{\Sigma-}\delta t \tag{A3.4}$$

$$\mathbf{x}(t_{\Sigma+}) = \mathbf{x}(t_{\Sigma-} + \delta t) = \mathbf{x}(t_{\Sigma-}) + f_{\Sigma+}\delta t \tag{A3.5}$$

By substituting equations A3.4, A3.5 into equation A3.3, the following is obtained:

$$\begin{aligned} \Delta\mathbf{x}(t_{\Sigma+}) &= \tilde{\mathbf{x}}(t_{\Sigma+}) - \mathbf{x}(t_{\Sigma+}) = \tilde{\mathbf{x}}(t_{\Sigma-}) - \mathbf{x}(t_{\Sigma-}) + (f_{\Sigma-} - f_{\Sigma+})\delta t \\ &= \Delta\mathbf{x}(t_{\Sigma-}) + (f_{\Sigma-} - f_{\Sigma+})\delta t \end{aligned} \tag{A3.6}$$

Switching conditions satisfy the following relationship:

$$\begin{cases} h(\mathbf{x}(t_{\Sigma-}), t_{\Sigma-}) = 0 \\ h(\mathbf{x}(t_{\Sigma+}), t_{\Sigma+}) = 0 \end{cases} \tag{A3.7}$$

Also using the Taylor series expansion on h(x(t),t), an expression can be derived in terms of δt:

$$\begin{aligned} h(\tilde{\mathbf{x}}(t_{\Sigma+}), t_{\Sigma+}) &= h(\mathbf{x}(t_{\Sigma-}) + \Delta\mathbf{x}(t_{\Sigma-}) + f_{\Sigma-}\delta t, t_{\Sigma-} + \delta t) \\ &= \underbrace{h(\mathbf{x}(t_{\Sigma-}), t_{\Sigma-})}_{0} + m\delta t + \mathbf{n}^T(\Delta\mathbf{x}(t_{\Sigma-}) + f_{\Sigma-}\delta t) = 0 \end{aligned} \tag{A3.8}$$

where:

$$\mathbf{n} = \frac{\partial h}{\partial \mathbf{x}}\bigg|_{(t_\Sigma, \mathbf{x}(t_\Sigma))} \tag{A3.9}$$

and:

$$m = \frac{\partial h(\mathbf{x}(t_{\Sigma-}), t_{\Sigma-})}{\partial t} = \frac{\partial h(\mathbf{x}(dT), dT)}{\partial t} = \frac{\partial h}{\partial t}\bigg|_{x(dT), dT} \tag{A3.10}$$

Here, **n** represents the normal to the switching manifold. The expression for δt can be obtained as:

$$\delta t = -\frac{\mathbf{n}^T \Delta\mathbf{x}(t_{\Sigma-})}{\mathbf{n}^T f_{\Sigma-} + m} \tag{A3.11}$$

Substituting equations A3.8, A3.9 and A3.10 into equation A3.11, the relationship between the perturbations vectors before and after the switching is shown as follows:

$$\Delta \mathbf{x}(t_{\Sigma+}) = \Delta \mathbf{x}(t_{\Sigma-}) + (f_{\Sigma+} - f_{\Sigma-}) \frac{\mathbf{n}^T \Delta \mathbf{x}(t_{\Sigma-})}{\mathbf{n}^T f_{\Sigma-} + m} \qquad (A3.12)$$

Comparing equations A3.2 and A3.12, the saltation matrix can be written as:

$$\mathbf{S} = \mathbf{I} + \frac{(f_{\Sigma+} - f_{\Sigma-})\mathbf{n}^T}{\mathbf{n}^T f_{\Sigma-} + \dfrac{\partial h}{\partial t}} \qquad (A3.13)$$

Appendix 4

Method for varying-phase sinusoid injections

A diagram of the supervising controller is given in Figure.A4.1.The main concept of the proposed varying-phase sinusoid injection method is to change the term of $\partial h / \partial t$ in equation 2.7 from 0 to a controllable variable, by introducing the sinusoid signal to the reference V_{ref}. The expression of the new reference V_{ref} becomes:

$$V_{ref} = V_{ref}^{'}(1 + a\sin(\omega t + \varphi)) \tag{A4.1}$$

Now the expression of $\partial h / \partial t$ is changed as follows:

$$\frac{\partial h}{\partial t} = K_p V_{ref}^{'} a\omega\cos(\omega t + \varphi) \tag{A4.2}$$

By choosing the proper parameter "a" in the new Monodromy matrix, the eigenvalues of this matrix are located within the unit circle which indicates a stable period-1 operation. In order to achieve only a minimal influence of the switching instant on the normal operation of the converter, the term of the sine should be small enough.

(a)
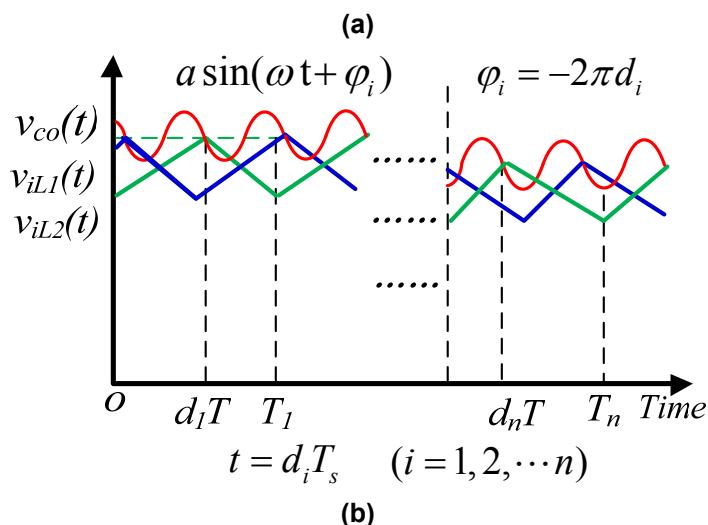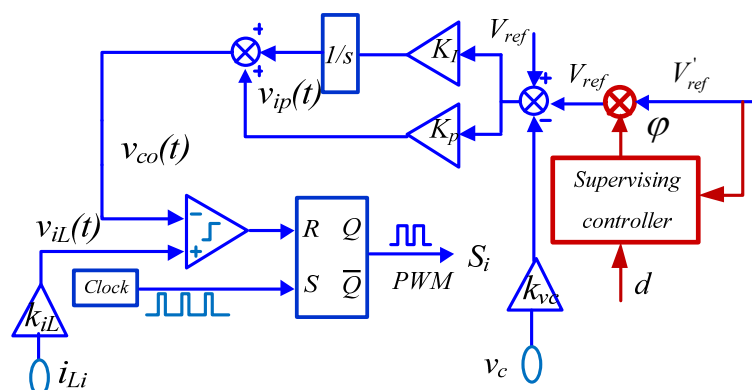
(b)
Figure.A4.1 (a) Diagram of supervising controller;
(b) illustration of varying-phase sinusoid injection method

Hence, the appropriate phase of the sinusoid φ can be chosen in each clock cycle, which makes the zero crossing coincide with the nominal steady-state switching instant. Specifically, φ can be set as -2πd in this case. But since $\partial h / \partial t$ contains the cosine term which attains a maximum value at the switching instant, this alters the Monodromy matrix significantly to stabilize the system. The illustration of this varying-phase sinusoid injection method is shown in Figure. A4.1.

The specification of simulation parameters is shown as follows: V_i=250V~400V, V_{out}=600V, L_1=L_2=200µH, C=250µF, R=6Ω, f=20kHz, a=-0.05, K_i=200, K_p=1, K_{vc}=1/120, K_{iL}=1/120, V_{ref}=5V. P_{out}=60kW. The diagram of the corresponding control algorithm in Matlab/Simulink is illustrated in Figure A4.2.
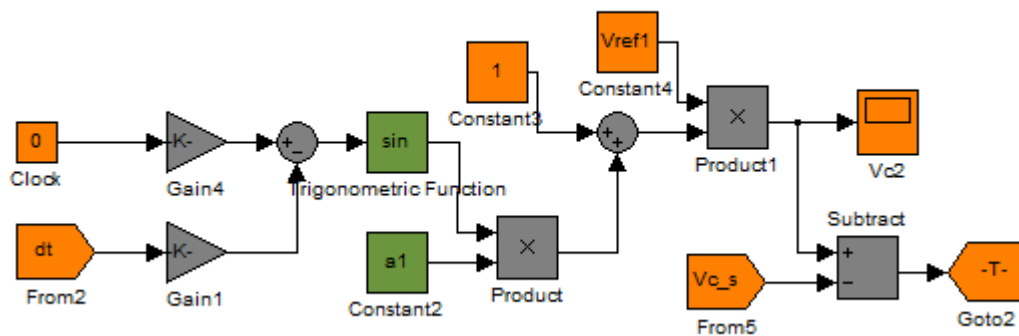
Figure A4.2. Diagram of corresponding control algorithm in Matlab/Simulink

The bifurcation diagram and corresponding locus of eigenvalues with conventional peak current control are presented in Figure A4.3 (a) and (b). The bifurcation point of the original system without supervising control can be indicated by the locus of eigenvalues of the Monodromy matrix. When the input voltage equals 329.5V, the system jumps into the period of bifurcation as shown in Figure A4.3 (a); meanwhile, one of the corresponding eigenvalues reaches the border of unit circle in Figure A4.3 (b), which means that the system becomes unstable. In contrast, Figure A4.3 (c) shows the diagram of output voltage vs. input voltage in the system with supervising control, which demonstrates that the system can remain stable within the whole range of input voltage from 250V to 400V. The corresponding locus of eigenvalues of the Monodromy matrix in Figure A4.3 (d) indicates that the related eigenvalues are located within the unit circle and they are varying on a certain track with different input voltages.

Therefore, this proves that the proposed control method extends the stable operating

region effectively. In addition, the evolution of inductor currents at the condition of V_{in} equals 329.7V with time is illustrated in Figure A4.4, which is the pattern produced in the process. It shows the behaviour of inductor current around the bifurcation point and that the system is changing from the stable period-1 to other periods.

Input voltage vs. output voltage

(a)

Locus of eigenvalues under different input voltages

(b)

(c)

159
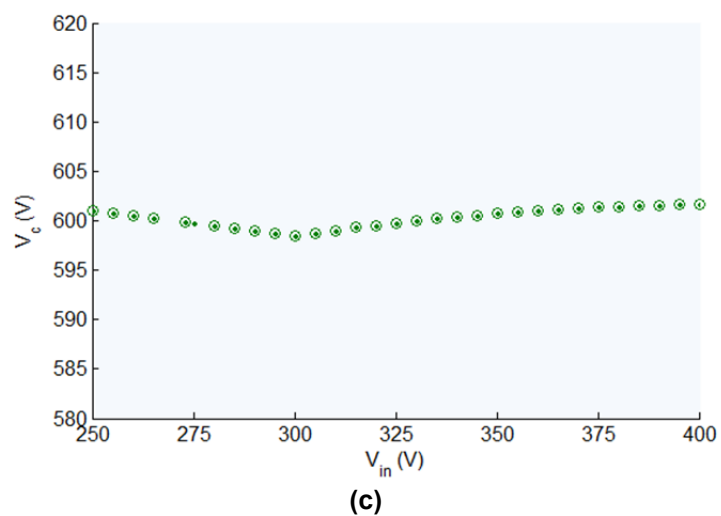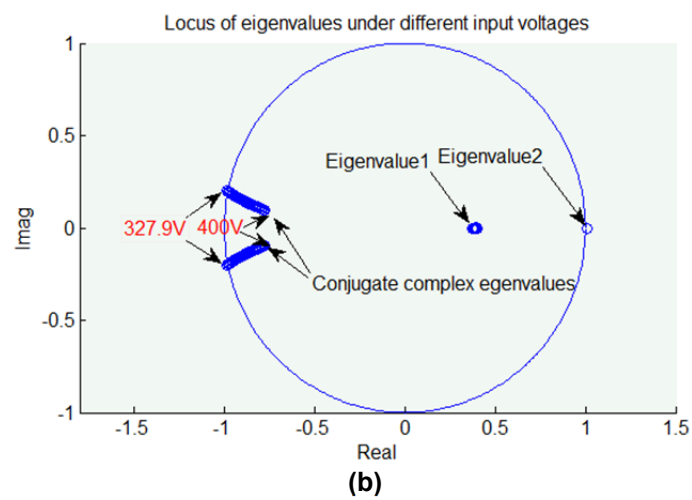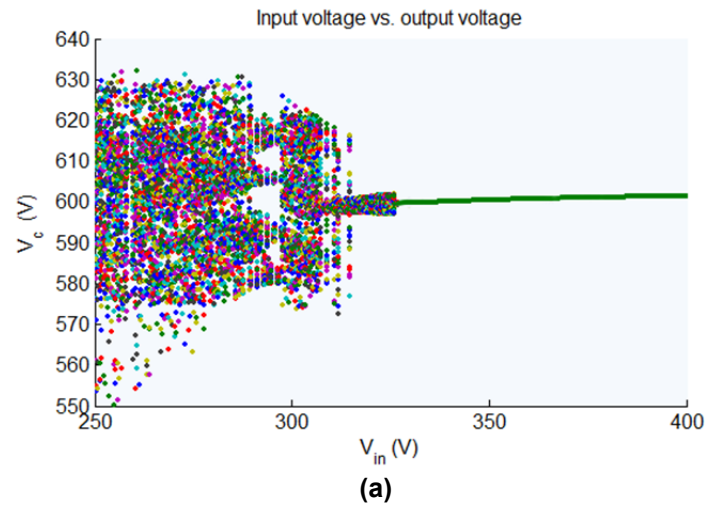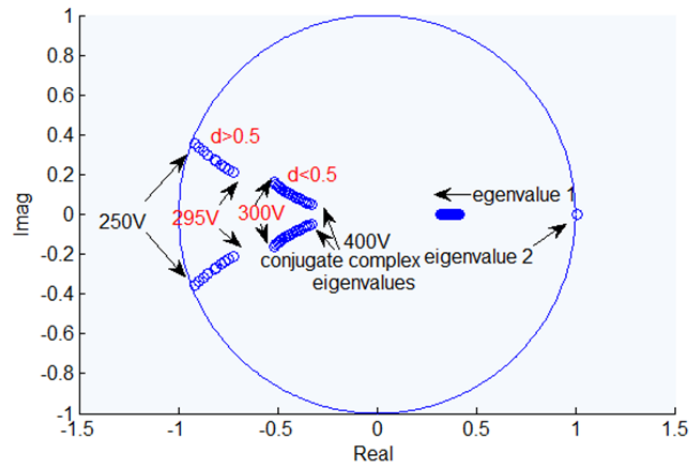
(d)

**Figure A4.3 (a)~(b) Bifurcation diagram and corresponding locus of eigenvalues
without supervising control;
(c)~(d) output voltage and corresponding locus of eigenvalues with supervising control**
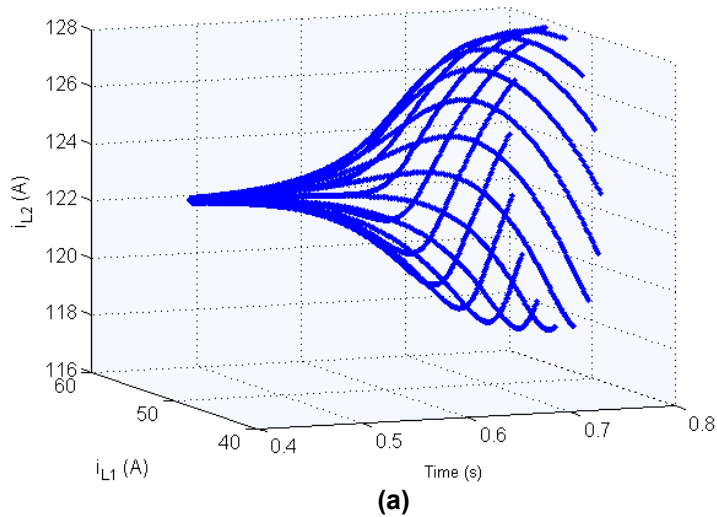
(a)
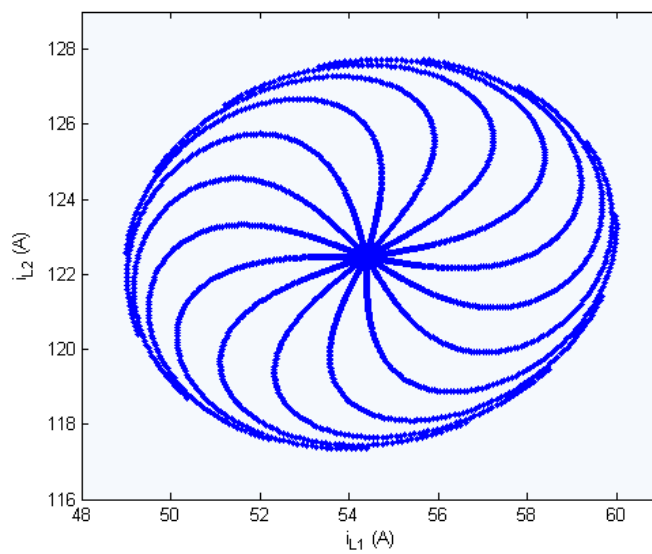
(b)

Figure A4.4 (a)~(b) Behaviour of the bifurcation point (a) 3-D (b) x-z view

Appendix 5

1. Main codes in the DSP controller

The program starts with the initialisation codes in the main function, which are used for the setting of a variable definition and appropriate configurations for the relevant registers, such as system clocks, peripheral interrupt expansion (PIE), GPIO, ePWM and ADC. Then the program executes the Labview data exchange loop. The function of this loop is to continuously communicate with the Labview user control panel via the RS232 interface, receiving the commands from the user and sending back sampled data to the control panel. The time of each action of communication can be set in Labview. For each switching period, the code is set to jump into the subfunction of interrupt service routine (ISR), named 'interrupt void ISREPwm1_Zero(void)'. This is used to achieve the functions of ADC sampling, the implementation of Digital PID and updating the output of external waveform generators.

```c
int main(void)

{
// system initialize: pll clock:100M;hispcp=1 100m/2; lospcp=2 100m/4;periferals clock enabled
    InitSysCtrl();
// Initialise the pins for the SCI-A port (RS232).
    InitSciaGpio();
// Init the pins for the SPI-A port (DAC).
   InitSpiaGpio();

//EPwm initialize
    InitEPwm1Gpio();
    InitEPwm2Gpio();
    InitEPwm3Gpio();
    InitEPwm6Gpio();

// Initialise GPIO (gate drives, external trip zone control, DAC and test points)
     gpio_init();

// Clear all interrupts and initialize PIE vector table:
// Disable CPU interrupts
    DINT;
// Initialize the PIE control registers to their default state.
    InitPieCtrl();
// Disable CPU interrupts and clear all CPU interrupt flags:
   IER = 0x0000;
   IFR = 0x0000;
//initialize Pie interrupts and enable pie
   InitPieVectTable();

//user defined interrupt initialize
   EALLOW;
   PieVectTable.TINT0 = &cpu_timer0_isr;    //Cpu timer0 interrupt
   PieVectTable.EPWM1_INT=&ISREPwm1_Zero;  //EPwm1 counter underflow interrupt
```

```c
//      PieVectTable.EPWM2_INT=&ISREPwm2_Zero;    //EPwm2 counter underflow interrupt
    PieVectTable.EPWM6_INT=&ISREPwm6_Zero;
    EDIS;
    //CPU timer0 initialize
    InitCpuTimers();
// Configure CPU-Timer 0 to interrupt every msecond:
// 150MHz CPU Freq, 4.5m second Period (in uSeconds)
    ConfigCpuTimer(&CpuTimer0, 100, 3000);
// These function is in DSP2833x_CupTimers.h file
    StartCpuTimer0();


//ADC initialize
    InitAdc();

//ADC setup
    SetupAdc();
    EALLOW;
    SysCtrlRegs.PCLKCR0.bit.TBCLKSYNC = 0;   // ePWM TBCLK stopped
    EDIS;


// Here we configure
    InitEPwmMods();
    EPwm6Regs.CMPA.half.CMPA =EPwm6_Compare;
    EPwm3Regs.CMPA.half.CMPA =EPwm3_Compare;
    EPwm2Regs.CMPA.half.CMPA =EPwm2_Compare;
    EPwm1Regs.CMPA.half.CMPA =EPwm1_Compare;


    EALLOW;
    SysCtrlRegs.PCLKCR0.bit.TBCLKSYNC = 1;   // All enabled ePWMs synchronised with rising edge
of TBCLK
    EDIS;
// Set up SPI for DAC
    spi_fifo_init();   // Initialize the Spi FIFO
    spi_init();        // init SPI

//      InitFlash();

    scia_fifo_init();        // Initialise the SCI FIFO
    scia_echoback_init();  // Initialise SCI for echoback

    LoopCount = 0;          // Set LabVIEW data transfer counter to zero
    ErrorCount = 0;
    i=0;                // Set RS232 character counter to zero

    IncPIDVar(&VoltLoopPID,VLoop_P,VLoop_I,VLoop_D); // Initial parameter calculation

    GpioDataRegs.GPBSET.bit.GPIO62 = 1;    //GPIO62 is connected with Trigger pin, high, trigger off
    init_AD9106_EBZ ();
    DELAY_US(2);
    GpioDataRegs.GPBCLEAR.bit.GPIO62 = 1;    //Low, trigger on
    DELAY_US(10);

    GpioDataRegs.GPBSET.bit.GPIO32 = 1;   // DISABLE PWM

    //enable interrupts: Cpu timer int1.7 ; epwm1 int3.1 epwm2 int3.2
    EnableInterrupts();

// Main loop for the communications with LabVIEW
    for(;;)
    {
```

162

```c
        i=0;
        do {
          // Wait for incoming character from RS232 port
              while(SciaRegs.SCIFFRX.bit.RXFFST !=1) {timer_flag++; }     // wait for XRDY =1 for empty
state
          ReceivedChar = SciaRegs.SCIRXBUF.all;      // Get character
          temp = ReceivedChar & 0xFF;              // strip off the error bits
          letter[i]=temp;
          i++;
        }while(temp != '\n');

        // Get incoming parameters from LabVIEW GUI
        nc =
sscanf(letter,"%d %d %d %d %d %d %d %d %d",&par1,&par2,&par3,&par4,&par5,&par6,&par7,
&par8,&par9,&par10);
          update_panel(); //update the display of front panel of Labview
          transfer_data();// transfer the stored data of output voltage to Labview
          LoopCount++;        // Count LabVIEW data transfer cycles
   }


interrupt void ISREPwm1_Zero(void)
{

     signal_gen_control (RAMUPDATE,0x0001);
     signal_gen_control (PAT_STATUS,0x0001);

      AdcRegs.ADCTRL2.bit.RST_SEQ1 = 1;    // Reset SEQ1/SEQ - instantaneous reset
(RST_SEQ1 bit doesn't stay at 1)
      AdcRegs.ADCTRL2.bit.SOC_SEQ1 = 1;    // Allows SEQ1/SEQ to be started by ePWM1SOCA
trigger
     Adc_Inquire();
     Current_iL1   = B0;    //from ADCINA0
     Current_iL2   = B1;    //from ADCINB0
     Voltage_Input = B2;    //from ADCINA1
     Voltage_Output = B3;    //from ADCINB1

       s1[datacount]= B0;
       datacount++;
     if (datacount==32)
        datacount=0;

       s2[datacount2]= B3;
         datacount2++;
      if (datacount2==32)
        datacount2=0;

     phase_offset=0;

     signal_gen_control (START_ADDR2,0x2ee0); //0x2ee0
     signal_gen_control (STOP_ADDR2,0x8ca0); //0xfff0 final address 1500points 0x8ca0


     EPwm1Regs.CMPA.half.CMPA =par2;
     EPwm3Regs.CMPA.half.CMPA =par2;
     EPwm6Regs.CMPA.half.CMPA =par3;

//    adjust the phase shift between PWM clock signal and conpensated waveform
     EALLOW;
     EPwm1Regs.TBPHS.half.TBPHS = 0;         // Phase is 0
     EPwm3Regs.TBPHS.half.TBPHS = (int)(par9);
```

163

```
    if((int)par9<=1499)
    EPwm6Regs.TBPHS.half.TBPHS = (int)(par9+1500);
    else if ((int)par9>1499)
    EPwm6Regs.TBPHS.half.TBPHS = (int)(par9-1500);

     EDIS;

  ISR_count1++;

  PWM2_flag++;
 if (PWM2_flag==20000)   //
  {
  PWM2_flag=0;
  EPwm2_Compare+=10;
  }
 if (EPwm2_Compare>=1400)
  EPwm2_Compare=10;

  dutycycle=EPwm1Regs.CMPA.half.CMPA;

  EPwm1Regs.ETCLR.bit.INT=1;
  PieCtrlRegs.PIEACK.all=PIEACK_GROUP3;


  if(par8&0x0004)
   GpioDataRegs.GPBCLEAR.bit.GPIO32 = 1;    //TRIP ON, DISABLE PWM
  else
    GpioDataRegs.GPBSET.bit.GPIO32 = 1;    //TRIP OFF, ENABLE PWM

   if(par8&0x0005)
    gain=4000-B2*15;   //if yes, gain is calculated by input voltage
    else
    gain=par7; //if no the value of gain is set by sliding bar step-up bottom
  if (gain<=0)
   gain=0;

    Vout_Ref=(int)(par10*21);
   V_loop_return=VoltLoopControlArith(Vout_Ref,Voltage_Output);

    T0_count = CpuTimer0Regs.TIM.half.LSW; // Latch lower 16-bits of timer0
}

void signal_gen_control (int16 addr,int16 command)
{

GpioDataRegs.GPACLEAR.bit.GPIO12 = 1;
SpiaRegs.SPITXBUF=addr;               //  Register address

SpiaRegs.SPITXBUF=command;            // Register command

DELAY_US(1.2); //1.5
GpioDataRegs.GPASET.bit.GPIO12 = 1;    //Pulse CS high disable

}

void update_panel(void)
{
   Uint16 nc1;              // sprintf error code
   static char sbuf[100];      // output string for sprintf
```

164

```
    nc1 =
sprintf(sbuf,"%u %u %u %u %lu %lu %lu %d %u %d\r\0",B2,B3,B0,B1,LoopCount,ISR_count1,ISR_co
unt2,offset,dutycycle,T0_count);
    scia_msg(sbuf);


}

void transfer_data(void)

{
    int dx;
    int ii=0;
    int jj=0;
    Uint16 nc;                  // sprintf error code
    static char sbuf[100];      // output string for sprintf

    for (ii=0;ii<=32;ii++)
    {
        dx=s1[ii];
        nc = sprintf(sbuf,"%d \r\0", dx);
        scia_msg(sbuf);
    }

    for (jj=0;jj<32;jj++)
    {
        dx=s2[jj];
        nc = sprintf(sbuf,"%d \r\0", dx);
        scia_msg(sbuf);
    }

    dx=s2[32];
    nc = sprintf(sbuf,"%d \r\n\0", dx);
    scia_msg(sbuf);
}
```

2. Calculation of Monodromy matrix in Matlab

The Monodromy matrix can be calculated numerically in Matlab/Simulink. The following codes show the process of calculation according to the theoretical derivation presented.

```
% Initialisation
clc, clear, cnt=1;
syms d a phia;
syms tau x0_1 x0_2 x0_3 x01 x0 x0_4
x0=[x0_1; x0_2; x0_3; x0_4];
Vin=100; L1=200e-6; L2=200e-6;C=20e-6; R=57.6/2; T=10e-6;Ki=500;Kp=5;Kil=1/4;Kvc=5/240;mc=-
0.3;
 iL10=0; iL20=0;Vc0=0; Vp0=0;Vref1=5;a1=0;

A_on_on=[-1/R/C 0 0 0; 0 0 0 0 ; 0 0 0 0 ; Ki*Kvc 0 0 0];
A_on_off=[-1/R/C 0 1/C 0;0 0 0 0;-1/L2 0 0 0;Ki*Kvc 0 0 0];
A_off_on=[-1/R/C 1/C 0 0 ;-1/L1 0 0 0;0 0 0 0;Ki*Kvc 0 0 0];
A_off_off=[-1/R/C 1/C 1/C 0;-1/L1 0 0 0;-1/L2 0 0 0;Ki*Kvc 0 0 0];
Ba=[ 0 0 0 0; 0 0 1/L1 0; 0 0 1/L2 0;0 0 0 -Ki];% Bb=Ba;Bc=Bb;Bd=Bc;
Ua=[0; 0; Vin;Vref1*(1+a1*sin(4*pi*tau/T-4*pi*d))];
Ub=[0; 0; Vin;Vref1];
```

165

```matlab
Vin1=80:1:125;
hold on;
for ii=38:42
% ***********************************************
Vin=Vin1(ii);
sim('Interleaved_close_loop_supervision_control_slope_compensation');

iL100=iL1n(end-2,2);
iL200=iL2n(end-2,2);
Vc00=Vc1(end-2,2);
int00=Int(end-2,2);

x00=[Vc00;iL100;iL200;int00];

%duty cycle calculation
duty=Dutycycle1(end-1,1)/T;

B1=Ba;U=Ua;

if duty<0.5
  %%%%%%%%% When d<0.5;
  A1=A_on_off; A2=A_off_off;A3=A_off_on;A4=A_off_off;
  phi1=expm(A1*d*T); phi2=expm(A2*0.5*(1-2*d)*T);
  phi3=expm(A3*d*T); phi4=expm(A4*0.5*(1-2*d)*T);

  I1=int(expm(A1*(d*T-tau))*B1*U,tau,0,d*T);
  I2=int(expm(A2*(0.5*T-tau))*B1*U,tau,d*T,0.5*T);
  I3=int(expm(A3*((0.5+d)*T-tau))*B1*U,tau,0.5*T,(0.5+d)*T);
  I4=int(expm(A4*(T-tau))*B1*U,tau,(0.5+d)*T,T);

else if duty>0.5
  %%%%%%%%%%% When d>0.5
  A1=A_on_on; A2=A_on_off; A3=A_on_on; A4=A_off_on;

  phi1=expm(A1*0.5*(2*d-1)*T); phi2=expm(A2*(1-d)*T);
  phi3=expm(A3*0.5*(2*d-1)*T); phi4=expm(A4*(1-d)*T);

  I1=int(expm(A1*(0.5*(2*d-1)*T-tau))*B1*U,tau,0,0.5*(2*d-1)*T);
  I2=int(expm(A2*(0.5*T-tau))*B1*U,tau,0.5*(2*d-1)*T,0.5*T);
  I3=int(expm(A3*(d*T-tau))*B1*U,tau,0.5*T,d*T);
  I4=int(expm(A4*(T-tau))*B1*U,tau,d*T,T);

  else if duty==0.5
   %%%%%%%%%%% When d=0.5
  %A1=A_on_off; A2=A_off_on;A3=A_on_off;A4=A_off_on;
    end
   end
end

 %----------------------------------
x1=phi1*x0+I1;
x2=phi2*x1+I2;
x3=phi3*x2+I3;
x4=phi4*x3+I4;

x1=subs(x1,[d,x0_1,x0_2,x0_3,x0_4],[duty,Vc00,iL100,iL200,int00]);
x2=subs(x2,[d,x0_1,x0_2,x0_3,x0_4],[duty,Vc00,iL100,iL200,int00]);
x3=subs(x3,[d,x0_1,x0_2,x0_3,x0_4],[duty,Vc00,iL100,iL200,int00]);
```

166

```
x4=subs(x4,[d,x0_1,x0_2,x0_3,x0_4],[duty,Vc00,iL100,iL200,int00]);

phi1=subs(phi1,d,duty); phi2=subs(phi2,d,duty);
phi3=subs(phi3,d,duty); phi4=subs(phi4,d,duty);

if duty<0.5
   %%%%%%%%% When d<0.5;

   spa=-Kp*Kvc*(x1(3)*R-x1(1))/R/C-Kil*Vin/L1+Ki*(Vref1-Kvc*x1(1));
   spb=-Kp*Kvc*(x3(2)*R-x3(1))/R/C-Kil*Vin/L2+Ki*(Vref1-Kvc*x3(1));
    sa=mc/T;

    S12=[1-Kp*Kvc*x1(2)/C/(spa+sa) -Kil*x1(2)/C/(spa+sa) 0 x1(2)/C/(spa+sa);
    Kp*Kvc*x1(1)/L1/(spa+sa) 1+Kil*x1(1)/L1/(spa+sa) 0 -x1(1)/L1/(spa+sa);
    0 0 1 0;
    0 0 0 1];

    S34=[1-Kp*Kvc*x3(3)/C/(spb+sa) 0 -Kil*x3(3)/C/(spb+sa) x3(3)/C/(spb+sa);
    0 1 0 0;
    Kp*Kvc*x3(1)/L2/(spb+sa) 0 1+Kil*x3(1)/L2/(spb+sa) -x3(1)/L2/(spb+sa);
    0 0 0 1];

    M=phi2*S12*phi1*phi4*S34*phi3;
    eig(M)

else if duty>0.5
   %%%%%%%%%% When d>0.5

   spa=Kp*Kvc*x1(1)/R/C-Kil*Vin/L1+Ki*(Vref1-Kvc*x1(1));
   spb=Kp*Kvc*x3(1)/R/C-Kil*Vin/L2+Ki*(Vref1-Kvc*x3(1));

   sa=mc/T;

    S12=[1-Kp*Kvc*x1(3)/C/(spb+sa) 0 -Kil*x1(3)/C/(spb+sa) x1(3)/C/(spb+sa);
    0 1 0 0;
    Kp*Kvc*x1(1)/L2/(spb+sa) 0 1+Kil*x1(1)/L2/(spb+sa) -x1(1)/L2/(spb+sa);
    0 0 0 1];

    S34=[1-Kp*Kvc*x3(2)/C/(spa+sa) -Kil*x3(2)/C/(spa+sa) 0 x3(2)/C/(spa+sa);
    Kp*Kvc*x3(1)/L1/(spa+sa) 1+Kil*x3(1)/L1/(spa+sa) 0 -x3(1)/L1/(spa+sa);
    0 0 1 0;
    0 0 0 1];
      M=phi2*S12*phi1*phi4*S34*phi3;
    eig(M)

   else if duty==0.5
    %%%%%%%%%% When d=0.5
   A1=A_on_off; A2=A_off_on;A3=A_on_off;A4=A_off_on;
      end
    end
end

 plot(real(eig(M)),imag(eig(M)),'o','MarkerSize',10,'color','g');

 end
```

167
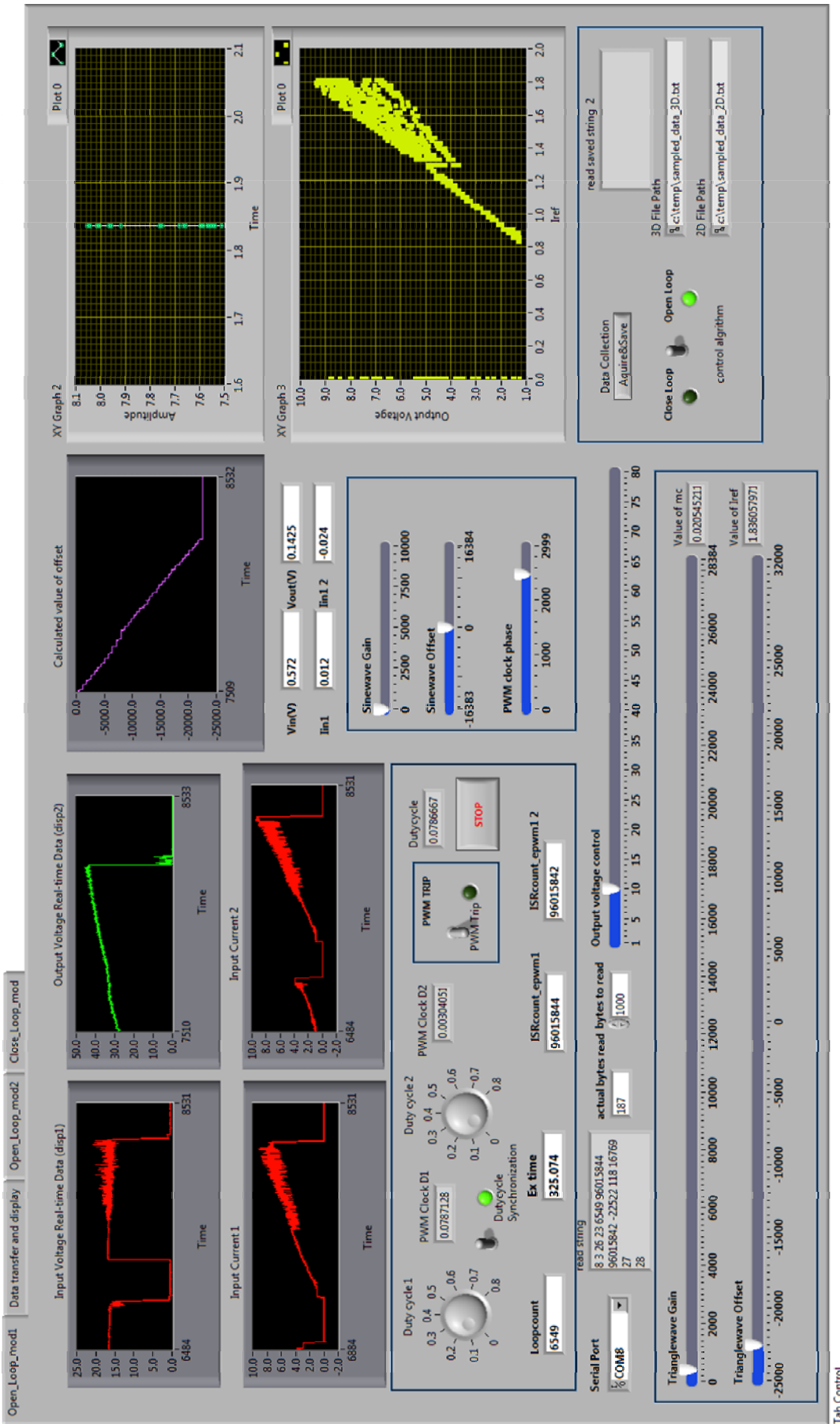
Figure A5.1 User interface panel in Labview

Figure A5.1 shows the complete user interface panel in Labview. This panel is used to monitor and display the sampled variables and the calculated values of digital PID. The operational conditions of the converter can be changed manually using the relevant control buttons. By using the button for data collection, the sampling results are transferred and generated as a date file which is stored in the user's laptop.

(a)

(b)
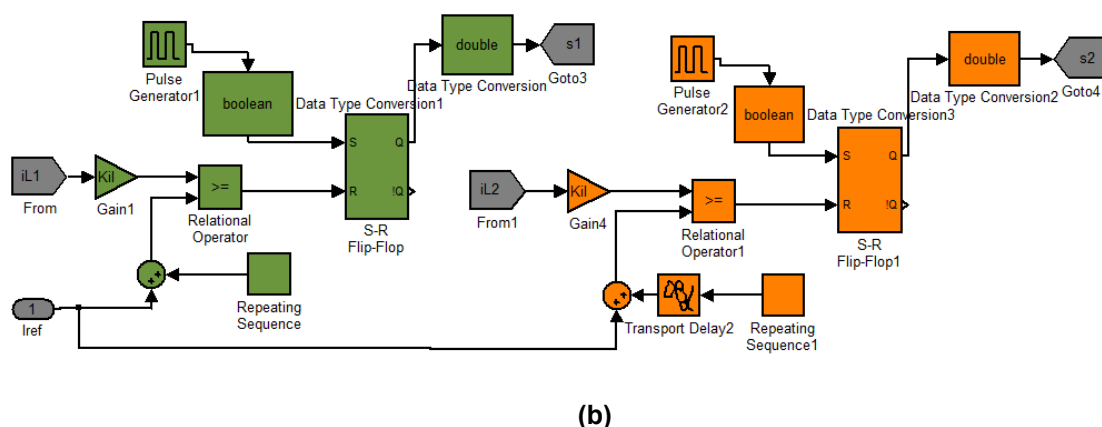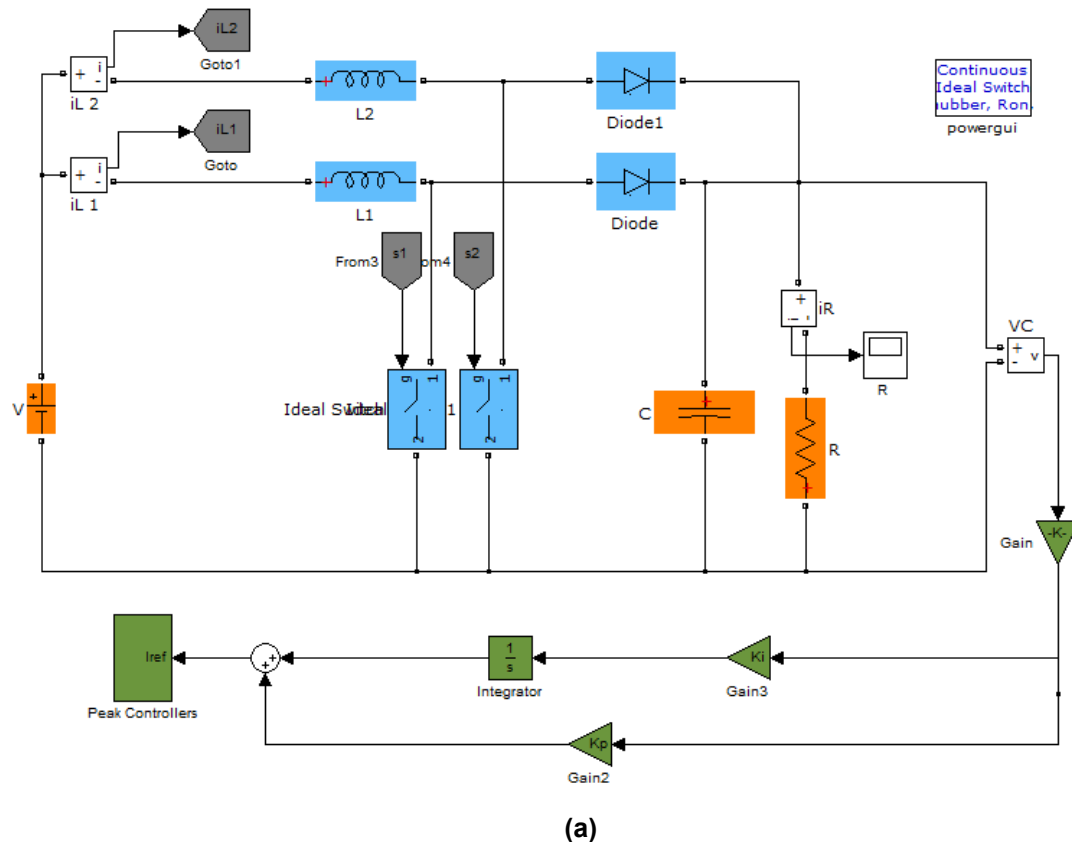
Figure A5.2 Diagram of simulation blocks in Matlab/Simulink: (a) main circuit of interleaved boost converter; (b) corresponding control blocks of peak current controller

The main circuit of the interleaved boost converter and its corresponding control blocks of the peak current controller are illustrated in Figure A5.2.

169

A photograph of the prototype of the interleaved boost converter is presented in Figure A5.3 and the tested conversion results of employed voltage and current Hall sensors are illustrated in Figure A5.4. Both graphs demonstrate excellent linear performance at various input signals.
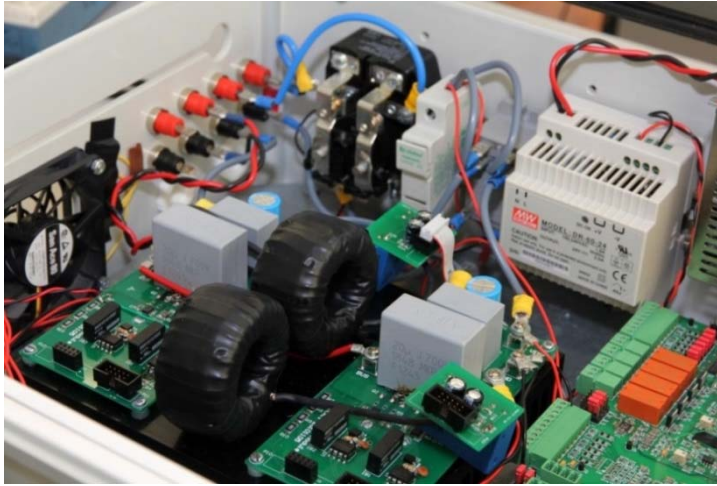
Figure A5.3 Prototype of the interleaved boost converter
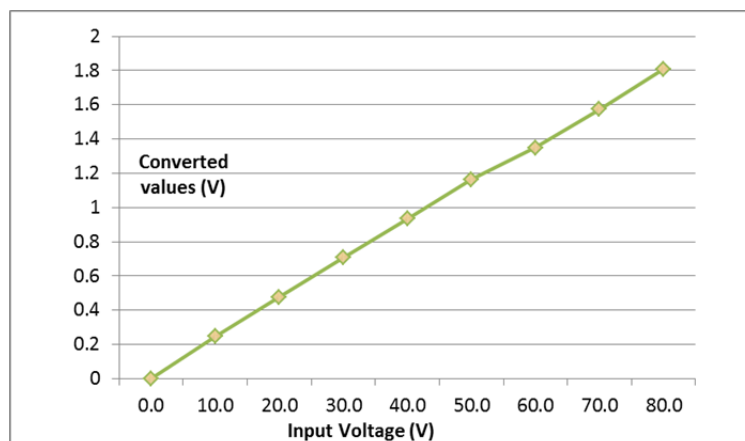
(a) voltage Hall sensor
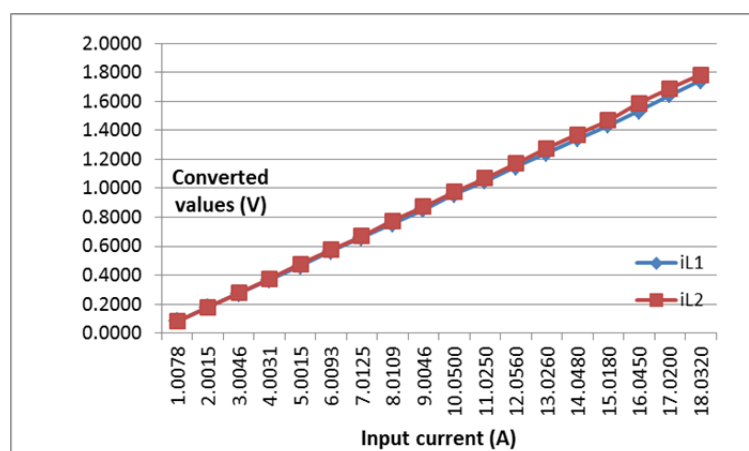
(b) current Hall sensors

Figure A5.4 Tested conversion results of voltage and current Hall sensors

170

Figure A5.5 TI f28335 based Digital Signal Controller (DSC)

Figure A5.5 presents the TI f28335 based Digital Signal Controller, which is used in the testing bench.